

https://dspace.org/

Titanium dioxide-carbon spheres composites for use as supports in cobalt Fischer-Tropsch synthesis

Phadi, Thabiso Terence

2013-02-14
http://hdl.handle.net/10539/12426

Downloaded from a DSpace repository. https://dspace.org/

TITANIUM DIOXIDE-CARBON SPHERES COMPOSITES FOR USE AS SUPPORTS IN COBALT FISCHER-TROPSCH SYNTHESIS

Thabiso Terence Phadi

A thesis submitted to the Faculty of Science at The University of the Witwatersrand, Johannesburg, in fulfilment of the requirements for the degree of

Doctor of Philosophy

Johannesburg, 2012

DECLARATION

I know the meaning of plagiarism and I declare that all the work in this thesis is my own, unaided work under the supervision of Professor Neil J. Coville. It is being submitted for the degree of Doctor of Philosophy in the University of the Witwatersrand, Johannesburg. It has not been submitted before for any degree or examination in any other body or organization or person outside the University of the Witwatersrand, Johannesburg.

_____

(Signed) Thabiso Terence Phadi

On this ____day of _____2012

ABSTRACT

Fischer-Tropsch (FT) synthesis is a reaction which entails the conversion of synthesis gas, also known as syngas (a mixture of H_2 and CO gases), to liquid hydrocarbon fuels, oxygenated hydrocarbons, chemicals and water. This syngas mixture is obtained from natural gas, coal, petroleum, biomass or even from organic wastes. In this study cobalt catalysts supported on novel carbon sphere-titania (CS-TiO_2) composite materials were synthesized and tested for their performance in the FT process.

Initially carbon spheres (d = 80-120 nm) were prepared in a vertical swirled floating chemical vapour deposition reactor without the use of a catalyst. The rate of production was controlled and the highest production rate of about 195 mg/min was obtained at an acetylene (C_2H_2) flow rate of 545 mL/min at 1000 °C. The produced carbon spheres (CSs) had a narrow size distribution with a uniform diameter size. Purification and functionalisation of the CSs improved the total surface area, due to the removal of PAHs which blocked the CS pores. The introduction of functional groups to the CSs was achieved and these changed the wetting properties of the CSs. Functionalising the CSs for longer than 17 h in HNO_3 destroyed the morphology of the CSs.

After successful preparation of functionalised CSs, the interactions between CSs and TiO_2 were studied by in the TiO_2 composite using two different sol-gel methods, namely the conventional sol-gel and the surfactant wrapping sol-gel method. The surfactant wrapping sol-gel method entailed the modification of the CSs by dispersing them in a surfactant, in this case hexadecyltrimethylammonium bromide or CTAB [$(CH_3(CH_2)_{15}N(CH_3)_3Br$]. This introduced alkyl “tails” which eased the dispersability of the CSs before coating them with $Ti[O(CH_2)_3CH_3]_4$ (a source of TiO_2) to produce a homogeneously coated CS-TiO_2 composite material (defined as ASW3). It should be mentioned that many, many experiments were performed to develop an efficient and reliable method to make homogeneously

coated CS-TiO_2 composites since it was found to be very difficult to achieve an interaction between carbonaceous materials and TiO_2 especially by sol-gel procedures.

The traditional sol-gel method was used to prepare CS-TiO_2 composites with different ratios viz. 1CS-1SG, 1CS-2.5SG, 1CS-5SG, 1CS-10SG, 1CS-25SG and 1CS-50SG. These composites showed weak interactions between CSs and TiO_2 even at high TiO_2 loading ratio. Interestingly the surface area of these composites showed high values of 80 and 85 m^2/g for 1CS-5SG and 1CS-10SG, respectively. At lower TiO_2 ratios the measured surface area was similar to that of CSs, i.e 10 m^2/g for 1CS-1TiO_2. At high TiO_2 ratios the measured surface area was similar to that of TiO_2, i.e 49 m^2/g for 1CS-50TiO_2.

The TEM images of CS-TiO_2 (ASW3) composites prepared by surfactant wrapping methods showed a successful TiO_2 coating of CSs. The TiO_2 grain size was 8.0 nm with both anatase and rutile phases. High surface areas (up to 98 m^2/g) of composite materials were achieved by employing this procedure. The high surface areas achieved suggest that the interaction between CSs and TiO_2 was homogeneous and the increase was due to the "bridge" formed between CSs and TiO_2.

A series of cobalt catalysts (10% by weight) supported on these materials was carried out by the deposition precipitation method using $Co(NO_3)_2 \cdot 6H_2O$ as the metal precursor. After appropriate drying and calcination the catalysts were characterized using traditional characterisation techniques and tested in the FT reaction using a fixed bed reactor. The the 10%Co/CS catalyst produced a CO conversion of 15.2% while the catalyst had a low total BET surface area (6 m^2/g) compared to non-carbonaceous catalysts with higher BET surface areas. This observation suggests that the surface area did not necessarily play a role in the CO conversion, but that other properties (reducibility and dispersion) of CSs influenced the catalyst activity. After coating CSs with TiO_2 and loading cobalt to produce 10%Co/ASW3 both the BET surface area of the catalyst and the CO

conversion increased to 83 m^2/g and 20.1%, respectively. CO-TPD of 10%Co/ASW3 showed a large amount of strongly adsorbed CO. This increased CO was due to the interaction between CSs and TiO_2 which developed CO adsorptive sites.

DEDICATION

- I dedicate this to the following people:

- My parents Mapule and Freddy Olckers, my sister (Cynthia), and my brother (Ian) for all the support and motivation throughout the years. I love you.

- My grandmother Merriam Mabuya and to the memory of my late grandfather, Simon Mabuya for giving me all the wisdom.

ACKNOWLEDGEMENTS

This thesis would not be complete if the people and institutions that contributed in making this work a success are not acknowledged. This science would not have been possible without the kind and unwavering support of you all. Thank you all very much for the love and support:

Firstly a big thank you goes to my supervisor Professor Neil J. Coville for his guidance, support, brilliant ideas during the research and for proofreading all the manuscripts. I thoroughly enjoyed working with him and loved the atmosphere in the group. I especially enjoyed the tone of our meetings which allowed me to express my views openly.

Many thanks are due to Mr Basil Chassoulas for all the technical assistance and all the times we spent together in the lab.

My friends and colleagues in the CATOMAT research group.

The School of Chemistry and the entire staff members for giving me the grounds to conduct my research. This department has been home away from home.

The electron microscopy unit personnel: Professor Michael Witcomb, Mr. Abe Seema (*late*), Mrs. Caroline Lalkhan and Prof. Ziegler for teaching me how to use the TEM

David and Elias from the chemistry stores, for assisting me with the delivery of the heavy cylinders to Gate House (8^{th} floor)

Mr Rudolf Erasmus for doing the Raman analysis, Natsayi for helping me with all the XRD measurements and Zikhona for helping me with the TEM measurements

I fully acknowledge DST Centre of Excellence in Catalysis (c*change) bursary, The University of the Witwatersrand Postgraduate Merit scholarship, The Vice-Chancellor Merit scholarship award, The Bradlow scholarship and the NRF (extension) for financial assistance.

Last but not least, The God Almighty, for granting me the strength to overcome obstacles and for guiding me throughout this journey.

CONFERENCE PRESENTATIONS

T.T. Phadi, N. J. Coville, SACI conference (The year of chemistry), Wits University, *Titanium dioxide-carbon sphere composites for use as supports in cobalt catalysed Fischer-Tropsch synthesis*, January 2011

T.T. Phadi, N. J. Coville, Wits University postgraduate symposium, "*A new catalyst for the production of fuel for automobiles*" October 2010,

T.T. Phadi, N. J. Coville, Worcester, CATSA conference, *TiO_2 utilised as a possible dress code for carbon spheres as supports for Fischer-Tropsch synthesis* November 2009,

T.T. Phadi, N. J. Coville, Parys, CATSA conference, *Titania coated potassium titanates as supports for catalysts used in Fischer-Tropsch synthesis*, November 2008

PUBLICATIONS

- T.T. Phadi, N. J. Coville, *Carbon sphere-titania composite materials.* **To be submitted**

- T.T. Phadi, N. J. Coville, *Titanium dioxide-carbon sphere composites for use as supports in cobalt catalysed Fischer-Tropsch synthesis.* **To be submitted**

TABLE OF CONTENTS

DECLARATION ..... **I**

ABSTRACT ..... **II**

DEDICATION ..... **V**

ACKNOWLEDGEMENTS ..... **VI**

CONFERENCE PRESENTATIONS ..... **VIII**

PUBLICATIONS ..... **IX**

TABLE OF CONTENTS ..... **X**

LIST OF FIGURES ..... **XV**

LIST OF TABLES ..... **XIII**

LIST OF SYMBOLS ..... **XXV**

Chapter 1 ..... **1**

1. Introduction and literature review **1**

1.1 A brief historical overview and current prospects *1*

1.2 The Fischer-Tropsch synthesis *6*

1.3 The Fischer-Tropsch reaction *8*

1.3.1 Other reactions taking place 8

1.4 Fischer-Tropsch product spectrum *9*

1.5 Factors influencing product selectivity *11*

1.5.1 Operating conditions 11

1.6 Fischer-Tropsch reactors *12*

1.7 Catalysts for Fischer-Tropsch synthesis *15*

1.7.1 Active metals 15

1.7.2 Catalyst supports and promoters 16

1.7.3 Catalyst activation and deactivation 18

1.8 Preparation of Fischer-Tropsch catalysts *21*

1.8.1 Incipient wetness impregnation method 22

1.8.2 pH-controlled precipitation method 23

1.8.3 Deposition-precipitation method 24

1.9 Effect of support on FT catalysts *24*

1.9.1 Carbon-titania composite materials 25
1.9.2 Sol-gel method for composite materials synthesis 28
1.10 Aims and objectives of the study *29*
1.11 Thesis outline *30*
1.11 References *32*

Chapter 2 ..... **39**

2. Experimental Methods **39**

2.1 Introduction *39*
2.2 Preparation of catalyst and support materials *40*
2.2.1 Support preparation 40
2.2.2 Support preparation 41
2.3 Characterization of catalysts and supports *42*
2.3.1 Transmission electron microscopy (TEM) and energy dispersive X-ray spectroscopy (EDS) 42
2.3.2 Thermogravimetric analysis (TGA) 44
2.3.3 X-ray Fluorescence (XRF) spectroscopy 45
2.3.4 BET surface area measurements/BJH pore size distributions 45
3.3.5 X-ray diffraction (XRD) 47
2.3.6 Temperature-programmed techniques (H_2-TPR, CO-TPR and CO-TPD) 48
2.3.7 H_2 chemisorption and O_2 titration analysis 48
2.4 Fischer-Tropsch Synthesis experiments *53*
2.4.1 Reactor system and experimental setup 53
2.4.2 Reactor and catalyst packing 55
2.4.3 Experimental procedure for catalyst evaluations 57
2.5 Product analysis *57*
2.5.1 Gas chromatographic analysis 57
2.5.2 Data work-up 61
2.6 References *64*

Chapter 3.....67

3. Catalyst-free preparation of carbon spheres and their functionalisation. Use of a swirled floating vertically positioned chemical vapour deposition reactor 67

3. 1 Introduction 67

3. 2 Experimental 69

3.2.1 Carbon sphere preparation 69

3.2.2 The purification and functionalization of the carbon spheres..... 71

3.3 Characterisation..... 72

3.3.1 Transmission Electron Microscopy (TEM) 72

3.3.2 Thermogravimetric analysis (TGA)..... 73

3.3.3 Raman spectroscopy 73

3.3.4 XRD 73

3.3.5 BET surface area analysis 74

3.3.6 Zeta Potential measurements 74

3.4 Results and discussion..... 75

3.4.1 Effect of C_2H_2 flow rate..... 75

3.4.2 Purification and functionalisation of CSs 82

3.4.3 Acid group functionalisation 87

3.5 Conclusion..... 91

3. 6 Future work arising from this chapter 91

3.6 Reference..... *92*

Chapter 4.....95

4. Carbon sphere-titania composite materials.....95

4.1 Introduction..... 95

4.2 Experimental 99

4.2.1 CS-TiO_2 composite preparation..... 99

4.2.2 Characterisation 105

4.3 Results and discussion..... 108

4.3.1 Conventional sol-gel method..... 108

4.3.2 Surfactant wrapping..... 132

4.3.2.1 TEM 133
4.3.3 Carbon coated titania materials *147*
4.4 Conclusion *150*
4.5 References *152*

Chapter 5 ..... **156**

5. Titanium dioxide-carbon sphere composites for use as supports in cobalt catalysed Fischer-Tropsch synthesis **156**

5.1 Introduction *156*
5.2 Experimental *159*
5.2.1 Support preparation 159
5.2.2 Catalyst preparation 162
5.3 Catalyst characterization *164*
5.3.1 Transmission electron microscopy (TEM) 164
5.3.2 Thermogravimetric analysis (TGA) 164
5.3.3 BET surface area analysis 165
5.3.4 XRD and XRF measurements 165
5.3.5 Temperature programmed reduction 166
5.3.6 H_2-chemisorption and O_2 titration 166
5.4 Results and discussion *168*
5.4.1 TEM 168
5.4.2 N_2 adsorption-desorption 173
5.4.3 TGA 174
5.4.4 TPR and TPD 177
5.4.5 H_2-Chemisorption and O_2 titration 184
5.4.6 Fischer-Tropsch synthesis 187
5.4.7 Discussion 191
5.5 Conclusion *193*
5.6 References *195*

Chapter 6..... 198

6. General conclusions 198

6.1 Future studies may entail:..... 201

LIST OF FIGURES

CHAPTER 1

Figure 1.1 The worlds rise and fall of oil price over time. Adapted from [6]..... 2

Figure 1.2 Summarised worldwide gtl activity and announcements. Adapted from [3]..... 2

Figure 1.3 Simple FT stepwise growth process (where '∗' symbolises a surface). Adapted from [24]..... 7

Figure 1.4 Theoretical FTS product distribution of products produced by the Anderson-Schulz-Flory model as a function of chain growth probability [30] 10

Figure 1.5 Product distribution with iron and cobalt based catalysts [31]..... 12

Figure 1.6 Deactivation mechanisms: (a) coke formation, (b) poisoning, (c) sintering of active metal particles and (d) sintering and solid-solid phase transitions and encapsulation of active metal particles [56] 20

Figure 1.7 Schematic representation of experimental set up for incipient wetness impregnation. Adapted from [53] 22

Figure 1.8 CNT-TiO_2 composites. (a) TiO_2 nanoparticles on SWCNTs [102], (b) TiO_2 nanoparticles on mwcnts [103], (c) SWCNTs on TiO_2 nanoparticles [104], (d) TiO_2 coated SWCNTs [105], (e) TiO_2 coated MWCNTs [106], (f) CNT and TiO_2 embedded in polymer nanofibres [107], (g) laminate composite films [108], (h) intermixed CNTs and TiO_2 nanotubes [109], (i) MWCNTs grown or deposited on bulk TiO_2 [110], (j) CNTs grown in TiO_2 nanotube arrays [111], (k) Yttrium treated CNT- TiO_2 [112] and (l) TiO_2 nanotube arrays produced via sacrificial CNT templates [113]. Adapted from [114]..... 27

CHAPTER 2

Figure 2.1 schematic representation of a vertically positioned swirled floating chemical vapour deposition reactor setup. 41

Figure 2.2 TEM Fei Technai Spirit G^2 43
Figure 2.3 Perkin Elmer STA 4000 Thermogravimetric analyzer coupled to an auto sampler: *(left)* manual-single sample analysis and *(right)* an autosampler-multiple samples analysis (with an autosampler arm in operation) 44
Figure 2.4 (a) Micromeritics flow prep 060, (b) micromeritics tristar 3000 and (c) liquid N_2 coolant dewar depicting the Isothermal Jacket^{TM} method of maintaining the cold/warm volume ratio in the sample tube 46
Figure 2.5 The bruker D8 X-ray diffractometer.....47
Figure 2.6 Micromeritics Auto Chem II.....49
Figure 2.7 Micromeritics ASAP 2020 50
Figure 2.8 A schematic diagram for the reactor system.....54
Figure 2.9 Gas chromatography one fitted with fid and the other with a TCD detector.....55
Figure 2.10 A diagrammatic representation (top) and a digital image (bottom) of a stainless-steel fixed bed reactor that has been used 56
Figure 2.11 A typical spectrum for the synthesis gas (bypass) using TCD-GC ...58
Figure 2.12 A typical product and unreacted syngas spectrum using TCD-GC ...58
Figure 2.13 A typical FT spectrum for gaseous products obtained from an FID-GC. 60
Figure 2.14 A typical FT spectrum (spiked with octane 1l) for gaseous products obtained from an FID-GC (only major peaks are labeled here).....60
Figure 2.15 A typical FT spectrum (spiked with octane) for gaseous products obtained from an FID-GC (only major peaks are labeled here).....61

CHAPTER 3

Figure 3.1 The structure of carbon black showing some functional groups on the surface of the carbon sphere structure [32] 68
Figure 3.2 Schematic representation of a vertically positioned swirled floating chemical vapour deposition reactor setup. 69

Figure 3.3 Photograph of soot collected from the cyclones (match stick used as reference to give a sense of size)..... 70
Figure 3.4 Schematic representation of conventional soxhlet extraction set-up for the purification of CSs 71
Figure 3.5 TEM images of P-CS prepared at different C_2H_2 flow rates with their corresponding particle size distributions (solid line = particle size distribution histogram, and dashed line = Gaussian distribution): (a) and (d) 300 ml/min; (b) and (e) 400 ml/min; and (c) and (f) 545 ml/min..... 76
Figure 3.6 Rate of CS growth as a function of C_2H_2 flow rate 77
Figure 3.7 Rate of CS growth as a function of C_2H_2 flow rate 78
Figure 3.8 TGA and DTG of P-CS left in the quartz reactor for: 4 min (*top)* and 8 min *(bottom)*..... 79
Figure 3.9 TEM image and particle size distribution (solid line = particle size distribution histogram, and dashed line = Gaussian distribution) of CSs sample that was annealed for 6 h in CVD..... 80
Figure 3.10 TGA (*top*) of P-CS left in the quartz reactor for 8 min and 6 h with their respective DTG (*bottom*) curves..... 81
Figure 3.11 Xrd patterns of P-CS and T-CS 82
Figure 3.12 Raman spectra of P-CS produced at 300 ml/min, T-CS, F-CS and F-T-CS 83
Figure 3.13 TGA of P-CS, soxhlet extracted CSs and F-Cs 84
Figure 3.14 TEM micrographs of CSs: (a) P-CS, (b) T-CS, (c) F-CS17h, (d) F-CS24h, (e) F-CS30h and (f) F-CS40h..... 85
Figure 3.15 BJH pore size distributions (calculated from the adsorption arms of N_2 isotherms) of P-CS, T-CS and F-CS17h..... 86
Figure 3.16 FTIR spectra of (a) pristine CSs, (b) T-CSs, (c) F-CS0.5h, (d) F-CS1h, (e) F-CS2h, (f) F-CS5h, (g) F-CS10h, (h) F-CS17h and (i) F-CS40h. (*inset)*: magnified FTIR spectra of pristine CSs (between 1450 and 1800 cm^{-1})..... 88
Figure 3.17 Settling pictures of (a) P-CS, (b) F-CS1h, (c) F-CS2h, (d) F-CS5h and (e) F-CS17h in H_2O..... 89

Figure 3.18 Zeta potential of P-CS, F-CS5h and F-CS17h suspensions as a function of pH 90

CHAPTER 4

Figure 4.1 Rising interest in photocatalysis and the potential role of carbonaceous nanomaterials. The graphs show the approximate annual number of publications relating to (a) TiO_2, (b) carbonaceous nanomaterials and, (c) carbonaceous nanomaterials coupled with TiO_2 employed in photocatalysis. Adapted from [5]..... 97

Figure 4.2 A schematic representation of the set up used for the preparation of cs-TiO_2 composites by the conventional sol-gel method. Adapted from [46]. 100

Figure 4.3 A schematic representation of the CS-TiO_2 composite prepared via the surfactant wrapping sol-gel method. 102

Figure 4.4 TEM image of pure TiO_2 (*top*) and particle size distribution (*bottom*) prepared without the presence of css by a conventional sol-gel method. (solid line = particle size distribution histogram, and dashed line = Gaussian distribution). 109

Figure 4.5 TEM images of CS-TiO_2 composites prepared by a conventional sol-gel method: (a) 1CS-1SG, (b) 1CS-2.5SG, (c) 1CS-5SG, (d) 1CS-10SG, (e) 1CS-25SG and (f) 1CS-50SG 110

Figure 4.6 EDX spectrum corresponding to the surface coverage shown in Fig. 4.5(c). C and Ti were detected; the Cu signal corresponds to the Cu grid substrate for tem analysis. 111

Figure 4.7 TGA profiles of the F-CS, uncalcined 0CS-SG and the calcined 0CS-SG (350 °C) samples..... 112

Figure 4.8 DTG of F-CS, uncalcined 0CS-TiO_2 and the calcined 0CS-SG..... 112

Figure 4. 9 TGA of P25 TiO_2, P25 TiO_2 mixed with HNO_3, and P25 TiO_2 mixed with butanol (*inset*) 114

Figure 4.10 DTG of P25 TiO_2 mixed with hno_3 and P25 TiO_2 mixed with butanol 114

Figure 4.11 TGA uncalcined 1CS-2.5SG, 1CS-5SG, 1CS-10SG, 1CS-25SG and 1CS-50SG 115

Figure 4.12 DTG of uncalcined 1CS-2.5SG, 1CS-5SG, 1CS-10SG, 1CS-25SG and 1CG-50SG 115

Figure 4.13 Analysis of css weight loss and residue tio$_2$ for the composite samples as a function of CS-TiO_2 composite ratio. Data were obtained from TGA measurements..... 117

Figure 4.14 TGA of 1CS-10SG samples after calcination at: 1 bar 350 °C for 6 h; 1 bar 350 °C for 13 h; 5 bar 350 °C for 6 h; and 5 bar 400 °C for 6 h..... 118

Figure 4.15 TEM images of 1CS-10SG samples after calcination at: (a) 1 bar 350 °C for 6 h; (b) 1 bar 350 °C for 13 h; (c) 5 bar 350 °C for 6 h; and (d) 5 bar 400 °C for 6 h 120

Figure 4.16 XRD patterns of calcined sol-gel derived TiO_2 (0CS-SG) and F-CS. The peaks marked with (a) and (002, 100) correspond to TiO_2 (anatase) and CSs, respectively 121

Figure 4.17 XRD patterns of calcined sol-gel derived composite materials, where A = anatase phase, B = brookite and R = rutile phase. 122

Figure 4.18 Raman spectra of uncalcined 0CS-SG sample; and of calcined 0CS-SG samples at: 1 bar 350 °C for 6 h, and 1 bar 400 °C for 6 h. Raman spectra of bulk commercial TiO_2 material (P25 TiO_2) is shown on the *inset*. 123

Figure 4.19 Raman spectra of calcined F-CS produced, showing D and G-bands 125

Figure 4.20 Raman spectra of calcined bulk 0CS-SG (calcined at 400 °C) and calcined CS-TiO_2 composites prepared by conventional sol-gel with ratios of: 1CS-2.5SG, 1CS-5SG and 1CS-25SG (calcined at 400 °C). 125

Figure 4.21 Nitrogen adsorption-desorption isotherm and its BJH pore size distribution curve (*inset*) of F-CS 129

Figure 4.22 Nitrogen adsorption-desorption isotherms of calcined (350 °C) P25 TiO_2, uncalcined 0CS-SG, and calcined 0CS-SG (at 350 and 400 °C) 130

Figure 4.23 Nitrogen adsorption-desorption isotherms of 1CS-1SG, 1CS-2.5SG, 1CS-10SG, and 1CS-25SG 131

Figure 4.24 BJH pore size distributions (calculated from the adsorption arms of N_2 isotherms) of 1CS-1SG, 1CS-2.5SG, 1CS-10SG, and 1CS-25SG 132

Figure 4.25 TEM images of CS-TiO_2 composites prepared by a surfactant wrapping sol-gel method, for: (a) A1, (b) A3, (c) SW1, (d) SW3, (e) ASW1 and (f) ASW3, where (A = acid treated but not surfactant wrapped CSs, SW1 = surfactant wrapped, but not acid treated CSs, ASW = acid treated and surfactant wrapped CSs). 1 and 3 represents the number sol-gel coating cycles 135

Figure 4.26 Particle size distribution of TiO_2 in ASW3 (solid line = particle size distribution histogram, and dashed line = Gaussian distribution) prepared by a surfactant wrapping sol-gel method 136

Figure 4.27 EDX spectrum corresponding to the F-CS surface coverage by TiO_2 shown in Fig. 4.25 (f). C and Ti were detected; the Cu signal is corresponding to the Cu grid substrate for TEM analysis. 137

Figure 4.28 TEM images of TiO_2 residue from combusted ASW3 composite. Samples were combusted in air at 5 bar for 6h at: (a) 300 °C and, (b) 400 °C 138

Figure 4.29 EDX spectrum of TiO_2 residue corresponding to sample (b) in Fig. 4.28 138

Figure 4.30 XRD patterns of TiO_2 residues from combusted ASW3 composite material where A = anatase phase, B = brookite and R = rutile phase. Samples were combusted in air at 5 bar for 6h at: 300 °C and at 400 °C, respectively. XRD pattern of the F-CS is shown on the *inset.* 139

Figure 4.31 Raman spectra of of TiO_2 residue from combusted AS3 composite sample. Samples were combusted in air at 5 bar for 6h at: (a) 300 °C and, (b) 400 °C. Raman spectra of bulk uncombusted ASW3 is shown on the *inset*. 140

Figure 4.32 TGA (*left*) and DTG (*right*) of uncalcined A1, A2 and A3 142

Figure 4.33 TGA (*left*) and DTG (*right*) of uncalcined SW1, SW2 and SW3 .. 142

Figure 4.34 TGA (*left*) and DTG (*right*) of uncalcined ASW1, ASW2 and ASW3 142

Figure 4.35 Nitrogen adsorption-desorption isotherms of uncombusted ASW3 composite, calcined in air (300 °C, 6 h, 1 bar) and TiO_2 residue from combusted ASW3 at 400 °C in air 6h 5 bar 147

Figure 4.36 TEM images of carbon coated titania materials (C-TiO_2) prepared by CVD: (a) C0-TiO_2, (b) C5-TiO_2, (c) C30-TiO_2, (d) C60-TiO_2, (e) C120-TiO_2 and (f) C240-TiO_2 149

CHAPTER 5

Figure 5.1 Cobalt time yield for a variety of Co/Al_2O_3, Co/SiO_2 and Co/TiO_2 supported catalysts. Adapted from [9]. 15/

Figure 5.2 (a) and (b) TEM images of 10%Co/F-CS1h indicating cobalt crystallites forming aggregated clusters (cluster size ~ 81 nm based on 50 clusters); (c) and (d) 10%Co/F-CS17h indicating well dispersed cobalt particles on the surface (cobalt particle size ~ 4 nm based on 80 particles) 168

Figure 5.3 TEM images showing cobalt dispersed at different supports: (a) 10%Co/SG, (b) 10%Co/P25, (c) 10%Co/AS3, (d) 10%Co/CNT, (e) 10%Co/CNT-TiO_2 and (f) 10%Co/TNT 171

Figure 5.4 (a), (b) and (c) EDX spectra corresponding to the surface coverage shown in Fig. 5.3 (a), (c) and (e), respectively. C and Ti were detected; the Cu signal corresponds to the Cu grid substrate used in the TEM analysis. 172

Figure 5.5 TGA and DTA profiles for the 10%Co/CS catalyst in air atmosphere; (a) before calcination and (b) after heating in N_2 (220 °C, 150 min) 175

Figure 5.6 TGA profiles for the 10%Co/P25, 10%Co/SG, 10%Co/ASW3, 10%Co/CNT-TiO_2, 10%Co/TNT and 10%Co/C-TNT catalysts in air atmosphere before calcination..... 176

Figure 5.7 TPR of uncalcined unsupported cobalt oxide precursor..... 177

Figure 5.8 H_2-TPR of SG, CS and CNT 179

Figure 5.9 H_2-TPR of P25, TNT and ASW3..... 179

Figure 5.10 H_2-TPR of calcined supported cobalt catalysts..... 179

Figure 5.11 CO-TPD of calcined supports; i.e. ASW3, CNT-TiO_2, CNT, SG and CS..... 182

Figure 5.12 CO-TPD of calcined supported cobalt catalysts 182

Figure 5.13 CO conversion with time on stream for 10%Co/CS, 10%Co/SG, 10%CO/CNT and 10%CO/TNT 187

Figure 5.14 CO conversion with time on stream for 10%CO/ASW3, 10%CO/CNT-TIO_2, 10%CO/P25 and 10%CO/C-TNT..... 190

LIST OF TABLES

CHAPTER 1

Table 1.1 Summary of dominant plants that produced liquid products by FTS since the early 1950's 5

Table 1.2 Comparison of reactor types - 1980 [33] 13

Table 1.3 An overview of Fischer-Tropsch reactor developments 14

Table 1.4 Temperature values of metals that are relevant for FTS and support materials similar to those used in this work [58, 59] 21

CHAPTER 2

Table 2.1 H_2 analysis and O_2 titration conditions for cobalt containing catalysts 51

Table 2.2 Conditions for gas chromatographic analyses 59

CHAPTER 3

Table 3.1 Raman data for pristine CSs prepared at different flow rates 78

Table 3.2 Raman data for pristine, purified and functionalised CSs..... 83

Table 3.3 Textural properties of CSs before and after purification and functionalisation 87

CHAPTER 4

Table 4.1 Summary of the methods used to prepare CS-TiO_2 composites 101

Table 4.2 Summary of carbon coated samples prepared at different durations of acetylene passing CVD 105

Table 4.3 Values of intensity ratio (I_g/I_d) and the positions at which the bands (D and G) occur for calcined F-CS, 0CS-SG, 1CS-2.5SG, 1CS-5SG and 1CS-25SG composite samples (as depicted in Fig. 4.18) 126

Table 4.4 BET total surface area and porosity measurements for uncalcined and calcined materials of F-CS, 1CS-1SG, 1CS-2.5SG, 1CS-5SG, 1CS-10SG, 1CS-25SG, 1CS-50 and 0CS-SG 127

Table 4.5 Total percentage weight loss and temperature weight loss range as estimated by TGA for uncalcined CS-TiO_2 composite materials of A1, A2, A3, SW1, SW2, SW3, ASW1, ASW2 AND ASW3 143

Table 4.6 BET total surface area and porosity measurements for uncalcined and calcined CS-TiO_2 composite materials of A1, A2, A3, SW1, SW2, SW3, ASW1, ASW2 AND ASW3 145

Table 4.7 BET total surface area and porosity measurements for C5-TiO_2, C10-TiO_2, C20-TiO_2, C30-TiO_2, C45-TiO_2, C60-TiO_2, C120-TiO_2 and C240-TiO_2 150

CHAPTER 5

Table 5.1 Summary of catalysts prepared by DPU method 163

Table 5.2 Summary of calcinations conditions and cobalt loading on supports 164

Table 5.3 BET surface areas, pore volumes and pore diameters of the calcined catalysts 173

Table 5.4 H_2-Chemisorption results for all calcined catalysts[a] 185

Table 5.5 Fischer-Tropsch synthesis performance of supported cobalt catalysts 189

LIST OF SYMBOLS AND ACCRONYMS

ASF	Anderson-Schulz-Flory
A (1, 2, 3)	CSs were functionalised for 17 h (and not dispersed in CTAB) followed by a sol-gel coating (number of TiO_2 coating cycles).
ASW (1, 3 or 3)	CSs were initially functionalised for 17 h in HNO_3, followed by dispersion in CTAB for 1 h and then sol-gel coating (number of TiO_2 coating cycles).
BASF	Badische Anilin und Soda Fabrik
BET	Brunauer-Emmett-Teller
C_2H_2	Acetylene
$CaCO_3$	Calcium carbonate
CaO	Calcium oxide
CVD	Chemical vapour deposition
CNFs	Carbon nanofibers
CNTs	Carbon nanotubes
CNT-TiO_2	Carbon nanotubes-titania nanocomposite material
CO_2	Carbon dioxide
CSs	Carbon sphere
CS-TiO_2	Carbon spheres- titania composite material
C-TNT	Titania coated potassium titanates
CTL	Coal-to-liquid
EDX	Energy dispersive X-ray spectroscopy
EM	Electron miscopy
FT	Fischer-Tropsch
FTS	Fischer-Tropsch synthesis
GC	Gas chromatography
GTL	Gas-to-liquid
GHSV	Gas hourly space velocity
h	Hour
H_2	Hydrogen
HNO_3	Nitric acid
LN_2	Liquid nitrogen
mL/min	Millilitre per minute
MS	Mass spectrocopy
N_2	Nitrogen
nm	Nanometre
P-CS	Pristine carbon spheres
SPD	Slurry-phase Distillate
SW	CSs were not functionalised, but only dispersed in CTAB for 1 h and then sol-gel coated (number of TiO_2 coating cycles)
TCD	Thermal conductivity detector
T-CS	Toluene washed or extracted carbon spheres
TEM	Transmission electron microscopy
TGA	Thermogravimetric analysis

TNT	Potassium titanates (titania nanotubes)
TPD	Temperature programmed desorption
TPD-MS	Combined Temperature programmed desorption with Mass spectroscopy
TPR	Temperature programmed reduction
TOF	Turnover frequency
WGS	Water gas shift
wt. %	Weight percentage
α	Alpha value

Chapter 1

1. Introduction and literature review

1.1 A brief historical overview and current prospects

The modern global economy is dependent on oil as a source of energy [1]. Oil was discovered in the USA in 1859 and oil has since been a source of cheap energy [2]. Its relatively low price and its perceived long term availability have made the world's economies dependent on it. However, many now predict that oil production is peaking throughout the world and the high demand for oil over recent years has put strain on the world's oil resources [3]. The fears of a limited supply of oil [2, 3], the ever increasing demand driven by rapid expansion in the economies of South East Asia and political agitation in the major oil producing nations such as Iran, Nigeria and Venezuela has driven oil prices to historic highs [4]. Recently these prices have been pushed higher by tropical storms off the US Gulf coast, the US 9/11 attack, the Iraq war, and the hurricane Katrina in the USA. The global economic recession has continued to influence oil production [5-7]. Fig. 1.1 demonstrates the global rise and fall of oil prices since the mid 90's. The combination of these global forces and the large amount of natural gas reserves which are distributed relatively evenly (as compared to crude oil) around the world has led some economic commentators to go as far as labelling this century the "gas" century and the end of "cheap" oil [8]. This premise has created an overwhelming push for alternate fuels. The conversion of natural gas to liquid fuel, i.e. gas-to-liquid (GTL), via the Fischer-Tropsch synthesis (FTS) stands out as a most promising and proven technology that has potential to revolutionize the

fuel industry [3]. A summarised overview of world GTL activity is shown in Fig. 1.2.

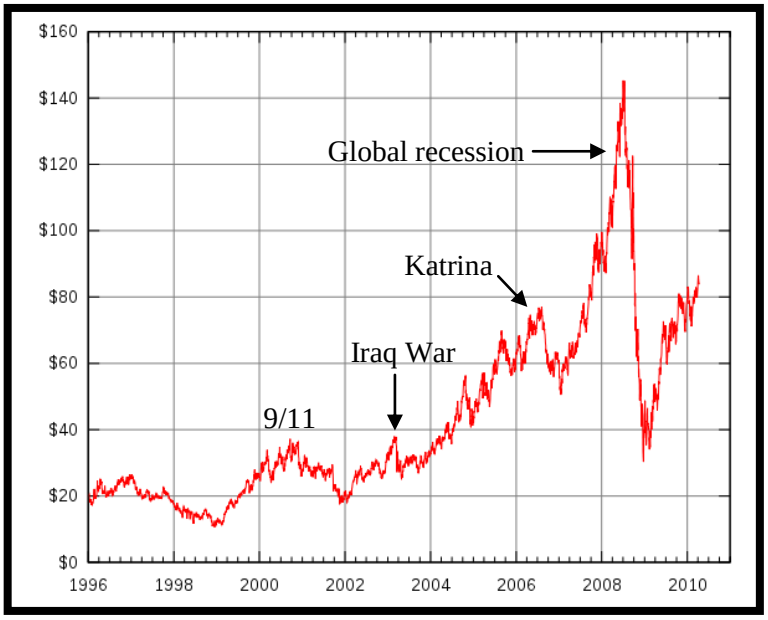


Figure 1.1 The worlds rise and fall of oil price over time. Adapted from [6]

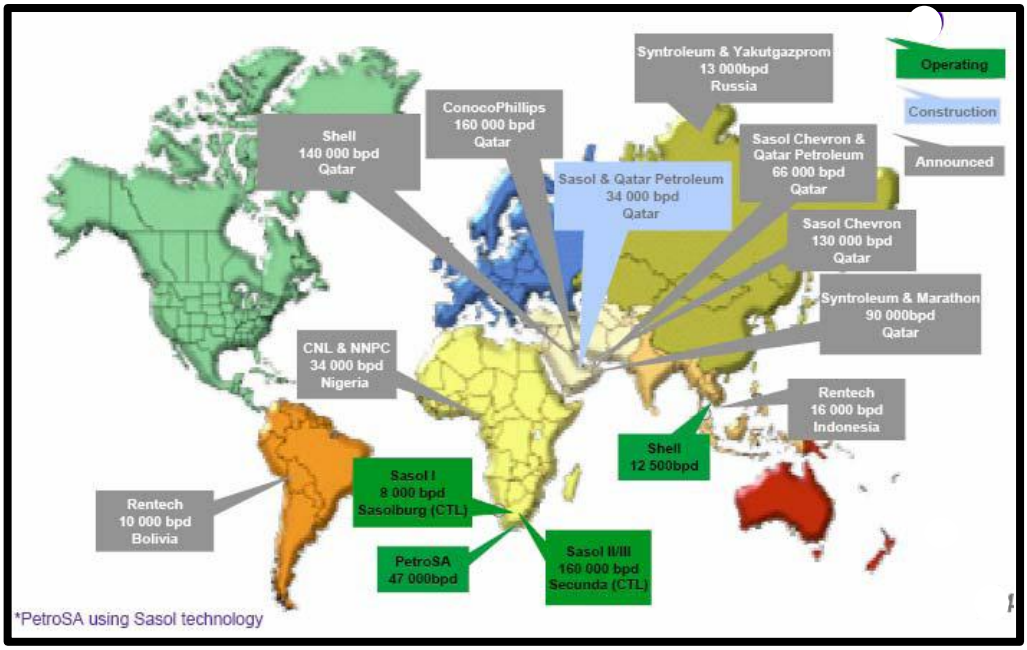


Figure 1.2 Summarised worldwide GTL activity and announcements. Adapted from [3]

FTS is a reaction which entails the conversion of synthesis gas, also known as syngas (a mixture of H_2 and CO gases), to liquid hydrocarbon fuels, oxygenated

hydrocarbons, chemicals and water. This syngas mixture is obtained from natural gas, coal, petroleum, biomass or even from organic wastes. The first FTS experiments were carried out at the beginning of the 20th century [9]. It was in 1902 that Sabatier and Senderens discovered that methane could be synthesised from a mixture of CO and H_2 over nickel or cobalt catalysts at atmospheric pressure [10]. In 1913 Badische Anilin und Soda Fabrik (BASF) reported the production of liquid products from CO and H_2 by using cobalt catalysts [11]. A decade later, in 1923, Hans Fischer and Franz Tropsch proposed the Synthol process, which gave a mixture of aliphatic oxygenated compounds through the reaction of CO with H_2 over iron chips at 400 °C under high pressures, of 10 to 15 MPa [12]. This product was transformed into a mixture of hydrocarbons after heating under pressure and this mixture was known as "Synthine".

In 1936 Pichler made the important discovery that when the syngas pressure was increased from atmospheric to 15 bar the life of an iron catalyst was markedly improved. It was also discovered that even at lower pressures (*ca.* 7 bar) hydrocarbons could be produced, but it was found that the iron catalysts deactivated rapidly at this pressure. A lot of work was then focused on the use of cobalt and nickel as catalysts at low pressures. Nickel too had to be discarded due to its high tendency to produce methane and also because its activity deteriorated rapidly due to loss of active nickel particles from the reactor in the form of $Ni(CO)_4$ [13]. Ruthenium has also been found to be capable of achieving the required activity for a commercial Fischer-Tropsch (FT) application, but unfortunately it is more costly and the amount of ruthenium that is available on earth is insufficient for large scale application [14]. Subsequently, early work in the literature revealed that both cobalt and iron catalysts were excellent for the production of higher hydrocarbons. It is now generally accepted that most group 8-10 metals have measurable CO hydrogenation activity with the distinguishing factor being the product distribution [15, 16]. Iron catalysts have advantages over cobalt catalysts in the conversion of coal or biomass to liquid fuels. These advantages include their low cost, low methane selectivity, flexible product slate and robustness in converting coal- or biomass-derived syngas at a low H_2/CO

ratio [17]. However, in general cobalt catalysts are more active, more stable and a better match for converting natural gas-derived syngas to hydrocarbon liquids.

All FT plants built in Germany during World War II employed a cobalt based catalyst in fixed-bed reactors. In the 1950's USA scientists attempted to employ fluidized-bed reactors to convert syngas from natural gas into petrol, but they were largely unsuccessful. In 1951 five offers were received by Sasol for the design and expansion of a coal-to-oil plant they wished to commission. Sasol decided to take two of the offers; one from M.W. Kellogg relating to the design of a circulating fluidized-bed (CFB) reactor and one from Arbeit-Gemeinschaft Lurgie and Ruhrchemie relating to construction of Arge fixed-bed reactors. In 1955 the first commercial FT plant, Sasol I, was commissioned in South Africa (Sasolburg) and the driving force for this plant was the large coal reserves in South Africa and the need to reduce the country's dependence on imported oil. This proved to be successful and the result was that South Africa managed to reduce its imports from about 100% of crude to about 50%. Today Sasol operates at a profit without government support and it appears that it maintains a larger staff than other international companies of a similar size [18]. Since the 1960s other plants and developments in FT have been made. In 1980 and 1982, the Sasol II and Sasol III plants came on stream in Secunda, South Africa. These plants used entrained CFB reactors and produced mainly gasoline and diesel fuels. Hydrocarbon selectivities of up to 70% C_5-C_{10} olefin and up to 60% olefin selectivity for C_{11}-C_{18} hydrocarbons were achieved at these plants. These plants were later scaled up to what is known today as the commercial Sasol Advanced Synthol (SAS) reactor plants with a capacity of 11 000 bbl/day (barrels per day)[*]. Since then and particularly in the early 1990's Sasol has replaced their sixteen CFB reactors with eight SAS reactors and four of these have capacities of 20 000 bbl/day. In June 1992 the onshore plant construction of the Mossgas (now known as PetroSA) facility in South Africa was completed and went into full production in January 1993. This plant utilized Sasol's CFB reactor technology and was constructed with three 14 000 bbl/day reactors. Unlike Sasol, PetroSA uses

[*] 1 barrel/day is approximately equivalent to 159 liters/day

natural gas as its feedstock. Even though PetroSA experienced problems with natural gas supply and shutdowns due to an explosion and corrosion in the reformers, they have been operating for more than 10 years at near capacity levels with an on stream factor above 90%. Currently they are joining with Statoil to operate a 1000 bbl/day slurry bubble column reactor at their gas-to-liquid (GTL) plant. Shell started designing a 12 500 bbl/day plant in 1989 in Malaysia using the so-called Shell Middle Distillate Synthesis (SMDS). The facility started operating in 1993. It was only at the end of 1996 that Shell reported they could produce 98% capacity in their operation for sale to the market. Shell has since divulged little specific information about the details of their fixed-bed FTS unit as it is operated in the SMDS process. In 2000 the SMDS plant improved their cobalt based catalysts and their capacity increased by 25%. A summary of these (and succeeding) developments in the FT industry is given in Table 1.1.

Table 1.1 Summary of dominant plants that produced liquid products by FTS since the early 1950's

Start-up	Country (Location)	Owner	Technology	Production (bbl/day)
1955	South Africa (Sasolburg)	Sasol I	Sasol Slurry and Arge (Fe)	500
1980	South Africa (Secunda)	Sasol II	Sasol Advanced Synthol (Fe)	11 000 (later 20 000)
1982	South Africa (Secunda)	Sasol III	Sasol Advanced Synthol (Fe)	11 000 (later 20 000)
1989	Malaysia (Bintulu)	Shell	SMDS FB (Co)	12 500
1993	South Africa (Mossel Bay)	PetroSA	Sasol CFB (Fe)	36 000
1990's	USA (Houston)	BP	Fixed Bed reator	70
1990's	Qatar (Ras Laffan)	Conoco-Phillips	-	100
1999	USA (Texas)	Exxon Mobil	Slurry bed (Co)	200
2007	Qatar (Ras Laffan)	Sasol-Qatar (Oryx-GTL)	SMDS FB (Co)	34 000
2009	Nigeria (Escarvaros)	Oryx-Chevron	Sasol SPD Slurry bed (Co)	140 000
2015	Nigeria (Escarvaros)	Oryx-Chevron	Sasol SPD Slurry bed (Co)	450 000 (projected expansion)

Other companies that were linked to the construction of FT pilot plants in the 1990's era include Exxon (now Exxon Mobil), BP and Conoco-Phillips. All of these pilot plants used the abundant natural gas reserves found in other parts of the

world. Exxon Mobil developed a slurry reactor which operated at 200 bbl/day, BP's fixed-bed reactor operated at 70 bbl/day while the Conoco-Phillips plant produced 400 bbl/day. In 2003, Oryx, which is a joint venture between Qatar Petroleum and Sasol constructed a second-generation GTL complex in the Ras Laffan industrial city complex in Qatar. This location was chosen as it is close to the large natural gas reserves (proven to be over 260 000 billion liters per day) in the North of Qatar. The $900 million plant's construction was completed by December 2005 and the operation officially started in late June 2006 after a stringent commissioning and validation process was made. This plant is able to produce 34 000 bbl/day of liquids. Plans to evaluate the expansion of this plant to produce 100 000 bbl/day of liquids were made between Qatar Petroleum and Sasol in conjunction with Chevron. However, if this plant is built it will require the construction of a three-train facility that can handle a capacity of about 65 000 bbl/day. The start-up date of the first train was 2009 while that of the subsequent trains commenced in 2011. In addition to this, plans to build a 10 000 bbl/day upstream/downstream integrated GTL facility based upon the Sasol slurry phase distillate process which will also exploit the reserves of the Qatar North gas field had been proposed. A tentative start-date for this was set to be 2012. Sasol and Qatar Petroleum have projected that the plant will produce 450 000 bbl/day of liquids in 2015 with several other new facilities planned in the years ahead [19].

1.2 The Fischer-Tropsch synthesis

Fischer-Tropsch synthesis (FTS) is perhaps the most promising route to chemicals and fuels from a non-petroleum based supply such as natural gas and coal [20]. Ever since Fischer, Tropsch and co-workers [21-23] undertook their studies on cobalt and iron-based catalysts, there has been a tremendous interest towards the commercialization of this synthesis technology. This process is a promising option for environmentally sound production of chemicals and fuels from coal since the reserves of crude oil are being depleted and the price of crude oil continues to rise [21]. Significant advances in coal gasification technology for the production of syngas suggest that the Fischer-Tropsch (FT) process will be a major contender on the energy scene.

In the FT process a wide range of high molecular weight hydrocarbons and oxygenated hydrocarbons are produced from smaller starting materials (i.e. H_2 and CO) irrespective of operating conditions. This has consequently been likened to a polymerisation reaction since analogous steps are followed during the formation of polymers as found in converting CO to C_n hyndrocarbons. Dry suggested a simple stepwise growth process to give FT products, similar to that shown in Figure 1.3 [24]. It is however to be noted that the figure (Fig. 1.3) does not show an actual FT mechanism, but detailed mechanisms have been proposed in the literature for this FT reaction. Although there are controversies about the actual mechanism for the FTS process all of the proposed models assume that the growth of the hydrocarbon chains occurs via a stepwise process [24-26].

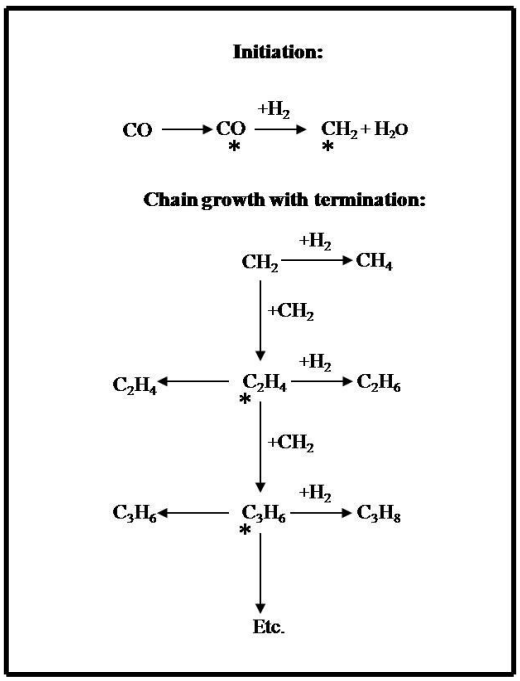


Figure 1.3 Simple FT stepwise growth process (where '∗' symbolises a surface). Adapted from [24]

The stepwise growth process occurs on the surface of the catalyst and when CO is hydrogenated CH_2 units are formed and these are taken as the "monomers" in a stepwise oligomerization process. These adsorbed units can either desorb or be hydrogenated further to form primary FT products or another monomer unit can add to the chain to continue the chain growth. This process can take place at each

stage of growth. Principally two termination reactions in FTS are possible, namely α-hydrogenation, yielding a paraffin, or β-dehydrogenation, producing an α-olefin as primary products. Chain termination can occur at any time during the chain growth process to yield an α-olefin or an n-paraffin once the product desorbs. Large amounts of alcohols and aldehydes are also formed and these appear to be some of primary products involving insertion of some form of oxygenated species into a metal alkyl group on the catalyst surface (CO insertion mechanism) [10, 11]. The formation of these functional groups is considered to be a termination step because it occurs at the end of the growing chain by inserting a CO molecule into the alkyl chains that have previously been formed during the FT growth process [28]. In this process the majority of the products are α-olefins and n-paraffins. Regardless of the product type, they are predominantly linear with high olefin content.

1.3 The Fischer-Tropsch reaction

The Fischer-Tropsch (FT) reaction (1.1) is defined as the hydrogenation of carbon monoxide over transition metals (from groups 8-10) to form a wide range of hydrocarbons and oxygenated hydrocarbons. This reaction is the chemical heart of GTL technology. Water is a primary product, whilst the main products are α-olefins and *n*-paraffins.

$$\textit{FT reaction:}\quad 2nH_2 + nCO \rightarrow -[CH_2]_n- + nH_2O, \quad \Delta H_{r,\,270^oC} = \textit{-151.9kJ/mol} \quad (1.1)$$

The FT reaction is highly exothermic ($\Delta H_{r,\,270^oC}$ = -151.9kJ/mol) and an extremely large amount of heat is produced during the reaction.

1.3.1 Other reactions taking place

The produced water can react further via the water gas shift (WGS) reaction as represented in equation (1.2):

$$\textit{WGS reaction: } H_2O + CO \leftrightarrow CO_2 + H_2, \qquad \Delta H_{r,\,270^oC} = \textit{-39.3 kJ/mol} \qquad (1.2)$$

The WGS has been known since the 19th century and was noted to occur during the production of domestic and industrial fuel from the pyrolysis of coals. The reaction is mainly catalyzed by iron catalysts whilst with cobalt catalysts this can only be achieved at high temperatures. One advantage of this side reaction is that it can adjust the H_2:CO feed ratio of the syngas if it is lower than stoichiometrically required. However, the WGS reaction is undesirable for FTS with hydrogen-rich syngas produced from natural gas as it results in a low carbon efficiency in the gas-to-liquid process since carbon is lost in the form of CO_2.

The other side reaction taking place during a FT reaction is known as the Boudouard reaction (1.3). This reaction involves the disproportionation of CO and leads to the formation of CO_2 and carbon [28]. The produced carbon can cause catalyst deactivation.

$$\textit{Boudouard reaction: } 2CO \leftrightarrow C + CO_2, \qquad \Delta H_{r,\,270^oC} = -172.4\ kJ/mol \qquad (1.3)$$

1.4 Fischer-Tropsch product spectrum

Figure 1.4 is a graphic representation of the product distribution that occurs during the FTS process. This plot is known as the Anderson-Schulz-Flory (ASF) model and is represented by the following equation (1.4):

$$W_n = n(1-\alpha)^2\alpha^{n-1} \qquad (1.4)$$

where W_n is the weight percent of a product containing n carbon atoms and, α (or p_g), is the chain growth probability. This model suggests that the probabilities of chain growth and chain termination are independent of the chain length. The selectivities of various hydrocarbons can therefore be predicted based on simple statistical distributions calculated from chain growth probabilities and carbon numbers. The model shows the predicted distributions for several products and product ranges of particular interest.

The FTS is unquestionably not a selective process in terms of its product spectrum since the achievement of selectivity to a single organic product, except for production of the C_1 products (methane and methanol), has not yet been possible. Senden and co-workers also showed that only methane can be produced with a selectivity of 100% [29]. This observation agrees with the ASF model as depicted in Figure 1.4.

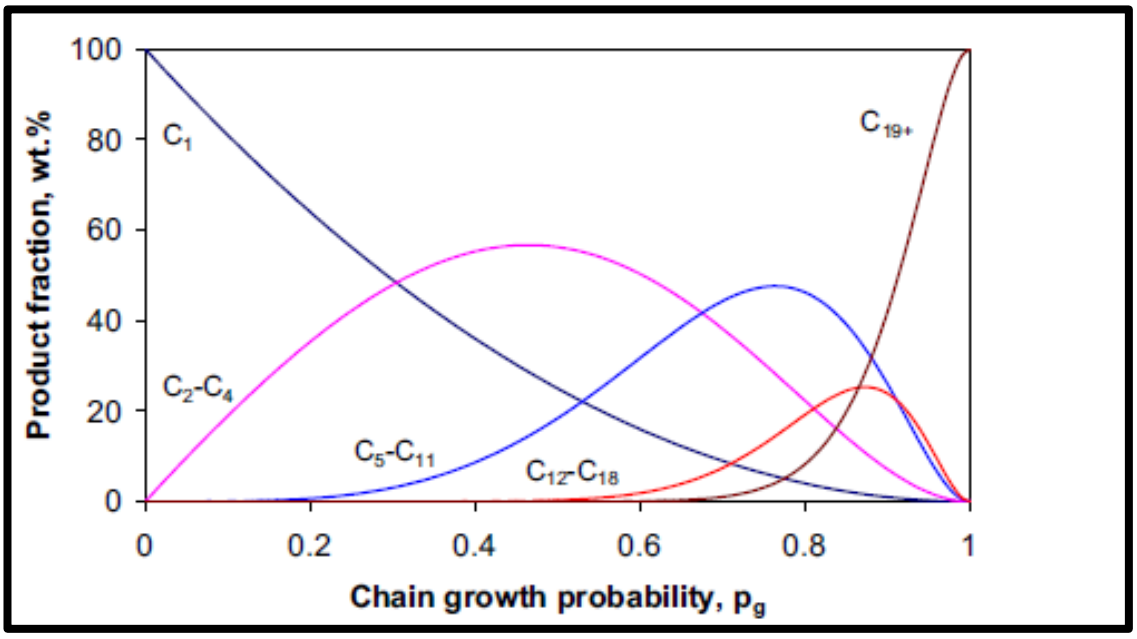


Figure 1.4 Theoretical FTS product distribution of products produced by the Anderson-Schulz-Flory model as a function of chain growth probability [30]

The only other product that can be produced with high selectivity is heavy paraffin wax. The selectivity of the gasoline product fraction has a maximum selectivity of 48% while that of the diesel product fraction is closer to 40%. However, it has to be noted that the selectivity for the diesel product fraction varies depending on the range of carbon numbers in the product cut. The variables that influence the product distribution are the process operating conditions, the reactor type and the catalyst properties.

1.5 Factors influencing product selectivity

1.5.1 Operating conditions

The cost of producing syngas is high and it is therefore important that the maximum amount used is converted in the downstream reactors. It is required that the composition of the syngas matches the overall usage. For the cobalt based catalysts a ratio of 2.15:1 for a H_2 to CO mixture is normally used since the dominant reaction is FTS. The ratio for the syngas when iron is used changes due to the WGS side reaction that takes place. For the low-temperature FT (LTFT, 200-240 °C) process using iron the ratio is typically 1.7:1, while for the high-temperature FT (HTFT, 250-350 °C) it is 1.05:1 since the WGS is rapid and the produced CO_2 is allowed to be converted into FT products via the reverse WGS followed by the FT reaction [24].

The industrial reaction conditions used in the FT reaction range between 200-350 °C and 25-40 bar. It is difficult to operate at high temperatures (e.g. above 350 °C) because most of the catalysts that are used degrade or deactivate at high temperatures. Cobalt for instance is known as a LTFT catalyst since it performs well at temperatures between 220-250 °C for the production of long chain products, mainly diesel and wax. If it is used at higher temperatures, methane will be the abundant product formed. Iron on the other hand performs well at higher temperatures (250-350 °C) for the production of light products, petrol and chemicals [28]. Two demonstrations of product distributions are given in Fig. 1.5, the first with iron catalyst and the second with cobalt catalyst [31]. The x-axis represents chain length (C_n), while the y-axis shows percentage by weight basis (%Wt).

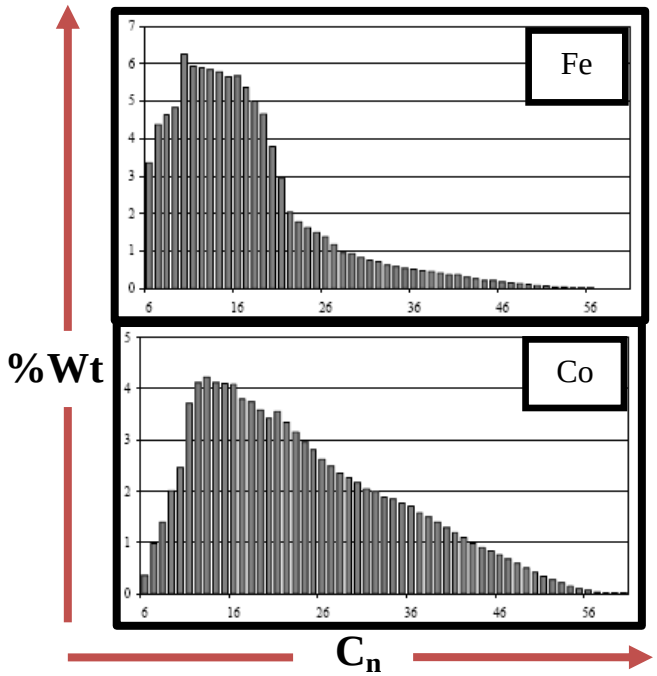


Figure 1.5 Product distribution with iron and cobalt based catalysts [31]

In the last two decades the development of most FT technologies has been based on LTFT processes. These processes use natural gas as the feed stock for the syngas which is generated by vapour reforming, auto-thermal reforming or partial oxidation. Too much heat produced in the FT reaction can "kill" the catalyst performance because the reaction temperature can be exceeded by an extreme temperature overshoot caused by the exothermic behavior of the reaction. It is crucial that the generated heat be removed or minimized during the reaction. Appropriate reactors that can assist in the rapid heat removal are carefully designed and selected for specific reactions. Also, slow temperature heating/ramping rates are normally applied during catalyst pretreatments and during the reaction to assist in the minimization of the unwanted exothermic behavior.

1.6 Fischer-Tropsch reactors

The governing factors in the control of product distribution include the reactor type that is used and the type of operation used during FTS. The efficient and speedy removal of the accompanying large heat of reaction is a major consideration since high temperatures lead to excessive methane yields, carbon

deposition and particle fragmentation. A catalyst can also experience an increased rate of deactivation due to sintering and fouling [20, 24].

After the discovery of FTS, rapid developments and construction of commercial plants took place in Germany. Badger outlined the prospects for the development of FTS [32]. Ever since then attempts at the invention of new FT reactors have continued on unabated because principles that defined a unit operation were understood. Reactors used in the laboratory by Fischer and Tropsch were glass tubes with about a 5 mm internal diameter and the catalyst held in a fixed position [35]. For larger reactors the reactor design is of great importance since it is essential to obtain optimum product selectivity and long catalyst life by effectively removing the exothermic heat of reaction. Table 1.2 shows a comparison between the fixed-bed, fluid bed and slurry reactors [33]. Depending on the process involved and the type of products required an appropriate reactor that takes into account of the details tabulated in Table 1.2 will achieve optimum FT results.

Table 1.2 Comparison of reactor types - 1980 [33]

Feature	**Fixed bed**	**Fluid bed /circulating**	**Slurry**
Temp. control	Poor	Good	Good
Heat exchanger surface per feed	240 m^2 per 1000 m^3	15-30 m^2 per 2000 m^3	50 m^2 per 1000 m^3
Max. reactor diameter	<0.08 m	Large	Large
CH_4 formation	Low	High	As fixed bed/lower
Product	Full range	Low mol. weight	Full range
Space-time yield (C_{2+}) in a day	>1000 kg/m^3	4000-12000 kg/m^3	1000 kg/m^3
Cat. effectivity	Lowest	Highest	Intermediate
Back-mixing	Little	Intermediate	Large
Min. H_2/CO feed	As slurry or higher	Highest	Lowest
Construction			Simplest

Recently, Davis gave a brief overview of FT reactors in the period since 1924 and other future developments in reactor design [18]. This overview is summarized in Table 1.3.

Table 1.3 An overview of Fischer-Tropsch reactor developments

Reactor developments and potentialities
1924-1945:
↳ Models of temperature profile in a double tube reactor were made.
↳ Trial-and-error techniques were used to design reactors.
↳ Limitations of reactor modeling due to the pre-computer age.
1945:
↳ Introduction of high-pressure reactors for lab use [18].
↳ Utilization of high-pressure autoclaves, fixed-bed and slurry phase reactors.
↳ Reactors were then classified into 2 categories: LTFT and HTFT reactors.
1945-1970 (Golden Age):
↳ Approaches to achieve optimum operating temperatures for stirred reactors were defined.
↳ Sasol utilized fluid bed reactors for FTS.
↳ M.W. Kellogg company developed a CFB reactor
↳ In 1950's Sasol upgraded the Kellogg reactors into the synthol process reactors.
↳ Kölbel and co-workers developed a slurry phase reactor that produced gasoline as the dominant liquid product [38].
↳ By 1980, sufficient data existed for comparisons between fixed bed, fluid bed and slurry reactors (see Table 1.2).
1970 till date:
↳ Major advance has been the introduction of computers into FTS reactor modeling.
↳ In early 1990's Sasol developed a slurry bubble column reactor technology.
↳ PetroSA utilized Sasol's CFB reactor technology and had a turnover of 14000 barrels/day
↳ During the past 50 years attention has been directed toward bubble column reactors due to its potential to maximize reactor productivity [39].
The Future:
↳ Interest is now in the development of micro reactors.
↳ Microchannel reactors - replacements of one large reactors with many smaller reactors that provide improved control of operating conditions
↳ Adaptation of monolith reactor technology.
↳ Fixed-bed reactor still attractive - highest catalyst loading and hence the highest potential productivity reactor volume.
Problems that need to be overcome:
1) Diffusion limitations within the catalyst particle.
2) Decreasing the temperature exotherm.
3) Eliminating the reduced conversion due to accumulation of heavy products inside the catalyst pellet.

1.7 Catalysts for Fischer-Tropsch synthesis

1.7.1 Active metals

It is generally accepted that most group 8-10 metals are able to catalyse the FT reaction to liquid hydrocarbons since they can dissociatively adsorb H_2 and CO. Ruthenium followed by iron, nickel, and cobalt are known to be the most active metals for the hydrogenation of CO. It has been shown in the literature (Vannice *et al.*) [34] that the average molecular weight of the hydrocarbons produced by FTS decreases in the following sequence:

$$Ru > \boldsymbol{Fe} > \boldsymbol{Co} > Rh > Ni > Ir > Pt > Pd$$

Thus, only ruthenium, iron, cobalt, and nickel have the required activity for commercial production of FT products [24]. Ruthenium is the most active catalyst and shows high selectivity to high molecular weight products at low temperatures. Unfortunately it is too expensive to use commercially. Furthermore, reserves of ruthenium are insufficient for large-scale application. Nickel catalysts under practical operating conditions produce too much methane and do not have the broad selectivity for producing high molecular weight products. This metal is basically a methanation catalyst. Fischer and Tropsch initially proposed cobalt and iron as the best catalysts for syngas conversion [21]. Both cobalt and iron catalysts have been used in industry for the synthesis of hydrocarbons. Cobalt catalysts are more expensive that iron catalysts, but are more resistant to deactivation. Whilst the activity of these two metals is comparable, the productivity at higher conversion is more significant with cobalt catalysts, even at lower synthesis pressures. However, a higher catalyst cost can be offset by lower operating costs. Iron has a stronger tendency than both nickel and cobalt to produce carbon that deposits on the surface that will deactivate the catalyst. Iron readily forms carbides, nitrides and carbonitrides with metallic character that also have FT activity. Iron catalysts also favour the WGS reaction while cobalt catalysts do not have WGS activity (except at high temperatures), which leads to improved carbon conversion to products because CO_2 is not formed. Chain

growth probabilities of about 0.95 for iron and 0.94 for cobalt have been reported at relatively low temperature (200-250 °C) [37-37].

Cobalt catalysts yield mainly straight chain hydrocarbons and very few oxygenates in contrast to iron which produces larger amounts of oxygenates. Iron catalysts produce hydrocarbons and oxygenates under different pressures, temperatures (up to 350 °C) and H_2/CO ratios while cobalt catalysts operate within a very narrow range of temperatures and pressures. An increase in temperature leads to a spectacular methane selectivity. Iron catalysts usually produce more olefins than do cobalt catalysts. Both cobalt and iron catalysts can be used in the LTFT process for the synthesis of linear long-chain hydrocarbon waxes and paraffins [39, 40]. Cobalt catalysts represent the optimal choice for synthesis of long-chain hydrocarbons in the LTFT because of their stability, higher per pass conversion and high hydrocarbon productivity. Besides the active catalytic agent, FT catalysts often contain supports and promoters.

1.7.2 Catalyst supports and promoters

The principal function of the catalyst support in FT catalysis is to disperse the active metal and produce stable metal catalyst particles after reduction. The porous structure of the support could control the sizes of supported metal particles. Supported catalysts exhibit better characteristics than unsupported ones. Some of these characteristics include an improved catalyst texture and porosity, controlled particle size, an increased metal dispersion, reduction in the formation of hardly reducible active metal oxides, facilitation of the reducibility and enhancement of mechanical properties and attrition resistance of active metals [41-43]. The effects of different supports used in FTS have been extensively studied and the support has been shown to be an important component affecting the properties of the catalysts [42, 44-46]. Among the supports, Al_2O_3, SiO_2 and TiO_2 have been most often employed for FTS. This is due to the high surface areas that they possess. Recently Storsæter *et al*. have reported the characterization of Al_2O_3-, SiO_2- and TiO_2-supported cobalt catalysts when used as FT catalysts [47]. It was observed that the cobalt particle size and reducibility

increased with increasing average pore diameter of the support. The pore structure of the support has a significant effect on the size, location, shape and appearance of the FT active metal catalysts.

Reuel and Bartholomew studied the catalytic activity of cobalt-based catalysts as a function of support and found the cobalt activity to decline in the following order: $Co/TiO_2 > Co/Al_2O_3 > Co/SiO_2 > 100\%$ Co > Co/MgO [44]. Iglesia *et al.* found that at pressures greater that 5 bar, and at high conversions, the influence of the support on the selectivity in methane and C_{5+} formation could be insignificant [45]. One of the greatest functions of the support is to dissipate the heat released by the reaction and thus reduce the temperature gradient in fixed-bed reactors.

Mesostructured materials with adjustable porous networks have shown a great deal of promise for designing heterogeneous catalysts [42, 48 and 49]. These materials can have a surface area that approaches 1000 m^2/g. The pore sizes ranging from 2 to 30 nm can be adjusted at the stage of synthesis using templates comprising different surfactants. Common mesoporous materials are MCM-41 and SBA-15. Larger cobalt particles used in FTS have been prepared from these large pore silicas [48]. High cobalt reducibilities and higher dispersion have generally been found in these large particles.

A few reports on the use of carbon as a support for FT catalysts have been described over the years [49-51]. Carbon-based materials are advantageous over the oxide supports because they do not react with the active metal to form inactive materials such as mixed oxides (aluminates, silicates or titanates) that are only reducible at high temperatures. Bezemer *et al*. have recently proposed a cobalt on carbon nanofiber catalyst as a model system to study the effect of cobalt particle sizes on FT turnover frequency [52]. It was found that the turnover frequency was almost independent of cobalt particle size for cobalt particle sizes larger than 6-9 nm. The smaller cobalt particle size affected the FT reaction rates with catalyst particles having rates much lower than expected. This Co/C system showed significant changes in hydrocarbon selectivities. Despite all the advantages of

carbon supports over inorganic oxides supports, they are less stable and can gasify in the presence of hydrogen.

Promotion of an active catalytic component with oxides has been one of the methods used to improve the activity, hydrocarbon selectivity to long-chain paraffins and low WGS activity of cobalt and iron FT catalysts [53]. Oxide promoters such as ZrO_2, La_2O_3, MnO and CeO_2 have been the most employed. Jacobs *et al.* reported support effects for the reducibility of cobalt catalysts in FTS after examining different supports (SiO_2, TiO_2, Al_2O_3 and ZrO_2) [54]. These authors found that ZrO_2 addition increased the cobalt dispersion and decreased the reducibility of cobalt species in Al_2O_3 supported FT catalysts. A recent study by Enache *et al.* showed that the presence of ZrO_2 in supported cobalt catalysts promoted formation of the poorly crystallized hexagonal phase of cobalt [55]. This phase was found to be more active in FTS than the known cobalt cubic phase. Therefore, the use of ZrO_2 as promoter for cobalt FT catalysts could be due to the higher concentration of a cobalt hexagonal phase in ZrO_2-promoted catalysts.

Promotion with noble metals (such as Ru, Rh, Pt and Pd) has a strong impact on the structure and dispersion of active cobalt catalyst as well as, reaction rates and selectivities. Introduction of noble metals to FT catalysts could result in the following phenomena: much easier reduction of metal oxide particles, formation of bimetallic particles and alloys, a lower fraction of barely reducible mixed oxides, enhancement of metal dispersion, inhibition of catalyst deactivation, appearance of additional sites for hydrogen activation and an increase in the intrinsic reactivity of surface sites [53].

1.7.3 Catalyst activation and deactivation

The three key properties of FT catalysts are activity, product selectivity and lifetime stability. In the last 5 decades optimization of these properties has been the focus for the use of catalysts in commercial applications. There are a variety of strategies which can be used to affect these properties and these include: the use

of supports, promoters, catalyst preparation, pretreatment (drying and calcination) and reduction, selective poisoning and catalyst deactivation.

Studies by Reuel and Bartholomew indicated that activity/selectivity properties of cobalt and iron FT catalysts can be significantly altered by variations in calcination and reduction conditions [44]. They found that the average carbon number of the hydrocarbon product increased by 10 to 15% when the reduction temperature for Co/Al_2O_3 and Co/TiO_2 is increased from 375 or 400 to 525 °C.

FT catalysts are normally activated after preparation by calcining them at high temperatures (300-500 °C) to remove impurities and unwanted metal precursors, such as nitrates, if metal nitrates were used. Calcination steps also allow the active metals to be redistributed evenly in the catalyst pores. After the catalysts have been calcined the active metals will be in the oxide form, e.g. Co_3O_4 in the case of cobalt. Before the FT reaction the catalysts are activated by reducing them to their metallic forms in pure hydrogen. Depending on the catalyst preparation and type of active metal support and promoter used the reduction temperatures can vary between 250 and 500 °C. Figure 1.6 shows a schematic representation of the deactivation mechanisms involved during the FTS.

Fouling and coke formation: Fouling due to formation of carbonaceous species during FTS may totally encapsulate a metal crystallite and render the crystallite inactive. The pores may be plugged such that access of reactants is denied to the catalyst crystallites found inside these pores [57].

Poisoning: Catalysts may lose their activity during FTS due to poisoning by contaminants such as sulphur in the feed. Irreversible adsorption of either reactants or products could also poison the catalyst by blocking the catalyst active sites.

Sintering: Sintering is probably the main cause of deactivation of FT catalysts. Agglomeration (crystallite growth) of smaller catalytic particles to larger particles takes place at high temperatures. If this happens then the formation of FT products

may either be minimal or may not be feasible. The sintering mechanism is directly related to the melting temperature and is defined by the so-called Hüttig and Tamman temperatures which indicate the temperature at which sintering starts. Equations 1.5 and 1.6 are the semi-empirical relations that are commonly used to obtain the Hüttig and Tamman temperatures.

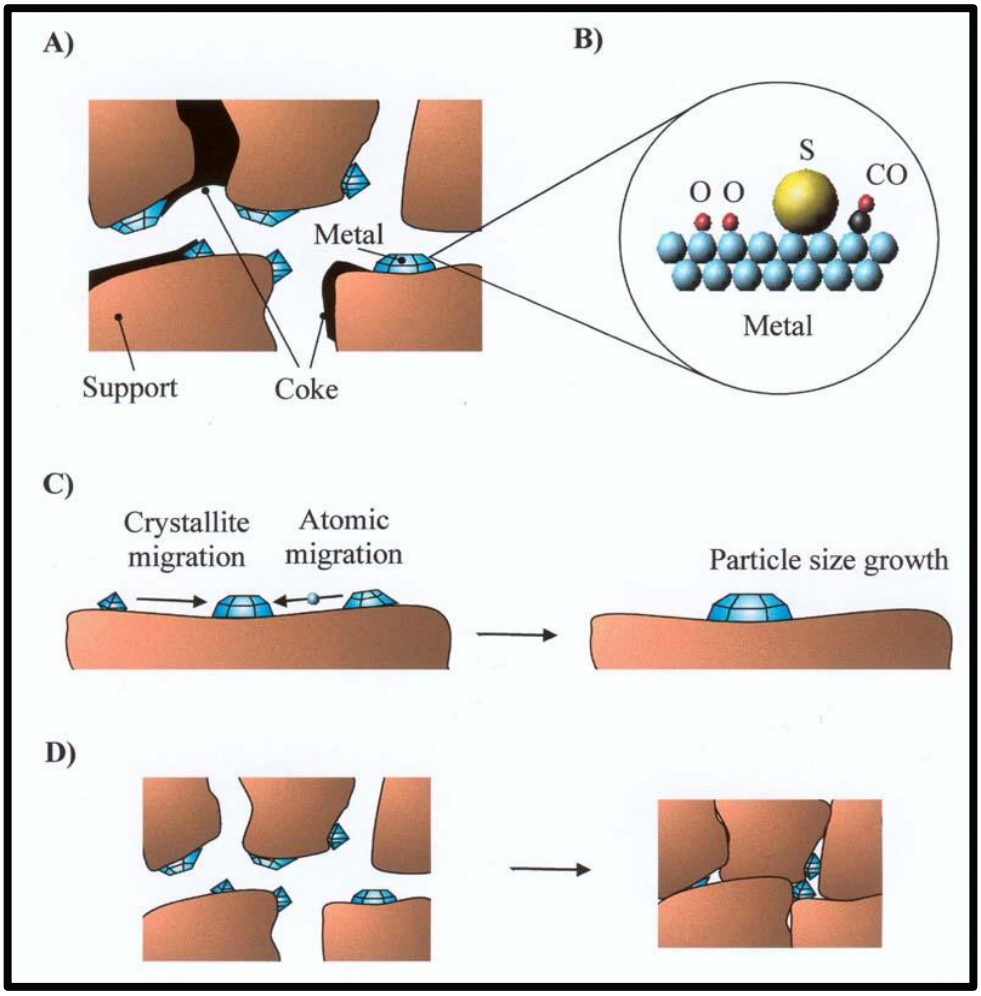


Figure 1.6 Deactivation mechanisms: (A) coke formation, (B) poisoning, (C) sintering of active metal particles and (D) sintering and solid-solid phase transitions and encapsulation of active metal particles [56]

$$T_{Tamman} = 0.5\ T_{melting} \qquad (1.5)$$

$$T_{Hüttig} = 0.3\ T_{melting} \qquad (1.6)$$

Table 1.4 gives T_{Tamman} and $T_{Hüttig}$ data for commonly used FT metals and support materials similar to those used in this thesis study. Sintering of crystallites is irreversible and it is important to prevent this phenomenon.

Table 1.4 Temperature values of metals that are relevant for FTS and support materials similar to those used in this work [58, 59]

Element/Compound	T_{Tamman} /K	$T_{melting}$ /K	$T_{Hüttig}$ /K
Co	877	1753	526
Fe	904	1808	542
Ni	863	1725	513
Ru	1362	2723	817
C	1958	3915[a]	1175
TiO_2	925	1850[b]	555

[a] Sublimation point of C, [b] Melting point for the rutile phase

1.8 Preparation of Fischer-Tropsch catalysts

Catalyst preparation methods are crucial steps in FTS because the catalytic performance is strongly dependent upon them. There are several steps that are involved in the preparation of FT catalysts. This includes the selection of appropriate catalyst supports, choice of method of deposition of the active phase onto the support, catalyst promotion and oxidative and reductive treatments. The goal of active phase formation is to spread the active metal onto a porous support and provide a metal cluster precursor. The number of metal sites, the catalyst properties, characteristics and localization on the support can be controlled by promotion with noble metals and oxides.

There are various ways of preparing FT catalysts and these include; incipient wetness impregnation, pH controlled precipitation, co-precipitation [60], deposition-precipitation [61], sol-gel [62], preparation of eggshells [63], monolithic catalyst preparation [64], colloidal [65], microemulsion [66], solvated

metal atom dispersion [67], chemical vapor deposition [68] and plasma methods [69].

For the purpose of this work only two preparation methods are discussed; the incipient wetness impregnation and the pH controlled impregnation method because these were the only methods used in the thesis study.

1.8.1 Incipient wetness impregnation method

The incipient wetness impregnation method, or the pore volume impregnation method, is a common method used to prepare FT catalysts and is normally described as being the simplest practical way to impregnate an active phase onto the support. However, this is not necessarily true because the fundamental phenomena underlying impregnation and drying are extremely complex. In this method a salt solution, typically a metal-nitrate is added to a dry porous support, as demonstrated in Figure 1.7.

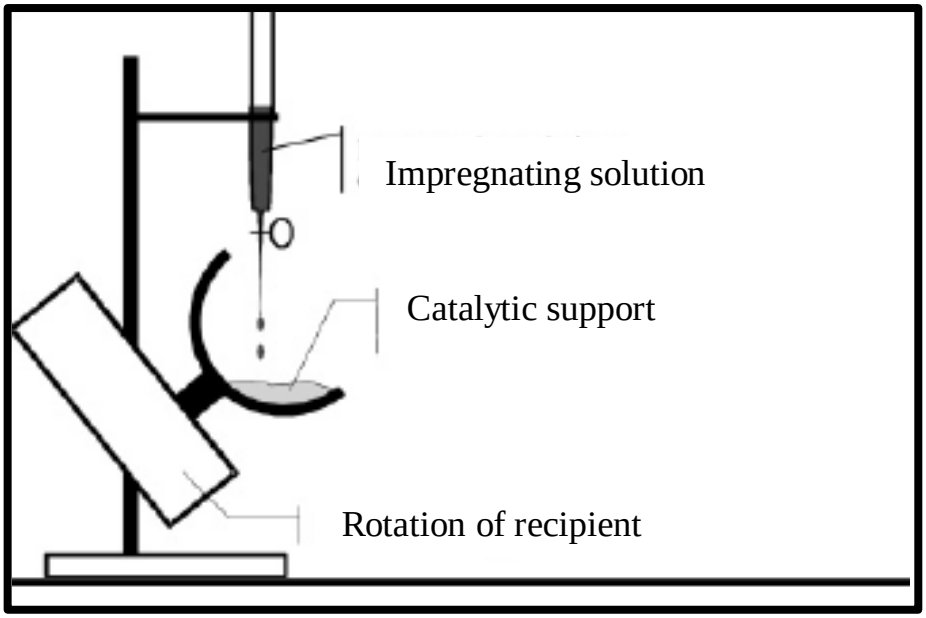


Figure 1.7 Schematic representation of experimental set up for incipient wetness impregnation. Adapted from [53]

After contact, the solution is drawn into the pores of a support by capillary forces. When all pores of the support are filled with the liquid and when there is no more

excess liquid required to fill the pores then the incipient wetness process has occurred. The liquid is then removed in a drying or calcination step resulting in the preparation of the oxidic catalyst precursor. When the concentration of metal salt is high then large metal particles will be dispersed in the pores and when it is dilute then small metal particles will be dispersed in the support pores [70].

In order to reproduce the catalyst synthesis careful control of all impregnation parameters are required. These include the rate of addition of the impregnation solution, temperature and time of support drying, and temperature and time of calcination.

1.8.2 pH-controlled precipitation method

Classical impregnation techniques may result in a non-uniform catalyst distribution through the particles and pellets. Recently developed precipitation techniques in which the solution pH is carefully controlled enable the uniform deposition of the active precursor material at practical loadings. The syntheses of a well-dispersed low loaded ZSM-5-supported Fe/Cu/K catalyst by the pH-controlled precipitation method has been reported in a patent by Mobil [71]. Bartholomew *et al.* have also used pH-controlled precipitation to generate a series of nickel supported catalysts with higher specific activities than those obtained from an impregnation method [72].

Catalyst preparation by the pH-controlled precipitation method involves the dissolution of the precursors of the active components, usually in their salt forms, in water or another suitable medium to form a homogeneous solution. The corresponding solution is then subjected to pH adjustment so as to force the metal ions to precipitate. The support is then impregnated with the corresponding precipitate. After drying and calcination, oxidic catalyst precursors are obtained. The problem with this method is that it requires careful selection of the concentration of the metal precursor and it is a tedious procedure and requires a lot of time.

1.8.3 Deposition-precipitation method

The deposition precipitation method (DP) is based on the use of precipitation combined with deposition from a liquid medium [73]. This method combines all the advantages of the precipitation method related to size distribution, and size control of precipitated particles, but reduces the risk of the formation of bulk mixed compounds of the support and active phase [74, 75]. A most important feature of this method of catalyst preparation is the prevention of precipitation occurring far from the support surface [73].

The DP method, using urea as the precipitating agent called (DPU) [76, 77], makes it possible to avoid local pH increases and metal hydroxide precipitation in the bulk solution. A solution of the precursor salt and urea is added to the support and under slow heating, the OH^- ions precipitate slowly throughout the bulk solution due to the hydrolysis of urea, that occurs at 90 °C (balanced equation shown in equation 1.7):

$$CO(NH_2)_2 + 3H_2O \longrightarrow 2NH_4^+ + CO_2 + 2OH\text{-} \qquad (1.7)$$

When the precipitation is complete, the precursor-support is generally washed to remove undesirable soluble ions, dried, and finally pre-treated (calcined) to decompose the catalyst precursor. This method has been reported by Bahome *et al.* [78, 79], and van Steen and Prinsloo [80] to prepare high loadings (10 wt.%), of well-dispersed metal particles on carbon with narrow size distributions suitable for Fischer-Tropsch synthesis.

1.9 Effect of support on FT catalysts

The increase in the number of surface metal atoms available for FT catalysis is achieved by dispersing metals on a variety of supports. The use of a support also stabilizes the resulting dispersed small metal crystallites [81, 82]. The effect of a support is assumed to be physical in nature. This assumption would imply that

catalytic properties would be independent of the type of support used. This is not true, even though some controversial effects on the use of supports were reported in early studies. For example, Schuit and van Reijen [83] reported that unsupported nickel and silica supported nickel had similar properties when compared per unit area of metal surface. On the other hand Bond [70] reported a subtle influence of the support (silica, silica-alumina, alumina) used for the reaction of ethylene and deuterium on platinum. He then suggested that more sensitive techniques would be needed to approach the problem. This phenomenon is also applicable in supports used for FT synthesis.

1.9.1 Carbon-titania composite materials

Titania, also known as titanium dioxide, was discovered in 1821. It was mined as rutile and ilmenite (which is a mixture of iron, titanium and oxygen) [84]. Because of its availability and relatively low cost, titania has been widely used in catalysis as a catalyst or support. Moreover, its low surface area is an important limitation for catalytic applications [85-87]. In order to alleviate this problem scientists have developed a variety of new synthesis procedures so as to prepare titania with a higher specific surface area [88]. Nevertheless, for many other applications, titanium dioxide can also be modified by insertion of metal ions to enhance both performance and activity [89].

High surface area TiO_2 has been reported to provide a highly active photo-catalyst material [90] and it is being investigated for utility as a material for highly efficient solar cells [91-93]. TiO_2 is a versatile material with a number of applications associated with its optical, semi-conductor and chemical properties. Although TiO_2 is a dielectric material, it behaves like a semiconductor due to structural defects. Since titania has three naturally occurring polymorphs, viz. anatase, rutile and brookite its applications and functional properties may be largely influenced by the material phase. Rutile crystallises in the tetragonal system, in which six oxygen atoms form a distorted octahedron around the titanium atom with four shorter and two longer Ti-O bonds. Anatase has a similar

tetragonal structure with slightly different octahedral dimensions. The use of nanosized TiO_2 which is accompanied by a surface area enlargement and enhanced optical properties of the material holds promise in catalysis [94]. Today various forms of nanosized TiO_2 have attracted immense attention in catalysis. The interest in the development of TiO_2 materials with specialised properties was driven by the desire to produce well-structured, porous, high surface area and complex forms of TiO_2 based materials which could be used in the development of TiO_2 nanocomposites [94].

Carbon nanotubes (CNTs) have recently been determined to be more attractive catalyst supports than activated carbons, because of their combination of electronic, adsorption, mechanical and thermal properties [95]. The unique electronic properties of CNTs make them semiconducting, semi-metallic or metallic, depending on their diameter and tube helicity [96]. They also allow for surface chemical modifications to control the type of bonds that can be formed with material like TiO_2, be they chemically bonded or van der Waals bonded.

The carbon nanotube titania (CNT-TiO_2) composites are believed to have numerous applications. The mixture of titania and CNT to form a CNT-TiO_2 composite should possess a large area where pollutants (organic or inorganic reactants) can adsorb [97]. These CNT and TiO_2 show cooperative effects and synergy with metal oxides and carbon phases, as described by Wang *et al* [98]. In the case of TiO_2, several researchers have found that CNTs are efficient adsorbents of dioxin, fluoride and cadmium [99-101]. CNTs can conduct electrons, and have strong adsorption and specific semiconducting characteristics. Therefore, CNT-TiO_2 composites can be regarded as a promising material for use in environmental cleaning and as catalyst supports.

Many different forms of carbon-TiO_2 composites have been reported. In Fig. 1.8 TEM images demonstrating different forms of CNT-TiO_2 composites are shown, where SWCNT and MWCNT refer to single wall carbon nanotubes and multiwall carbon nanotubes, respectively. It can be clearly seen that achieving a

homogeneous interaction between TiO_2 and CNT using a sol-gel (Fig. 1.8 (a, b, and c)) method remains a challenge. A brief discussion of the sol-gel method is given in section 1.9.2 below.

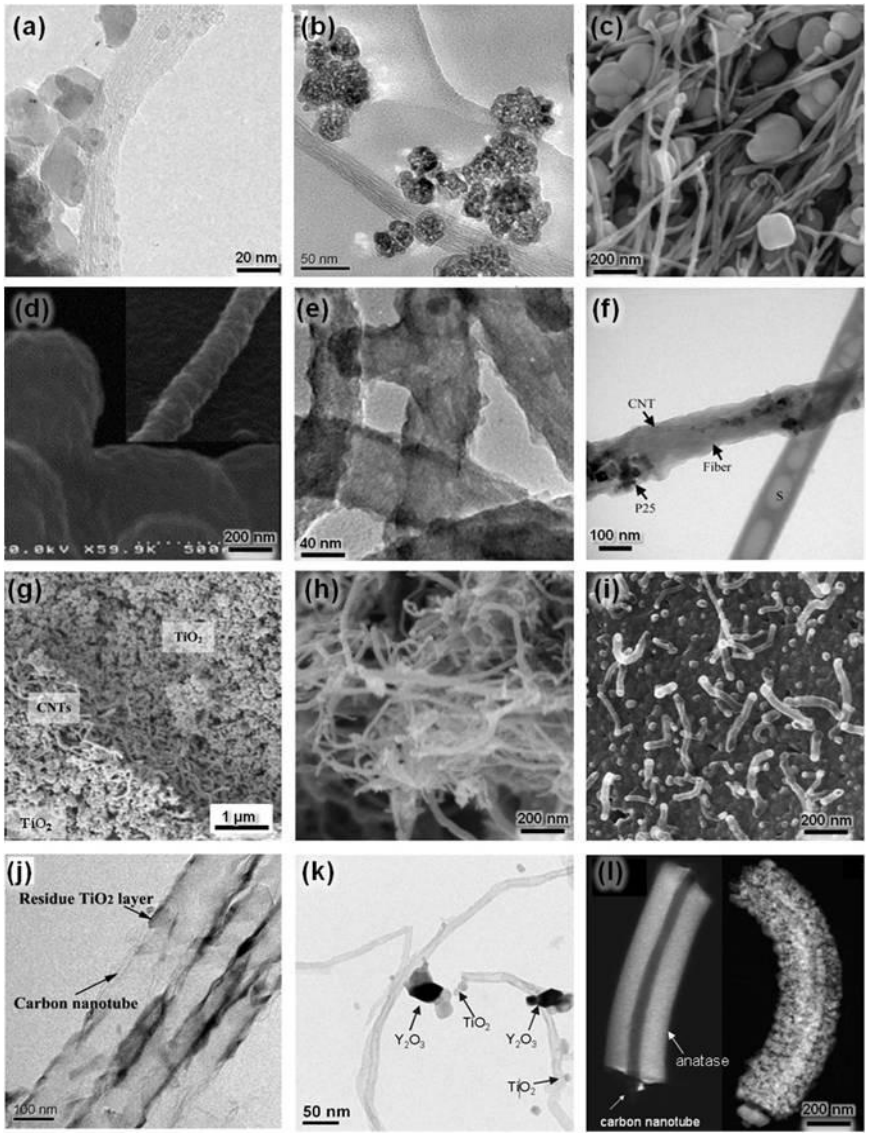


Figure 1.8 CNT-TiO_2 composites. (a) TiO_2 nanoparticles on SWCNTs [102], (b) TiO_2 nanoparticles on MWCNTs [103], (c) SWCNTs on TiO_2 nanoparticles [104], (d) TiO_2 coated SWCNTs [105], (e) TiO_2 coated MWCNTs [106], (f) CNT and TiO_2 embedded in polymer nanofibres [107], (g) laminate composite films [108], (h) intermixed CNTs and TiO_2 nanotubes [109], (i) MWCNTs grown or deposited on bulk TiO_2 [110], (j) CNTs grown in TiO_2 nanotube arrays [111], (k) yttrium treated CNT-TiO_2 [112] and (l) TiO_2 nanotube arrays produced via sacrificial CNT templates [113]. Adapted from [114]

1.9.2 Sol-gel method for composite materials synthesis

In the last 20 years the sol-gel process has become one of the successful techniques for preparing nanocrystalline metallic oxide materials. In particular, the preparation of multi-component oxide materials by this method exhibits a number of advantages over conventional preparation methods [115, 116]. One of the advantages is that the method has the ability to produce materials which show improved surface areas, porosity, stability and homogeneity of the multi-component system [116, 117]. This method is normally used in catalysis for the preparation of oxide supports with high surface areas.

This multistage process involves the formation of a sol and then the transformation of a sol into a gel through hydrolysis and polycondensation reactions. The sol is formed when a gel of a metal alkoxide is dissolved in an alcohol. For the reaction to take place, water and a catalyst are added to the solution. Typical catalysts used are simple acids, e.g., hydrochloric acid, acetic acid and nitric acid. Acetylacetone can also be used as a modifier to moderate the reaction rate [118].

Many reports have shown that TiO_2 can be prepared using the sol-gel technique with the formation of only the anatase phase [119, 120-122]. In addition Jung *et al.* reported that the sol-gel technique can be used to prepare titania that can be used as a deep-coating agent for tubular materials in the preparation of new inorganic materials [122].

This method of incorporating materials (i.e. CNTs or CSs) into an inorganic matrix such as TiO_2 by the sol-gel method is attractive because the properties of these materials can be maintained while only changing the surface properties of the coated materials.

1.10 Aims and objectives of the study

The aims of this research work are to synthesize a series of novel supports that can be used for Co-based Fischer-Tropsch catalysts and to test their catalytic performance in the FT reaction. These supports include carbon spheres (CSs), TiO_2 and a range of carbon sphere titania (CS-TiO_2) composites. These aims will be achieved through the following objectives:

- (I) To synthesize carbon spheres (CSs) with a narrow size distribution using a catalyst-free chemical vapour deposition method (CVD) by employing a swirled floating vertically positioned reactor. Acetylene will be used as the carbon source.

- (II) To purify the synthesised CSs using toluene using conventional soxhlet extraction apparatus.

- (III) To functionalize the synthesized CSs using nitric acid (HNO_3).

- (IV) To synthesise a titania (TiO_2) support using a sol-gel method

- (V) To synthesise novel CS-TiO_2 composite materials by using the sol-gel method with CSs (synthesized as in (I)) homogeneously coated by TiO_2. (This is a very difficult task to achieve and is highly criticised in the literature. To our knowledge there have been no reports on the successful preparation of this composite material). A conventional sol-gel, a surfactant wrapping sol-gel and a carbon coated method were used in the study.

- (VI) To characterize the synthesized, purified and functionalised CSs and to establish: using Transmission Electron Microscopy (TEM) - morphology, size and structure; N_2 physisorption - specific surface area, pore diameter and pore volume; Zeta potential (Zp) - CS surface charge; Thermogravimetric analysis (TGA) - purity, composition, thermal

stability; Fourier Transform Infra-Red (FTIR) spectroscopy - qualitative evaluation of oxygen containing surface groups; and Raman spectroscopy - extent of carbon graphitization.

- (VII) To characterize the synthesized TiO_2 and CS-TiO_2: Transmission Electron Microscopy (TEM) - morphology, size and structure; N_2 adsorption-desorption - specific surface area, pore diameter and pore volume; Thermogravimetric analysis (TGA) - purity, composition, thermal stability; and Raman spectroscopy - extent of graphitization.

- (VIII) To load cobalt (Co) onto the CSs, TiO_2, CS-TiO_2 by the deposition precipitation method with urea as the precipitating agent, and to characterize (i.e. measure the physical and chemical properties assumed to be responsible for the Co performance in a given reaction) the catalysts using TEM, XRF, XRD, N_2 physisorption, TGA, H_2- and CO-Temperature Programmed Reduction (H_2- and CO-TPR), CO-Temperature Programmed Desorption (CO-TPD) and H_2-Chemisorption.

- (VII) To evaluate the catalysts in terms of their Fischer-Tropsch activity and selectivity in a fixed-bed micro reactor.

- (VIII) To explore issues such as support type, shape and pre-treatment, on the activity and selectivity of the catalyst during the Fischer-Tropsch reaction.

1.11 Thesis outline

In Chapter 1 a general literature review and objectives of this Thesis were presented. The literature review is followed by Chapter 2 which describes in detail the experimental procedures used in this study. Chapter 3 presents the results and discussion of work done on the "Catalyst-free preparation of carbon spheres and their functinalisation. Use of a swirled floating vertically positioned chemical vapour deposition reactor". In Chapter 4, work done on "Carbon sphere-titania

composite materials" is presented. Chapter 5 presents the results and discussion of work done on "Titanium dioxide-carbon sphere composites for use as supports in cobalt Fischer-Tropsch synthesis". Chapter 6 gives the conclusions that emanate from the analyses of the results obtained whilst conducting the research and recommendations for further studies.

Aspects of the study have been presented at numerous conferences, symposia and workshops. Publications have started emanating from the study and more will follow and be published in early 2012.

1.11 References

1. Institute for the analysis of global security, "The future of oil", http://www.iags.org/futureofoil.html (accessed on 03 July 2011).
2. Energy Bulletin, "Back to the post-oil future", http://www.energybulletin.net (accessed on 01 February 2011).
3. The Catalyst Review Newsletter, "Gas-to-Liquids: Peering into the crystal ball", (April 2011) P.4.
4. Health and Energy, "The era of expensive oil", http://www.healthandenergy.com, (accessed on 11 July 2011).
5. USA Today, "Recovery of the Gulf Coast", (26 February 2011).
6. http://www.suite101.com/view_image.cfm/2245115 (accessed on 04 June 2011).
7. http://www.guardian.co.uk (accessed on 04 June 2011).
8. The Economist print edition, "The rise of big gas", (accessed on 06 January 2011).
9. A. Y. Khodakov, W. Chu, P. Fongarland, Chem. Rev. 107 (2007) 1692.
10. P. Sabatier, J. B. Sederens, C. R. Acad. Sci. Paris 134 (1902) 514.
11. BASF: German Pat. 293 (1913) 787.
12. F. Fischer, H. Tropsch, Brennst. Chem. 4 (1923) 276.
13. M. E. Dry, The Fischer-Tropsch Synthesis, In: J. R. Anderson, M. Boudart (Eds.), Catalysis Science and Technology, Vol. 1, Springer-Verlag, New York, (1981) 159.
14. G. Olive-Henrichi and S.Olive, In: Herley, Patai (Eds.), The chemistry of the metal-carbon bond, John Wiley and sons, New York Vol. 3 (1985).
15. F. Fischer, H. Tropsch, Ber. Dtsch. Chem. Ges. 59 (1926) 830.
16. A. A. Adesina, Appl. Catal. A: General, 138 (1996) 345.
17. J. Xu, C. H. Bartholomew, J. Sudweeks, D.L. Eggett, Top. Catal., 26 (2003) 55.
18. B. H. Davis, Top. Catal. 32 (2005) 143.
19. http://www.hydrocarbonstechnology.com/project_printable.asp?ProjectID=3065 (accessed on 02 July 2011).

20. H. Storch, N. Golumbic, R. B. Anderson, The Fischer-Tropsch and related Syntheses, Wiley, New York, (1951).
21. R. B. Anderson, The Fischer-Tropsch Synthesis, Academic Press, New York, (1984).
22. M. E. Dry, Catal. Today 71 (2002) 227.
23. M. E. Dry, J. Appl. Catal. A: General, 138 (1996) 319.
24. M. E. Dry, Catal. Today, 6 (1990) 183.
25. H. Schulz, G. Schaub, M. Claeys, T. Riedel, Appl. Catal. A: General 186 (1999) 215.
26. H. A. J. van Dijk, The Fischer-Tropsch Synthesis: A mechanistic study using transient isotopic tracing, Proefschrift, Technische Universiteit Eindhoven (2001).
27. E. A. Van Schalkwyk, Msc. Dissertation, University of Cape Town, Rodenbosch (1998).
28. M. E. Dry, FT catalysts, In: A. Steynberg, M. E Dry (Eds.), Fischer Tropsch Technology, Stud. Surf. Sci. Catal. Elsevier, Amsterdam, Vol. 152 (2004) 533.
29. M. M. G. Senden, S. T. Sie, M. F. M. Post, J. Ansorge, "Engineering aspects of the conversion of natural gas into middle distillates", NATO ASI Series, Series E: Applied Sciences 225 (1992) 227.
30. E. I. Mabaso, PhD Thesis, University of Cape Town, Rodenbosch (2005)
31. S. Fürnsinn, K. Ripfel, R. Rauch, H. Hofbauer, Diesel aus Holz - Die FS Synthese als zukunftsweisende Technologie zur Gewinnung flüssiger Brennstoffe aus Biomasse, 4. Internationale Energiewirtschaftstagung an der TU Wien (2005).
32. W. L. Badger, Ind. Eng. Chem. 36 (1944) 397.
33. D. S. van Vuuren, CSIR CENG (1982) 432.
34. M. A. Vannice, J. Catal. 37 (1975) 449.
35. B. Jager, Stud. Surf. Sci. Catal. 119 (1998) 25.
36. R. L. Espinoza, A. P. Steynberg, B. Jager, A. C. Vosloo, Appl. Catal. A., 186 (1999) 13.
37. B. Jager, R. Espinoza, Catal. Today 23 (1995) 17.

38. V. N. Ipatieff, Catalytic reactions at High Pressures and Temperatures, Macmillan, New York (1936).
39. H. Kölbel, M. Ralek, Catal. Rev. Sci. Eng. 21 (1980) 225.
40. J. Zhang, R. L. Espinoza, S. R. Mohedas, WO 03/052335 A2 (2003).
41. M. Voβ, D. Borgmann, G. Wedler, J. Catal. 212 (2004) 10.
42. A. Y. Khodakov, A. Griboval-Constant, R. Bechara, V. L. Zholobenko, J. Catal. 206 (2002) 230.
43. B. Jongsomjit, C. Sakdamnuson, P. Praserthdam, Mater. Chem. Phys. 89 (2004) 395.
44. R. C. Ruel, C. H. Bartholomew, J. Catal. 85 (1984) 78.
45. E. Iglesia, S. L. Soled, R. A. Fiato, J. Catal. 137 (1992) 212.
46. A. Aaserud, A.-M. Hilmen, E. Bergene, S. Eri, D. Schanke, A. Holmen, Catal. Lett. 94 (2004) 171.
47. S. Storsæter, B. Tøtdal, J. C. Walmsley, B. S. Tanem, A. Holmen, J. Catal. 236 (2005) 139.
48. A. Corma, Chem. Rev. 87 (1997) 2373.
49. K. M. Ryan, N. R. B. Coleman, D. M. Lyons, J. P. Hanraham, T. R. Spalding, M. A. Morris, D. C. Steytler, R. K. Heenen, J. D. Holmes, Langmuir 18 (2002) 4996.
50. A. Y. Khodakov, W. Chu, P. Fongarland, Chem. Rev. 107 (2007) 1692
51. L. Fu, C.H. Bartholomew, J. Catal. 92 (1985) 367.
52. G. L. Bezemer, J. H. Bitter, H. P. C. E. Kuipers, H. Oosterbeek, J. E. Holewijn, X. Xu, F. Kapteijn, A. J. van Dillen, K. P. de Jong, J. Am. Chem. Soc. 128 (2006) 3956.
53. M. C. Bahome, L. L. Jewell, D. Hildebrandt, D. Glasser, N. J. Coville, Appl. Catal. A: General 287 (2005) 60.
54. G. Jacobs, T. K. Das, Y. Zhang, J. Li, G. Racoillet, B. H. Davis, Appl. Catal. A: General 233 (2002) 263.
55. D. I. Enache, B. Rebours, M. Roy-Auberger, R. Revel, J. Catal. 205 (2002) 346.
56. http://herkules.oulu.fi/isbn9514269543/html/x546.html (accessed on 04 July 2011).

57. C. H. Bartholomew, Appl. Catal. A: General 212 (2001) 17.
58. J. A. Mouljin, E. van Diepen, F. Kapteijn, Appl. Catal. A: General 212 (2001) 3.
59. S. Matsuda, A. Kato, Appl. Catal. 8 (1983) 149.
60. A. A. Khassin, T. M. Yurieva, V. V. Kaichev, V. I. Bukhtiyarov, A. A. Budneva, E. A. Paukshtis, V. N. Parmon, J. Mol. Catal. A 175 (2001) 189.
61. C. J. G. van Der Grift, P. A. Elberse, A. Mulder, J. W. Geus, Appl. Catal. 63 (1990) 19.
62. K. Okabe, X. Li, M. Wei, H. Arakawa, Catal. Today 89 (2004) 431.
63. R. Baratti, V. Feckova, M. Morbidelli, A. Varma, Ind. Eng. Chem. Res. 3416 (1997) 3416.
64. A. F. Pére-Cadenas, M. M. P. Zieverink, F. Kapteijn, J. A. Mouljin, Catal. Today 105 (2005) 623.
65. A. Roucoux, J.Schulz, H. Patin, Chem. Rev. 102 (2002) 3757.
66. I. Capek, Adv. Colloid Interface Sci. 110 (2004) 49.
67. D. H. Ralston, K. J. Klabunde, Appl. Catal. 3 (1982) 13.
68. M. Kurhinen, T. A. Pakkanen, Langmuir 16 (2000) 2658.
69. A. Rautiainen, M. Lindblad, L. B. Backman,R. L. Puurunen, Phys. Chem. Chem. Phys. 4 (2002) 2466.
70. G. C. Bond, In: P. W. Atkins, J. C. E Holker, A. K. Holliday (Eds.), Heterogeneous Catalysis: Principles and applications, Oxford University Press, New York 70 (1990).
71. W. K. Bell, W. O. Haag, G. W. Keirkes, D. J. Klocke, US Patent 4686313 (1987).
72. C. H., Bartholomew, R. B., Pannell, J. Catal. 65 (1980) 390.
73. N. A. Pakhomov, R.A. Buyanov, Kinetics and Catalysis 46 (2005) 669.
74. P. Burattin, M. Che, C. Louis, Journal of Physical Chemistry B 103 (1999) 6171.
75. P. Burattin, M. Che, C. Louis, Journal of Physical Chemistry B 104 (2000) 10482.
76. J.W. Geus, Studies in Surface Science and Catalysis 16 (1983) 1.

77. R.J. Farrauto, C.H. Bartholomew, Fundamentals of industrial catalytic processes, Blackie Academic and Professional New York, 1997.
78. M.C. Bahome, L.L. Jewell, K. Padayachy, D. Hildebrandt, D. Glasser, A.K. Datye, N.J. Coville, Applied Catalysis A: General 328 (2007) 243.
79. M.C. Bahome, L.L. Jewell, D. Hildebrandt, D. Glasser, N.J. Coville, Applied Catalysis A, General 287 (2005) 60.
80. E. van Steen, F. Prinsloo, Catalysis Today 71 (2002) 327.
81. A. Corma, Chem. Rev. 87 (1997) 2373.
82. B. Storsæter, J. Tøtdal, B. Walmsley, A. Tanem, A. Holmen, J. Catal. 236 (2005) 139.
83. G.C Schuit, L.L. Reijen, Advances in Catalysis 10 (1958) 242.
84. T. Sugimoto, X. Zhou, and A. Muramatsu, Journal of Colloid and Interface Science 259 (2003) 43.
85. A. Fernandez, J. Leyrer, A. Gonzalez, G. Munera and H. Knozinger, J. Catal. 112 (1988) 489.
86. Z. Wei, Q. Xin, X. Guo, E. Sham, P. Grange and B. Delmon, Appl. Catal. 63 (1990) 305.
87. P. Wauthoz, M. Ruwet, T. Machej and P. Grange, Appl. Catal. 69 (1991) 149.
88. J. Retuert, R. Quijada and V. Arias, Chem. Mater. 10 (1998) 3923.
89. G.M. Pajonk, Appl. Catal. 72 (1991) 217.
90. J.C Yu, J.G. Yu, J.C. Zhao, Appl. Catal., B. Environ. 36 (2002) 31.
91. M. Adachi, Y. Murata, M. Harada, S. Yoshikawa, Chem. Lett. 8 (2000) 942.
92. B. O'Regan, J. Moser, M. Anderson, M. Gratzel, J. Phys. Chem. 94 (1990) 8720.
93. Z.B. Zhang, C.C. Wang, R. Zakaria, J.Y. Ying, J. Phys. Chem. 102 (1998) 1087.
94. D.M. Antonelli, Y.J. Ying, Angew. Chem. Int. Ed. Engl. 34 (1995) 2014.
95. P. Serp, M. Corrias and P. Kalck, Appl. Catal. A 253 (2003) 337.
96. Ebbesen T W, Lezee H J, Hiura H, Neentt J W, Ghaemi H F and Thio T Nature 382 (1996) 54.

97. A. Jitianu, T. Cacciaguerra, R. Benoit, S. Delpeux and F. B´eguin, Carbon 42 (2004) 1147.
98. W. Wang, P. Serp, P. Kalck and J. Faria, J. Mol. Catal. A 235 (2005) 194.
99. R. Long and R.Yang, J. Am. Chem. Soc. 123 (2001) 2058.
100. Y. Li, Chem. Phys. Lett. 350 (2001) 412.
101. Y. Li, S. Wang, Z. Luan, J. Ding, C. Xu and D. Wu, Carbon 41 (2003) 1057.
102. C. Dechakiatkrai, J. Chen, C. Lynam, S. Phanichphant, G. Wallace, J. Electrochem Soc. 154 (2007) A407.
103. K. Dai, T. Peng, D. Ke, B. Wei, Nanotechnology 20 (2009) 125603.
104. Y. Yao, G. Li, S. Ciston, R. Lueptow, K. Gray, Environ. Sci. Technol. 42 (2008) 4952.
105. S. Orlanducci, V. Sessa, M. Terranova, G. Battiston, S. Battiston, R. Gerbasi, Carbon 44 (2006) 2839.
106. B. Gao, G. Chen, G. Li Puma, Appl. Catal. B 89 (2009) 503.
107. S. Kedem, D. Rozen, Y. Cohen, Y. Paz, J Phys. Chem. C, 113 (2009) 14893.
108. J. Cho, S. Schaab, J. Roether, A. Boccaccini, J. Nanopart. Res. 10 (2008) 99.
109. R. Doong, L. Chiang, Sci. Technol. 58 (2008) 1985.
110. Y. Ou, J. Lin, S. Fang, D. Liao, Chem. Phys. Lett. 429 (2006) 199.
111. L. Yang, S. Luo, S. Liu, Q. Cai, J. Phys. Chem. C 112 (2008) 8939.
112. F. Zhang, M. Chen, K. Zhang, W. Oh, Bull. Korean Chem. Soc. 31 (2010) 133.
113. A. Hungria, D. Eder, A. Windle, P. Midgley, Catal. Today 143 (2009) 225.
114. R. Sellappan, J. Zhu, H. Fredriksson, R. Martins, M. Zach, D. Chakarov, J. Mol. Catal. A: Chemical 335 (2011) 136.
115. X.-Z. Ding, X.-H. Liu, Materials Science and Engineering A224 (1997) 210.
116. G. E. Dobler, K. S. Syslick, A. I. Ko, In: D. Helms (Ed.), Novel Approaches to Catalyst Preparation, Catalytica Studies Division (1993).

117. N. N. Madikizela-Mnqanqeni, N. J. Coville, Appl. Catal. A: General 317 (2007) 195.
118. Y. Nosaka, M. Jimbo, M. Aizawa, N. Fujii, R. Igarashi, J. Mater. Sci. Lett. 10 (1991) 406.
119. M. Schneider, A. Baiker, Catal. Today 35 (1997) 339.
120. I. A Montoya, T. Viveros, J. M. Domiguez, L. A. Canales, I. Schifter, Catal. Lett. 15 (1992) 207.
121. T. Sugimoto, X. Zhou, A. Muramatsu, J. Colloid Interface Sci. 259 (2003) 43.
122. J. H. Jung, H. Kobayashi, K. J. C. van Bommel, S. Shinkai, T. Shimizu, Chem. Mater. 14 (2002) 1445.

Chapter 2

2. Experimental Methods

The techniques used to prepare and characterise the catalysts in this study are briefly described in this section.

2.1 Introduction

Methods of catalyst preparation determine the overall catalytic performance in Fischer-Tropsch Synthesis (FTS) [1]. This is affected by the support used to disperse the catalyst. It is critical to choose a catalyst support that will be suitable for enhancing the catalytic performance. The method of deposition of an active phase onto the appropriate support also plays a role in affecting the FTS activity. Control of the product distribution by controlling the reaction temperature, total pressure, H_2/CO ratio and the nature of the catalyst still remain a challenge [1]. In this chapter these aspects are discussed.

The experimental method section describes the choice and preparation of different catalytic supports and the deposition of an active phase onto these supports to synthesise catalysts. Characterisation techniques and the information that can be obtained from them are outlined. Lastly the methods and experimental procedures for catalyst evaluation in FTS are also presented.

2.2 Preparation of catalyst and support materials

Catalyst preparations were conducted by the deposition precipitation method adapted from the literature [2, 3]. The corresponding metal solution precursors were then impregnated into a support.

2.2.1 Support preparation

Preparation, purification and functionalisation of carbon spheres (CSs) with uniform size and a narrow distribution were some of the vital aspects that are addressed in this work. A chemical vapour deposition (CVD) method was employed in the synthesis of CSs. A swirled floating chemical vapour deposition reactor setup (Fig 2.1) was used to achieve this. A study of the synthesis of CSs is discussed in Chapter 3. The different types of support materials which were prepared and used as catalyst for Fischer-Tropsch synthesis include the following:

- *Carbon spheres (CSs),*
- *Titania coated carbon spheres made via conventional sol-gel method (CS-SG)*
- *Titania coated carbon spheres made via surfactant wrapping sol-gel method (CS-SW)*
- *Titania coated carbon spheres, combusted in air (CS-CSW)*
- *Carbon nanotubes (CNTs),*
- *Titania coated carbon nanotubes made via surfactant wrapping sol-gel method (CNT-SW)*
- *P25 Degussa titania (P25),*
- *Sol-gel titania (SG),*
- *Titanate nanotubes (TNTs),*
- *Titania coated titanate nanotubes (C-TNTs)*

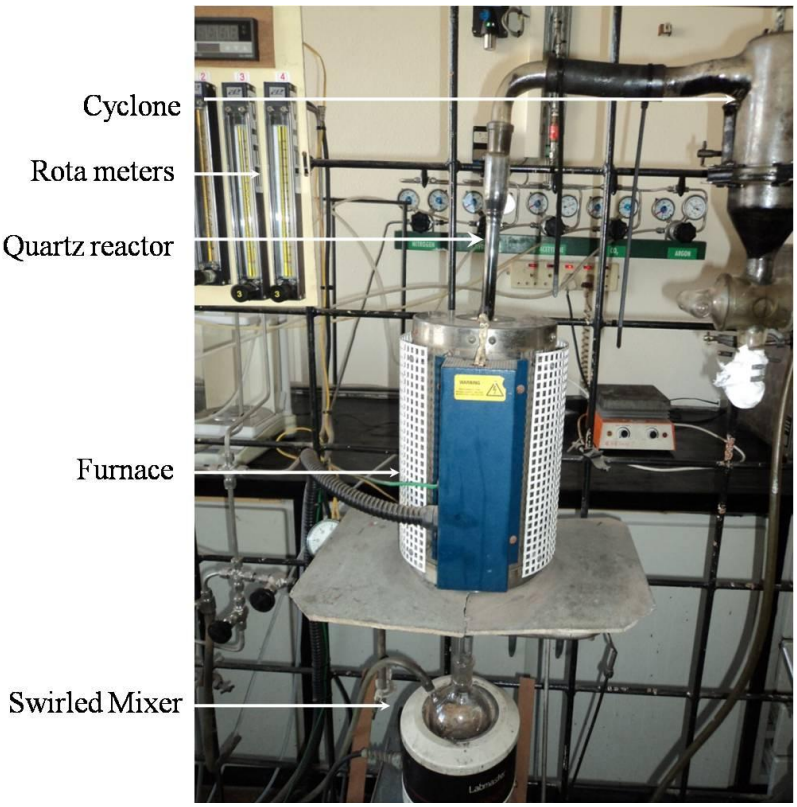


Figure 2. 1 Schematic representation of a vertically positioned swirled floating chemical vapour deposition reactor setup.

2.2.2 Support preparation

The supported catalysts were prepared by the deposition precipitation (DPU) method using urea [2, 3]. In the DPU method, the calculated weight of $Co(NO_3)_3 \cdot 9H_2O$ and urea were dissolved in de-ionized water, at 90°C, and added to the support to achieve a total loading of 10 weight %. The urea was added to facilitate the uniform formation of metal hydroxides onto the surface of the support [4]. After allowing sufficient time (at least 2 h) for the hydrolysis of the urea, the sample was air dried. To decompose the nitrate all the samples were further dried in an oven (120 °C, overnight) and then calcined at 250 °C for 2.5 h in nitrogen (for all those with carbon based supports) or at 350 °C for 6.5 h in air for all those placed on titania based supports.

2.3 Characterization of catalysts and supports

For a better understanding of the catalyst properties, both the supports and the catalysts were characterized by the following characterization techniques:

- *Transmission electron microscopy (TEM)*
- *Thermogravimetric analysis (TGA),*
- *Brunauer-Emmett-Teller (BET) surface area analysis method,*
- *X-ray fluorescence (XRF) spectroscopy,*
- *X-ray diffraction (XRD)*
- *Temperature programmed techniques:*
    - *H_2-Temperature programmed reduction (H_2-TPR),*
    - *CO-Temperature programmed reduction (CO-TPR),*
    - *and CO-Temperature programmed desorption (CO-TPD).*
- *and H_2-chemisorption analysis.*

These catalysts were also evaluated in a Fischer-Tropsch synthesis (FTS) reactor.

2.3.1 Transmission electron microscopy (TEM) and energy dispersive X-ray spectroscopy (EDS)

The morphologies of the calcined supports and catalysts were determined using Transmission Electron Microscopy (TEM) (FEI Technai Spirit G^2) (Fig. 2.2). Energy dispersive X-ray spectroscopy (EDS) was used to identify and confirm the presence of the metal particles. Specimen samples for TEM analysis were prepared by dispersing very small samples in about 1 mL of methanol. The mixture was sonicated for about 15 min to obtain a homogeneous suspension. One drop of each suspension was poured onto an SPI-carbon coated copper grid and was allowed to dry before it was placed in the microscope. The morphology of the samples was observed and the data was processed on a computer screen. The image diameters of the samples

obtained from TEM analysis were measured using ImageJ 1.43u software and about 150 particles' diameters were measured per sample.

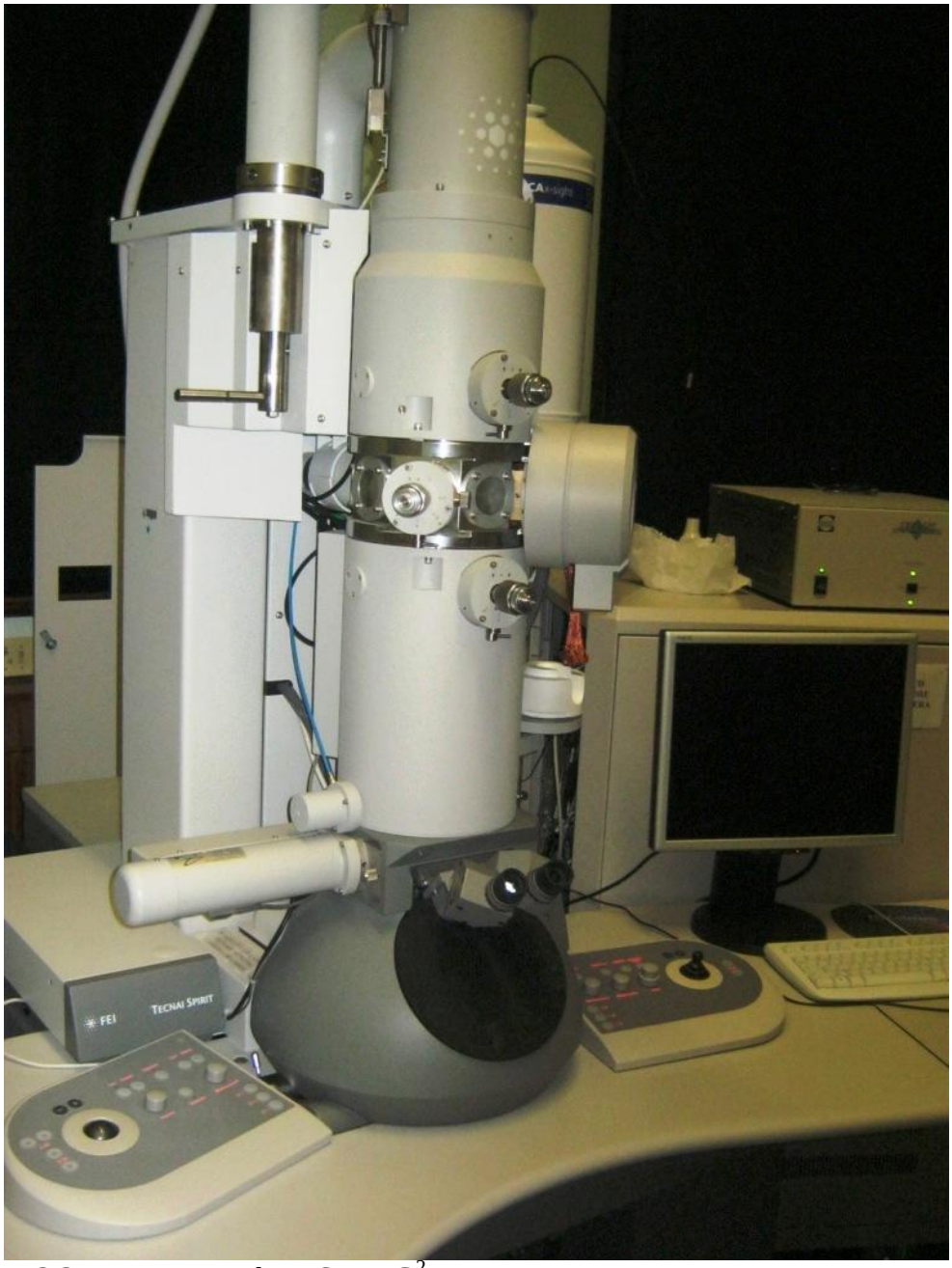


Figure 2.2 TEM FEI Technai Spirit G^2

2.3.2 Thermogravimetric analysis (TGA)

Thermogravimetric analysis (TGA), conjugated with a derivative curve of the weight loss (DTG) measurements was carried out on a Perkin Elmer STA 4000 analyser coupled with an auto sampler that can perform up to 45 sample analyses at a time (Fig 2.3). About 10 mg of CS samples was placed in a pan (ceramic) and then put in the instrument's furnace. The sample temperature was ramped from room temperature to 950 °C under a flowing air or nitrogen atmosphere (20 mL/min) at a heating rate of 10 °C/min. A TGA weight loss plot provided information about the nature, stability and composition of the investigated sample. The derivative curve of this plot on the other hand provided the maximum temperature at which the weight loss took place. The temperature of the sample was monitored by a digital computer coupled with Pyris Software V9.0.2. The weight of the sample was expressed on a percentage basis.

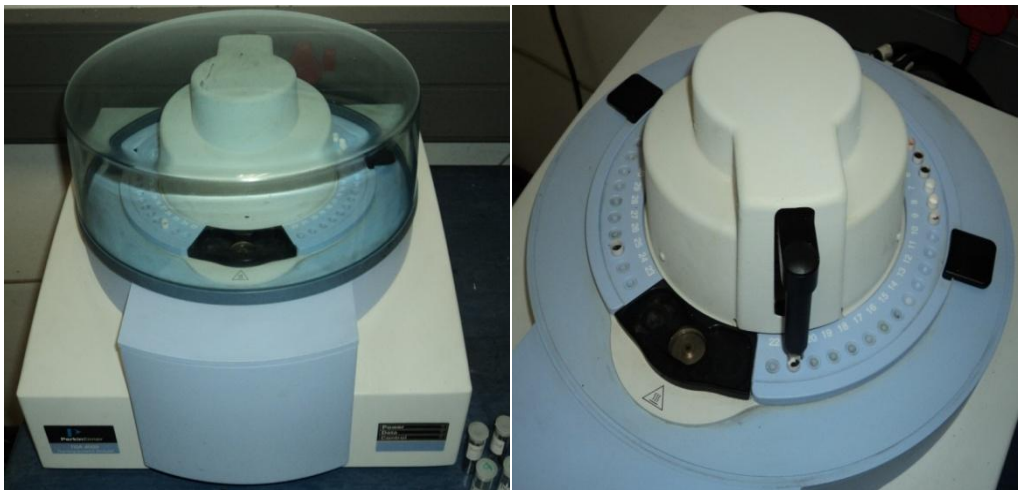


Figure 2.3 Perkin Elmer STA 4000 thermogravimetric analyzer coupled to an auto sampler: *(left)* manual-single sample analysis and *(right)* an autosampler-multiple samples analysis (with an autosampler arm in operation)

2.3.3 X-ray Fluorescence (XRF) spectroscopy

The XRF measurements were carried out on a PW2404 wavelength dispersive XRF spectrometer Panalytical model instrument. A rhodium target tube was used to generate the X-rays with K_α = 24.9 and K_β = 22. Powder samples were mixed with 2% polyvinyl glue Mowiol binder before being pressed to pellets using 10 MPa pressure prior to analysis.

2.3.4 BET surface area measurements/BJH pore size distributions

Adsorption of gases onto solid surfaces and in pores is a complex phenomenon which involves mass and energy interactions and phase changes [5]. The physical adsorption of gases by solids increases with decreasing temperature and with increasing pressure. This non-destructive process is exothermic. Many techniques can be used to determine the kinetics and thermodynamics of adsorption. However, the surface area and the pore structure of solid materials can only be investigated by adsorption (or desorption) isotherms [6]. Normally a Langmuir isotherm is used. This isotherm gives a measure of the molar quantity of gas taken up, or released, at a constant temperature by an initially clean (degassed) solid surface as a function of gas pressure. Most frequently this test is conducted at a cryogenic temperature, usually that of liquid nitrogen (LN_2) at its boiling point (-196 °C, at 1 atm). The BET method, developed by Brunauer, Emmett and Teller is based on a theory that uses the Langmuir adsorption isotherms and multimolecular layer adsorption to determine surface area and give information about pore structure [7]. This method operates in an area of low relative pressures (0.05 - 0.35).

In this thesis about 0.2 g of powder samples were degassed in flowing N_2 at 120 °C for 4 h (unless otherwise stated) prior to analysis using a Micromeritics Flow Prep 060 (Fig. 2.4a), sample degas system. The degasser has six heating stations for degassing samples and six cooling stations. The surface areas and pore size distributions were then obtained at -196 °C. The pore size distribution with specific

surface areas of the calcined supports and supported catalysts, were determined via N_2 adsorption/desorption according to the BET method using a Micromeritics Tristar 3000 surface area and porosity analyzer (Fig. 2.4b). This analysis took about 2 h to complete a measurement.

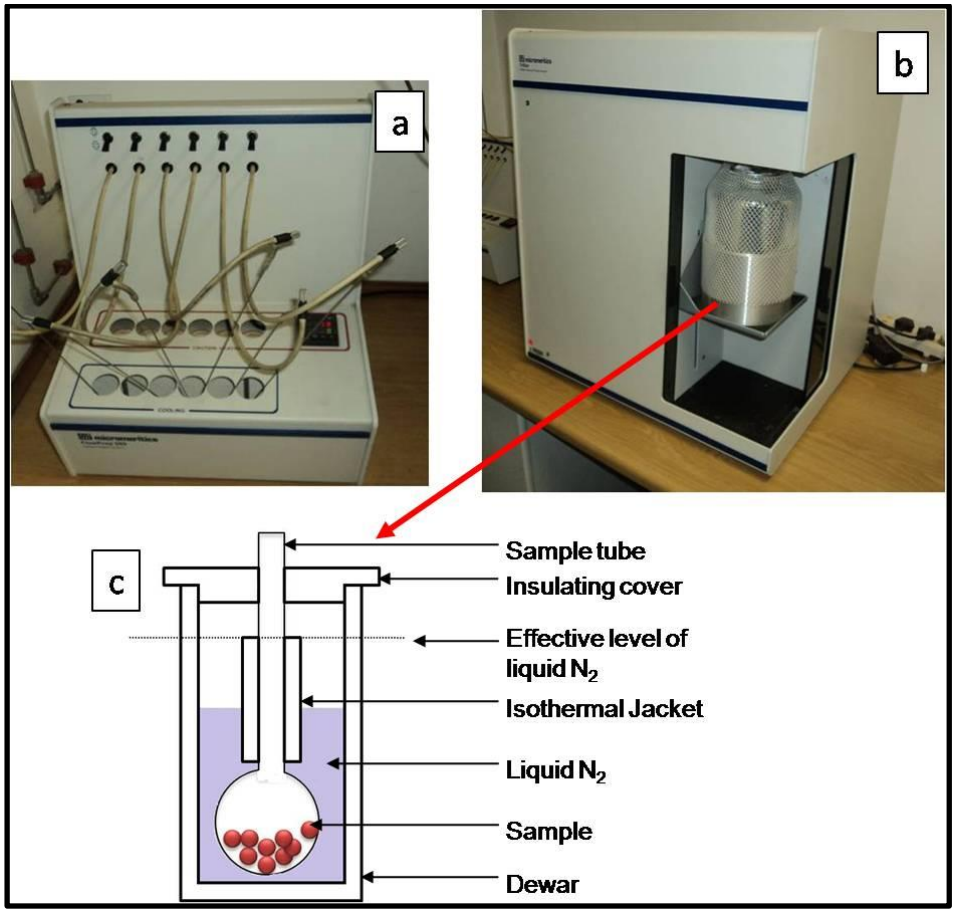


Figure 2.4 (a) Micromeritics Flow Prep 060, (b) Micromeritics Tristar 3000 and (c) liquid N_2 coolant Dewar depicting the Isothermal Jacket^{TM} method of maintaining the cold/warm volume ratio in the sample tube

The specific adsorption pore volumes (i.e. pore size distribution) were calculated by the Barrett-Joyner-Halenda (BJH) method [8]. Pore size distribution analysis (i.e. multipoint analysis) for samples studied in this thesis often took about 22 h to complete a single measurement. It is therefore crucial to control cryogen levels during the analysis. To avoid evaporation of LN_2 and the consequent fall of N_2 levels in the containing Dewar an Isothermal Jacket^{TM} (Fig. 2.4c) was employed. This basically is

a close-fitting, porous sleeve that surrounds the sample tube stem and maintains, by capillary action, a fixed level of LN_2 around the tubes as long as its lower end dips into LN_2. The upper end of the jacket creates a sharp temperature demarcation line below which the temperature is that of LN_2. The stable temperature boundary environment can be maintained for as long as 60 hours [5].

3.3.5 X-ray diffraction (XRD)

Average metal sizes, crystallinity and phase compositions of the support and catalysts were examined using X-ray diffraction analysis on a Bruker D8 Avance X-ray diffractometer (Fig 2.5) with a primary beam Göbel mirror, a radial soller slit, and a V Åntec-1 detector using Cu-K_α (1.5406Å) radiation at 40 kV and 40 mA.

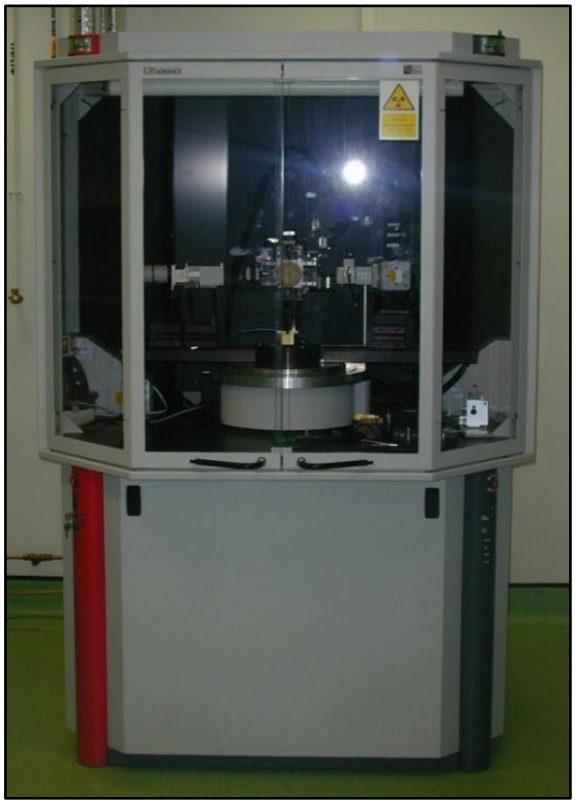


Figure 2.5 The Bruker D8 X-Ray diffractometer

The scan range was $5° < 2\theta < 90°$ in 0.021 steps, using a standard speed with an equivalent counting time of 14.7 seconds per step. The obtained diffraction peaks

were then compared with those of standard compounds reported in the Diffrac^{plus} evaluation package using the EVA (V11.0, rev .0, 2005) software package.

2.3.6 Temperature-programmed techniques (H_2-TPR, CO-TPR and CO-TPD)

Since catalyst reduction is a critical step in FTS, it was necessary to study the reduction behavior of the cobalt loaded-catalysts. The reduction temperatures required for the reduction of cobalt oxide to metallic cobalt before FTS reaction were determined. This confirmation is required since metallic cobalt is the active component for a successful FTS reaction.

H_2-TPR and CO-TPR experiments were carried out with a Micromeritics Auto Chem II unit (Fig 2.6a). About 0.2 g of calcined samples was placed in a U-shaped quartz reactor. Prior to analysis the samples were degassed in high purity argon at 1 bar pressure and a temperature of 150 °C (10 °C/min) for 45 min, to drive off water or impurities, and then cooled down to 50 °C. Then 5% H_2/Ar (or 5% CO/He) was switched on at a flow rate of 50 mL/min at 1 bar pressure while the temperature was raised from 50 to 900 °C at a heating rate of 10 °C/min. The H_2 and CO consumption was monitored by the change of thermal conductivity (TCD) of the effluent gas stream. The resulting TPR profiles, with TCD signals, were then collected from the PC equipment.

The CO-TPD experiments were performed in the same system as used in CO-TPR with He as a carrier gas. About 0.2 g of calcined sample was loaded in a U-shaped quartz reactor. Prior to analysis the samples were reduced at 350 °C (1 bar pressure) in high purity H_2 (50 mL/min) for 12 h. After reduction, the sample was cooled to 100 °C and then purged with high purity He for 35 min to remove the weakly adsorbed H_2. A 5% CO/He gas mixture was switched on at a flow rate of 50 mL/min

at 1 bar pressure and CO was adsorbed for 1 h. The He was again purged for 35 min to remove weakly adsorbed CO, and then TPD (50-900 °C) was carried out in He.



Figure 2.6 Micromeritics Auto Chem II

2.3.7 H_2 chemisorption and O_2 titration analysis

Chemisorption analysis is a very useful technique that can be used to determine metal dispersion on a support, metal crystallite size, degree of reduction and the number of adsorption sites. This is achieved by adsorbing gaseous molecules onto catalyst samples. The analysis procedure gives information on the number of active metal sites within the catalyst. H_2 chemisorption analysis was performed with a Micromeritics ASAP 2020 (Fig 2.7), surface area and porosity analyzer instrument.

The calcined pre-weighed catalyst samples (about 0.5 g) were placed in a U-shaped quartz tube sample holder which was evacuated under vacuum. These samples were degassed using pure He at 150 °C. Removal of the He was then performed at 100 °C before reduction of the catalyst at 425 °C in pure H_2 for 16 hours. After the initial reduction the catalysts were further reduced in pure H_2 at a temperature that was 25

°C below the reduction temperature (425 °C) for 1 hour prior to analysis. All physisorbed H_2 molecules were evacuated before measuring adsorption isotherms for H_2 at 100 °C.

Detailed information of the analysis conditions procedure is given in Table 2.1. The conditions obtained from the TPR experiments were used for the cobalt oxide reduction in the reactor. The total H_2 uptake was determined by extrapolating the straight-line portion of the adsorption isotherm to zero pressure.



Figure 2.7 Micromeritics ASAP 2020

After H_2 chemisorption was conducted for each sample, the same sample was evacuated using He at 100 °C to remove the adsorbed H_2. Evacuation of all weakly adsorbed He molecules was then performed at 400 °C after which O_2 titration was carried out using a stream of pure O_2 at 400 °C. Detailed information of the O_2 titration analysis conditions procedure is also given in Table 2.1. Extents of reduction were calculated using the O_2 uptake that was obtained by extrapolating the straight-line portion of the adsorption isotherm to zero pressure, this being the method that was proposed by Bartholomew and Farrauto [9]. The reaction of reduced cobalt with

oxygen was considered to proceed to Co_3O_4 [10]. The adsorption measurements were reproducible and had an error bar of ± 0.6%.

Table 2.1 H_2 analysis and O_2 titration conditions for cobalt containing catalysts

Condition	Ramp rate /°Cmin^{-1}	Temperature /°C	Time /min
H_2 Analysis:			
Evacuate He	5	150	30
Evacuate	10	100	10
Flow H_2	2	425	480
Flow H_2	2	400	60
Evacuate	2	400	240
Leak	-	35	10
Evacuate	-	35	10
Analyze H_2[a]	1	100	-
O_2 titration:			
Evacuate He	10	100	30
Evacuate	10	400	30
Analyze O_2[b]	10	400	-

[a] Pressure points: 100,150, 200, 250, 300, 350, 400, 425, and 450 mmHg

[b] Pressure points: 100, 200, 300, 400 and 450 mmHg

Metal dispersions (*D%*) and crystallite diameters (d_p) were calculated using the equations that were proposed by Bartholomew *et al.* [11, 12 and 13]. These calculations were based on the assumption that cobalt metal was present as spherical particles of uniform size and the assumptions that unreduced cobalt was present in a separate dispersed layer in intimate contact with the support [10]. Accordingly, the percentage dispersion was calculated according to the following equation (2.1):

$$D\% = \frac{1.179X}{Wf} \qquad (2.1)$$

where X is the total H_2 uptake in millimoles per gram of catalyst, W is the weight percentage of cobalt and f is the cobalt reduction extent determined from the O_2 titration.

The average crystallite diameters (d_p) were calculated from $D\%$, assuming spherical metal crystallites with a site density (s) of 14.6 atoms/nm^2. The following formula (3.2) was used:

$$d_p = \frac{6.59s}{D\%} \tag{2.2}$$

The number (N_s) of active cobalt metal sites was calculated using the same formula (2.3) that was used by Webb *et al.* [5]:

$$N_s = \frac{V_m \times N_A \times F_s}{V_{mol}} \tag{2.3}$$

where N_A is the Avagrado's number, V_m is the quantity of H_2 irreversibly adsorbed on the sample (monolayer volume) and V_{mol} the molar volume of the adsorptive gas. F_s is the stoichiometry factor, and this was considered to be equal to 2, for H_2 on cobalt. The FT reaction turnover frequency (*TOF*) was evaluated by combining the number of active cobalt sites with the rate of CO conversion during the FT reaction [14].

The formula is as follows:

$$TOF = \frac{-r_{CO} \times N_A}{N_s} \tag{2.4}$$

where $-r_{CO}$ is the rate of CO consumption in (mol/s) and the *TOF* is therefore expressed in (s^{-1}).

2.4 Fischer-Tropsch Synthesis experiments

2.4.1 Reactor system and experimental setup

A schematic diagram for the reactor system is shown in Fig. 2.8. All the gases that were used were supplied by AFROX (African Oxygen) Ltd. The gas cylinders were accompanied by a certificate that indicated the purity of the components available in a particular gas mixture. The gases used for the catalyst characterization and catalyst reduction prior to the FTS were Ultra High Purity (UHP) grade gases (99.997% purity). Gas cylinders that contained $H_2/CO/N_2$ mixtures (syngas) (0.60/0.30/0.10 vol. Purity: 99.99%) were used to supply the reactant gas stream to the catalyst. N_2 was used as an internal standard in order to ensure accurate mass balances. Ar (20 mL/min) gas was used as carrier gas for both the flame ionization detector (FID) and the thermal conductivity detector (TCD) gas chromatographs (GC). Digital images of both GC's are depicted in Fig 2.9. Pressure regulators on the cylinders were used to set the pressure on the system. The system was equipped with two pressure gauges. The one installed between the gas cylinders and the reactor indicated the pressure of gas that entered the reactor, while the other one was installed between the cold trap and the TCD-GC. This was set at atmospheric pressure and was used to allow consistent volumetric gas flow rates that were measured with the soap bubble meter connected to the FID-GC. All gas lines after the reactor were kept at 150 °C. Two product traps were installed below the reactor; a hot trap which was heated at 150 °C was used to collect wax while the cold trap (ambient temperature) was used to collect liquid products (oil and water). The gaseous products were directed to the GC's which were connected in series (on-line) for analysis. The reactor temperature and line temperatures were controlled electronically by using electronic temperature controllers connected to the system.

All the lines used in the system consisted of 1/4" and 1/8" stainless steel tubing and the fittings used were Swagelok stainless steel fittings. The on/off valves were SS

Valco valves with Viton seals and the needle valves were Whitey valves. The system was also equipped with a PC coupled with DataApex Clarity™ software which was used to collect all chromatograms from both the FID-GC and the TCD-GC.

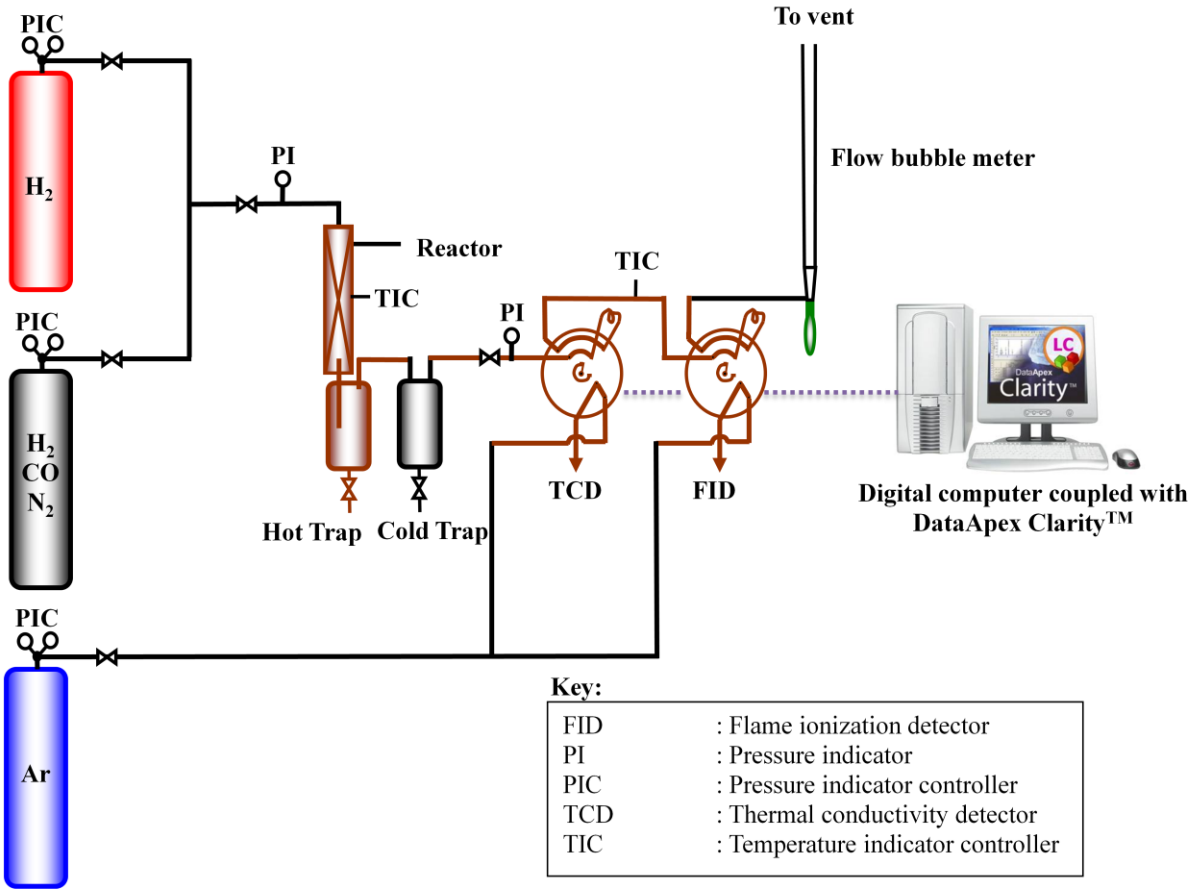


Figure 2.8 A schematic diagram for the reactor system

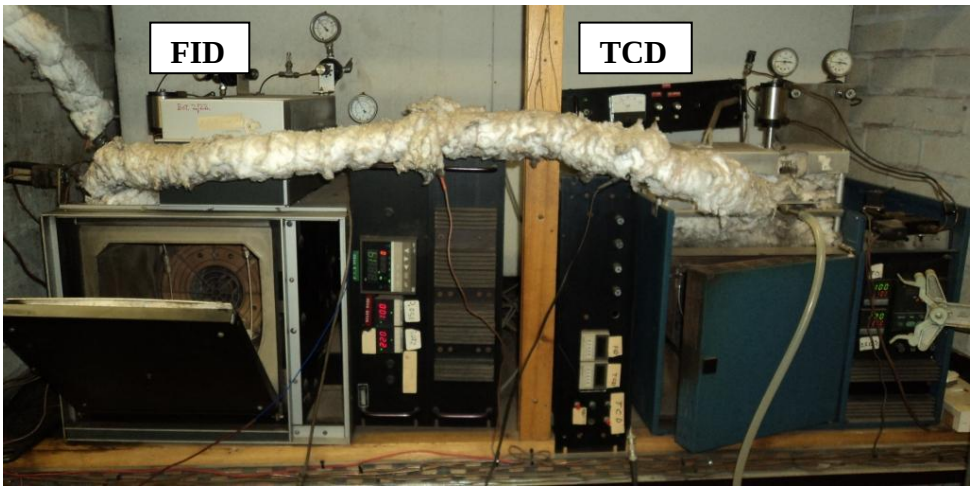
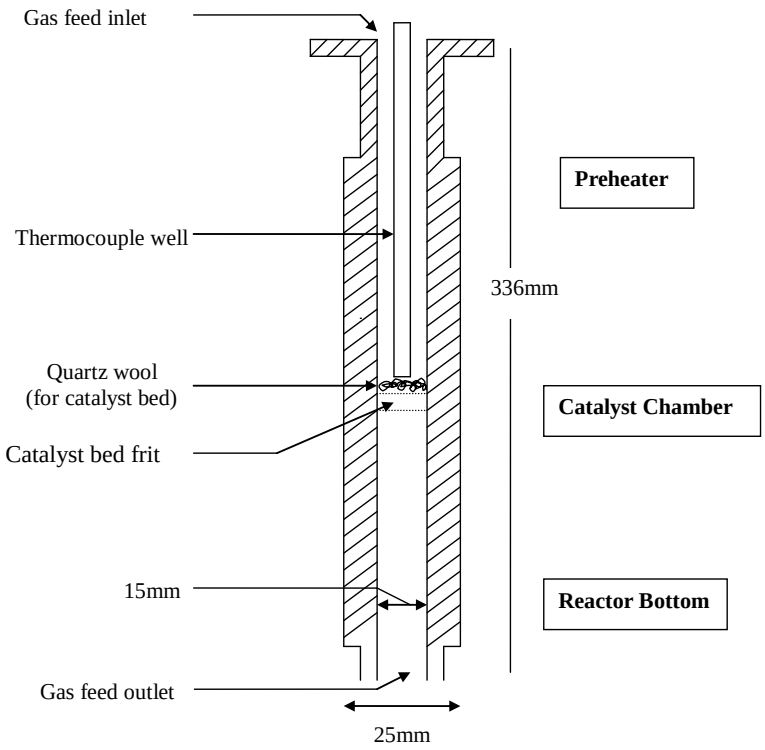


Figure 2.9 Gas chromatography one fitted with FID and the other with a TCD detector

2.4.2 Reactor and catalyst packing

In Figure 2.10, a diagrammatic representation as well as a digital image of a stainless-steel fixed bed reactor (FBR) used is shown. The reactor comprised of three zones, the pre-heater zone where the gas entering is heated through a bed, the catalyst chamber where the reaction takes place in the catalyst bed and the reactor bottom, the region below the catalyst bed.

The thermocouple was inserted into the thermocouple well touching the catalyst embedded on quartz wool. Gases which emerged from the gas cylinders entered through the gas feed inlet of the reactor to the catalyst bed and the products were collected through the gas feed outlet which was connected to the two knockout ports (product traps). Catalyst (0.5 g) diluted with 1 g silicon carbide (Aldrich) was packed inside the reactor on a quartz bed. This catalyst mass was chosen to ensure that the gas would flow through the catalyst bed without any blockages. In essence the particle sizes (d_p) of the support and therefore that of the catalytic material were designed in such a way that they are smaller than a tenth of the inner diameter of the



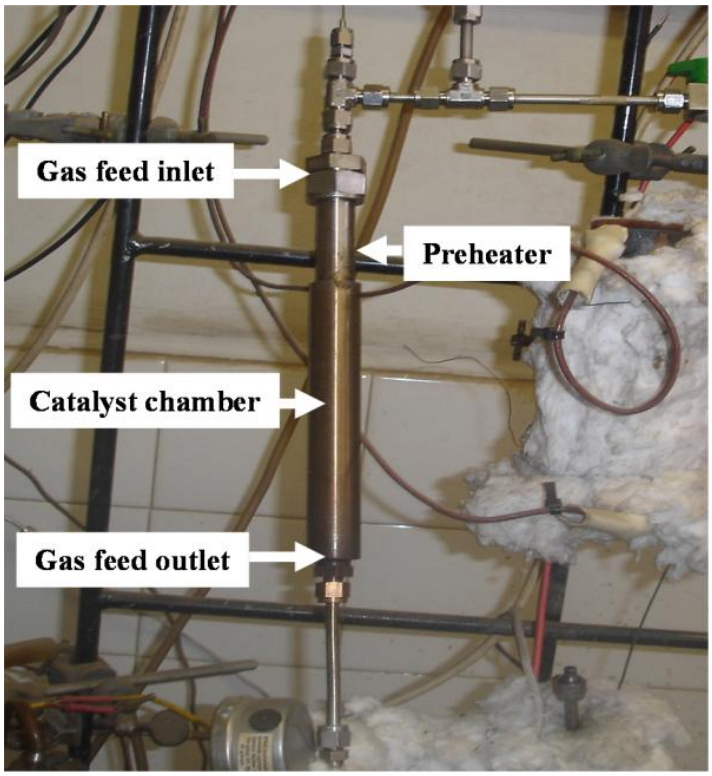


Figure 2.10 A diagrammatic representation (top) and a digital image (bottom) of a stainless-steel fixed bed reactor that has been used

reactor ($ID_{reactor}$) as required by formula (2.5). This ensured ideal plug flow behavior with negligible wall effects [15]. The flows were large enough to allow mobility of the gases through the interstices between packed catalytic particles in the reactor.

$$\frac{ID_{reactor}}{d_p} > 10 \qquad (2.5)$$

2.4.3 Experimental procedure for catalyst evaluations

A catalyst sample (about 0.5 g) was reduced *in-situ* in pure H_2 at 1 bar pressure with a flow rate of 45 mL/min/g for 16 hours at 350 °C using a heating rate of 5 °C/min. During the reduction step the shut-off valve for the syngas bottle was closed so as to stop syngas flow to the reactor. After cooling, the H_2 shut-off valve was closed while the syngas valve was opened. The pressure on the syngas gauge was set to 1 bar and the TCD was calibrated (bypass) with syngas at a standard concentration so as to determine the amount of syngas entering the reactor. This calibration was continued until consistent areas of H_2, N_2 and CO were obtained. A bypass trace is depicted in Fig 2.11. The syngas pressure was then slowly adjusted to 8 bar at a volumetric flow rate of 30 mL/min/g while the temperature was ramped to the reaction temperature (230 °C, unless otherwise stated) at a heating rate of 5 °C/min.

2.5 Product analysis

2.5.1 Gas chromatographic analysis

Product analysis was divided into two segments. The first segment involved analysis of gaseous products on-line using two GC's; a thermal conductivity detector (TCD) and a flame ionization detector (FID). The second segment (off-line FID-GC analysis) involved syringe injection (0.2 μL) of oil and wax products. These were collected from the knockout traps. The conditions used on the GC's are given in Table 2.2. The analyses of oil and wax products were performed using different

temperature programs on an off-line FID-GC. A typical online product and unreacted gas (syngas) analysis of a TCD-GC spectrum is shown in Fig. 2.12.

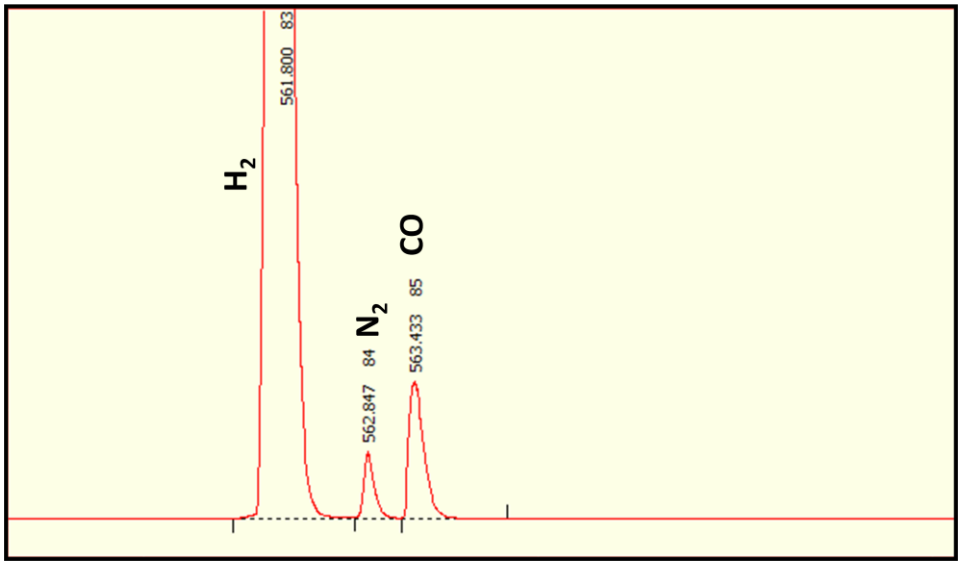


Figure 2.11 A typical spectrum for the synthesis gas (bypass) using TCD-GC

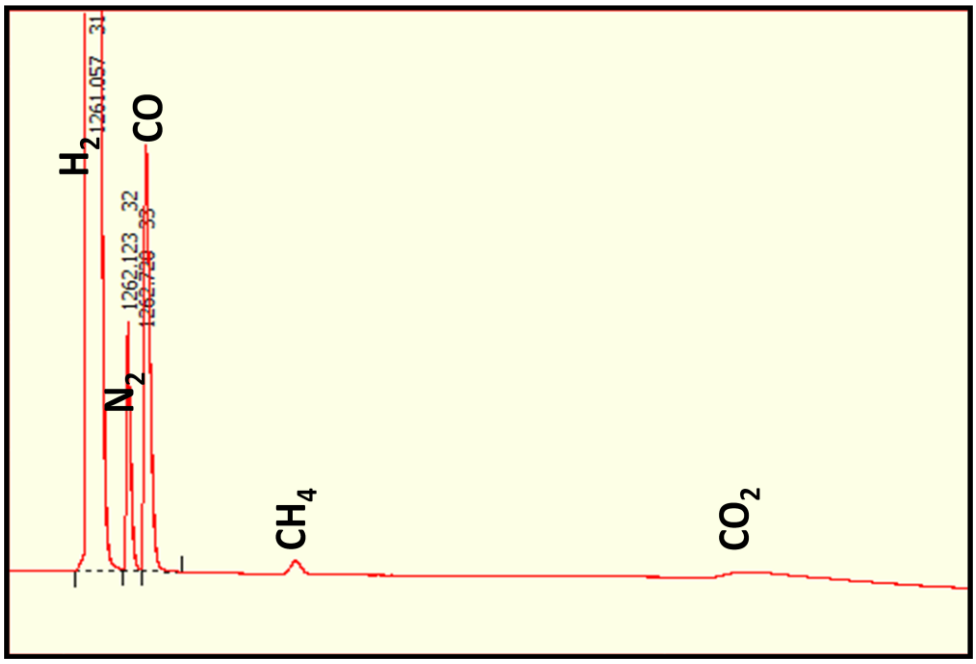


Figure 2.12 A typical product and unreacted syngas spectrum using TCD-GC

Table 2. 2 Conditions for gas chromatographic analyses

Gas chromtoraph (online)	**PYE Unicam (Series 204)**
Detector	TCD, T = 220 °C
Column type	Packed, stainless steel, 2m x 2.2mm, O.D = 1/8"
Stationary phase	Carbosieve S-II, 60-80 mesh
Sample valve temperature	150 °C
Carrier gas	Argon
Flow rate	20 mL(NTP)/min
Oven temperature	250 °C (isothermal)
Products analysis	H_2, N_2, CO,CH_4, CO_2
Gas chromtoraph (online)	**Hewlett Packard 5890**
Detector	FID, T = 220 °C
Column type	Packed, stainless steel, 1.5 m x 2.2 mm, O.D = 1/8"
Stationary phase	ZB-5, 80/100 mesh
Sample valve temperature	150 °C
Carrier gas	Argon
Flow rate	20 mL(NTP)/min
Oven temperature	250 °C (isothermal)
Products analysis	C_1 - C_8
Gas chromtoraph (off-line)	**Varian 3700**
Detector	FID, T = 350 °C
Column type	30 m x 5 µFT, O.D.= 0.53 mm
Stationary phase	ZB-1
Sample valve temperature	250 °C
Carrier gas	Air
Flow rate	30 mL(NTP)/min
Oven temperature program:	
Oil:	Heat to 60 °C at 10 °C/min, heat to 300 °C at 12.5 °C/min, hold at 300 °C for 30 min
Wax:	Heat to 220 °C at 74 °C/min, heat to 300 °C at 10 °C /min, hold at 300 °C for 240 min
Products analysis	$C_5 – C_{35}$

A typical product analysis spectrum by online FID-GC for gas, off-line FID-GC for oil and off-line FID-GC for wax are all shown in Fig 2.13, 2.14 and 2.15,

respectively. Relative errors (repeatability of these analysis techniques) were typically ± 3 % for TCD analyses and ±6 % for online FID and ±11% for offline FID analyses. The internal standards which were accurately fed to the product stream were used for calculation of flow rates of inorganic and organic components and subsequently their conversions, yields and selectivities.

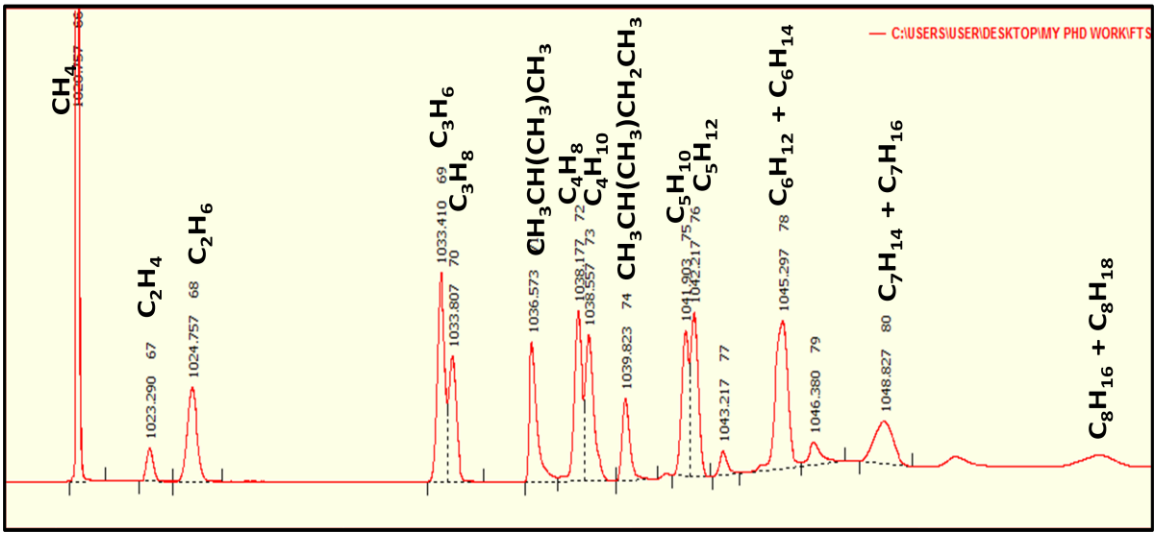


Figure 2.13 A typical FT spectrum for gaseous products obtained from an FID-GC.

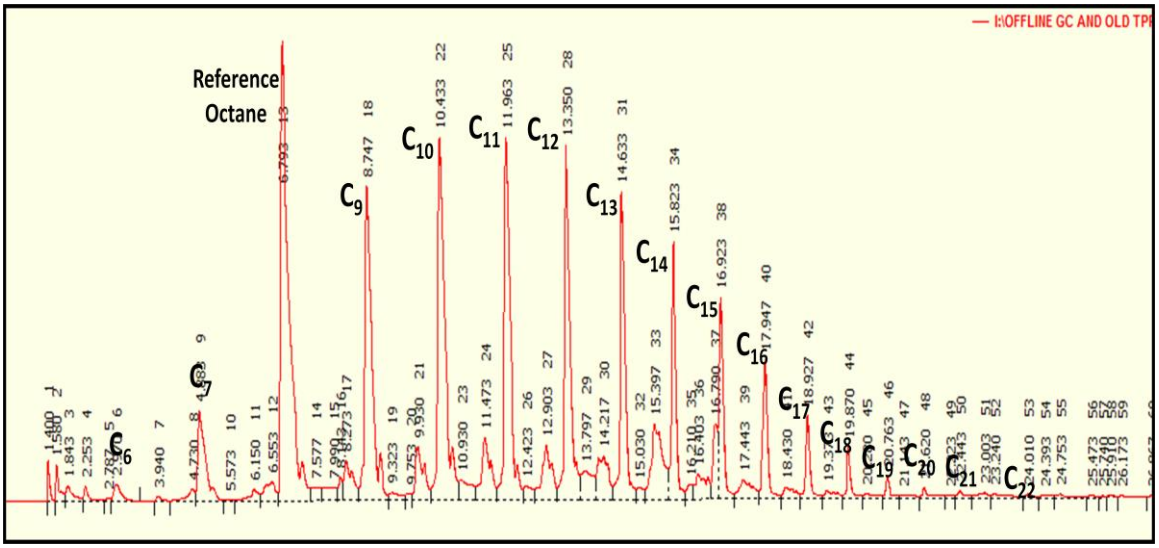


Figure 2.14 A typical FT spectrum (spiked with octane 1L) for gaseous products obtained from an FID-GC (only major peaks are labeled here).

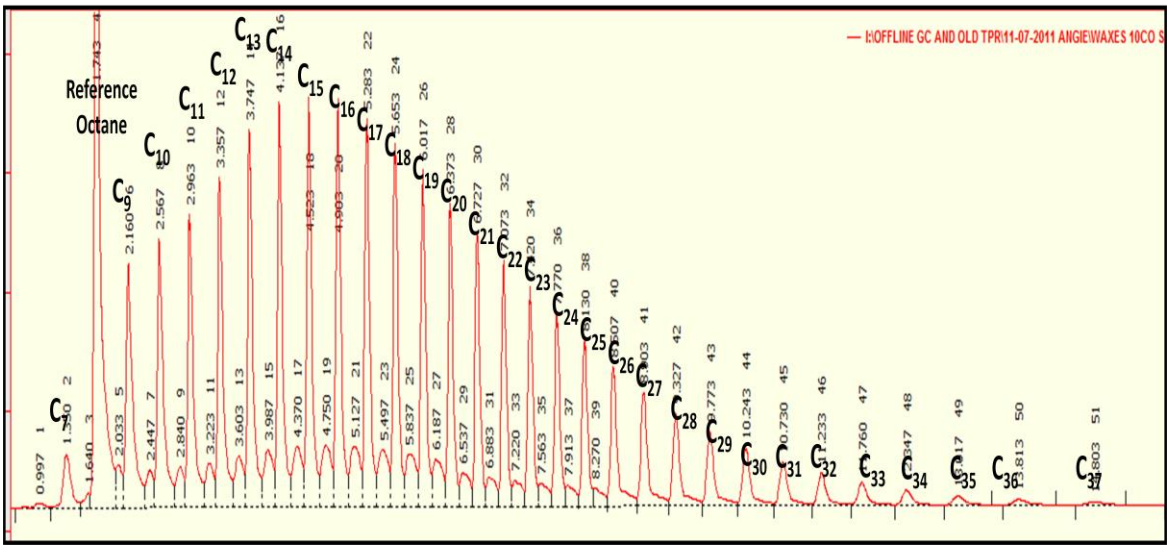


Figure 2.15 A typical FT spectrum (spiked with octane) for gaseous products obtained from an FID-GC (only major peaks are labeled here).

2.5.2 Data work-up

The calculations that were used to compute the mass balances are similar to those used by, Bahome [2], Nijs *et al*. [16], Mokoena [17], Duvenhage [18], Price [19], Mabaso [20] and Jalama [21]. Before every FTS reaction, the reactants, CO and H_2 bypassed the reactor and the samples were analyzed.

This represents the amount of reactants fed into the reactor. The mass balance was performed on carbon and oxygen. Mass balance data of 100 ± 5% was accepted as adequate. The amount of carbon and oxygen entering the reactor equals the amount of carbon and oxygen reacted to form products plus the unreacted carbon and oxygen leaving the reactor.

The % mass balance was calculated using equation (2.6) below:

$$\%\,\text{Mass balance} = \frac{N_X + N_Y}{N_Z} \qquad (2.6)$$

where N_x = moles of reacted carbon and oxygen

N_y = moles of unreacted carbon and oxygen

N_z = moles of carbon and oxygen entering the reactor to give products

A calibration gas containing a standard composition of CH_4, C_2H_6, C_2H_4, CO, CO_2, and N_2 was used to calibrate the FID and TCD data. This calibration was carried out once every six months. The amount of hydrocarbon product produced as determined by GC peak areas obtained from the FID data, were corrected for C_2H_4 (olefins) and C_2H_6 (paraffins) by using the response factors based on those reported by Dietz [22], and Scanlon *et al.* [23].

In all evaluations of catalyst data for FTS, the reaction steady state was normally reached 24 hours after the reaction had been started. At that point the oil and wax traps were decanted and the mass balance calculations were commenced. The time recorded at the end of the mass balance period was used to calculate the rates of the reaction (i.e. FTS, CO conversion and CO_2 formation). The oil and water mixture from the cold trap and the wax from the hot trap were collected successively and weighed. The oil was separated from water before analysis on an offline GC.

The %CO conversion was calculated using equation (2.7) below:

$$\%CO = \left[\frac{CO_{in} - CO_{out} \times \frac{N_{2\,(in)}}{N_{2\,(out)}}}{CO_{in}} \right] \qquad (2.7)$$

where CO_{in} and $N_{2\,(in)}$ are areas of CO and N_2 peaks obtained from the measurement of syngas feed mixture, respectively. CO_{out} and $N_{2\,(out)}$ are areas of CO and N_2 peaks obtained from the gaseous product streams, respectively.

The product selectivity (S_i) for hydrocarbons was calculated for component x_i using equation (2.8) as follows:

$$S_i = \left[\frac{\text{mass component } x_i}{\sum x_i} \right] \times 100\% \qquad (2.8)$$

The individual rates of reaction for FTS (r_{FTS}) and water gas shift WGS (r_{WGS}) were calculated from experimentally obtained quantities as:

$$r_{WGS} = r_{CO_2} \qquad (2.9)$$

$$r_{FTS} = r_{CO} - r_{CO_2} \qquad (2.10)$$

where r_{CO_2} is the rate of carbon dioxide formation and r_{CO} is rate of carbon monoxide conversion.

Since C_2H_4 and C_2H_6 were the only gaseous products that could be separated by the column, the olefin to paraffin ratio for C_2 could be determined (x_2) and was given as shown in equation (2.11):

$$\text{Olefin to Paraffin ratio } x_2 = \frac{\text{Mass olefin } x_2}{\text{Mass total hydrocarbon } x_2} \qquad (2.11)$$

2.6 References

1. M. E. Dry, The Fischer-Tropsch Synthesis, In: J. R. Anderson, M. Boudart (Eds.), Catalysis Science and Technology, Vol. 1, Springer-Verlag, New York, 159 (1981)
2. M. C. Bahome, PhD Thesis, University of the Witwatersrand, Johannesburg (2007)
3. E van Steen, F. Prinsloo, Catal. Today 71 (2002) 327
4. K. De Jong, A. Van Dillen, Heterogeneous Catalysis. Preparation, Characterisation and Application, Publicard: Utrecht (1999) 724
5. P. Webb, Analytical methods in fine particle technology, Micromeritics Instrument Corporation, Norcross, GA USA (1997)
6. S. Ross, J. Olivier, On Physical Adsorption, Interscience Publishers, New York (1964)
7. S. Brunauer, The adsorption of Gases and Vapors. Vol. I, Physical Adsorption, Princeton university Press, Princeton, N.J. (1943)
8. E. Berret, L. Joyner, P. Halenda, J. Am. Chem. Soc. 73 (1951) 373
9. C. H., Bartholomew, R. J., Ferrauto, J. Catal. 45 (1976) 41
10. R. L., Chin, D. M., Hercules, J. Phys. Chem. 86 (1982) 360
11. C. H., Bartholomew, R. B., Pannell, J. Catal. 65 (1980) 390
12. C. H., Bartholomew, B. P. Richard, J. L. Butler, J. Catal. 65 (1980) 335
13. D. G. Mustard, C. H. Bartholomew, J. Catal. 46 (1981) 340
14. K. Jalama, N. J. Coville, D. Hildebrandt, D. Glasser, L. L. Jewell, Appl. Catal. A: General 326 (2007) 164
15. G. Ertl, H. Knözinger, J. Weitkamp, In: G. Ertl, H. Knözinger and J. Weitkamp (Eds.): Handbook of heterogeneous catalysis. VCH, Weiheim, Federal Republic of Germany (1997) 439
16. H. H. Nijs, P. A. Jacobs, J. Chrom. Sci. 19 (1981) 40
17. E. M. Mokoena, PhD Thesis, University of the Witwatersrand, Johannesburg (2005)

18. D. J. Duvenhage, PhD Thesis, University of the Witwatersrand, Johannesburg (1992)
19. J. G. Price, PhD Thesis, University of the Witwatersrand, Johannesburg (1994)
20. E. I. Mabaso, PhD Thesis, University of Cape Town, Rodenbosch (2005)
21. K. Jalama, PhD Thesis, University of the Witwatersrand, Johannesburg (2007)
22. A. W. Dietz, J. Gas Chrom. 62 (1967)
23. J. T. Scanlon, D.E. Willis, J. Chrom. Sci. 23 (1985) 33

Chapter 3

3. Catalyst-free preparation of carbon spheres and their functionalisation. Use of a swirled floating vertically positioned chemical vapour deposition reactor

3. 1 Introduction

Ball-shaped carbon structures were first discovered in the 1940s [1]. Their discovery has led many researchers to develop an interest in studying spherically shaped materials that are in the nano size region [2, 3]. In the mid 1980's fullerenes were developed [4]. Within the last decade many different types of spherical carbons have been reported and these have been shown to be both hollow and solid viz. carbon onions [5, 6], carbon microspheres [7-11], carbon beads [12-14] and carbon pearls [15]. The fabrication of these spherical carbons was carried out using catalytic synthesis [9, 16] as well as direct pyrolysis of hydrocarbons [17, 18]. In recent literature reports carbon spheres, which are similar to carbon black particles [19, 20], have been developed from natural carbon sources such as natural gas or oil, typically in the presence of trace amounts of oxygen. One example is the acetylene black process, i.e. the use of acetylene as the synthesis gas under reduced oxygen environments [21-23]. The synthesis of carbon spheres in the absence of a catalyst has also been reported [24, 25]. The size and type of these materials can be controlled by varying preparation conditions and the carbon source. Due to the intrinsic properties of these materials, such as their high thermal resistance, light-weight and high strength, the

carbon spheres have many applications such as their use as catalyst supports [26], in high-strength composites [27], as absorbents and as wear-resistant materials [28, 29].

Since carbon spheres and other related carbon materials are hydrophobic, their dispersibility in water remains a challenge. A lot of research has been conducted on the chemical modification of the surface of carbon materials by the addition of functional groups and these modifications have been shown to enhance their ability to be dispersed in water [30, 31]. Fig. 3.1 depicts a cartoon of surface modified carbon spheres containing acidic surface OH and COOH functional groups. The degree of dispersion is dependent on the type and the amount of functional groups present. The functionalization also affects their activity and conductivity [32 -34].

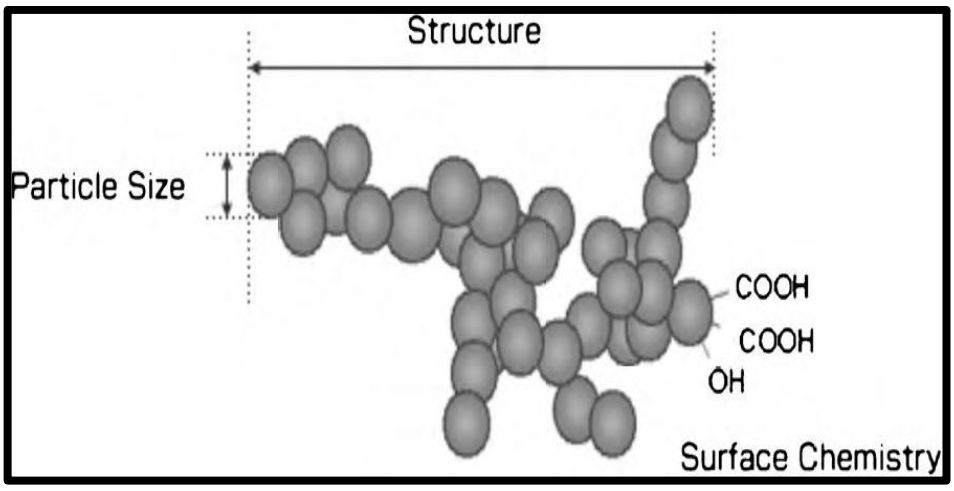


Figure 3.1 The structure of carbon black showing some functional groups on the surface of the carbon sphere structure [32]

In this study carbon spheres (CSs) have been produced without using a catalyst in a vertical reactor using a swirled vertical mixer i.e. the gases (inert carrier gas and carbon source gas, C_2H_2) are mixed homogeneously by a swirling mixer before entering the reactor. The method provides a means for the continuous production of high purity CSs with uniform diameter in the absence of a catalyst. Different reaction conditions were varied during the study, such as C_2H_2 flow rate and C_2H_2

residence time spent in the reactor. Purification and surface functionalisation of the synthesised CSs was also studied. The obtained materials were characterised by traditional methods, i.e. TEM, TGA, BET, XRD and Raman spectroscopy. FTIR spectroscopy and Zeta Potential measurements were used to study the CSs and the functional groups on the functionalised CSs.

3. 2 Experimental

3. 2.1 Carbon sphere preparation

Carbon spheres (CSs) were synthesised using a vertically positioned chemical vapour deposition (CVD) reactor without a catalyst. Iyuke *et al*. developed and patented this reactor [35, 36]. A schematic representation of this reactor set up is represented in Fig. 3. 2.

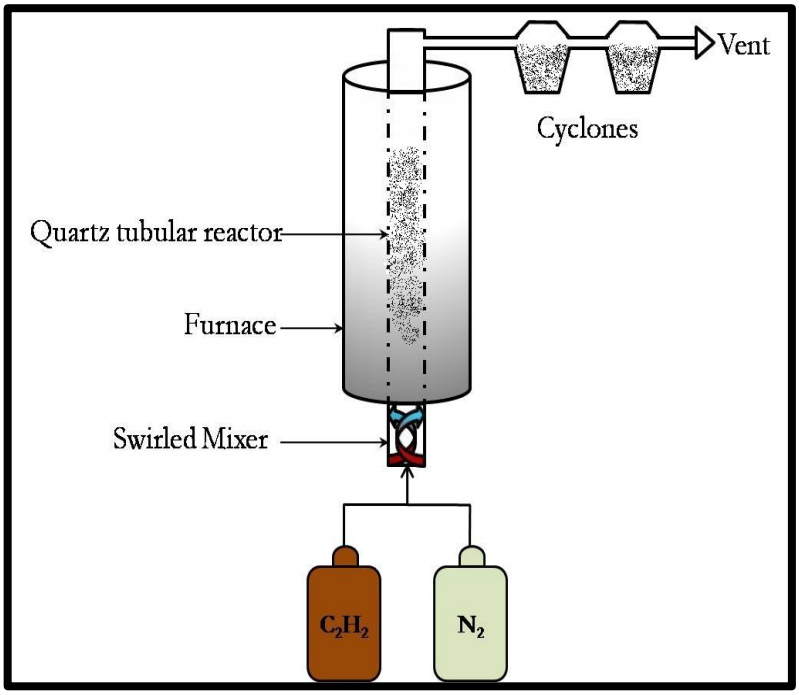


Figure 3.2 Schematic representation of a vertically positioned swirled floating chemical vapour deposition reactor setup.

Briefly, it consists of a quartz hollow tubular reactor loaded in a furnace and flowing gases (C_2H_2 and N_2 are passed through the reactor). The system consists of valves, rotameters, and a swirled coiled passage that enables mixing of the

gases before they enter the reactor. The furnace was first set to a desired temperature of 1000 ^{o}C (at 10 ^{o}C/min), under inert conditions (viz. N_2 flow at 30 mL/min). After the desired temperature was reached a N_2 flow valve was then switched to a flow of C_2H_2 which was fed through the reactor at specified flow rates (i.e. between 300 to 500 mL/min depending on the reaction studied). Acetylene (C_2H_2) was pyrolysed in the quartz reactor and yielded CSs.

A smoky carbon vapour together with black soot (Fig. 3.3) with some small traces of "oily material" from the direct pyrolysis of C_2H_2 was generated and carried to the upper end of the reactor where it was cooled in a condenser (ambient temperature) and collected in two cyclones.

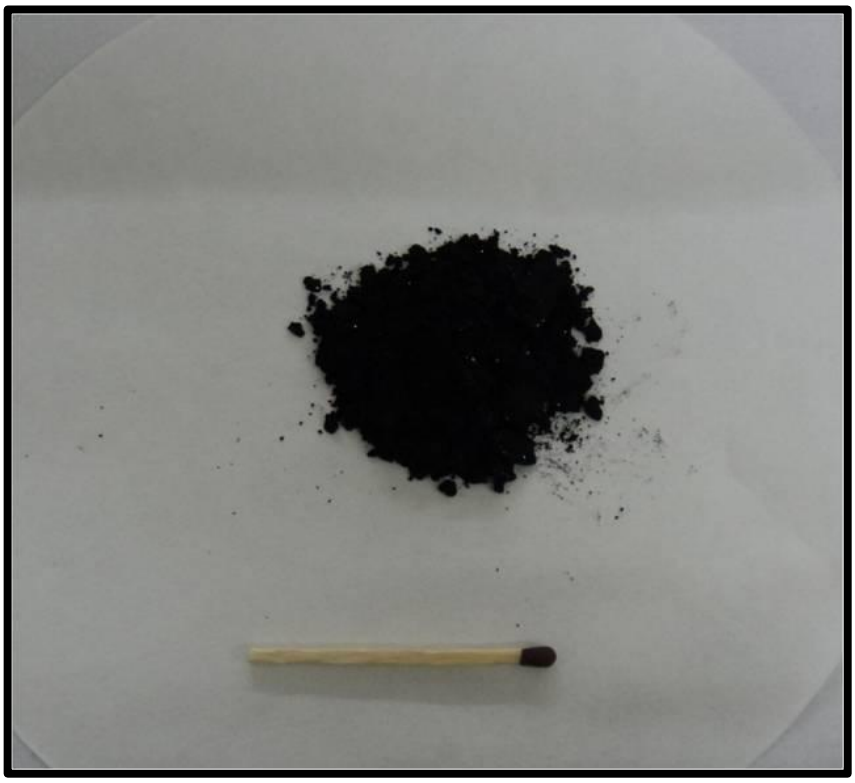


Figure 3.3 Photograph of soot collected from the cyclones (match stick used as reference to give a sense of size).

The C_2H_2 was allowed to flow continuously for precisely 4 minutes through the reactor for every reaction studied. When C_2H_2 was fed into the reactor for more than 4 minutes, a "hard rocky" solid soot was developed which was not collected

or studied. The feed was then stopped and switched to a continuous flow of N_2 (30 mL/min) until the furnace and the reactor had cooled to ambient temperature. After cooling, the N_2 flow was stopped and the quartz reactor was removed from the furnace. The bulk of the solid black soot was collected from the inner walls of the hot region of the reactor; this soot was collected by scraping with a glass rod, and the black sample weighed and analyzed. The other soot was collected from the cyclones. The yield produced per pyrolysis reaction was a combination of the soot collected from the inner walls of the reactor and from the two cyclones. Separate TEM analysis of soot collected from the cyclones and that collected from the inner walls of the reactor confirmed that the CSs had the same morphology and size. The sizes and surface area measurements of the CSs were determined using TEM and BET methods, respectively.

3.2.2 The purification and functionalization of the carbon spheres

Purification of pristine CSs (as-synthesised) was carried out in a conventional soxhlet extraction apparatus (Fig. 3.4).

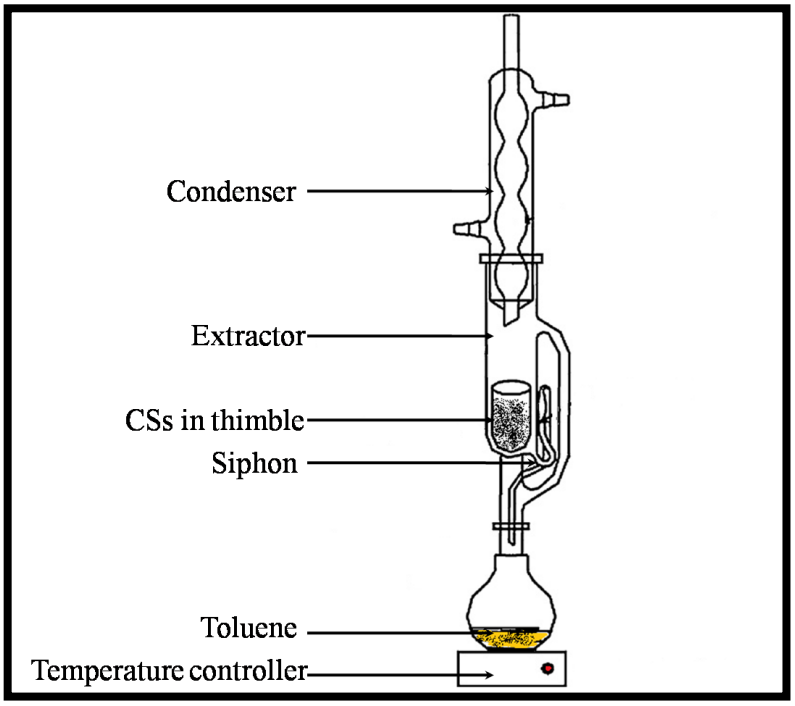


Figure 3.4 Schematic representation of conventional soxhlet extraction set-up for the purification of CSs

About 1 g of pristine CSs (P-CS) was placed in a cellulose thimble (Whatman®, 60 mm × 26 mm i.d., 28 mm e.d.). This thimble was transferred to a conventional soxhlet extraction apparatus. Toluene (bp = 110 °C) was used as a solvent and the oil bath was heated at 140 °C. The extraction process was continued overnight. The oily layer (aromatic hydrocarbons, PAHs) that was formed was removed by this process. During this separation the colour of toluene changed from colourless to a deep brown showing that the aromatic hydrocarbons were successfully removed. The material was then air dried and then oven dried (120 °C) for 4 hours. The toluene soxhlet extracted CSs will be called T-CSs.

For the functionalization of CSs, about 1.0 g of T-CSs was reacted in 100 mL of 55 vol.% HNO_3 at 90 °C under reflux for different time durations (0.5 h, 1 h, 5 h, 10 h, 17 h, 24 h, 30 h and 40 h), or as otherwise stated. Then, the mixture was filtered and washed with deionized water until the pH of the solution reached a value close to 7. The resulting material was dried overnight in an oven at 120 °C. These materials were referred as F-CS0.5h, F-CS1h, F-CS5h, F-CS10h, F-CS17h, F-CS24h, F-CS30h and F-CS40h, respectively, where F stands for functionalisation and the number followed by letter h symbolises the duration of the acid treatment (functionalisation time).

3.3 Characterisation

3.3.1 Transmission Electron Microscopy (TEM)

The product collected from the cyclones and the inner walls of the hot region of the reactor was analyzed using Transmission Electron Microscopy (TEM) (FEI Technai Spirit G^2). Specimen samples for TEM analysis were prepared by dispersing very small samples in about 1 mL of methanol. The mixture was sonicated for about 15 min to obtain a homogeneous suspension. One drop of the CS suspension was poured onto an SPI-carbon coated copper grid and was allowed to dry before it was placed in the microscope. The morphology of the P-CS, T-CS and F-CS samples were observed and the data was processed on a computer screen. The image diameters of the CSs obtained from TEM analysis

were measured using ImageJ 1.43u software and about 150 CS diameters were measured per sample.

3.3.2 Thermogravimetric analysis (TGA)

Thermogravimetric analysis (TGA), conjugated with a derivative curve of the weight loss (DTG) measurements were carried out on a Perkin Elmer STA 4000 analyser coupled with an auto sampler that can perform up to 45 samples. About 10 mg of CS samples was placed in a pan (ceramic) and then put in the instrument's furnace. The sample temperature was ramped from room temperature to 950 °C under a flowing air atmosphere (20 mL/min) at a heating rate of 10 °C/min. A weight loss plot (TGA) provided information about the nature, stability and composition of the investigated sample. The derivative curve of this plot on the other hand provided the maximum temperature at which the weight loss took place.

3.3.3 Raman spectroscopy

The Raman spectroscopic measurements were carried out on the P-CS, T-CS and F-CS samples using a Jobin-Yvon T64000 micro-Raman spectrometer equipped with a liquid nitrogen cooled charge coupled device detector and excitation laser wavelength of 514.5 nm. The backscattered data were analysed using a double-grating spectrometer and collected using a photometer. All measurements were taken at room temperature. The obtained Raman bands were deconvoluted using the Origin 6.0 Professional package to obtain areas under the peaks and the intensity of those peaks.

3.3.4 XRD

Crystallinity of the CSs before and after toluene soxhlet extraction was examined using X-ray diffraction analysis on a Bruker D8 Avance X-ray diffractometer with a primary beam Göbel mirror, a radial soller slit, and a V Åntec-1 detector using Cu-K_α (1.5406Å) radiation at 40 kV and 40 mA. The scan range was $5° < 2\theta <$

90° in 0.021 steps, using a standard speed with an equivalent counting time of 14.7 seconds per step. The obtained diffraction peaks were then compared with those of standard compounds reported in the Diffrac^{plus} evaluation package using the EVA (V11.0, rev .0, 2005) software package.

3.3.5 BET surface area analysis

The surface areas and pore size distributions of the calcined P-CS, T-CS and F-CS samples were determined via N_2 adsorption/desorption according to the Brunauer-Emmet-Teller (BET) method based on adsorption data in the partial pressure (P/P_0) range of 0.05-0.35 and the total pore volume was determined by the amount of N_2 adsorbed at P/P_0 = 0.995 using a Micromeritics Tristar 3000, surface area and porosity analyzer [37]. The average pore size was obtained from the adsorption data by the Barrett-Joyner-Halenda (BJH) method [38]. About 0.2 g of sample was degassed *ex-situ* under a flow of N_2 at 150 °C for 4 hours prior to analysis to remove moisture using a Micromeritics Flow Prep 060, sample degas system. The surface areas and pore size distributions were then obtained at -195 °C.

3.3.6 Zeta Potential measurements

The zeta potential of the P-CS, F-CS1h and F-CS17 suspensions was measured with dilute solutions of CSs using a Zetasizer nano-series from Malvern Instruments. About 10 mg of CSs were dispersed in deionised water at room temperature and the pH of suspensions was adjusted by adding either 0.1M HCl or 0.1M NaOH to obtain pH values between 3 and 12.

3.4 Results and discussion

3.4.1 Effect of C_2H_2 flow rate

The structural morphology and the CS sizes were studied with TEM. Fig. 3.5 shows TEM images and particle size distributions of the P-CS materials prepared at different C_2H_2 flow rates (300, 400, and 545 mL/min). No amorphous carbon

material was observed. Previous studies from the literature have shown two factors that contribute to the increase in CS production rate and these factors are: (i) an increase in reaction temperature at constant feed flow and production time, and (ii) an increase in feedstock flow rate (70 to 370 mL/min) at constant reaction temperature (1000 °C) and production time [25]. In this work the effect on the production yield rate of CSs as a function of acetylene flow rate was investigated at 1000 °C. In every experiment the reaction was stopped after 4 min and the carbon soot produced was collected and weighed. The spheres are quite uniform in size and have a narrow size distribution. An increase in feed flow rate did not change the structural morphology of the CSs. However, the size distribution changed. CSs prepared at the smallest feed flow rate, i.e. 300 mL/min, possessed the largest diameters with an average diameter of 123 nm. The size distribution decreased steadily with an increase in flow rate, i.e at 400 mL/min size distribution was 96 nm and it decreased further (84 nm) when the flow rate was increased to 545 mL/min. The particle size ranges are shown in Fig. 3.5.

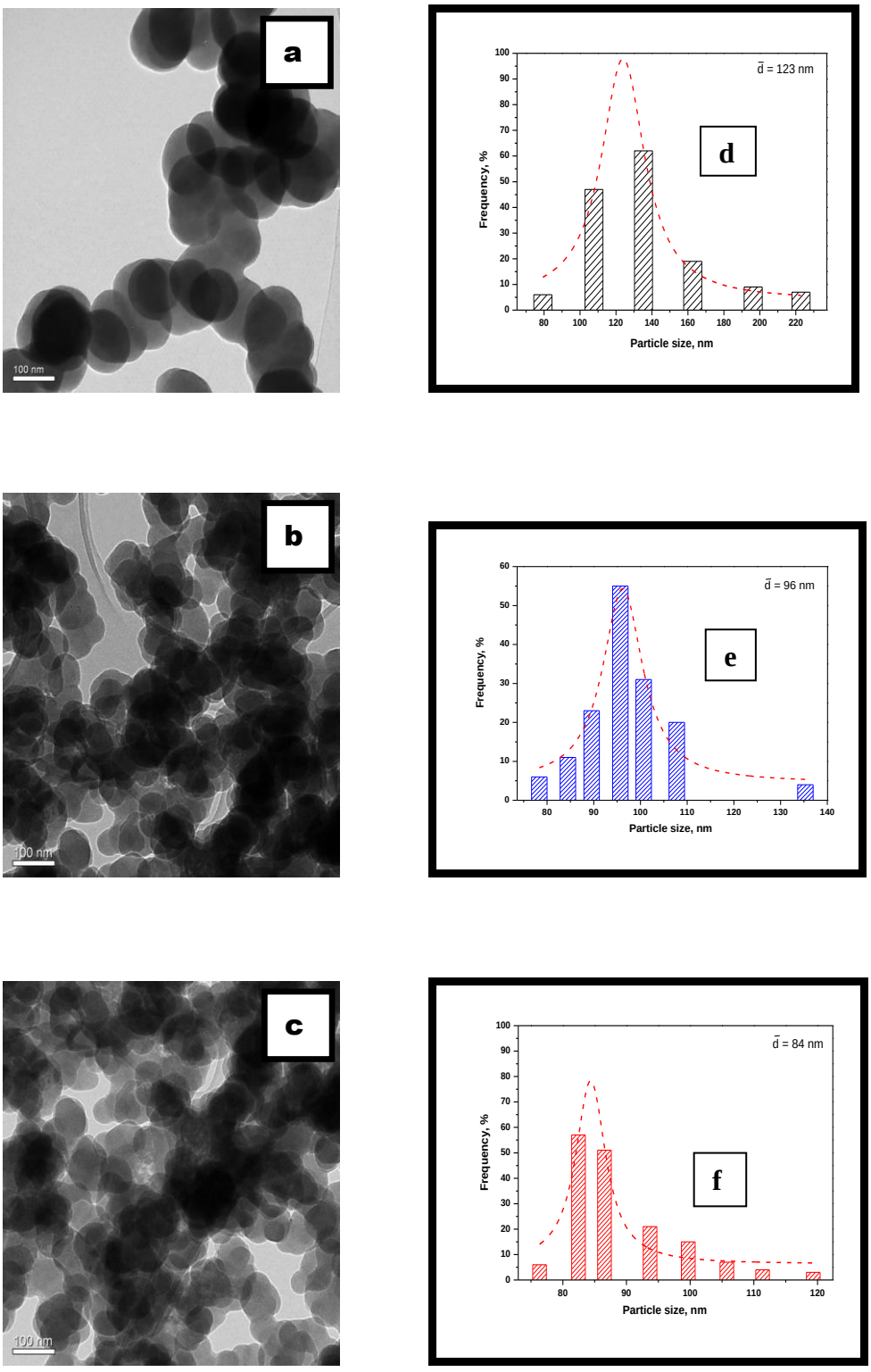


Figure 3.5 TEM images of P-CS prepared at different C_2H_2 flow rates with their corresponding particle size distributions (solid line = particle size distribution histogram, and dashed line = Gaussian distribution): (a) and (d) 300 mL/min; (b) and (e) 400 mL/min; and (c) and (f) 545 mL/min

Fig. 3.6 shows the yield of CSs produced via CVD in 4 min and the production rate of CSs, both as a function of flow rate. Both the yield and the production rate increased with an increase in C_2H_2 flow rate. This trend is similar to the one that was reported previously even though the feedstock flow rates in this study are higher than those used in previous studies [25]. A maximum production yield of 781 mg and rate of about 195 mg/min was obtained at 545 mL/min. When the production time was decreased to 2 min (at 545 mL/min), both the yield and the production rate decreased.

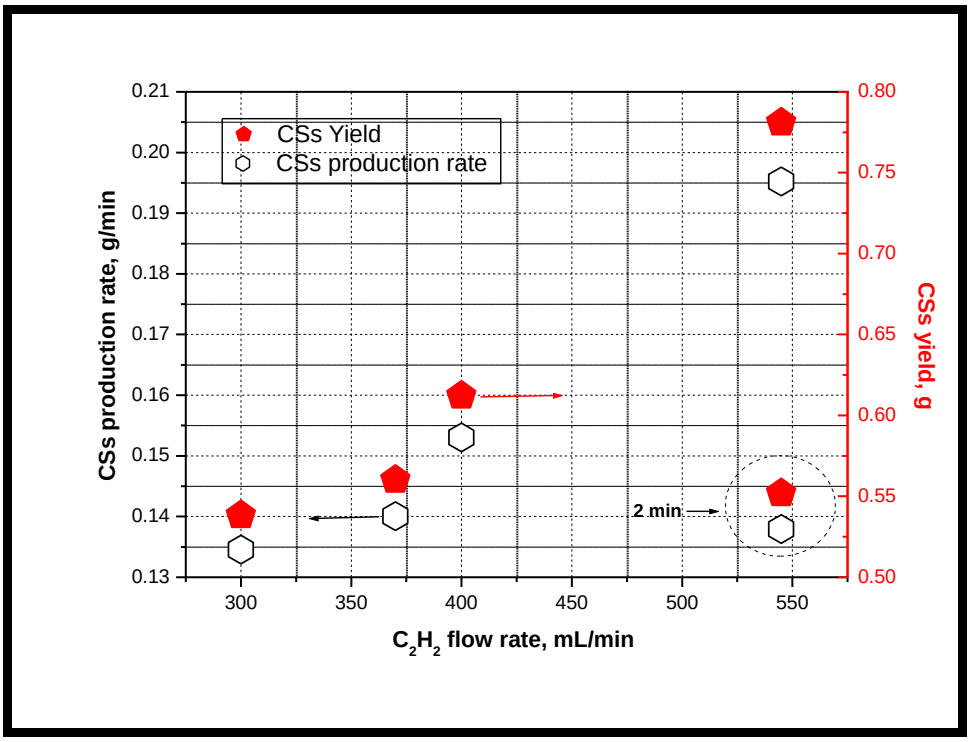


Figure 3.6 Rate of CS growth as a function of C_2H_2 flow rate

The Raman spectra (Fig. 3.7) of the P-CS samples produced at different C_2H_2 flow rates (300, 400, 545 mL/min) and constant temperature (1000 °C) show the presence of two broad peaks at about 1350 cm^{-1} and 1580 cm^{-1} corresponding to the tetrahedral sp^3 hybridised peak (D-band) also known as diamond peak and the sp^2 hybridised peak (G-band) also known as graphite peak, respectively. For all the three samples prepared at different flow rates, the peak occurred at the same positions. This suggests that the C-C bonds within the CSs structure do not move or change their position at different preparation flow rates.

The intensity ratio of the G-bands to the D-bands (I_G/I_D) serves as a measure of the graphitic order of the CSs; a higher I_G/I_D means a more perfect graphitic order of spheres [39]. The I_G/I_D ratios (derived from the peak intensities) as well the position of these bands are shown in Table 3.1. From the results, it is observed that the I_G/I_D decreases with an increase in flow rate. This observation implies that as the CS diameter increases the CSs become more ordered it becomes and the degree of graphitization changes.

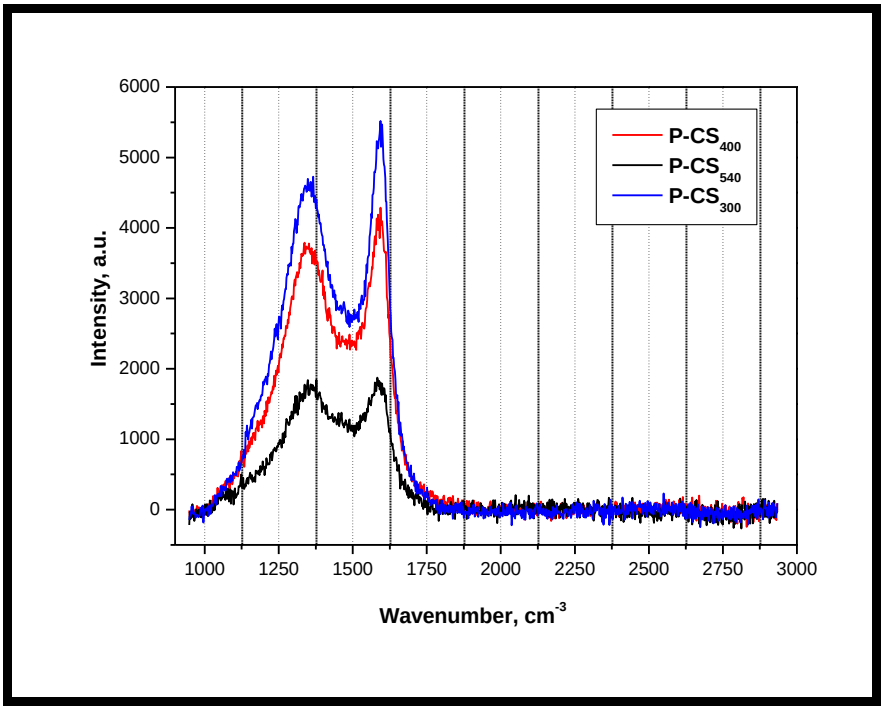


Figure 3.7 Rate of CS growth as a function of C_2H_2 flow rate

Table 3.1 Raman data for pristine CSs prepared at different flow rates

	Peak position/cm^{-1}		
Sample	**D-Band**	**G-Band**	***I_G/I_D***
P-CS$_{545\ mL/min}$	1351	1590	0.84
P-CS$_{400\ mL/min}$	1351	1589	0.97
P-CS$_{340\ mL/min}$	1352	1590	1.04

The thermal behavior in air of the CSs was investigated to gain an understanding of their thermal stability. The TGA profiles of CSs after 4 min and those prepared

for longer than 4 min (i.e. 8 min) were measured. TGA analysis of these samples is shown in Fig. 3.8.

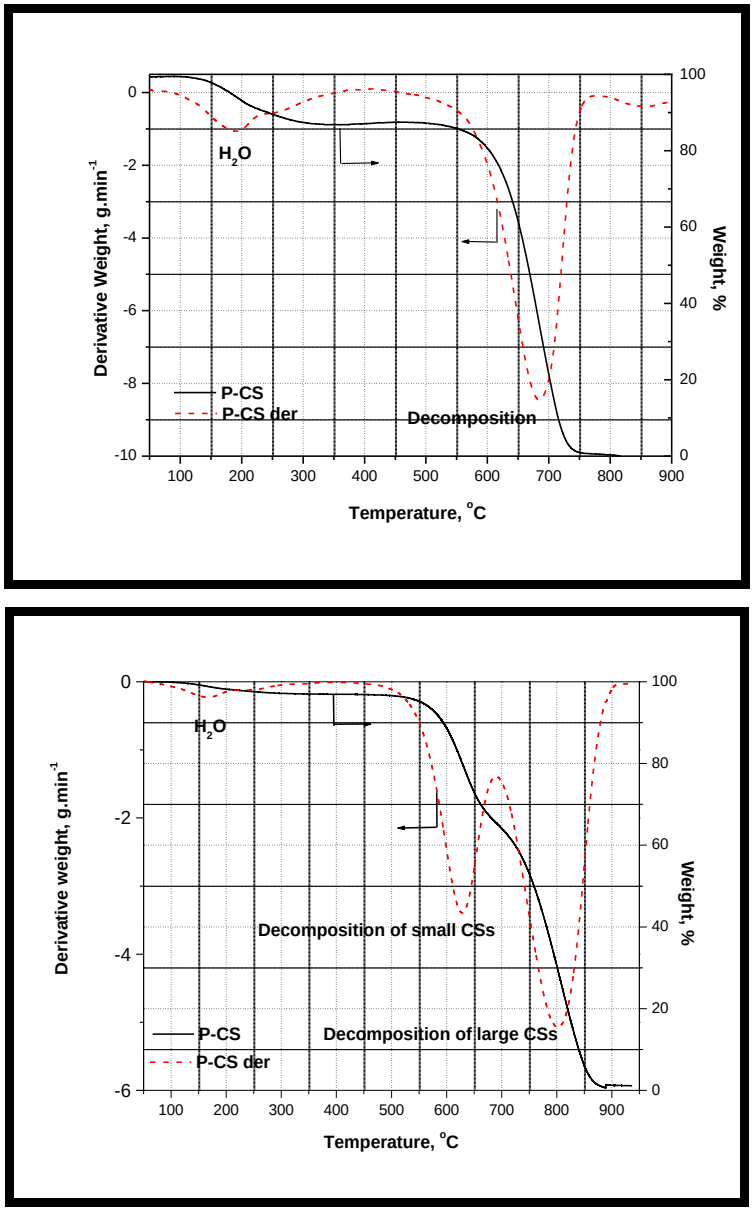


Figure 3.8 TGA and DTG of P-CS left in the quartz reactor for: 4 min (*top)* and 8 min *(bottom)*

The TGA profiles suggest that the CSs produced for longer durations are more stable in air than those produced for shorter durations because they can sustain higher temperatures before mass loss in an air environment. The TGA profile for CSs prepared within 4 min showed two weight loss steps. From the DTA curve,

the first broad peak with maxima observed at 176 °C was due to moisture in the sample and possibly some residue species (i.e polyaromatic hydrocarbons, PAHs) [25, 40] that were observed on the material after the CS preparation. The second peak maximum observed at around 685 °C was due to carbon oxidation. The profile for CSs prepared for 8 min showed three weight loss steps, the weight loss observed at 176 °C was due to moisture in the sample and the PAHs, the second and third weight loss steps observed at 647 °C and at 800 °C, respectively, were due to carbon oxidation of CSs with different sizes. The weight loss at 647 °C may be due to the oxidation of CSs with smaller diameters and the loss at 800 °C may be due to the oxidation of CSs with larger diameters.

To further confirm the the high temperature weight loss peak of P-CSs that were prepared within 4 min, this sample was loaded in a quartz reactor and annealed in Ar at 900 °C for 6 h. After cooling, the annealed sample was collected from the reactor. The observed material was further investigated with TEM and TGA under a flow of air. The texture of this material was harder than before. Fig. 3.9 shows the TEM image and particle size distribution of the CS sample that was annealed for 6 h. The image clearly shows that the average diameter has increased to 368 nm after annealing. The explanation for this is not clear.

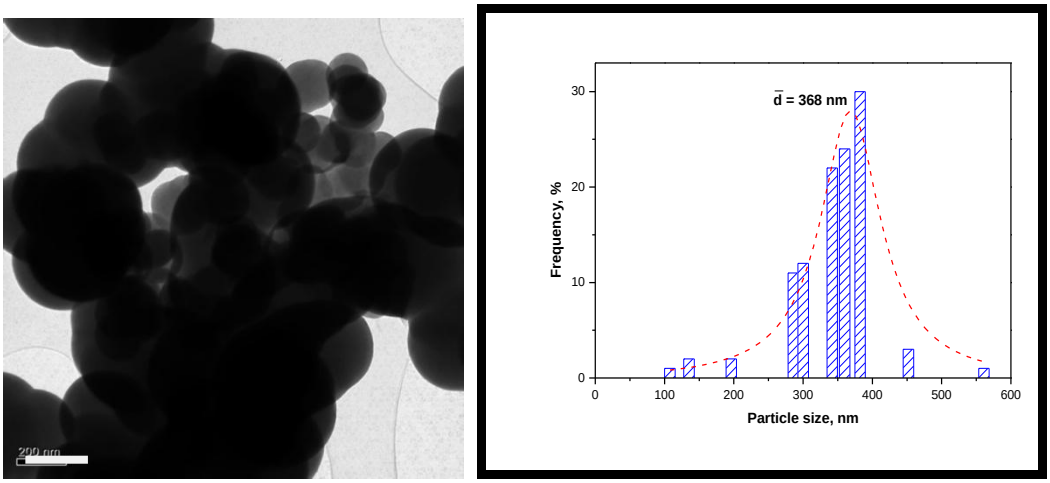


Figure 3.9 TEM image and particle size distribution (solid line = particle size distribution histogram, and dashed line = Gaussian distribution) of CSs sample that was annealed for 6 h in CVD

In Fig 3.10 TGA and DTA profiles of the CS sample annealed for 6 h is shown. The data is compared with that of TGA data obtained for sample annealed for 8 min. Three weight losses (176, 647 and 800 °C) were observed on the TGA profile for CSs sample that was prepared within 8 min (discussed above) and only one weight loss (at 749 °C) was observed for the sample that was annealed at 900 °C for 6 h. This weight loss can be attributed to the oxidation of CSs that are more difficult to decompose, with a harder texture and larger diameters. This confirms that the third weight loss that was observed at the CS sample prepared for longer than 4 min was due to CSs oxidation of a sample with a harder texture and larger diameters.

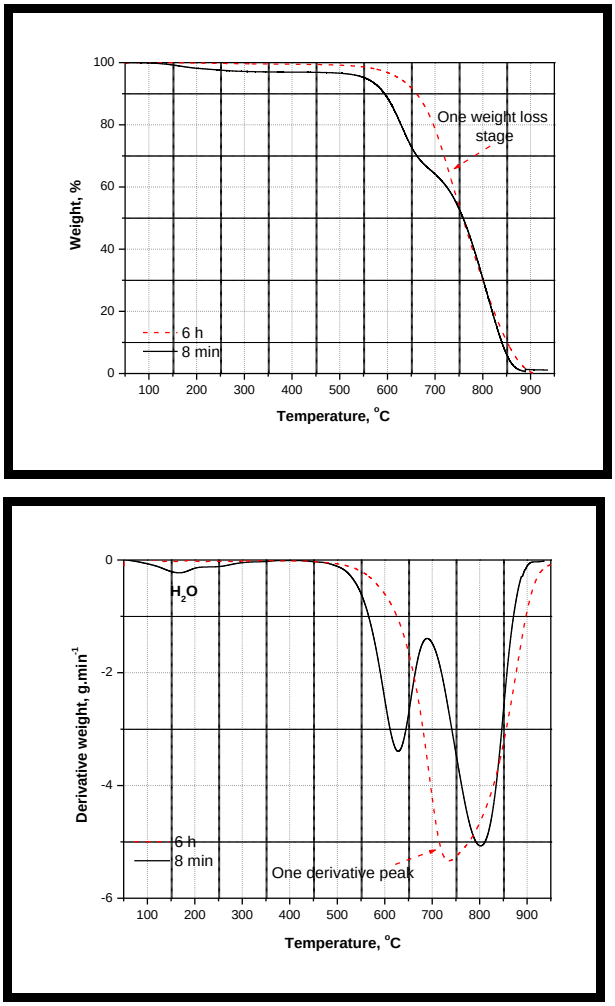


Figure 3.10 TGA (*top*) of P-CS left in the quartz reactor for 8 min and 6 h with their respective DTG (*bottom*) curves

3.4.2 Purification and functionalisation of CSs

3.4.2.1 PXRD, Raman and TGA

Crystallinity, or rather the degree of graphitization of the CSs, before and after they have been purified by soxhlet extraction was investigated using P-XRD. In Fig. 3.11 the P-XRD patterns of P-CS and T-CS are shown.

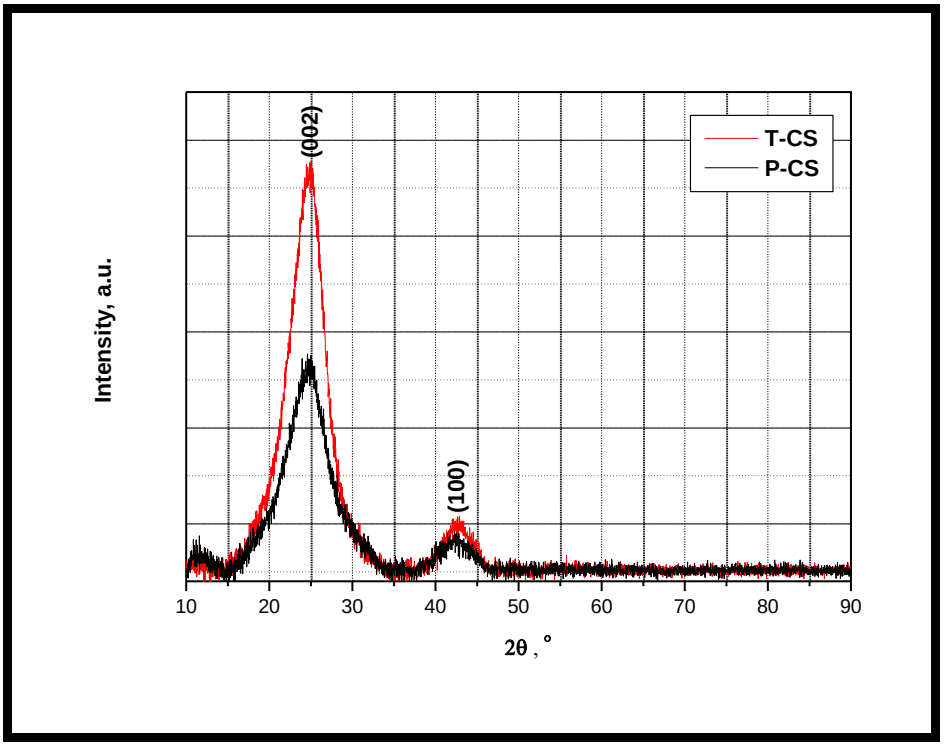


Figure 3.11 XRD patterns of P-CS and T-CS

Both samples give XRD profiles with two distinct peaks that are characteristic of carbon, viz. the (002) and the (100) planes that corresponds to peak positions at 2θ values of 24.9° and 44.9°, respectively [41]. For carbon materials, the degree of developed graphitic structure is directly proportional to crystallite size but is inversely proportional to the interlayer spacing [42]. Purification of P-CSs with toluene enhanced both peaks' intensities. This suggests that the removal of aromatic hydrocarbons on the CSs produced during CVD enhanced the degree of graphitization of the CSs due to a decreased interlayer spacing, $d_{(200)}$ and $d_{(001)}$, between the graphitic flakes.

The Raman spectra for P-CS_{300} (produced at 300 mL/min of C_2H_2), T-CS, F-CS and F-T-CS (purified then functionalized CSs samples) are shown in Fig. 3.12 and the corresponding data summarised in Table 3.2. The results indicate that I_G/I_D ratios of CSs increased after purification with toluene. After functionalisation, the ratio decreased. These results imply that purification of CS via soxhlet extraction in toluene increased the degree of graphitization; however, functionalisation of CSs with HNO_3 decreased the degree of graphitization. This result is in agreement with P-XRD results for the P-CS and T-CS samples.

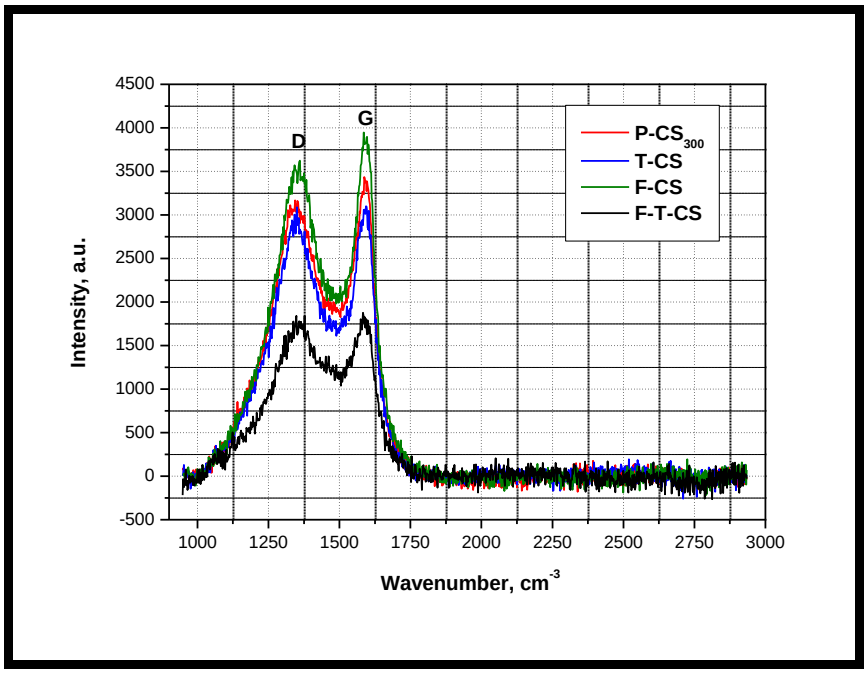


Figure 3.12 Raman spectra of P-CS produced at 300 mL/min, T-CS, F-CS and F-T-CS

Table 3.2 Raman data for pristine, purified and functionalised CSs

	Peak position/cm^{-1}		
Sample	**D-Band**	**G-Band**	I_G/I_D
P-$CS_{340\ mL/min}$	1350	1590	1.04
T-CS	1348	1590	1.10
F-CS	1347	1590	0.92
F-T-CS	1347	1590	0.89

3.4.2.2 TGA

Fig. 3.13 shows the TGA profiles of P-CS, T-CS and F-CS24h in air. P-CS and T-CS samples both showed a mass loss at *ca.* 200 °C. The observed weight loss at 200 °C for P-CS was higher (15%) than the one for the T-CS (5%) sample. This suggests that the removal of PAHs in the P-CS was achieved since weight loss of P-CS was higher than that of T-CS. The observed weight loss in the T-CS sample is possibly due to the loss of toluene which was used as a solvent during soxhlet extraction. The functionalized CSs, F-CS, showed no weight loss at lower temperatures, suggesting that there were neither PAHs nor toluene present in that sample. This sample was soxhlet extracted, functionalized then and oven dried at 120 °C (hence the absence of PAHs and toluene).

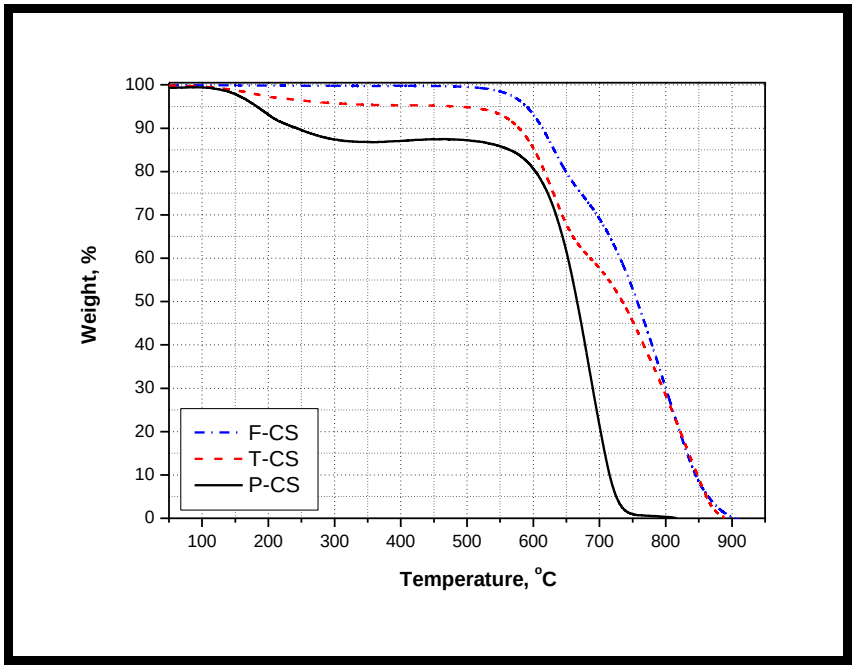


Figure 3.13 TGA of P-CS, soxhlet extracted CSs and F-CS

3.4.2.3 TEM

The TEM micrographs of the resulting P-CS, T-CS and the F-CS are shown in Fig. 3.14. No remarkable physical changes were observed for CSs after soxhlet extraction with toluene even after exposing them to HNO_3 for 17 h under reflux. These conditions indicate that treatment with either toluene or

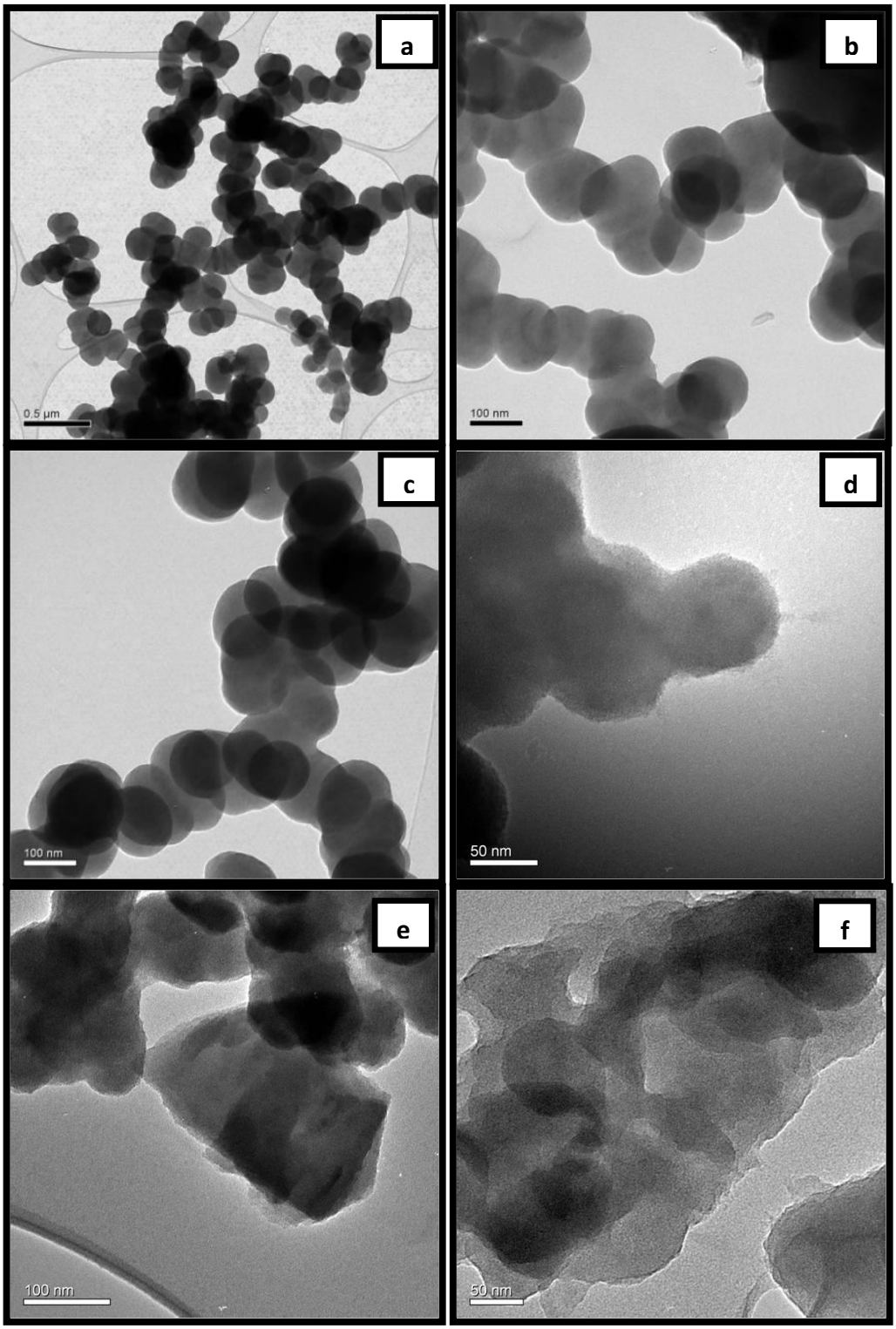


Figure 3.14 TEM micrographs of CSs: (a) P-CS, (b) T-CS, (c) F-CS17h, (d) F-CS24h, (e) F-CS30h and (f) F-CS40h

HNO_3 (17 h, under reflux at 90 °C) were mild enough not to cause surface chemical modification. When the CSs were functionalized for times longer than

17 h, physical damage on the CSs was observed. CSs that were functionalised for 24 h (Fig. 3.14d) had a rougher (pitted) surface. Increasing the functionalisation period further (30 h, 40 h) destroyed the shape and morphology of the CSs (Fig. 3.14 e and f). The same observation has previously been reported in the literature [43].

3.4.2.4 Porosity measurements

To investigate the nature and size of the pores in the CSs before and after purification and after functionalisation, the BJH method using N_2 adsorption-desorption isotherms was used. The pore size distribution for P-CS, T-CS and F-CS17h is shown in Fig. 3.15.

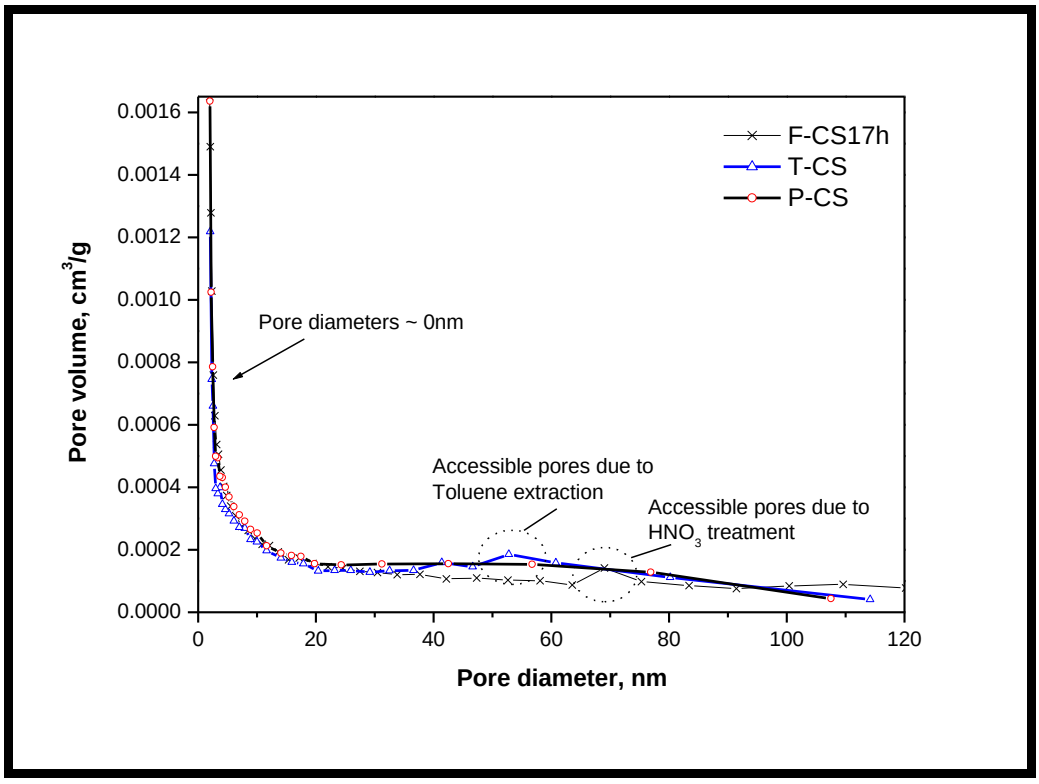


Figure 3.15 BJH pore size distributions (calculated from the adsorption arms of N_2 isotherms) of P-CS, T-CS and F-CS17h

It can clearly be seen that the pore diameters within the CS before and after purification and after functionalisation are very small with average diameter sizes that are less than 0.02 nm. The plot shows small peaks at ca. 47 nm and ca. 65 nm

for T-CS and F-CS17h, respectively. These may be due to the creation of "pores" between the CSs, following the removal of the oily layer that was formed during the CS preparation.

The total surface area, pore volume and pore diameter measurements for P-CS, T-CS and F-CS17 are tabulated in Table 3.3.

Table 3.3 Textural properties of CSs before and after purification and functionalisation

Sample	$S_{BET}{}^{a}$ (m^2/g)	$P_v{}^{b}$ (cm^3/g)	$P_D{}^{c}$ (nm)
P-CS	5.2	0.0144	9.6
T-CS	9.3	0.0151	9.5
F-CS 17h	9.6	0.0154	9.3

[a]Surface area, [b]P_v = pore volume, [c]P_D = pore diameter

The surface area of the P-CS is quite low (5.2 m^2/g). Purification and functionalisation of CSs gave an increase in the surface area to 9.3 and 9.6 m^2/g, respectively. This implies that the removal of the oily material (PAHs) was achieved through purification and functionalisation steps. An increase in surface area after the removal of PAHs suggests that they were blocking the CS pores.

3.4.3 Acid group functionalisation

Since the CSs are hydrophobic in nature, the addition of functional groups to the CSs was carried out in order to modify the wetability of the surface. This surface modification was carried out by HNO_3 treatment. The reaction was performed at 90 °C (55% HNO_3) for different time intervals under reflux. Fourier Transform Infra-Red (FTIR) spectroscopy was used to study the functionalities on the CS surface. FTIR spectra of P-CSs and F-CSs are shown in Figure 3.16. In the insert of Fig. 3.16, it can be noted that the P-CS sample has a trace of oxygen containing groups before functionalisation.

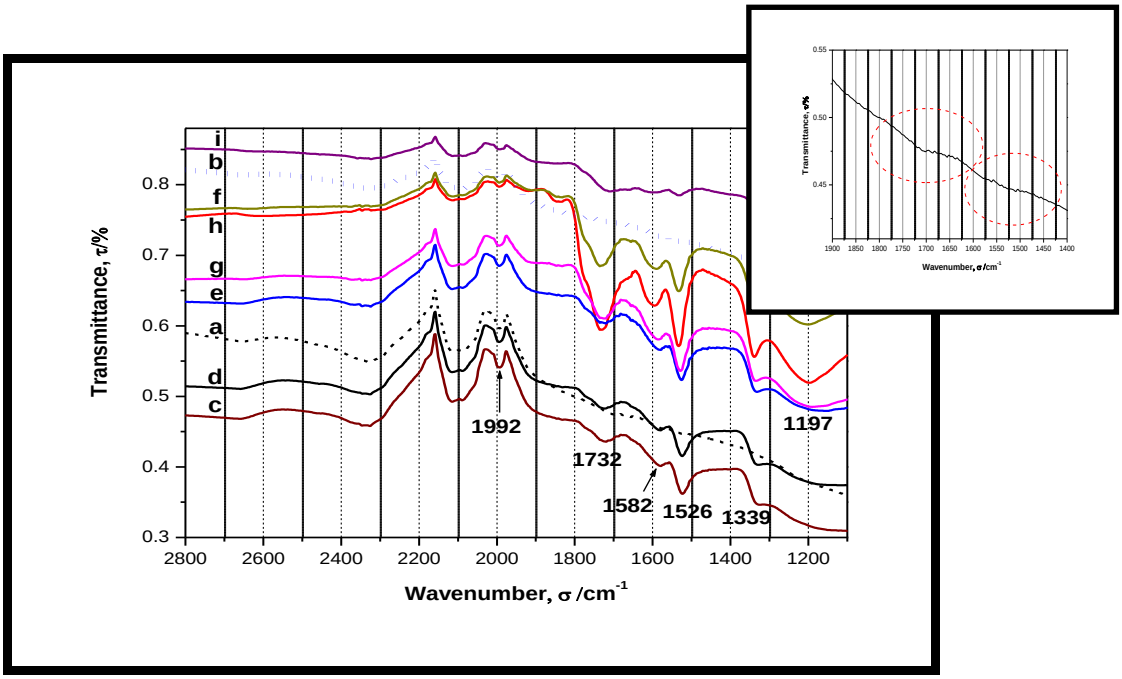


Figure 3.16 FTIR spectra of (a) Pristine CSs, (b) T-CSs, (c) F-CS0.5h, (d) F-CS1h, (e) F-CS2h, (f) F-CS5h, (g) F-CS10h, (h) F-CS17h and (i) F-CS40h. (*inset)*: magnified FTIR spectra of Pristine CSs (between 1450 and 1800 cm^{-1})

This observation has been reported elsewhere in the literature and is said to be due to chemisorbed oxygen on the CS surface obtained immediately after synthesis and is needed to satisfy valence requirements [44]. These functional groups are typically OH and COOH groups.

Functionalising of the CSs with HNO_3 increased the amount of these functional groups. The peak at 1732 cm^{-1} is assigned as the C=O stretch in carboxylic acid groups, at 1582 cm^{-1} to the C=O in the quinine structure, at 1526 cm^{-1} to the C=C stretch, at 1339 cm^{-1} to lactones and 1197 cm^{-1} is due to an overlap of both –OH and COC bending modes. As the functionalisation time was increased from 0.5 h to 17 h, so did the growth of the peaks associated with the carboxylic acid groups, lactones, quinones and lactones group increases. This implies that the amount of functional groups increased as the acid treatment time was increased. When the acid treatment time was increased to 40 h, the amount of functional groups decreased. This may be due to the destruction of the CSs as observed from TEM studies. The optimum funtionalisation time for the CSs is about 17 h. When the

functionalisation time was increased to times longer than 17 h the morphology of the CSs changed and was destroyed.

A dispersion test for the functionalized CSs was conducted by dispersing about 20 mg of CSs in deionised water. The mixture was shaken and then left to settle. After 1 min the settling behavior was observed and photographed. Visual characteristics of the dispersion are depicted in Fig. 3.17. These differed and depended on the duration of HNO_3 functionalisation. Non-functionalised CSs and P-CS showed no dispersion in water. Mild functionalising of the CSs showed a certain level of dispersion in water and this level increased with prolonged acid treatment time. After 17 h of HNO_3 treatment the CSs could be fully dispersed in water (sample (e) on Fig. 3.17).

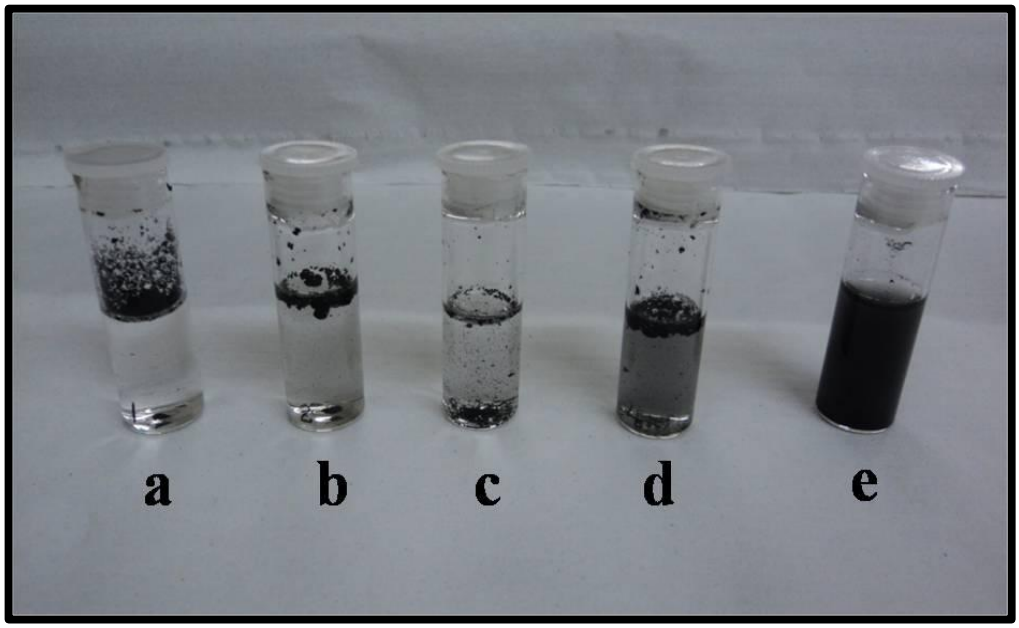


Figure 3.17 Settling pictures of (a) P-CS, (b) F-CS1h, (c) F-CS2h, (d) F-CS5h and (e) F-CS17h in H_2O

The pH of an aqueous slurry of carbons gives a measure of the surface charge on the carbon surface. Brönsted acidic groups on the carbon surface tend to donate their protons to water molecules, and hence the surface becomes negatively charged while Lewis bases adsorb protons from solution, becoming positively charged. Thus, various surface functionalities are responsible for the amphoteric

nature of carbon, the pH of the aqueous solution, and the CS surface charge [45]. The surface charge of carbons is governed by the nature of the surface groups and the pH. In an electrolyte solution, charged particles of carbons are surrounded by ions of opposite sign, which alter the dispersive and electrostatic interactions of the carbon surface and the electrolyte. The effect of acid group functionalisation of the CSs by HNO_3 can be seen in the electrophoretic characteristics of a carbon colloid, i.e. the Zeta potential. Liquid suspensions that are well dispersed can be obtained with large Zeta potential values of the samples because of the strongly repulsive force generated by very high surface charges [46]. In Fig. 3.18, the effect of pH on the zeta potential for P-CS, CS5h and CS17h in deionised water is shown. P-CS showed aggregation at all the pH values studied (i.e. between 3 and 11) because all the absolute values of the zeta potentials of CSs are very low [47].

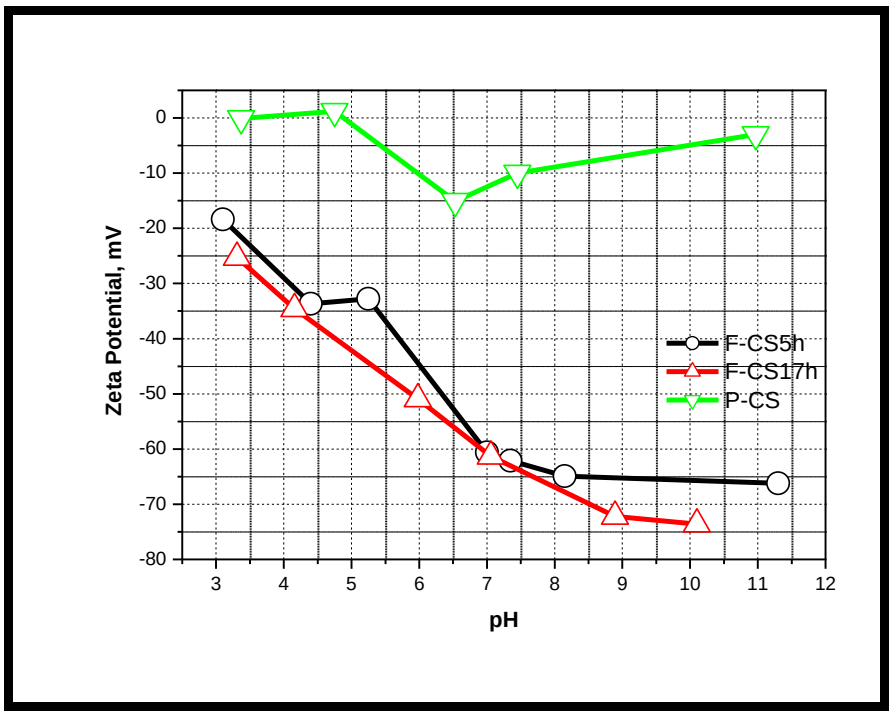


Figure 3.18 Zeta potential of P-CS, F-CS5h and F-CS17h suspensions as a function of pH

Functionalised CSs showed relatively higher absolute zeta potential values than the P-CS. This is because acid treatment of CSs created active acid containing surfaces and this made it possible for them to be able to be dispersed in deionised

water. CSs that were functionalized for longer periods (CS17h) showed higher absolute zeta potential values compared to those that were functionalized for shorter durations (CS5h). This observation suggests that prolonged acid treatment period increased the surface acid charge on the CSs. This behavior confirms the FTIR data showing that the amount of surface acid functional groups increased with the acid treatment period.

3. 5 Conclusion

CSs with diameters in the range between 80 and 120 nm have been synthesized in a vertical swirled floating chemical vapour deposition reactor without a catalyst. The rate of production was controlled and the highest production rate of about 195 mg/min was obtained at a C_2H_2 flow rate of 545 mL/min at 1000 °C. The produced CSs had a narrow size distribution with uniform diameter size. If the CSs were produced for longer than 4 min (i.e. 8 min), disordered accreted carbon flakes formed on the outer surface of the CSs, the texture of the CSs became harder and the diameter of CSs increased. Purification and functionalisation of the CSs improved the total surface area, due to the removal of PAHs which blocked the CS pores. The introduction of functional groups to the CSs was achieved and these changed the wetting properties of the CSs. Functionalising the CSs for longer than 17 h in HNO_3 destroyed the morphology of the CSs.

3. 6 Future work arising from this chapter

For an explanation of the increase in the diameter of CSs due to heating at 900 °C further investigation will be needed.

3.6 Reference

1. W. Smith, Encyclopaedia of Chemical Technology, Interscience: New York (1949)
2. L. Dai (Ed.), Carbon nanotechnology: Recent Developments in Chemistry, Physics, Material Science and Device Applications, Elsevier, New York (2006)
3. M. Dresselhaus, G. Dresselhaus, P. Eklund, Science of Fullerenes and Carbon Nanotubes, Academic press, New York (1996)
4. H. Kroto, J. Heath, S. O'Brian, R. Curl, R. Smalley, Nature, 318, (1985) 162
5. D. Ugarte, Nature, 359, (1992) 707
6. F. Banhart, M. Ajayan, Adv. Mater., 9, (2004) 261
7. Z. Kang, Z. Wang, L. Philos. Mag. B, 73, (1996) 905
8. Z. Wang, Z. Kang, J. Phys. Chem., 100, (1996) 17725
9. Z. Kang, Z. Wang, J. Phys. Chem., 100, (1996) 5163
10. Z. Wang, Z. Kang, Carbon, 35, (1997) 419
11. M. Sharon, K. Mukhopadhyay, K. Yase, S. Iijima, Carbon, 36, (1998) 507
12. M. Inagaki, M. Washiyama, M. Sakai, Carbon, 26, (1988) 169
13. K. Kamegawa, H. Yoshida, Carbon, 35, (1997) 631
14. Y. Wang, Y. Chang, S. Ishida, Y. Korai, I. Mochida, Carbon, 37, (1999) 969
15. L. Biró, G. Márk, Z. Horváth, K. Kertész, J. Gyulai, J. Nagy, P. Lambin, Carbon, 42, (2004) 2561
16. Z. Kang, J. Wang, J. Mol. Catal. A: Chemical 118, (1997) 215
17. Q. Wang, J. Li, L. Chen, X. Huang, Carbon, 39, (2001) 2211
18. V. Pol, M. Motietei, A. Gedanken, J. Calderon-Moreno, M. Yoshimura, Carbon, 42, (2004) 111
19. M. Wissler, J. Power Sources, 156, (2006) 142
20. http://www.carbonblack.jp/en/cb/youto.html#top (accessed on 12 June 2011)
21. J. Lahaye, Carbon, 30, (1992) 309
22. F. Fallcheri, Y. Schwob, J. Hydrogen Energy, 20, (1995) 197.

23. D. Scully, R. Davies, Carbon from Aromatic Hydrocarbons, Manchester, Vol. 9, (1965) 185
24. S. Mhlanga, K. Mondal, N. Naidoo, N. Kunjuzwa, M. Witcomb, N. Coville, S. Afr. J. Sci., 105 (2009) 304
25. S. Mhlanga, N. Coville, S. Iyuke, A. Afolabi, A. Abdulkareem, N. Kunjuzwa, J. Expr. Nanoscience, 5 (2010) 40
26. E. Auer, A. Freund, J. Pietsch, T. Tacke, Appl. Catal., 173 (1998) 259
27. Y. Jin, C. Gao, W. Hsu, Y. Zhu, H. Huczko, M. Bystrzejewski, M. Roe, C. Lee, S. Acquah, H. Kroto, D. Walton, Carbon, 43 (2005) 1944
28. V. Vignal, A. Morawski, H. Konno, M. Inagaki, J. Mater. Res., 14 (1999) 1102
29. M. Inagaki, V. Vignal, H. Konno, J. Mater. Res., 14 (1999) 3152
30. S. Camppidelli, C. Klumpp, A. Bianco, D. Guldi, M. Prato, J. Phys. Org. Chem., 19 (2006) 531
31. E. Flahaut, A. Peigney, C. Laurent, C. Marliere, F. Chastel, A. Rousset, Acta Materialia, 48 (2000) 3803
32. J. Donnet, Carbon, 6 (1968) 161
33. D. Kohls, G. Beaucage, Curr. Opin. Solid State Mater. Sci., 6 (2002) 183
34. J. Leblane, J. Appl. Polym. Sci., 66 (1997) 2257
35. S. Iyuke, University of the Witwatersrand, Johannesburg. SA Patent Appl. No: 2005/03438 (2005)
36. S. Iyuke, A. Danna, J. Microp. Mesop. Mater., 84 (2005) 338
37. P. Webb, Analytical methods in fine particle technology, Micromeritics Instrument Corporation, Norcross, GA USA, (1997)
38. E. Berret, L. Joyner, P. Halenda, J. Am. Chem. Soc. 73, 373, (1951)
39. M. Nakamizo, Carbon, 29 (1991) 757
40. A. Deshmukh, S. Mhlanga, N. Coville, Mater. Scie. Eng. R, 70 (2010), 1
41. T. Bandosz, J. Jagiello, J. Shwarz, Anal. Chem, 64 (1992) 891
42. H. Pang, X. Wang, G. Zhang, H. Chen, G. Liu, S. Yang, Appl. Surf. Scie., 256 (2010) 6403
43. Q. Gong, Z. Li, Y. Wang, B. Wu, Z. Zang, Ji Liang, Materials. Research. Bulletin, 42 (2007) 474

44. M. Voll, H. Boem, Carbon 8, (1970) 741
45. P. Serp, J. Figueredo (Ed.), Carbon Materials for Catalysis, Wiley, New Jersey (2009)
46. B. Gao, C. Peng, G. Chen, G. Li Puma, Appl. Cat. B 85 (2008) 17
47. L. Cheng, H. Xie, Y. Li, Wei Yu, Colloids Surf. A 330 (2008) 176
48. I. Madni, C-Y Hwang, S-D park, Y-H Choa, H-T Kim, Colloids Surf. A, 358 (2010) 101

Chapter 4

4. Carbon sphere-titania composite materials

4.1 Introduction

Titatinum dioxide (TiO_2) is a well studied and well known photocatalyst that has been extensively studied since the pioneering work of Fujishima and Honda on the splitting of water with light [1]. Since this pioneering work, many researchers have reported on many valuable and potential applications of TiO_2. These include: environmental control, such as for use in energy conversion technologies used in solar cells [2], production of solar hydrogen [1], purification of organic waste or air pollutants [3], and as a catalyst support [4]. TiO_2 is recognized for its characteristic properties that include the strong oxidation potential of photogenerated holes, its chemical stability, non-toxicity and low cost [5]. TiO_2 crystallizes into three phases; anatase, rutile and brookite, among which the anatase phase typically has a higher photocatalytic activity due to its band position with respect to the hydrogen redox potential [6]. Anatase can be converted into rutile and brookite phases at high temperatures [7]. Rutile and brookite phases are stable at high temperatures and cannot be converted into anatase.

Experiments in which TiO_2 has been deposited on different substrates have been described [8]. These reports have revealed that TiO_2 possesses enhanced characteristic properties, i.e. activity and stability, compared to non-supported TiO_2 counterparts. Sol-gel processing can readily yield both inorganic and hybrid organic-inorganic materials. Preparation of pure unsupported TiO_2 and TiO_2

supported on substrates by means of sol-gel and hydrothermal procedures has been extensively studied; many reports are available in the literature [9-14]. Successful commercial hybrid organic-inorganic polymers have been part of manufacturing technology since the 1950's [15].

Carbonaceous materials, such as carbon nanotubes (CNT) and carbon spheres (CSs), have attracted considerable interest because of their intrinsic properties, such as their high thermal resistance [16] and their light-weight and high strength [17, 18]. This has resulted in their use in many applications such as catalyst supports [19], in high-strength composites [20], absorbents and as wear-resistant materials [21, 22].

Multi-phase materials containing nanoscale structures, i.e. nanocomposites, represent a new emerging area in nanotechnology. During their preparation, nanoparticles typically are dispersed into a matrix material during processing, and in favourable cases the resulting composite exhibits drastically enhanced properties when compared to the matrix [23]. The coupling of TiO_2 with carbonaceous materials (activated carbons, CNTs) has been shown to provide a synergistic effect which can enhance the overall performance of TiO_2 in catalytic processes [24-28]. Well dispersed CNTs in surfactants can provide a support for the growth of metal oxide nanoparticles (i.e. TiO_2) on the surface of CNTs via non-covalent attachment [29]. The use of carbonaceous nanomaterials to enhance TiO_2 for catalytic processes has attracted considerable attention. This arises from the unique and controllable structural and electrical properties of the carbons. Figure 4.1 depicts the number of publications over the years that have reported on studies of carbonaceous nanomaterials, TiO_2 and their combination. These studies have led to better catalysts for photocatalysis. The plots show an exponential growth in the number of publications with time. In 2009 over 600 publications were reported on the study of carbon-TiO_2 composites. Very recently Leary and Westwood have published a review entitled "Carbonaceous nanomaterials for the enhancement of TiO_2 photocatalysis" [27]. This review has briefly outlined the different carbonaceous materials that have previously been reported to achieve the

enhancement of the properties of TiO_2. The materials listed include, activated carbon, graphitic carbon, CNTs, and C_{60} (Fullerene).

The most fundamental route for the creation of carbon-TiO_2 nanocomposites involves simple mixing. This is usually performed in solution, and usually with pre-functionalization of surfaces. This pre-functionalization step is introduced to enhance the carbon dispersion if water is to be used as the solvent since carbonaceous nanomaterials are hydrophobic. This method has been criticized for the low level of interaction generated between TiO_2 and the carbonaceous nanomaterials [13, 30, and 31]. The simplest way to dope TiO_2 with carbon is by direct oxidation of Ti metal in a burner flame [32-34].

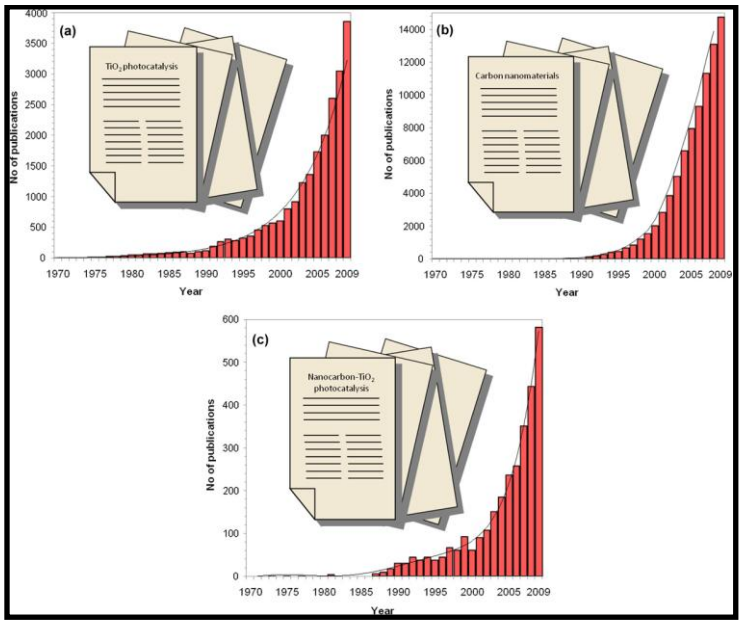


Figure 4.1 Rising interest in photocatalysis and the potential role of carbonaceous nanomaterials. The graphs show the approximate annual number of publications relating to (a) TiO_2, (b) carbonaceous nanomaterials and, (c) carbonaceous nanomaterials coupled with TiO_2 employed in photocatalysis. Adapted from [5]

The most widely applied method in which intimate mixing or chemical interaction of carbon nanomaterials and TiO_2 is achieved is by use of the sol-gel technique [35]. The sol-gel synthesis typically involves the formation of a colloidal

suspension (the "sol") followed by hydrolysis and polymerisation of the precursors, which are usually inorganic metal salts or metal organic compounds such as metal alkoxides. Promotion of polymerisation and evaporation leads to the transition of the sol into a rigid gel, which is usually then hardened by further drying and calcination. Reports showing a homogeneous coverage of carbonaceous materials by TiO_2 have not been achieved with good carbon-TiO_2 linkage since it is difficult to obtain an interaction between TiO_2 and carbonaceous material. These reports include the synthesis of composites by sol-gel preparation of doped TiO_2 nanomaterials [36], carbon nanotube-inorganic hybrids [37], activated carbon-TiO_2 photocatalysts [38] and carbon nanotube-TiO_2 composites [39]. After examination of most of the literature reports between CNTs and TiO_2 i.e. CNT/TiO_2 nanocomposites, it is clear that the problem of obtaining a good interaction between CNTs and TiO_2 has not been achieved.

Another carbonaceous material that has been studied over the decades is the carbon sphere (CS) [40-43]. The CS provides a pure carbonaceous material that can be used as a model system to study carbon-TiO_2 interactions. Some interesting features about CSs includes the following: they can be synthesized in the absence of a catalyst [44], their size can be controlled by varying preparation conditions and the carbon source [44-45], they are made of pure carbon, except for the surface, and they have variable surface areas.

In this thesis we have attacked the problem of the carbon-TiO_2 interaction by using CSs as the carbon source. Even though there is huge interest in the synthesis of carbon nanomaterial-TiO_2 composites (Fig. 4.1), to our knowledge, there have not been any reports on the synthesis of carbon sphere-titania composites (CS-TiO_2) using a sol-gel method.

The aim of this work was to establish a successful method for the production of CS-TiO_2 composite material with a homogeneous TiO_2 coating on the surface of carbon spheres. The CSs used in this study were synthesized using an in-house built vertically positioned chemical vapour deposition (CVD) method (see

Chapter 3, section 3.2.1 for full details). Different sol-gel methods were used to prepare the TiO_2 and CS-TiO_2 composites. Titanium butoxide was used as the precursor to make the titania for the CSs that were coated using a conventional sol-gel and a surfactant (CTAB) wrapping method. The synthesized composites were characterized by TEM, TGA, BET, XRD and Raman spectroscopy.

It should be mentioned that many, many experiments were performed to develop an efficient and reliable method to make CS-TiO_2 composites. Not all the studies will be reported here. Many of the studies generated material with limited CS-TiO_2 interactions and this data is not reported. Some of these experiments have been summarized in Appendix 1. During the course of this project, numerous methods to achieve a carbon-TiO_2 composite were reported in the literature. When appropriate these methods were tested in our laboratories. The study was thus influenced by developments in the area over the course of the study.

4.2 Experimental

4.2.1 CS-TiO_2 composite preparation

4.2.1.1 Conventional sol-gel method

A conventional sol-gel method was used to prepare a series of CS-TiO_2 composite materials. Titanium (IV) butoxide, $Ti[O(CH_2)_3CH_3]_4$ (≥ 98%, Sigma-Aldrich), was used as the precursor to make the titania, and 2-butanol (2-BuOH) was used as the solvent. Nitric Acid (≥ 55%, Merck), was added to monitor the hydrolysis reaction of $Ti[O(CH_2)_3CH_3]_4$ in deionised water. Different CS:$Ti[O(CH_2)_3CH_3]_4$ ratios (wt/wt) were used: 1:1, 1:2.5, 1:5, 1:10, 1:25 and 1:50, or as otherwise stated. These composites of CS/TiO_2 were called 1CS-1SG, 1CS-2.5SG, 1CS-5SG, 1CS-10SG, 1CS-25SG and 1CS-50SG, respectively, where SG means the TiO_2 was coated using a conventional sol-gel method. (See Table 4.1 for terminology). The numbers refer to the ratio used.

Initially the functionalized CS (17 h in HNO_3, see Chapter 3 for full details) materials were dissolved in a mixture of $Ti[O(CH_2)_3CH_3]_4$ with half the prescribed amount of 2-BuOH in order to avoid strong hydrolysis reactions. This mixture was sonicated for 30 min to allow the CSs to disperse homogeneously in the 2-BuOH solution. Water and HNO_3, dissolved in the remaining 2-BuOH, was added drop-wise to the butanolic solution of alkoxide while stirring continuously with a magnetic stirrer bar at ambient temperature (Fig. 4.2).

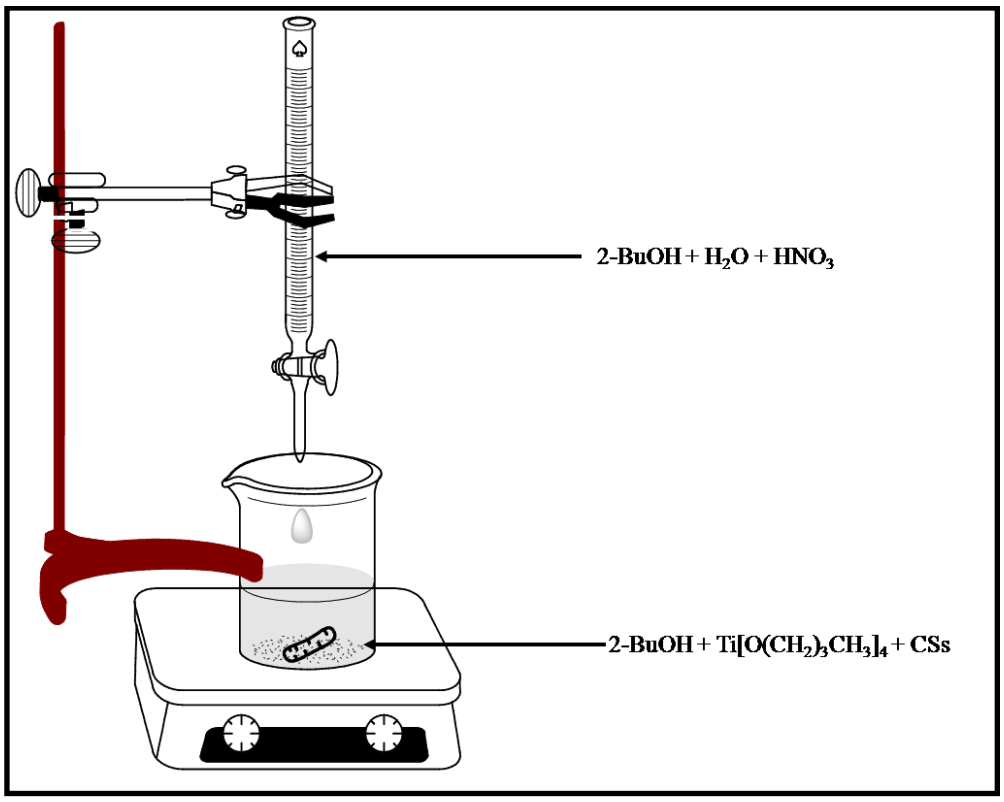


Figure 4.2 A schematic representation of the set up used for the preparation of CS-TiO_2 composites by the conventional sol-gel method. Adapted from [46]

The molar ratio of the reactants used was: $Ti[O(CH_2)_3CH_3]_4$:H_2O:2-BuOH:HNO_3 = 1:4:15:0.3, as suggested in the literature by Ding *et al.* [30]. During the addition of H_2O:2-BuOH:HNO_3 to $Ti[O(CH_2)_3CH_3]_4$ a sol formed. Through a sequence of hydrolysis and polycondensation reactions, the sol-gel transition took place gradually. The corresponding gel was filtered and washed with butanol followed by washing with deionised water to remove excess butoxide. The wet gels were

dried in an oven at 120 °C overnight. Calcination of the crushed powder materials was performed under flowing nitrogen at 350 °C for 6.5 h. About 2 g of powders were generated for every sol-gel synthesis.

Table 4.1 Summary of the methods used to prepare CS-TiO_2 composites

Composite	Sol-gel method	CSs functionalised*	CSs immersed in CTAB	No. of sol-gel cycles
1CS-1SG	Conventional	Yes	-	1
1CS-2.5SG	Conventional	Yes	-	1
1CS-5SG	Conventional	Yes	-	1
1CS-10SG	Conventional	Yes	-	1
1CS-25SG	Conventional	Yes	-	1
1CS-50SG	Conventional	Yes	-	1
A1	Surfactant wrapping	Yes	No	1
A2	Surfactant wrapping	Yes	No	2
A3	Surfactant wrapping	Yes	No	3
SW1	Surfactant wrapping	No	Yes	1
SW2	Surfactant wrapping	No	Yes	2
SW3	Surfactant wrapping	No	Yes	3
ASW1	Surfactant wrapping	Yes	Yes	1
ASW2	Surfactant wrapping	Yes	Yes	2
ASW3	Surfactant wrapping	Yes	Yes	3
P-CSs	Surfactant wrapping	No	Yes	3

* = CS initially functionalized in 55% HNO_3 for 17 h (see Chapter 3)

4.2.1.2 Surfactant wrapping sol-gel method

The surfactant wrapping sol-gel method used was based on a literature procedure [47-49] described for the dispersion of carbon nanotubes (CNT) in a surfactant. Sodium dodecylbenzesulfonate (NaDDBS) was the surfactant that was used, unless stated. In this method hexadecyltrimethylammonium bromide or CTAB ($CH_3(CH_2)_{15}N(CH_3)_3Br$ (≥ 99.0%, Sigma-Aldrich) was used to disperse the CSs. This surfactant was introduced to modify the conventional sol-gel method for the synthesis of well-defined CS-TiO_2 composites so as to obtain better TiO_2

coverage of the CS surfaces. A schematic representation of CSs-TiO_2 composite preparation via the surfactant wrapping method is shown in Fig. 4.3.

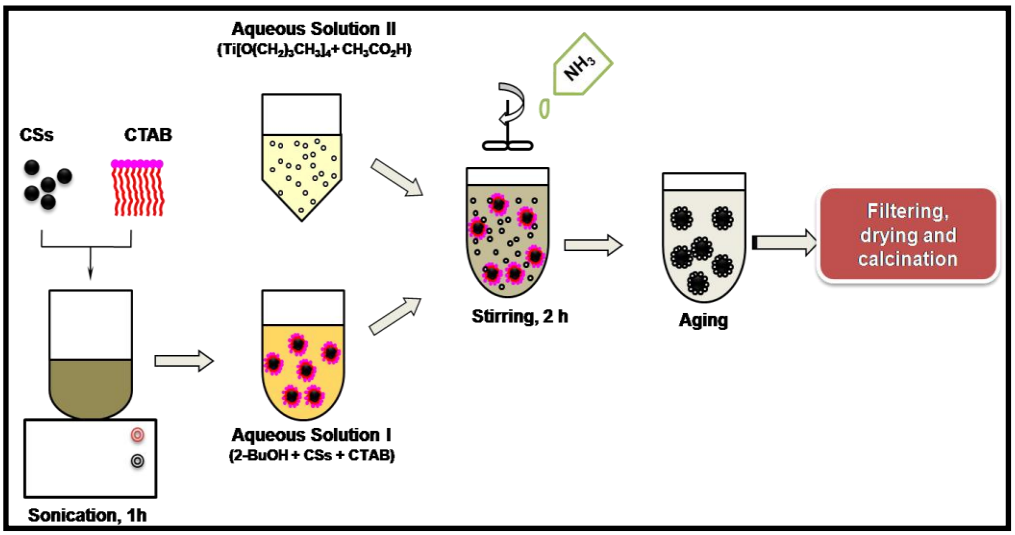


Figure 4.3 A schematic representation of the CS-TiO_2 composite prepared via the surfactant wrapping sol-gel method.

After experiments performed to make TiO_2 using the conventional sol-gel method, a weight ratio of 1:10, CS:TiO_2 (w/w) ratio was selected to prepare the CS-TiO_2 composites. Different preparation methods were explored for the surfactant wrapping sol-gel method to make a series of CS-TiO_2 composites with a ratio of 1CS:10TiO_2. The methods used were as follows (See Table 4.1 for a summary of procedures used):

(1) CSs were functionalised for 17 h (and not dispersed in CTAB) followed by a sol-gel coating. This material is referred to as sample A. The number of sol-gel cycles was varied.

(2) CSs were not functionalised, but only dispersed in CTAB for 1 h and then sol-gel coated. This material is referred to as sample SW. The number of sol-gel cycles was varied.

(3) CSs were initially functionalised for 17 h in HNO_3, followed by dispersion in CTAB for 1 h and then sol-gel coating. This material is referred to as ASW (see Fig. 4.3). The number of sol-gel cycles was varied.

(4) Pristine CSs.

In a typical synthesis of CS-TiO_2 composites, 1 g of functionalized carbon spheres (F-CSs) or pristine carbon spheres (P-CSs) were initially mixed with 70 mL of CTAB diluted to 0.5 weight % in aqueous solution. The final concentration of the CSs in H_2O was calculated such that it was 14.5 mg/mL. The suspension was then sonicated for 1 h to obtain a stable solution with a high weight fraction of CSs [29, 49]. Under these conditions, surfactant molecules assembled on the surface of the CSs with the alkyl chain groups presumably lying flat along the surface of the sphere [49]. The dispersed CSs were then diluted with 20 mL 2-BuOH while stirring. This suspension was stirred for 30 min to reach a uniform suspension (Solution I). A predetermined amount of $Ti[O(CH_2)_3CH_3]_4$ was mixed with 20 mL 2-BuOH and glacial acetic acid (≥ 99.85%, Sigma-Aldrich) while stirring vigorously. This suspension was allowed to stand for 30 min to form a clear solution (Solution II). Solution II was then added dropwise over 1 h into Solution I under vigorous stirring and the mixture was left at room temperature under stirring for 2 h to complete the reaction. At this stage of the synthesis, the Ti cations were captured by the negatively charged CS surface. To hydrolyse the residual precursor, 0.1 M NH_3 solution was added dropwise until a pH value of 9 was reached. This led to a TiO_2 coating on the CSs surface. The product was aged for 2 h and thereafter 20 ml of 2-BuOH was added to the CS-TiO_2 composite. The resulting suspension was filtered and washed with butanol followed by deionised water. The final precipitate (gel) was dried in an oven at 120 °C overnight to obtain a powder product. After cooling, the crushed powder product was re-dispersed in 2-butanol and the sol-gel coating step was repeated. This was repeated a third time in order to obtain a homogeneous coating of TiO_2 on the CS surface. After the three sol-gel coating cycles, the materials were crushed into a fine powder and then calcined at 350 °C for 6 hours under a flow of nitrogen.

These materials are referred to as ASW1, ASW2 and ASW3; the number indicates the number of cycles used to make the CS-TiO_2 composites prepared using method 3. SW1, SW2 and SW3 are the names given to the material prepared after the different number of sol-gel cycles used to make the CS-TiO_2 composites prepared using method 2. The symbols A1, A2 and A3 refer to the materials made from the three sol-gel cycles for the CS-TiO_2 composites prepared using method 1. Table 4.1 gives a summary of the methods used to prepare the CS-TiO_2 composites.

The calcined and the uncalcined composite materials were characterised by traditional characterisation methods to provide an understanding of their physico-chemical properties.

4.2.1.3 Carbon coated titania materials

Carbon coated titania materials were prepared using a horizontally positioned chemical vapour deposition (CVD) reactor. The description of this reactor was reported in Chapter 3 [50]. A synthesized TiO_2 material (using a conventional sol-gel method, as described above) was used as template (support) to be covered with carbon generated via pyrolysis of acetylene using a CVD method. Briefly, 0.2 g sample of TiO_2 was placed in a quartz boat. The material was spread evenly on the boat and was placed at the centre of the quartz tube. The tube was then placed in the furnace such that the boat was located in the middle of the furnace (the hottest region of the furnace). Pure nitrogen gas was introduced while heating the sample at a rate of 10 °C/min. This was done to create an inert atmosphere. At 900 °C, acetylene was introduced to replace nitrogen gas. This gas was allowed to pass through the reactor for different times (5, 15, 20, 30, 45, 120 and 240 minutes). These materials were called C5-TiO_2, C10-TiO_2, C20-TiO_2, C30-TiO_2, C45-TiO_2, C60-TiO_2, C120-TiO_2 and C240-TiO_2 for the acetylene that passed through the reactor for periods of 5, 15, 20, 30, 45, 120 and 240 min, respectively. Table 4.2 gives a summary of the samples that were prepared by the use of this

method. After cooling the soot was collected and characterized using TEM and BET procedures.

Table 4.2 Summary of carbon coated samples prepared at different durations of acetylene passing CVD

Time of C_2H_2 flow ***/min***	***Sample Name***
5	$C5TiO_2$
10	$C10TiO_2$
20	$C20TiO_2$
30	$C30TiO_2$
45	$C45TiO_2$
60	$C60TiO_2$
120	$C120TiO_2$
240	$C240TiO_2$

4.2.2 Characterisation

4.2.2.1 Transmission Electron Microscopy (TEM)

The prepared composites (calcined and non-calcined) were analyzed using Transmission Electron Microscopy (TEM) (FEI Technai Spirit G^2) and corresponding energy dispersive X-ray (EDX) procedures at 200 kV. Specimen samples for TEM and EDX analysis were prepared by dispersing very small samples in about 1 mL of methanol. The mixture was sonicated for about 15 min to obtain a homogeneous suspension. One drop of the CS-TiO_2 composite suspension was placed onto an SPI-carbon coated copper grid and was allowed to dry before it was placed in the microscope. The morphology of the composite samples was observed and the data was processed on a PC.

4.2.2.2 Thermogravimetric analysis (TGA)

Thermogravimetric analysis (TGA), conjugated with a derivative curve of the weight loss (DTG) measurements were carried out on a Perkin Elmer STA 4000 analyser coupled with an auto sampler that can perform up to 45 samples. About 10 mg of CS-TiO_2 composite samples was placed in a pan (ceramic) and then put in the instrument's furnace. The sample temperature was ramped from room temperature to 950 °C under a flowing air atmosphere (20 mL/min) at a heating rate of 10 °C/min. A TGA weight loss plot provided information about the nature, stability and composition of the investigated sample. The derivative curve of this plot provided the 'maximum' temperature at which the weight loss took place. The TGA-DTG analysis was carried out to determine the composites' behavior, decomposition and their stability in air environments. This technique was also used to estimate the CS content within the composites. The peak position obtained from DTG curves were used to define a maximum temperature at which a weight loss of a substance was achieved and this information was used to develop calcination temperature programs.

4.2.2.3 Raman spectroscopy

The Raman spectroscopic measurements were carried out on the CS-TiO_2 composite samples using a Jobin-Yvon T64000 micro-Raman spectrometer equipped with a liquid nitrogen cooled charge coupled device detector and excitation laser wavelength of 514.5 nm. The backscattered data were analysed using a double-grating spectrometer and collected using a photometer. All measurements were taken at room temperature. The obtained Raman bands were deconvoluted using the Origin 6.0 Professional package to obtain areas under the peaks and the intensity of those peaks.

4.2.2.4 XRD

The degree of crystallinity of the CS-TiO_2 composites were characterised using X-ray diffraction analysis on a Bruker D8 Avance X-ray diffractometer with a primary beam Göbel mirror, a radial soller slit, and a V Åntec-1 detector using Cu-K_α (1.5406Å) radiation at 40 kV and 40 mA. The scan range was $5° < 2\theta < 90°$ in 0.021 steps, using a standard speed with an equivalent counting time of 14.7 seconds per step. The obtained diffraction peaks were then compared with those of standard compounds reported in the Diffrac^{plus} evaluation package using the EVA (V11.0, rev .0, 2005) software package.

4.2.2.5 BET surface area analysis

Textual properties of the composite materials were determined via N_2 adsorption/desorption according to the Brunauer-Emmet-Teller (BET) method based on adsorption data in the partial pressure (P/P_0) range of 0.05-0.35 and the total pore volume was determined by the amount of N_2 adsorbed at $P/P_0 = 0.995$ using a Micromeritics Tristar 3000, surface area and porosity analyzer [51]. The average pore size was obtained from the adsorption data by the Barrett-Joyner-Halenda (BJH) method [52]. About 0.2 g of sample was degassed *ex-situ* under a flow of N_2 at 150 °C for 4 hours prior to analysis to remove moisture using a Micromeritics Flow Prep 060, sample degas system. The surface areas and pore size distributions were then obtained at -195 °C.

4.3 Results and discussion

4.3.1 Conventional sol-gel method

The preparation of CS-TiO_2 composite material using the conventional sol-gel method was achieved by initially dispersing functionalized CSs (F-CSa) in a mixture of $Ti[O(CH_2)_3CH_3]_4$ and 2-BuOH. After sonication, a mixture of HNO_3 and 2-BuOH was added drop-wise to the butanolic solution of alkoxide containing the F-CSs. Through a sequence of hydrolysis and polycondensation reactions, the sol-gel transition took place gradually. The wet gels were dried in an oven at 120 °C overnight. Calcination of the crushed powder materials was performed under flowing nitrogen.

4.3.1.1 TEM

The morphology and the particle size distribution of the calcined TiO_2 (0CS-SG) that was prepared without the presence of CSs, using a conventional sol-gel method, is shown in Figure 4.4 (TEM image and the histogram). The image reveals that TiO_2 is made of aggregated clusters of particles with an average size of about 8.4 nm. This morphology is similar to the one reported in the literature by Guo *et al.* [53]. The average particle size obtained for the synthesized TiO_2 is smaller than the one reported by Guo *et al.* (15 nm), yet comparable to the size previously reported in the literature [54, 55].

TEM images of CS-TiO_2 composites prepared by a conventional sol-gel method viz. 1CS-1SG, 1CS-2.5SG, 1CS-5SG, 1CS-10SG, 1CS-25SG and 1CS-50SG are depicted in Fig. 4.5. For all the materials with the different CS:TiO_2 ratios, both CSs and TiO_2 were detected. The EDX spectrum of CS-TiO_2 composite (Fig. 4.6) made with a 1:10 ratio (1CS-10SG), presented in image Fig. 4.5 (d), revealed the existence of C, Ti and O atoms in the sample. (The Cu signal is due to the Cu grid).

The CS-TiO_2 sample with ratio of 1:1 by weight (1CS-1SG) revealed that there is a minimal or no interaction between the CSs and TiO_2. The CSs appear uncovered by TiO_2 while the TiO_2 agglomerates are far removed from the 'naked' CSs (Fig. 4.5 (a)).

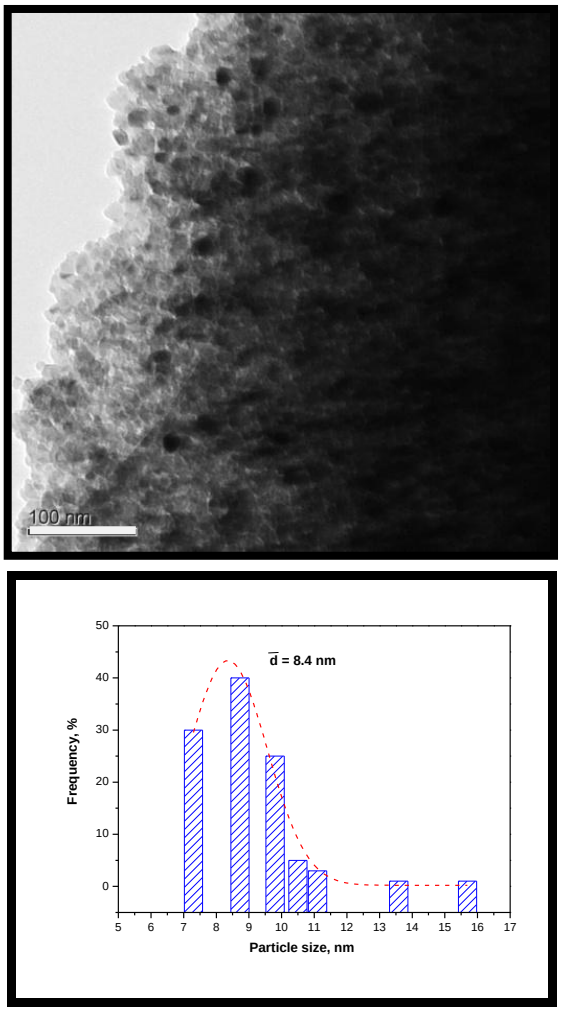


Figure 4.4 TEM image of pure TiO_2 (*top*) and particle size distribution (*bottom*) prepared without the presence of CSs by a conventional sol-gel method. (Solid line = particle size distribution histogram, and dashed line = Gaussian distribution).

Increasing the loading ratio of TiO_2 on the CSs from 1:1 to 1:2.5, 1:5, 1:10, 1:25 and to 1:50 increased the amount of TiO_2 aggregates; however a completely homogeneous coating of CSs for the preparation of CS-TiO_2 composites was

never achieved by the use of the conventional sol-gel method at all ratios investigated. In some instance some of the TiO_2 appears to have covered the CSs while most of the TiO_2 particles appear to agglomerate away from the CSs. This observation has also been reported by others when attempts were made to coat carbon nanotubes using a sol-gel method [14].

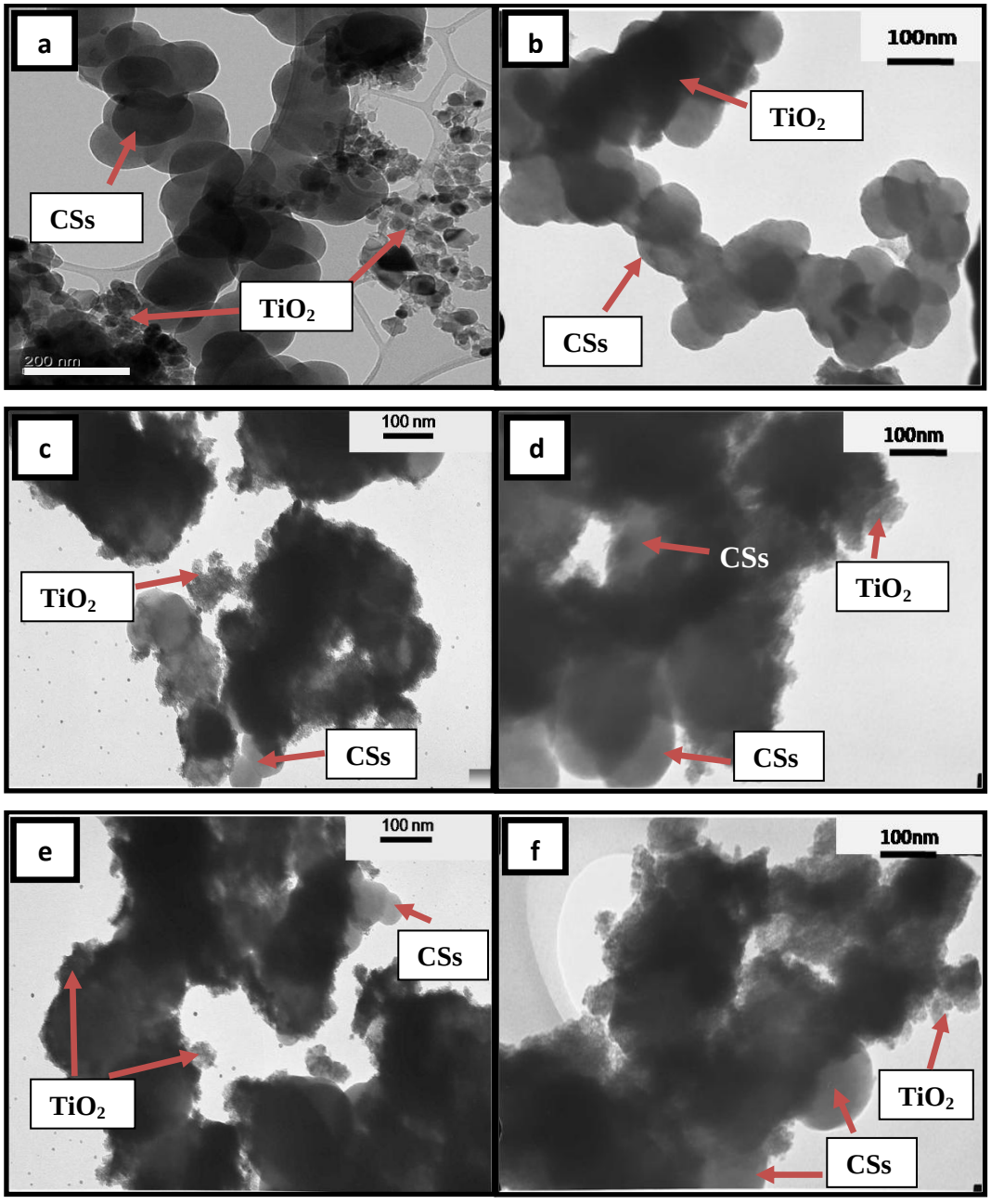


Figure 4.5 TEM images of CS-TiO_2 composites prepared by a conventional sol-gel method: (a) 1CS-1SG, (b) 1CS-2.5SG, (c) 1CS-5SG, (d) 1CS-10SG, (e) 1CS-25SG and (f) 1CS-50SG

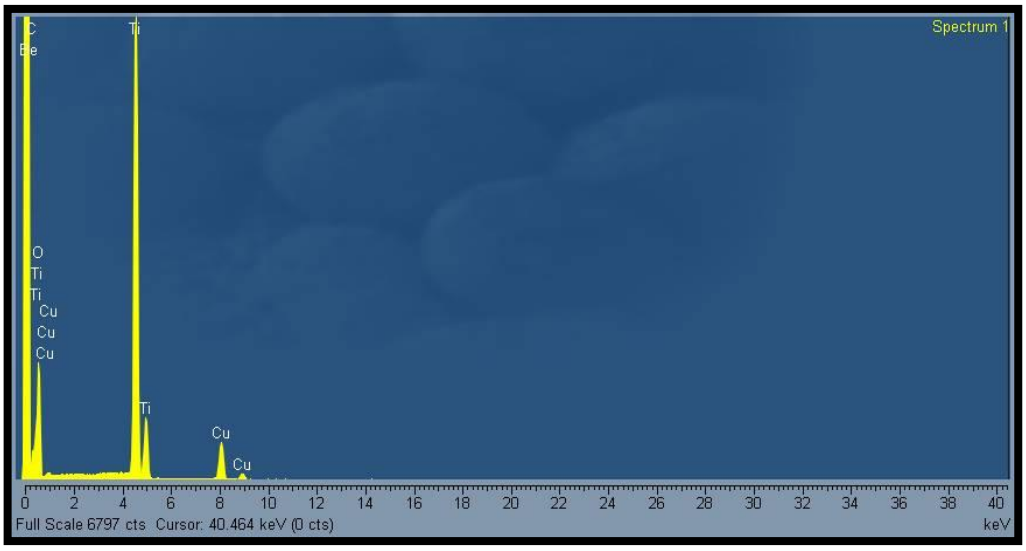


Figure 4.6 EDX spectrum corresponding to the surface coverage shown in Fig. 4.5(c). C and Ti were detected; the Cu signal corresponds to the Cu grid substrate for TEM analysis.

4.3.1.2 TGA

Figures 4.7 and 4.8 depict the TGA and DTG plots, respectively for the functionalized CSs (F-CSs), uncalcined TiO_2 uncalcined 0CS-SG and the calcined (350° C in air) 0CS-SG samples. The information obtained from these thermograms provides a reference for the TGA profiles of CS-TiO_2 composites.

A TGA profile of the F-CS sample showed only one weight loss stage with a peak maximum at around 740 °C. This observed weight loss was due to the oxidation of CSs. In the TGA profile of uncalcined 0CS-SG sample it can be seen that there are two weight-loss stages. The first weight loss stage with maximum at 101 °C represents removal of moisture within the sample, while the second weight loss stage with maximum at 349 °C represents the removal of organic components (butanol and alkoxide) and organic acid groups. The calcined 0CS-SG sample showed no weight loss under air. This observation suggests that calcination of the sol-gel prepared at 350 °C successfully removed all the alkoxides, HNO_3 and any other unwanted organic components within the sample.

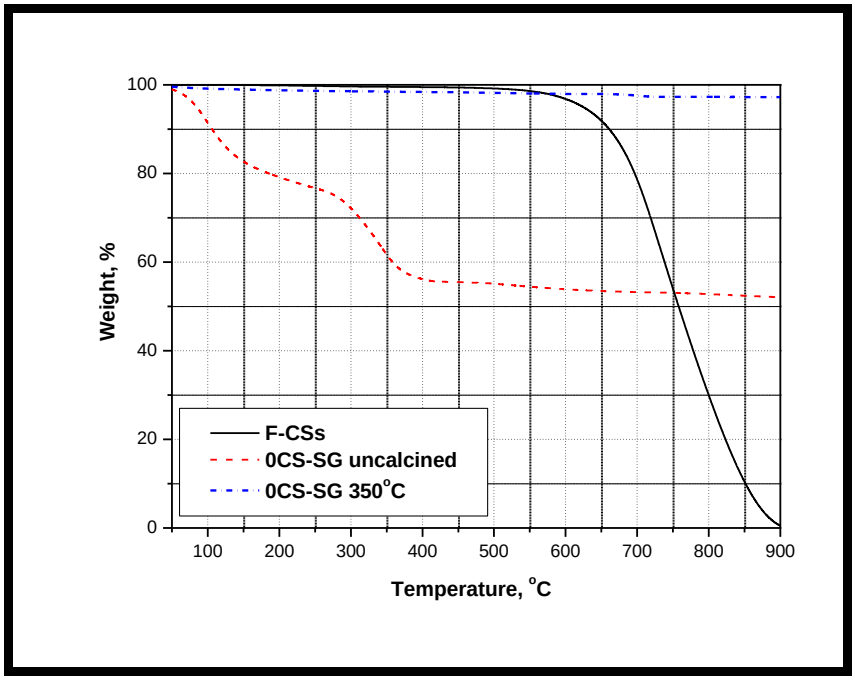


Figure 4.7 TGA profiles of the F-CS, uncalcined 0CS-SG and the calcined 0CS-SG (350 °C) samples

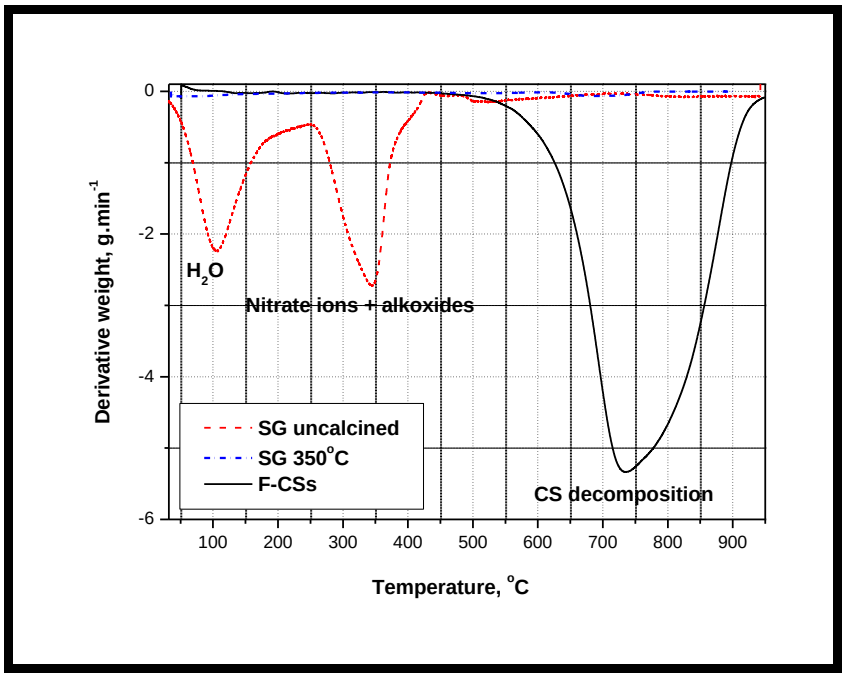


Figure 4.8 DTG of F-CS, uncalcined 0CS-SG and the calcined 0CS-SG

To further confirm that the organic components and HNO_3 weight loss stages occurred at around the same temperature; two samples (1 g each) of a commercially available TiO_2 material (P25 Degussa) were mixed with either 2 mL of HNO_3 or 2 mL of butanol. After air drying (overnight) at room temperature, the samples were subjected to TGA analysis under flowing air. Figure 4.9 and 4.10 shows the TGA and DTG profiles, respectively for P25 TiO_2 (DTG not shown), P25 TiO_2 mixed with HNO_3, and P25 TiO_2 mixed with butanol. In all the three samples a weight loss stage due to water was observed between 50 and 120 °C.

The TGA profile for P25 TiO_2 showed no weight loss stages. TGA profiles for a sample of P25 TiO_2 mixed with HNO_3 and a sample of P25 TiO_2 mixed with butanol showed further weight loss stages. These occurred between 200 and 300 °C for P25 TiO_2 mixed with HNO_3 and between 200 and 400 °C for P25 TiO_2 mixed with butanol. The DTG of the P25 TiO_2 mixed with the HNO_3 sample showed that the second weight loss stage consisted of two derivative peaks with their maxima at 260 and 375 °C. This therefore suggests that decomposition of nitrate ions from P25 TiO_2 immersed in HNO_3 occurred in two weight loss stages. It has been reported that NO_3^- ions decompose in one weight loss stage with maxima at around 250 °C [56]. No explanation for the presence of the second weight loss step observed for the decomposition of NO_3^- ions in our sample can be given as yet. The removal of butanol (organic material) from the DTG profile of P25 TiO_2 mixed with butanol sample showed one derivative peak with a maximum at 288 °C. This corresponds to the weight loss due to the butanol (presumably in the form of a butoxide ion). The DTG peak observed for the second weight loss stage in both samples overlaps with the second peak that was observed at 349 °C found in the uncalcined 0CS-SG sample (Fig 4.8).

Figures 4.11 and 4.12 depict the TGA and DTG profiles, respectively for the CS-TiO_2 composites prepared by the sol-gel method. These measurements were performed under flowing air. In the lower temperature region, i.e. between room temperature and 450 °C, all the weight loss stages that were observed in 0CS-SG

sample were also observed in the CS-TiO_2 composites (1CS-2.5SG, 1CS-5SG, 1CS-10SG, 1CS-25SG and 1CS-50SG). These weight loss stages were due to the removal of H_2O, NO_3^- ions and the organic component (as explained for the 0CS-SG sample above).

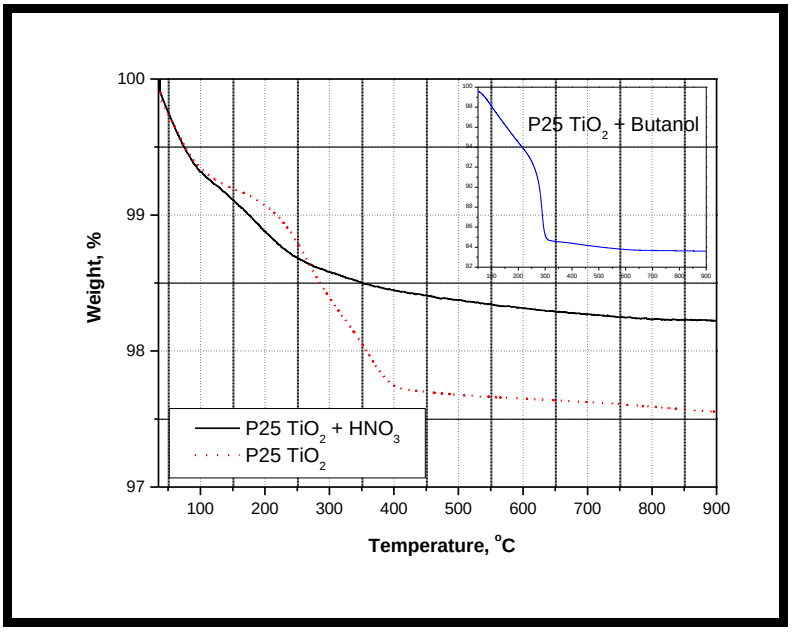


Figure 4. 9 TGA of P25 TiO_2, P25 TiO_2 mixed with HNO_3, and P25 TiO_2 mixed with butanol (*inset*)

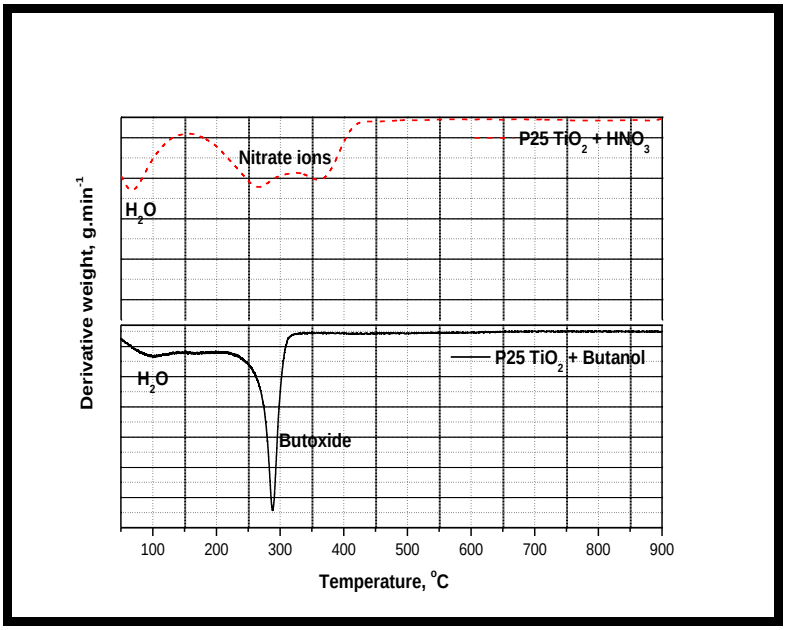


Figure 4.10 DTG of P25 TiO_2 mixed with HNO_3 and P25 TiO_2 mixed with butanol

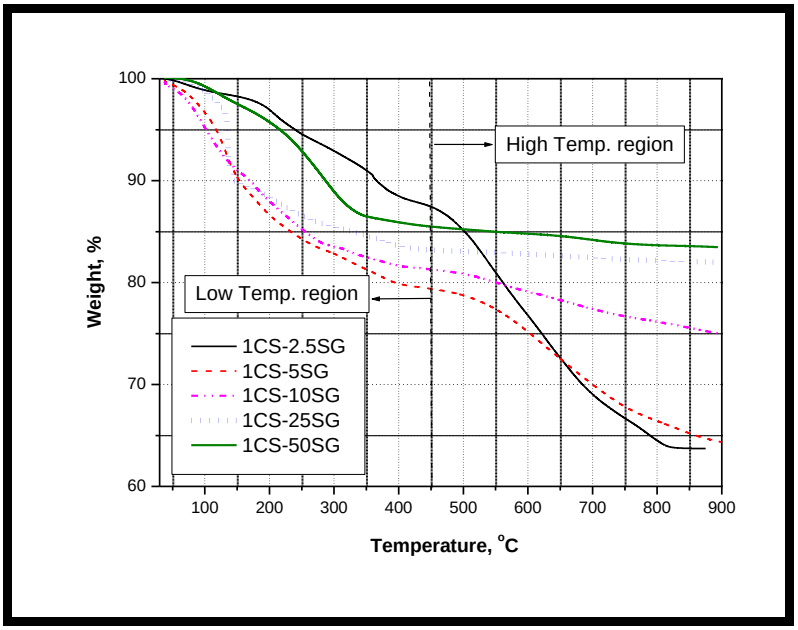


Figure 4.11 TGA uncalcined 1CS-2.5SG, 1CS-5SG, 1CS-10SG, 1CS-25SG and 1CS-50SG

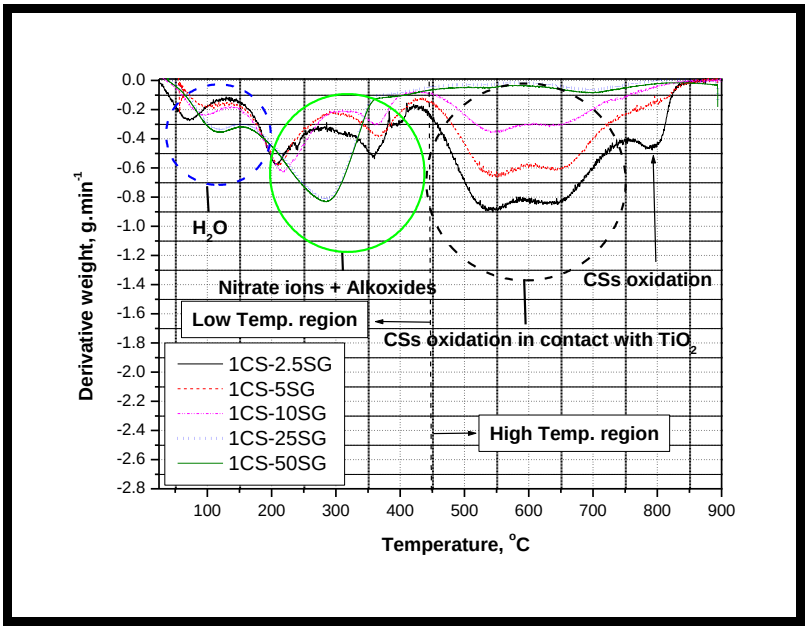


Figure 4.12 DTG of uncalcined 1CS-2.5SG, 1CS-5SG, 1CS-10SG, 1CS-25SG and 1CS-50SG

The DTG peak maxima for the components lost for the sample with the different composite ratios, shown in Fig. 4.12, occurred at different temperatures with their

positions (temperature) shifting to higher temperatures as the TiO_2 ratio was increased. This behavior suggests that since the TiO_2 introduced on the CS surface interacts with the solvents, precursors and hydrolyzing components; the higher the TiO_2 content, the more the interaction. The second weight loss step (organic component and nitrate ions) observed in composites with higher TiO_2 ratios, i.e. 1CS-25SG and 1CS-50SG, occurred as one broad peak (DTG) with a maximum at 397 °C.

In the lower region, the DTG traces of composites with lower TiO_2 ratios (1CS-2.5SG, 1CS-5SG and 1CS-10SG) shows that this peak splits into two derivative peaks; one in the range between 200 and 250 °C while the other one occurred between 320 and 420 °C. The composite with higher TiO_2 ratios (1CS-25SG and 1CS-50SG) shows no split peak, but only one broad peak which occurred between 150 and 350 °C. This relates to the amount of organic solvent (2-butanol) and alkoxide used to prepare composites with higher TiO_2 ratios. The peak was much larger at high TiO_2 ratios and it overlapped with the peak that appeared due to the loss of nitrate ions. For composites with lower TiO_2 ratios this split in the peak was evident because the amount of 2-butanol and alkoxide used was lower.

In the higher temperature TGA-DTG region, oxidation of CSs can be noted. As expected, the weight loss due to decomposition of CSs decreased with an increase with TiO_2 loading (Fig. 4.11). The DTG plots (Fig. 4.12) of all the composites depict that the oxidation of CSs occurred at two different temperatures (549 and 650 °C) except for 1CS-2.5SG sample which shows a third oxidation peak occurring at 800 °C. The peak occurring at 800 °C is at a position which correlates with the oxidation of F-CSs (see Fig. 4.8). This peak may therefore be due to the oxidation of CSs which were not successfully coated with TiO_2. This result correlates well with the TEM image noted for 1CS-2.5SG shown in Fig 4.5 (b). The two other peaks for the decomposition of CSs in the high temperature region of the TGA could be due to the CSs that were successfully coated with TiO_2. It is possible that the TiO_2 may catalyze the decomposition of CSs in air. The covering (or coating) of CSs by TiO_2 is not homogeneous (as depicted by TEM images)

leading to two different combustion temperatures. The higher temperature peak (650 °C) may be due to the combustion of CSs with less TiO_2 interaction while the peak at 549 °C may be due to combustion of CSs involving a larger interaction with TiO_2.

A TGA plot showing CS weight loss, and the uncombusted TiO_2 residue, for the different CS-TiO_2 composites as a function of CS-TiO_2 composite ratio is shown in Fig. 4.13. The CS weight loss percentages predicted for the composites were about 26, 16, 9, 3 and 1 % for 1CS-2.5SG, 1CS-5SG, 1CS-10SG, 1CS-25SG and 1CS-50SG respectively. Actual expected CS weight loss (as percent) of the respective composites were observed to be 29, 17, 9, 4 and 2 %.

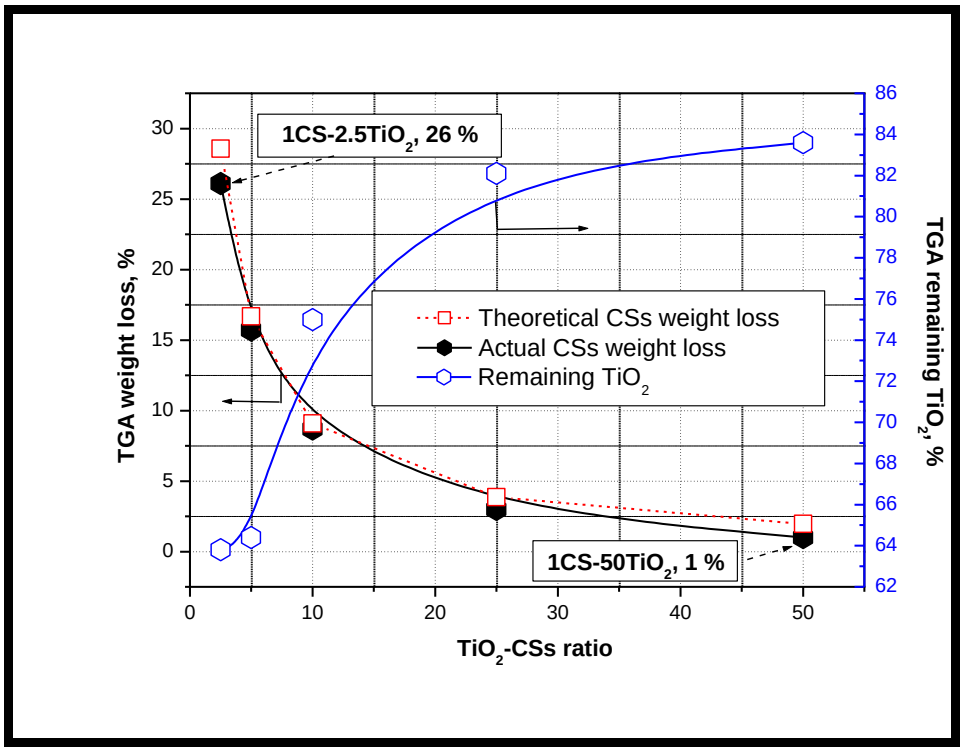


Figure 4.13 Analysis of CSs weight loss and residue TiO_2 for the composite samples as a function of CS-TiO_2 composite ratio. Data were obtained from TGA measurements.

The CS-TiO_2 composites after calcinations, using different procedure, were subjected to TGA. Figure 4.14 depicts the TGA profiles of the 1CS-10SG sample

calcined using different conditions, viz. (1) 1 bar 350 °C for 6 h; (2) 1 bar 350 °C for 13 h; (3) 5 bar 350 °C for 6 h; and (4) 5 bar 400°C for 6 h. These calcination temperatures were selected such that a correct method for the decomposition of CSs could be established in order to achieve a "hollow" TiO_2 material that did not contain any CSs.

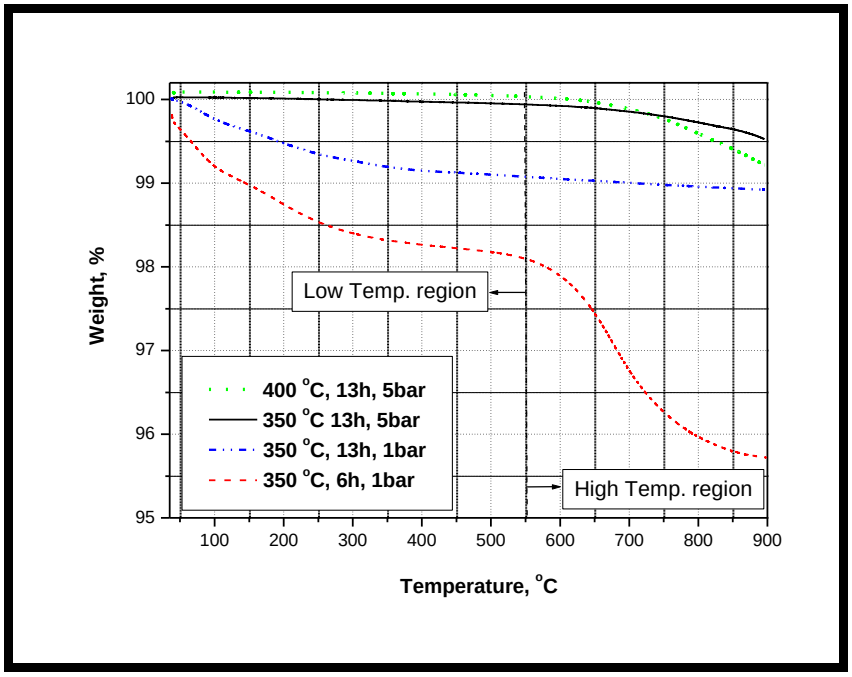


Figure 4.14 TGA of 1CS-10SG samples after calcination at: 1 bar 350 °C for 6 h; 1 bar 350 °C for 13 h; 5 bar 350 °C for 6 h; and 5 bar 400°C for 6 h

In the low temperature region of the TGA profile (between room temperature and 550 °C) a weight-loss stage was observed for the material calcined using conditions (1) and (2) and their respective weight losses were about 2 and 1%, respectively. These losses may be due to moisture and some organic components or NO_3^- ions. The thermograms of samples calcined using method (3) and (4) did not show any weight loss stages, suggesting that all the organic components and NO_3^- ions were completely removed using these conditions. In the high temperature region, a weight-loss of about 4% was observed between 600 and 900 °C due to decomposition of CSs for the sample calcined using method (1). This weight loss is comparable to the weight loss that was observed for the uncalcined

sample of 1CS-10SG in Fig. 4.13. A TGA profile of the sample calcined using method (2) showed an insignificant weight loss in the high temperature region. These observations suggest that successful removal of CSs from the composite (1CS-10TiO_2) occurred after annealing in air, for 13 h at 1 bar pressure.

TGA profiles of samples that were annealed for 6 h at high pressures (5 bar) at 350 and 400 °C showed small weight losses percentages, 0.8 and 0.5%, respectively at very high temperatures (700-900 °C). These weight losses may not to be due to the decomposition of CSs since high pressures (5 bar) were used to anneal these materials and carbon should be easy to remove by these methods. The weight-loss noted for calcination methods (3) and (4) may relate to the formation of a different TiO_2 phase. TiO_2 has been shown to undergo a phase change from anatase to rutile at 1 bar and 540 °C [7]. At even higher pressure conditions, 5 bar, this transition will also take place, as observed in Fig. 4.14. Method (4) shows a higher weight-loss stage compared to method (3) suggesting that at higher temperature and pressure, the anatase-rutile transition is enhanced (see below).

Fig. 4.15 shows TEM images of the 1CS-10SG sample calcined using different conditions, viz. (1) 1 bar 350 °C for 6 h; (2) 1 bar 350 °C for 13 h; (3) 5 bar 350 °C for 6 h; and (4) 5 bar 400°C for 6 h. No significant differences can be observed in the images; however all samples calcined using method (2), (3) and (4) shows the absence of CSs.

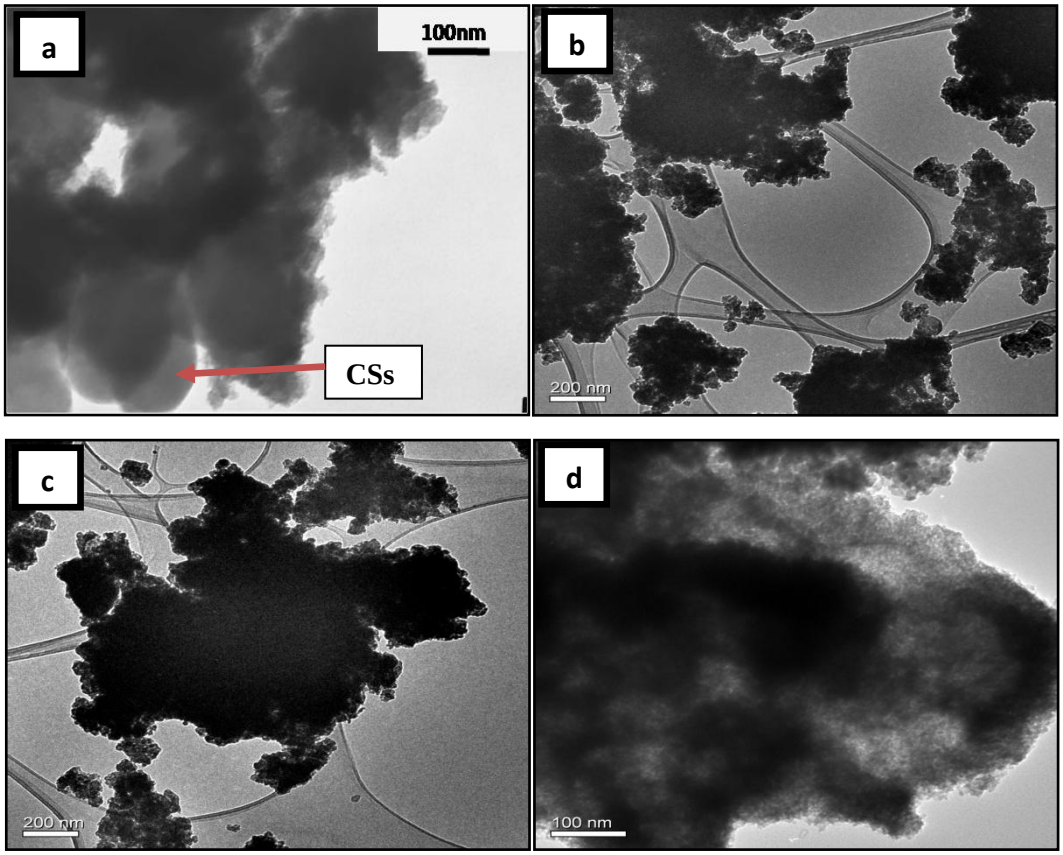


Figure 4.15 TEM images of 1CS-10SG samples after calcination at: (a) 1 bar 350 °C for 6 h; (b) 1 bar 350 °C for 13 h; (c) 5 bar 350 °C for 6 h; and (d) 5 bar 400°C for 6 h

4.3.1.3 XRD

In Fig. 4.16 the XRD patterns of calcined (350 °C, 6 h, 1 bar) sol-gel derived TiO_2 (0CS-SG) and the functionalized CSs (F-CS) are shown. The most intense peaks in the XRD pattern of F-CS corresponds to the (002), and (100) reflections. These peaks are a fingerprint for carbon. The XRD pattern of the calcined 0CS-SG revealed that only the pure anatase phase of TiO_2 was present. The anatase phase of TiO_2 had an approximate average grain size of 8.0 nm (obtained using the Scherrer equation). This size compares well with the size obtained from TEM analysis (8.4 nm).

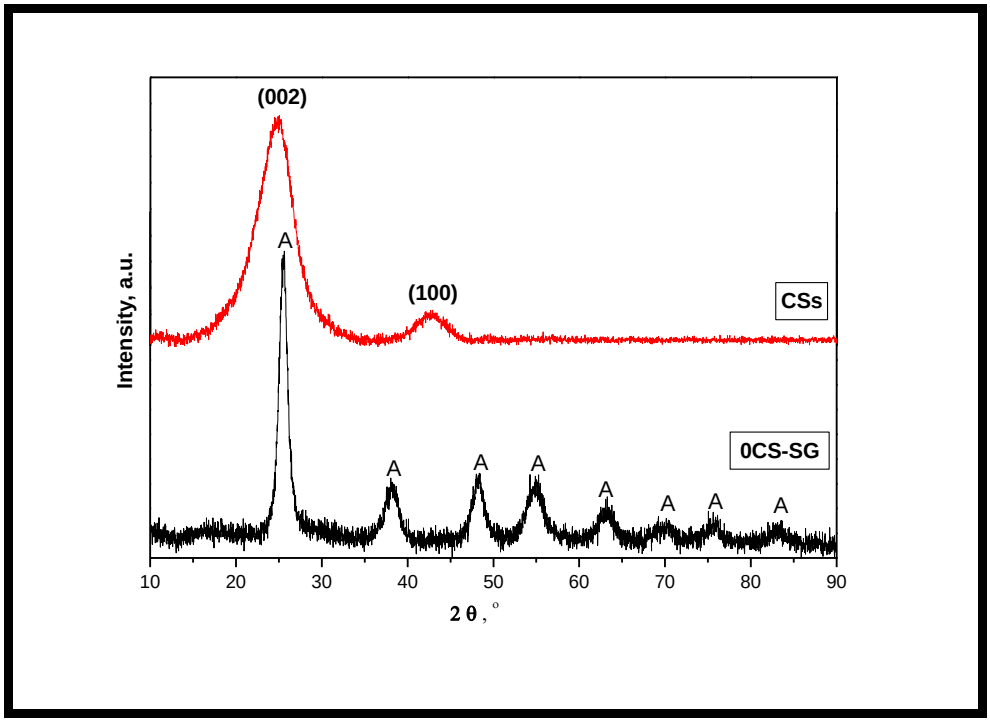


Figure 4.16 XRD patterns of calcined sol-gel derived TiO_2 (0CS-SG) and F-CS. The peaks marked with (A) and (002, 100) correspond to TiO_2 (anatase) and CSs, respectively

The XRD patterns of uncalcined 1CS-10SG sample, and calcined 1CS-10SG samples using different conditions, viz. (1) 1 bar 350 °C for 6 h; (2) 1 bar 350 °C for 13 h; (3) 5 bar 400 °C for 13 h; and (4) 5 bar 500°C for 13 h is shown in Fig. 4.17. The XRD pattern for the uncalcined material shows the presence of amorphous TiO_2 which is composed of an anatase phase with an average grain size of 9.1 nm. No F-CS peaks were observed from any of the calcination procedures carried out. The F-CS peaks may overlap with the anatase peaks and make it difficult to evaluate the presence of carbon. Annealing this material using calcination method (1) enhanced the crystallinity of the anatase. The average grain size was measured to be 8.0 nm after calcination. A decrease in anatase grain size could be due to the decomposition of organic molecules that were present before calcination. A prolonged calcination time (13 h) for this material at the same temperature (350 °C) and at an increased pressure (5 bar), showed the appearance

of a peak at about 27.3 2θ ° which does not match either the pattern of anatase or the F-CS.

When the calcination temperatures were further increased to 400 and 500 °C (13 h) and high pressure (5 bar) the evolution of a peak at a 2θ value of 30.7 ° was noted (calcination methods (3 and 4)). Calcination of this material using method (4) gave a material with an enhanced peak at 27.3 °. The peak observed at 27.3 ° matches with a rutile phase peak. This observation correlates with the observed weight loss from TGA results of the 1CS-10SG composite samples calcined at 5 bar and 350 °C for 6 h and 5 bar and 400°C for 6 h.

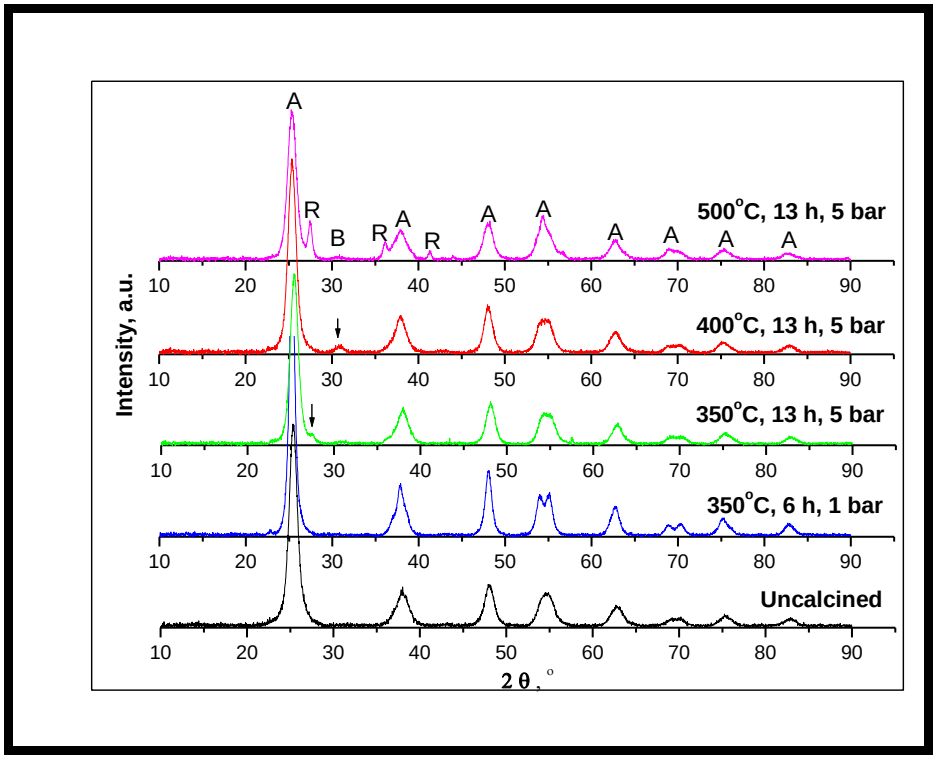


Figure 4.17 XRD patterns of calcined sol-gel derived composite materials, where A = anatase phase, B = brookite and R = rutile phase.

4.3.1.4 Raman spectroscopy

Figure 4.18 shows the Raman spectra for the bulk commercial TiO_2 (P25 Degussa TiO_2) material in comparison with the bulk TiO_2 material that was prepared by the sol-gel method (0CS-TiO_2).

The Raman spectra of three 0CS-TiO_2 samples that were calcined differently (uncalcined 0CS-SG, calcined 0CS-SG (1 bar, 350 °C, for 6 h) and calcined 0CS-SG (1 bar, 400 °C, for 6 h)) are compared with that of calcined P25 TiO_2 (1 bar, 350 °C, for 6 h) in Fig. 4.18. The spectrum of P25 TiO_2 shows the presence of five bands, viz. at 141, 195, 395, 514 and 636 cm^{-1}. In the literature, these bands are said to be representative of the E_g vibrational modes of the anatase phase of TiO_2 [57, 58]. All the Raman bands obtained in the uncalcined sample of 0CS-SG were broad; this suggests that they were amorphous. This was probably due to the presence of organic components from the precursors that were used to synthesise TiO_2. The intense 141 cm^{-1} peak that was obtained in the P25 TiO_2 sample was obtained at 152 cm^{-1} in this sample while the 195 cm^{-1} peak was absent.

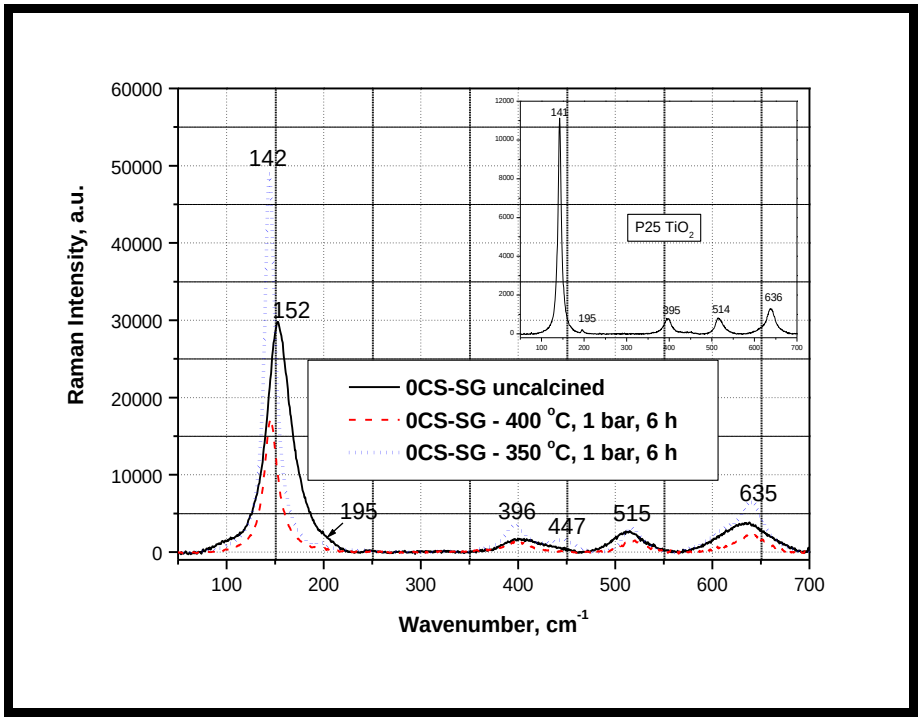


Figure 4.18 Raman spectra of uncalcined 0CS-SG sample; and of calcined 0CS-SG samples at: 1 bar 350 °C for 6 h, and 1 bar 400 °C for 6 h. Raman spectra of bulk commercial TiO_2 material (P25 TiO_2) is shown on the *inset*.

The Raman spectrum of calcined 0CS-SG at 350 °C for 6 h shows an improvement in the crystallinity of the anatase phase since:

(1) the Raman bands became sharper,
(2) the 152 cm^{-1} band shifted to a lower position (142 cm^{-1}),
(3) a broad band that appeared at 400 cm^{-1} in the uncalcined sample became sharper and was split into two bands (396 and 447 cm^{-1}), and
(4) the appearance of a 195 cm^{-1} band was evident.

Increasing the calcination temperature to 400 °C, further improved the anatase crystallinity since all the bands that were found in the Raman sprectrum of calcined P25 TiO_2 sample and in the 0CS-SG sample calcined at 350 °C, were present and well defined. The band obtained at 447 cm^{-1} in the spectrum of 0CS-SG sample calcined at 350 °C (absent in 0CS-SG sample calcined at 400 °C) could be due to the transition from amorphous to crystalline anatase, i.e. complete removal of organic components. The intensity of the 0CS-SG sample calcined at 400 °C is lower than that calcined at 350 °C. Unfortunately the Raman peak intensity is a function of the amount of sample used and does not give any further information on this point [59].

Figure 4.19 shows a Raman spectrum for F-CS, with two broad peaks occurring at 1352 cm^{-1} and 1591 cm^{-1} corresponding to the sp^3 carbon (D-band) and the graphitic (sp^2) (G-band) peaks, respectively. The intensity ratio (I_G/I_D) measured for F-CS was 0.92. A Raman study was conducted on the calcined (400 °C) 1CS-2.5SG, 1CS-5SG and 1CS-25SG composite samples in order to study the graphitic nature of CSs found in the composites.

Figure 4.20 shows the Raman spectra of these composites. The intensity of the Raman bands at wavenumbers greater than 1200 cm^{-1} is very small (note change in intensity scale at this point). A light area mapping program was used to detect TiO_2 and a dark area mapping program used to detect CSs. The data obtained were then combined and Raman spectra in Fig. 4.20 were produced. Interestingly the presence of the D and G bands was observed in all the composites. The observed intensity of the D and G bands with respect to the intensity of TiO_2 decreased, as the intensity of TiO_2 peaks increased.

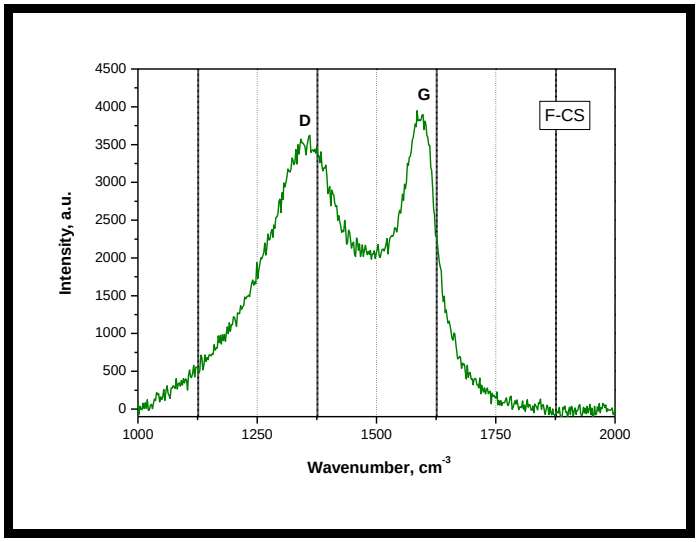


Figure 4.19 Raman spectra of calcined F-CS produced, showing D and G-Bands

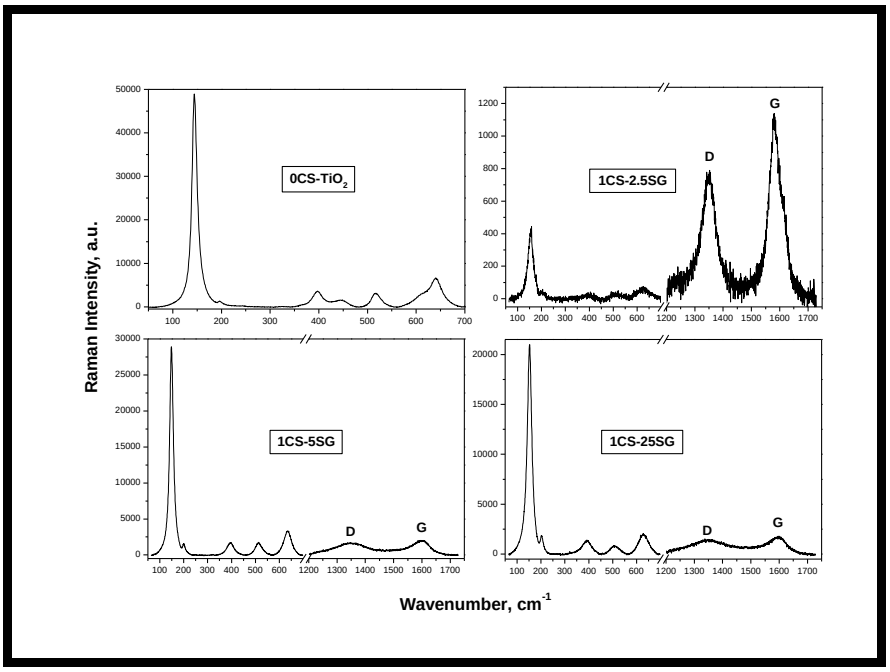


Figure 4.20 Raman spectra of calcined bulk 0CS-SG (calcined at 400 °C) and calcined CS-TiO_2 composites prepared by conventional sol-gel with ratios of: 1CS-2.5SG, 1CS-5SG and 1CS-25SG (calcined at 400 °C).

In the literature a well-behaved correlation between the TiO_2 grain size and its Raman spectrum has been established [57]. It was shown that both the peak position and the full-width at half maximum of the band at 141 cm^{-1} changed

when the TiO_2 crystallite size was smaller than about 34 nm. The broadening and the shift of the E_G mode to higher wavenumbers (142 cm^{-1} in bulk 0CS-SG) are attributed to phonon confinement as a consequence of the decrease in crystallite size [60].

The broadening of the band at about 156 cm^{-1} for 1CS-2.5SG and its shift from 142 cm^{-1} (in bulk 0CS-SG) to 154 cm^{-1} for 1CS-2.5SG, 1CS-5SG and 1CS-25SG, respectively indicates a TiO_2 size of *ca* 5 nm according to Swammy *et al.* [57]. XRD measurements of the average grain size of the nanostrtuctured TiO_2 (0CS-SG) was indeed found to be *ca* 8 nm.

The positions at which the D and G bands were observed in the composites and their corresponding I_G/I_D ratio are tabulated in Table 4.3. The relative intensity ratios of the D and G bands (I_G/I_D) for the F-CS with TiO_2 , viz. 0.88 for 1CS-2.5SG, 0.82 for 1CS-5SG and 0.70 for 1CS-25SG, were found to be lower than that of F-CS (0.92).

Table 4.3 Values of intensity ratio (I_G/I_D) and the positions at which the bands (D and G) occur for calcined F-CS, 0CS-SG, 1CS-2.5SG, 1CS-5SG and 1CS-25SG composite samples (as depicted in Fig. 4.20)

	Peak position/cm^{-1}		
Sample	**D-Band**	**G-Band**	I_G/I_D
F-CS	1352	1591	0.92
0CS-SG	-	-	-
1CS-2.5SG	1351	1591	0.88
1CS-5SG	1346	1589	0.82
1CS-25SG	1347	1590	0.70

An increase in I_G/I_D ratios implies an increased degree of graphitization, i.e. a decrease in disorder. Similar observations have been reported in the literature for the interaction between TiO_2 and functionalized multiwall carbon nanotubes (F-MWCNT) [61]. The authors explained that the increased disorder on their F-MWCNT was due to the presence of TiO_2 attached to their surface; this effect

broke the symmetry of the tubes. From this it can be concluded that the symmetry of the F-CS was broken in our composites.

4.3.1.5 Porosity measurements

The BJH method using N_2 adsorption-desorption isotherms was used to investigate the interaction between TiO_2 and the F-CS surface. In Table 4.4 BET total surface area and porosity values of uncalcined and calcined (350 °C in air) materials viz. F-CS, 1CS-1SG, 1CS-2.5SG, 1CS-5SG, 1CS-10SG, 1CS-25SG, 1CS-50 and 0CS-SG are shown.

Table 4.4 BET total surface area and porosity measurements for uncalcined and calcined materials of F-CS, 1CS-1SG, 1CS-2.5SG, 1CS-5SG, 1CS-10SG, 1CS-25SG, 1CS-50 and 0CS-SG

	Before calcination			**After calcination (350°C, 1bar, 6h)**		
Sample	$S_{BET}{}^{a}$ **(m^2/g)**	$P_v{}^{b}$ **(cm^3/g)**	$P_D{}^{c}$ **(nm)**	$S_{BET}{}^{a}$ **(m^2/g)**	$P_v{}^{b}$ **(cm^3/g)**	$P_D{}^{c}$ **(nm)**
F-CS	-	-	-	10	0.015	9.3
1CS-1SG	107	0.021	8.9	10	0.025	30.9
1CS-2.5SG	236	0.241	3.7	32	0.353	25.5
1CS-5SG	253	0.252	3.8	80	0.353	9.5
1CS-10SG	257	0.251	3.7	85	0.376	11.8
1CS-25SG	136	0.173	2.8	51	0.385	15.1
1CS-50SG	204	0.052	2.9	49	0.099	0.5
0CS-SG	142	0.075	2.1	51	0.135	5.8

[a]Surface area, [b]P_v = pore volume, [c]P_D = pore diameter

As can be seen, the total surface areas of all uncalcined composites are higher than their calcined counterparts. The pore volumes of the calcined materials are larger than their uncalcined counterparts. This observed decrease in surface area and an increase in pore volume was expected because TGA studies (in air) of these

uncalcined materials confirmed the presence of organic components (Fig 4.7 and 4.11). These components influence the surface area values in the composites, while the increase in total pore volumes may be due to the removal of organic components in the pores. A material without any F-CS (0CS-SG) also showed a high surface area before it was calcined. An observed decrease in surface area for calcined materials confirms the removal of organic components. Calcined F-CSs without any loaded TiO_2 had a surface area of 10 m^2/g. In general, for the calcined composite materials, it can be observed that the introduction of TiO_2 onto F-CS resulted in an increase in the surface area.

A low TiO_2 loading ratio on F-CS (1CS-1SG) showed no improvement in surface area. This may be due to the amount of F-CS dominating that of TiO_2 at low TiO_2 loadings as seen by TEM (Fig. 4.6 (a)). High surface area measurements of 80 and 85 m^2/g were achieved with composites of 1CS-5SG and 1CS-10SG, respectively. When the TiO_2 to F-CS ratio was increased further (i.e. 1CS-25SG and 1CS-50SG), the surface area decreased to 51 and 49 m^2/g, respectively. These surface areas were similar to the surface area of 0CS-SG (51 m^2/g). The observed decrease in total surface area at high TiO_2 ratios in the composite materials (1CS-25SG and 1CS-50SG), to a value close to the total surface area similar to that of 0CS-SG may be due to the amount TiO_2 dominating that of F-CS. The observed maximum surface areas for 1CS-5SG and 1CS-10SG, suggests that an interaction between CS and TiO_2 at ratios of 1:5 and 1:10 for CS to TiO_2 leads to the formation of a material in which the TiO_2 bridges the CSs; the actual pore volume is very similar to that of the 1CS-2.5SG and 1CS-25SG materials and so is not due to changes in porosity. This phenomenon may also be caused by the separation of TiO_2 crystalline particles due to the introduction of CSs.

Figure 4.21 shows the nitrogen adsorption-desorption isotherm and BJH pore size distribution curve (*inset*) of F-CS. The F-CS sample exhibits a Type IV adsorption isotherm with a H3-type hysteresis loop, indicating a microporous solid [51]. The narrow pore size distribution curve with average diameter sizes that are less than 0.02 nm imply that the F-CS has very uniform pore channels in the miro-porous

region. The BJH plot shows a very small peak at *ca* 69 nm that may be due to the pores between the CSs, following the removal of the oily layer (PAHs) that was formed during the CS preparation (see discussion in Chapter 3).

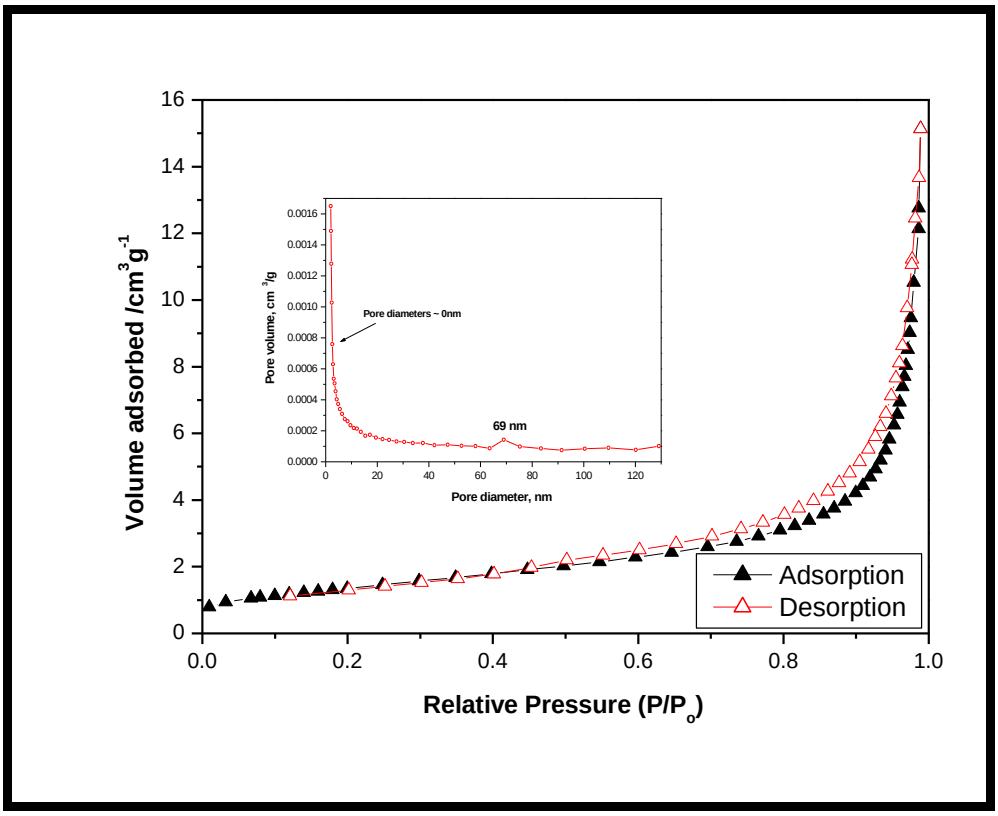


Figure 4.21 Nitrogen adsorption-desorption isotherm and its BJH pore size distribution curve (*inset*) of F-CS

Fig 4.22 shows a comparison between the nitrogen adsorption-desorption isotherms of calcined (350 °C) P25 TiO_2, uncalcined 0CS-SG, and calcined 0CS-SG (at 350 and 400 °C).

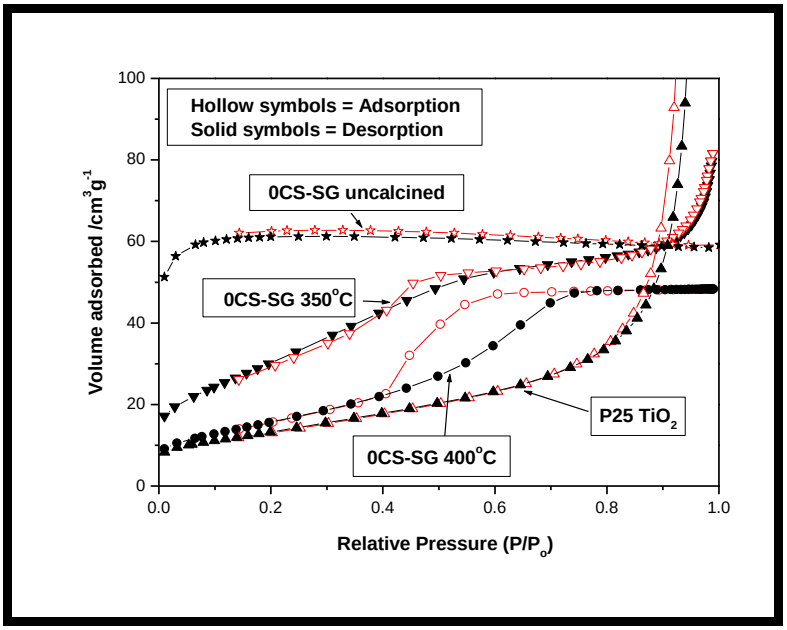


Figure 4.22 Nitrogen adsorption-desorption isotherms of calcined (350 °C) P25 TiO_2, uncalcined 0CS-SG, and calcined 0CS-SG (at 350 and 400 °C)

The adsorption pattern for uncalcined 0CS-SG followed a Type I adsorption isotherm, which indicates that the pore structure is microporous in nature [62, 63]. Calcination of this material at 300 and 400 °C respectively changed the pattern from Type I into Type IV, similar to that of a commercial, P25 TiO_2, indicating the presence of mesopores. However, differences can still be clearly distinguished by the shape and location of the hysteresis loops. The loop obtained for a composite calcined at 350 °C is small and occurs in the relative pressure range between 0.42-0.62. The loop of a composite calcined at 400 °C is larger and occurs in the relative pressure range of between 0.4-0.75, while that of calcined P25 TiO_2 occurs between 0.8 and 1. The composites calcined either at 350 or at 400 °C possess the H1-type hysteresis loop [13, 14]. More pores were noted for the sample calcined at 400 °C and fewer pores were noted for the sample calcined at 350 °C. This correlation ties in with TGA data.

Fig. 4.23 shows a comparison between the nitrogen adsorption-desorption isotherms of calcined composites, viz. 1CS-1SG, 1CS-2.5SG, 1CS-10SG and 1CS-25SG. Their corresponding pore size distribution plots are shown in Fig.

4.24. All the isotherms shown can be classified as type IV, indicating the presence of mesopores in the composite matrix. However, their differences can be clearly distinguished by the pore size distribution as depicted in Fig. 4.24. The CS-TiO_2 composites with low TiO_2 loadings, viz. 1CS-1SG and 1CS-2.5SG had narrow pore diameter distributions, viz. 32 and 26 nm, respectively. A pore diameter distribution observed for CSs without any loaded TiO_2 (F-CS) was observed at < 0.2 nm and 69 nm.

Composites with high TiO_2 loading ratios, viz. 1CS-10SG and 1CS-25SG showed a broad range and a bimodal pore size distribution. 1CS-10SG had pores with a size of 2 nm and pores with a size that ranged between 70 - 190 nm, while 1CS-25SG contained a bimodal pore size distribution, viz. pores with 34 and 872 nm diameters. The observed broad and bimodal pore size range in composites with high TiO_2 ratios may have been caused by high alkoxide (organic components) volumes that were used in their preparation. The removal of these organic components (during calcination), may have created larger pores.

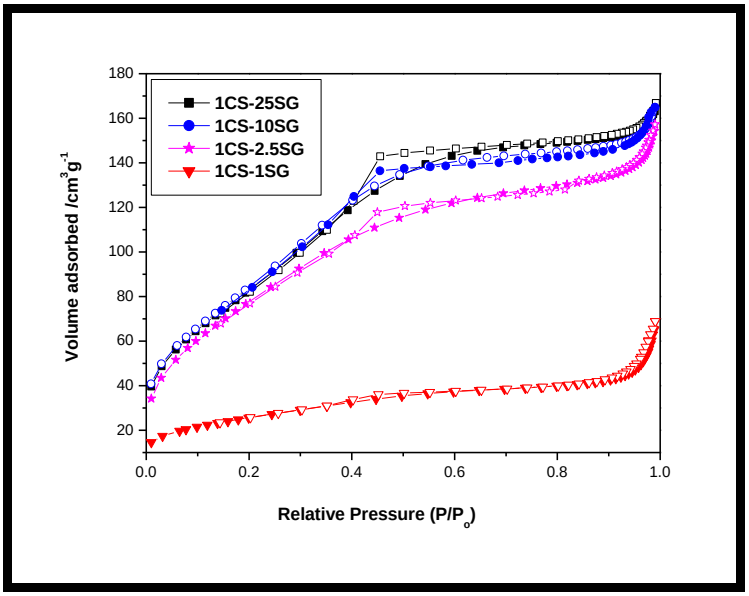


Figure 4.23 Nitrogen adsorption-desorption isotherms of 1CS-1SG, 1CS-2.5SG, 1CS-10SG, and 1CS-25SG

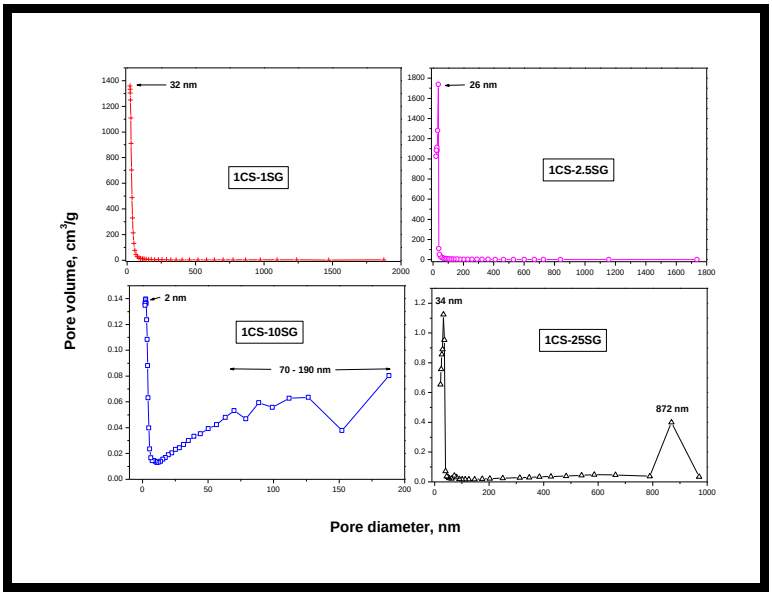


Figure 4.24 BJH pore size distributions (calculated from the adsorption arms of N_2 isotherms) of 1CS-1SG, 1CS-2.5SG, 1CS-10SG, and 1CS-25SG

Loading of TiO_2 on F-CSs may have blocked some of the pores, giving a reduced pore distribution for the composites. A composite with slightly higher TiO_2 loading (1CS-2.5SG), had smaller pore diameters (26 nm), possibly because some of the pores may have been blocked by TiO_2 particles.

4.3.2 Surfactant wrapping

The preparation of CS-TiO_2 composite materials using the surfactant wrapping sol-gel method was achieved by mixing 1 g of functionalized carbon spheres (F-CSs) or pristine carbon spheres (P-CSs) with 70 mL of CTAB. After sonication, the dispersed CSs were diluted with 2-BuOH to make a solution called Solution I. A predetermined amount of $Ti[O(CH_2)_3CH_3]_4$ was mixed with 2-BuOH and glacial acetic acid to form Solution II. Solution II was then added dropwise over 1 h into Solution I under vigorous stirring. To hydrolyse the residual precursor, 0.1 M NH_3 solution was added dropwise until a pH value of 9 was reached. This led to a uniform TiO_2 coating on the CSs surface. The product was aged. After appropriate washing the final gel was dried in an oven overnight to obtain a powder product. After cooling, the crushed powder product was re-dispersed in 2-

butanol and the sol-gel coating step was repeated. This was repeated a second and third time in order to obtain a homogeneous coating of TiO_2 on the CS surface. After the three sol-gel coating cycles, the materials were crushed into a fine powder and then calcined under a flow of nitrogen. The calcined and the uncalcined composite materials were characterised by traditional characterisation methods to provide an understanding of their physico-chemical properties.

4.3.2.1 TEM

TEM images of calcined 1CS-10TiO_2 composites that were prepared by a surfactant wrapping sol-gel method are shown in Fig. 4.25. Three different preparation methods were employed in achieving these composite materials (see section 4.2.1.2 and Table 4.1 for a full discussion). The images shown in Fig. 4.25 are of composites: (a) A1, (b) A3, (c) SW1, (d) SW3, (e) ASW1 and (f) ASW3, where A refers to acid treated but not surfactant wrapped CSs; SW refers to surfactant wrapped, but not acid treated CSs; and ASW refers to acid treated and surfactant (CTAB) wrapped CSs. For detailed acid treatment procedures see Chapter 3. The numbers 1 and 3 (in the acronyms) refer to the number of sol-gel coating cycles that were employed during the composite preparation (see scheme in Fig. 4.3). It can clearly be seen that some surfaces of F-CS in A1 were not homogeneously covered by TiO_2, even when the sol-gel cycles where repeated three times (A3). SW1 and SW3 (see Fig. 4.25 (c) and Fig. 4.25 (d), respectively) composites show a more homogeneous TiO_2 distribution compared to their A1 and A3 counterparts. This observation suggests that dispersing CSs in CTAB improved dispersability of CSs compared to CSs treated by HNO_3. In all instances it appears that TiO_2 particles prefer to form aggregates by themselves rather than covering the CS surface. TEM images of ASW1 and ASW3 showed that the TiO_2 homogeneously coated the CSs. An image of the SW3 (involving 3 sol-gel cycles in Fig. 4.25 (f)) showed that the surfaces of F-CS were homogeneously coated with TiO_2 while some excess TiO_2 particles appeared next to the composite. The average TiO_2 grain size covering the CSs was 8.1 nm (Fig. 4.26). This size was

similar to the TiO_2 made in a composite sample that was prepared by a conventional sol-gel method (8.4 nm).

Comparing TEM images of SW1 and SW3 with their ASW1 and ASW3 counterparts shows that the best TiO_2 coating was achieved when CSs were initially functionalised (17 h), and then dispersed in CTAB (1 h) before sol-gel coating cycles. This observation suggests that the wetting properties of CSs were enhanced by both the introduction of the functional groups (COOH and OH groups) and by dispersing them in a surfactant (CTAB).

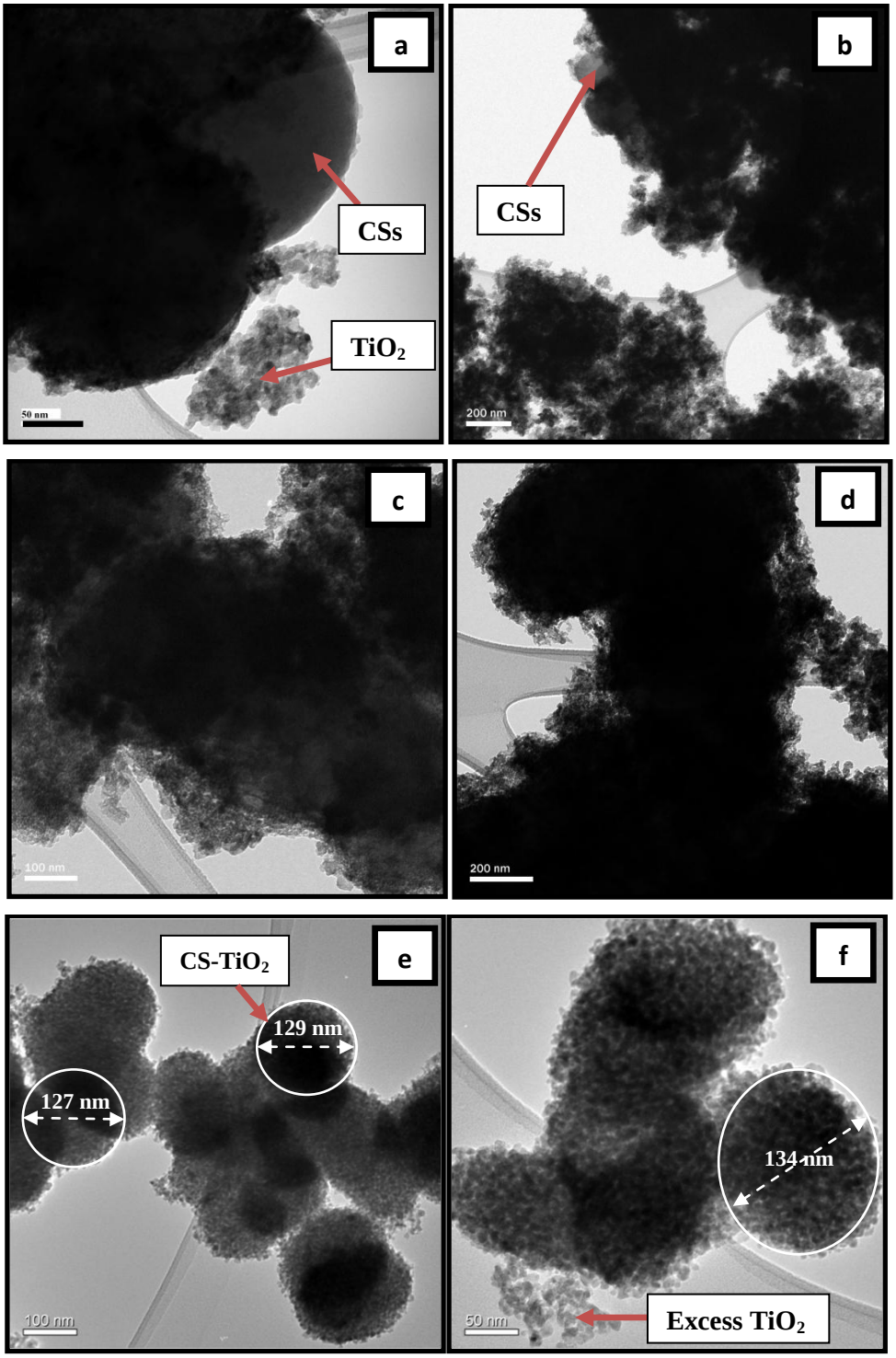


Figure 4.25 TEM images of CS-TiO_2 composites prepared by a surfactant wrapping sol-gel method, for: (a) A1, (b) A3, (c) SW1, (d) SW3, (e) ASW1 and (f) ASW3, where (A = acid treated but not surfactant wrapped CSs, SW1 = surfactant wrapped, but not acid treated CSs, ASW = acid treated and surfactant wrapped CSs). 1 and 3 represents the number sol-gel coating cycles

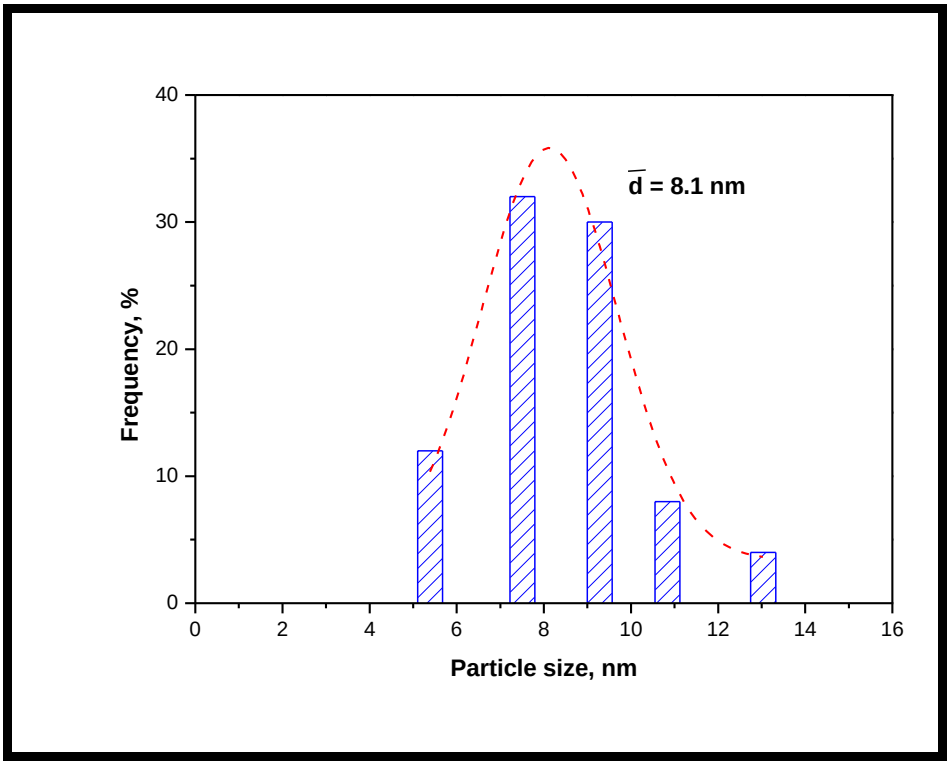


Figure 4.26 Particle size distribution of TiO_2 in ASW3 (solid line = particle size distribution histogram, and dashed line = Gaussian distribution) prepared by a surfactant wrapping sol-gel method

In order to further confirm the presence of CSs and TiO_2 in the CS-TiO_2 composites prepared by the surfactant wrapping sol-gel method, an EDX analysis was conducted. In Fig. 4.27 The EDX spectrum of an ASW1 composite sample (in Fig. 4.25 (e)) is shown. This EDX spectrum confirms the existence of C, Ti and O atoms. The Cu signal corresponds to the Cu grid substrate used for the TEM analysis.

After successfully synthesizing a CS-TiO_2 composite material with TiO_2 homogeneously covering the surface of CSs (by the use of a surfactant wrapping sol-gel method i.e. ASW), a combustion study on this new composite material was carried out. This study was conducted in order to remove the CSs in the composite so that only TiO_2 material would remain and its characteristic properties could then be investigated. The ASW3 composite sample was annealed

under a flow of air (6 h and 5 bar) in a stainless steel reactor (see Chapter 2 for details) at two different temperatures namely, 300 °C and 400 °C, respectively.

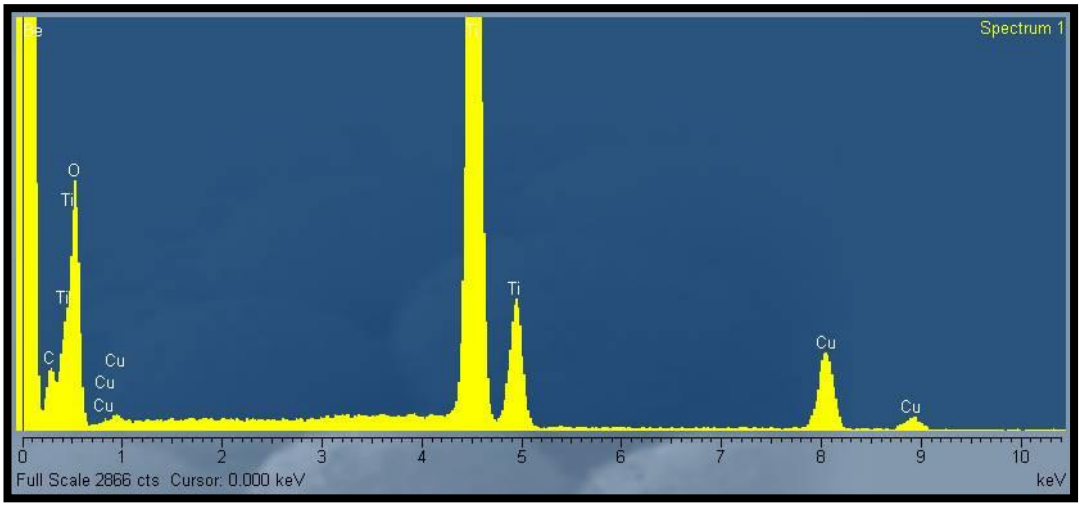


Figure 4.27 EDX spectrum corresponding to the F-CS surface coverage by TiO_2 shown in Fig. 4.25 (f). C and Ti were detected; the Cu signal corresponds to the Cu grid substrate used for TEM analysis.

The physical appearance and colour (viewed with the naked eye) of the residue TiO_2 samples obtained was different. The residue obtained from annealing the composite at 300 °C was grey, suggesting that the presence of traces of CSs, while the residue obtained from annealing in air at 400 °C was pure white. The morphology of the TiO_2 residue obtained after CS combustion of ASW3 is depicted in Fig. 4.28. It can be clearly seen that for both conditions used to combust CSs, there is an absence of CSs. Fig. 4.29 is the EDX spectrum of the residue TiO_2 obtained after annealing the ASW3 composite at 400 °C (Fig. 4.28). The spectrum confirms the absence of carbon in the residue since it only revealed the existence of Ti and O atoms in the sample. (The Cu signal is due to the Cu grid).

Interestingly the TiO_2 particle size distribution obtained from the residue was not the same as pure TiO_2 as in Fig. 4.4. Large particles (about 15-60 nm) were observed from the residue sample obtained after ASW3 was annealed at 400 °C,

while TiO_2 particles with an average size of about 9 nm were observed from residue sample annealed at 300 °C. This observation suggests that combustion of CSs was successful; however, combusting the composite in air at 400 °C and 5 bar for 6 h has caused the small TiO_2 particles to coalesce and form larger TiO_2 particles. Both these materials were further investigated by XRD and Raman spectroscopy (see section 4.3.2.2 and 4.2.2.3 below).

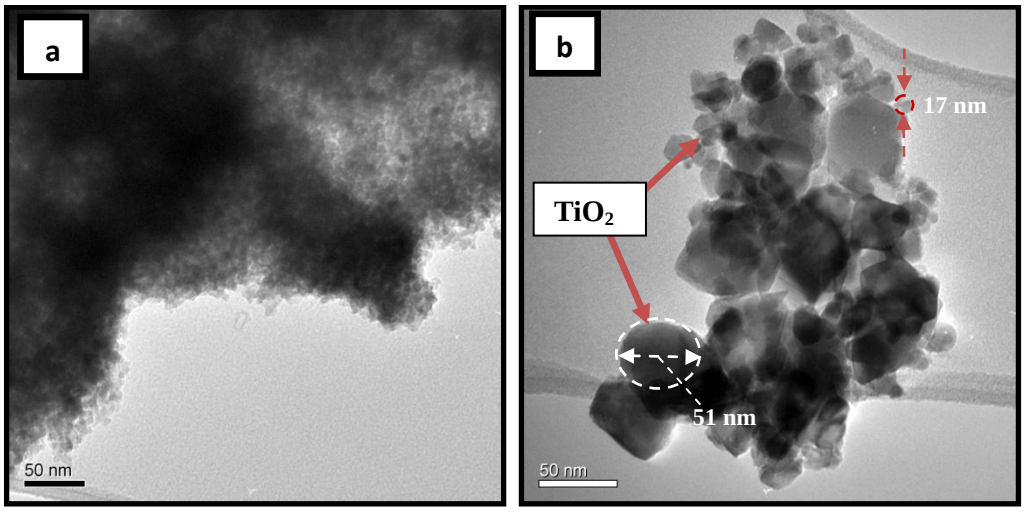


Figure 4.28 TEM images of TiO_2 residue from combusted ASW3 composite. Samples were combusted in air at 5 bar for 6h at: (a) 300 °C and, (b) 400 °C

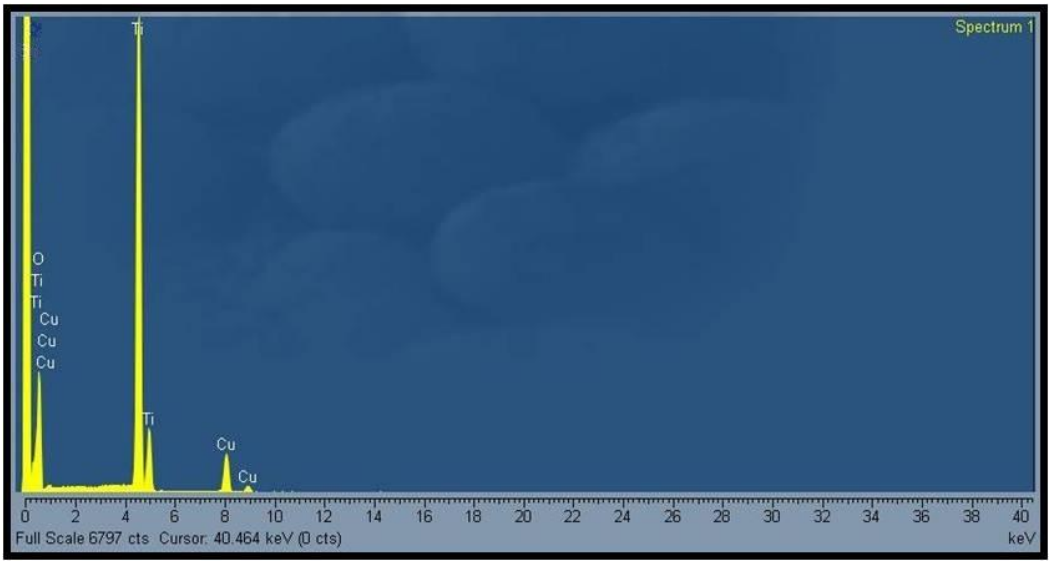


Figure 4.29 EDX spectrum of TiO_2 residue corresponding to sample (b) in Fig. 4.28

4.3.2.2 XRD

The XRD patterns of the TiO_2 residue from combusted ASW3 composite samples (300 and at 400 °C, respectively) are shown in Fig. 4.30. The XRD pattern for the F-CS is depicted in the *inset* of Fig 4.30.

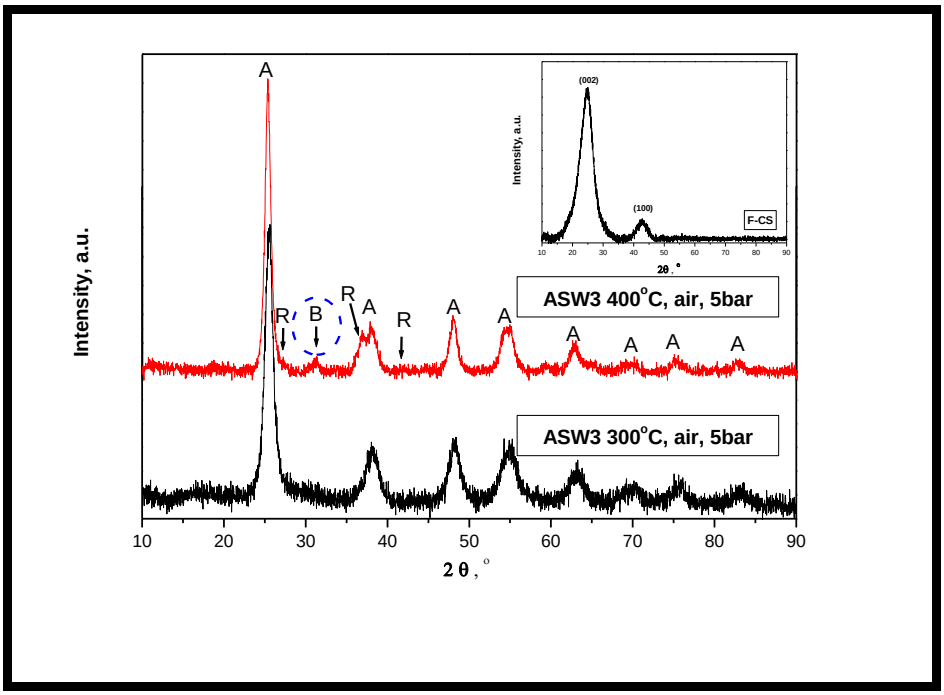


Figure 4.30 XRD patterns of TiO_2 residues from combusted ASW3 composite material where A = anatase phase, B = brookite and R = rutile phase. Samples were combusted in air at 5 bar for 6h at: 300 °C and at 400 °C, respectively. XRD pattern of the F-CS is shown on the *inset.*

No F-CS peaks were observed from either combusted TiO_2 sample. The average grain size was measured to be about 9.6 and 13.4 nm for TiO_2 residue of ASW3 combusted at 300 and at 400 °C, respectively. The TiO_2 residue pattern of the sample calcined at 400 °C showed a combination of anatase and rutile phases. The rutile count is much lower than typically found in commercial titanias (P25 Degussa). This sample (calcined at 400 °C) showed another peak at about 30.7 2θ ° which was absent in the XRD pattern of ASW3 sample combusted at 300 °C. This peak was found to match with a brookite phase [7].

4.3.2.3 Raman spectroscopy

The Raman spectra (Fig. 4.31) of the TiO_2 residue from combusted (at 300 and at 400 °C, respectively) ASW3 composite samples were compared with that of non-combusted ASW3 (shown on the *inset* of Fig 4.31).

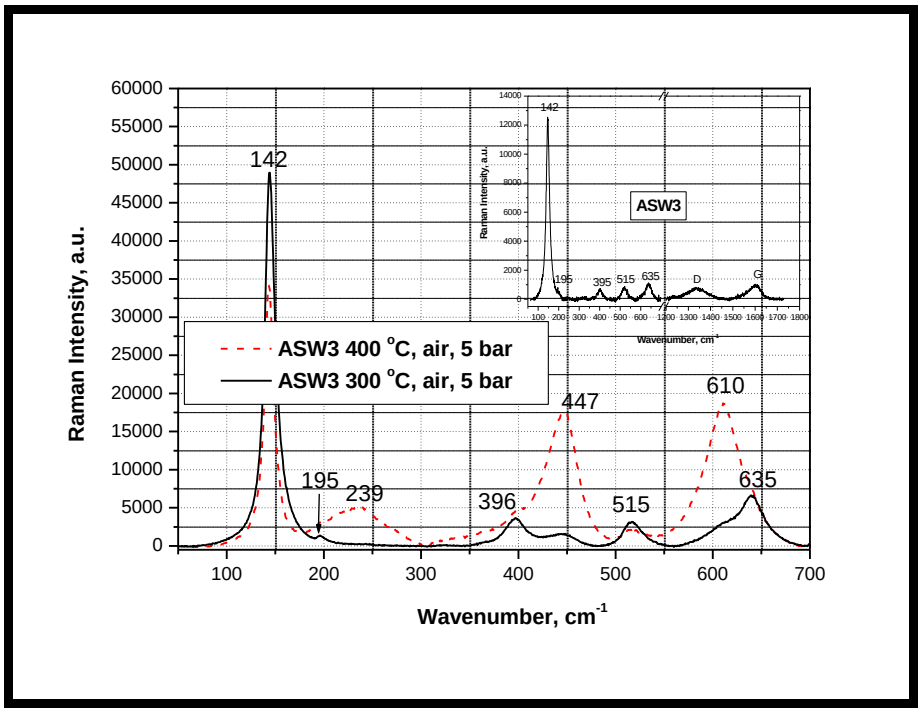


Figure 4.31 Raman spectra of of TiO_2 residue from combusted ASW3 composite sample. Samples were combusted in air at 5 bar for 6h at: (a) 300 °C and, (b) 400 °C. Raman spectra of bulk uncombusted ASW3 is shown on the *inset*.

The spectrum of ASW3 shows the presence of five bands, viz. at 142, 195, 395, 515 and 635 cm^{-1} between 100 and 700 cm^{-1}. In the literature, these bands are said to be representative of the E_g vibrational modes of the anatase phase of TiO_2 [64, 65]. The presence of carbon bands, D and G bands, were also observed in the spectrum of ASW3 between 1300 and 1600 cm^{-1} (see insert to Fig. 4.31). All the Raman bands that are representative of anatase and that were observed in the uncombusted sample of ASW3 were also observed in the TiO_2 residue sample (300 °C calcination). All the bands that were observed in the spectrum of the

sample that was combusted at 300 °C can clearly be seen, but the intensity of these bands was low. No F-CS (D and G) bands were observed in this sample (TiO_2 residue annealed at 300 °C). This suggests that CSs were successfully combusted.

The Raman spectrum of the ASW3 composite sample TiO_2 residue (combusted at 400 °C) is different to that of the composite combusted at 300 °C. The spectrum shows the presence of three bands; at 239, 447 and 610 cm^{-1}. The intensity of these bands was higher than that observed for the anatase phase. In the literature, these bands (with high intensity) are said to be representative of rutile phase of TiO_2 [56]. The increased particle size distribution observed in TEM could also be indicative of formation of a rutile phase.

4.3.2.4 TGA

Thermal stability/instability studies (in an air environment) of samples of CSs coated with TiO_2 via the surfactant wrapping sol-gel method was determined for all uncalcined TiO_2-CS composites prepared by different methods (as explained in section 4.2.1.2 and Table 4.1). TGA and DTG profiles for all these samples are shown in Figures 4.32-4.34. A summary of the results obtained from these studies is tabulated in Table 4.5.

In the low temperature region, all samples showed a weight loss due to moisture at temperatures between 30 and 196 °C. The lowest moisture loss of 8% was measured on sample ASW1, while the highest loss (16%) occurred for sample A3. For all these samples moisture was lost in one step since all the DTG curves showed one broad peak ranging between 30 and 196 °C. Another weight loss peak (192-441 °C), in the low temperature region, was observed for the samples. This weight loss was due to organic components (alkoxides, butoxides) and ammonia; and occurred in two steps (similar to Fig. 4.8). The DTG curves showed two peaks between 192-441 °C.

The total percentage weight loss varied between 9 and 12%. The weight loss trend observed in the low temperature range was similar for all the composites; however, a DTG curve of sample SW3 showed a peak at about 460 °C which was absent in the DTG curves of other composites. No explanation for the presence of a peak at 460 °C observed in DTG of SW3 can be given.

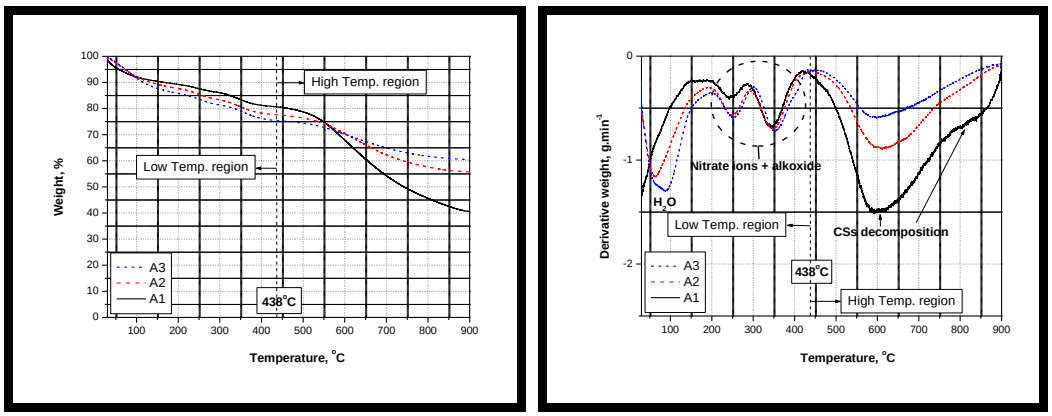


Figure 4.32 TGA (*left*) and DTG (*right*) of uncalcined A1, A2 and A3

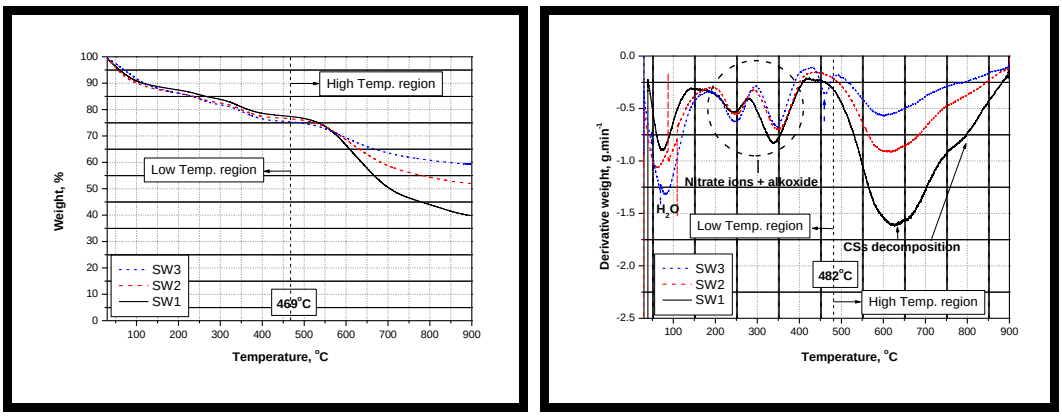


Figure 4.33 TGA (*left*) and DTG (*right*) of uncalcined SW1, SW2 and SW3

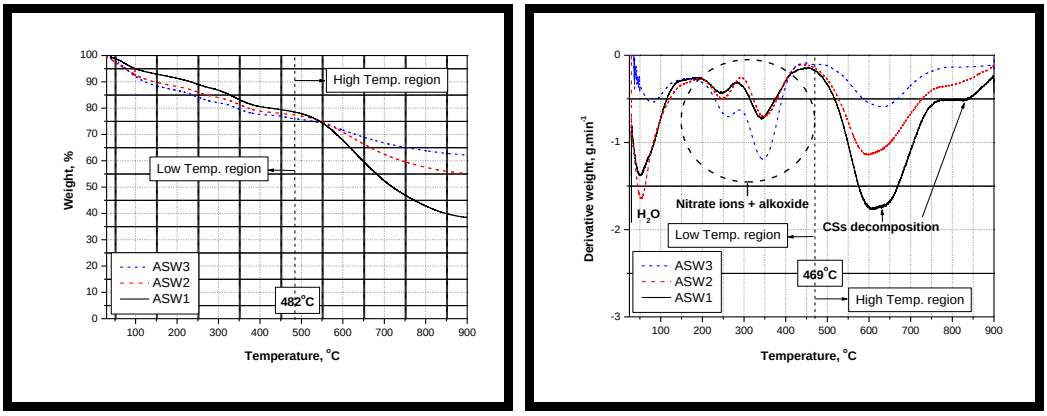


Figure 4.34TGA (*left*) and DTG (*right*) of uncalcined ASW1, ASW2 and ASW3

Table 4.5 Total percentage weight loss and temperature weight loss range as estimated by TGA for uncalcined CS-TiO_2 composite materials of A1, A2, A3, SW1, SW2, SW3, ASW1, ASW2 and ASW3

	Low Temperature region		**High temperature region**	
Sample	*Temperature range/ °C*	*Weight loss/%*	*Temperature range/ °C*	*Weight loss/%*
A1	<30 - 160	10	432 - 896	40
	202 - 421	9.1		
A2	33 - 196	14	448 - 885	21.7
	198 - 425	9.1		
A3	33 - 200	16	454 - 878	20.7
	202 - 441	11		
SW1	30 - 160	12	465 - 898	37.9
	194 - 434	9.5		
SW2	30 - 162	13	463 - 891	24.9
	194 - 434	9.6		
SW3	30 - 160	12	463 - 862	15.1
	194 - 434	11		
ASW1	40 - 165	8	488 - 876	39.2
	192 - 433	11.3		
ASW2	41 - 166	11	482 - 881	21.7
	192 - 433	9.8		
ASW3	41 - 167	13	480 - 892	16.5
	192 - 433	9.2	437 - 497	1.8

In the high temperature region of all composite samples, a weight loss due to the oxidation of CSs was observed. The observed weight loses in the high temperature region occured at temperatures between 438 and 900 °C for composites A1, A2 and A3; between 482 and 900 °C for composites SW1, SW2 and SW3; and between 469 and 900 ° for composites ASW1, ASW2 and ASW3. As expected, the weight loss due to decomposition of CSs decreased with an increase in TiO_2 loading.

The DTG plots (Fig. 4.32-4.34) of all the composites prepared from one sol-gel cycle (A1, SW1 and ASW1) depicts that the oxidation of CSs occurred at two different temperatures; a lower and a higher temperature. The observed

temperature maxima occurred at about 600 and 850 °C, respectively for A1; at about 640 and 800 °C, respectively for SW1; and at about 620 and 840 °C, respectively for ASW1. A large peak observed at higher temperature (about 800 °C) in all composites may be due to the oxidation of CSs which were not successfully coated with TiO_2. The lower temperature (about 600 °C) peak for the decomposition of CSs in the high temperature region of the TGA could be from CSs that were successfully coated with TiO_2. It is possible that the TiO_2 may catalyze the decomposition of CSs in air. This observation is similar to that observed for composites prepared by conventional sol-gel method, even though two lower temperature peaks were observed. A disappearance of this higher temperature peak was observed in all composites as the number of sol-gel cycles was increased (i.e. sol-gel repeated twice or three times). This suggests that a homogenous coating of TiO_2 on the CS surface was achieved by a surfactant wrapping method. It can be clearly seen that the shoulder observed on the high temperature (800 °C) peak for ASW2 is smaller than that observed for A2 and SW2. The DTG profile of ASW3 shows a complete disappearance of the high temperature peak. This suggests that CSs were homogeneously coated with TiO_2. This result correlates well with TEM results.

4.3.2.5 Porosity measurements

In Table 4.6, the BET total surface area and porosity values of uncalcined and calcined (350 °C) CS-TiO_2 composites materials that were prepared by a surfactant wrapping method; viz. A1, A2, A3, SW1, SW2, SW3, ASW1, ASW2 and ASW3 are shown. As can be seen, the total surface areas of all uncalcined composites are higher than their calcined counterparts. This behaviour is similar to the composite materials prepared by the conventional sol-gel method. The pore volumes of the calcined materials are larger than their uncalcined counterparts. This observed decrease in surface area and an increase in pore volume was expected because TGA studies (in air) of these uncalcined materials confirmed the presence of organic components (Fig 4.32-4.34). These components may be responsible for the high surface area values in the composites, while the increase

in total pore volumes may be due to the removal of organic components in the pores.

Table 4.6 BET total surface area and porosity measurements for uncalcined and calcined CS-TiO_2 composite materials of A1, A2, A3, SW1, SW2, SW3, ASW1, ASW2 and ASW3

	Before Calcination			**After Calcination (350 °C in air, 1 bar, 5h)**		
Sample	S_{BET}[a] (m^2/g)	P_v[b] (cm^3/g)	P_D[c] (nm)	S_{BET}[a] (m^2/g)	P_v[b] (cm^3/g)	P_D[c] (nm)
A1	155	0.188	4.8	81	0.156	8.1
A2	246	0.384	6.2	59	0.147	8.2
A3	275	0.305	4.7	54	0.176	8.5
SW1	204	0.251	4.9	83	0.211	9.2
SW2	252	0.302	4.8	68	0.306	12.6
SW3	300	0.381	5.1	62	0.307	12.3
ASW1	188	0.193	4.1	87	0.314	9.7
ASW2	194	0.281	5.8	90	0.418	14.6
ASW3	239	0.224	3.8	98	0.422	14.3

[a]Surface area, [b]P_v = pore volume, [c]P_D = pore diameter

The calcined CS-TiO_2 composite materials that were prepared by surfactant wrapping method 1, i.e. CSs were functionalised for 17 h (and not dispersed in CTAB) followed by a sol-gel coating (A1, A2 and A3), show a decrease in total surface area from 81 to 59 and 54 m^2/g as the number of sol-gel cycles were increased from 1 to more cycles (2 and 3), respectively. This observed decrease in total surface area may be due to an increase in the amount of TiO_2 dominating that of CSs. A similar observation was noticed for SW1, SW2 and SW3. Here the total surface areas observed decreased from 83 to 68 and 62 m^2/g, respectively with increasing coating cycles. The observed total surface areas for composite samples SW1, SW2 and SW3 are higher than their A1, A2 and A3 counterparts. This

suggests that the SW1, SW2 and SW3 composite materials consisted of a more homogeneous TiO_2 coated CS than the A1, A2 and A3 composites. This observation ties in well with TEM studies (Fig. 4.25).

In contrast to A1, A2, A3, SW1, SW2 and SW3, the calcined CS-TiO_2 composite materials that were prepared by method 3, i.e. CSs were initially functionalised for 17 h in HNO_3 followed by dispersion in CTAB for 1 h and then sol-gel coating (ASW1, ASW2 and ASW3), shows an increase in total surface area from 87 to 90 and 98 m^2/g as the number of sol-gel cycles was increased from 1 to 2 to 3 cycles. This observed increase in total surface area as the number of sol-gel cycles was increased may be due to the creation of a homogeneous TiO_2 coating on the CS surface as can be viewed in TEM 4.24 (e and f). This phenomenon may also be caused by the separation of TiO_2 crystalline particles due to the introduction of CSs, and consequently formation of a bridged layer between TiO_2 and CSs. A similar trend was observed by Li *et al*. in the TiO_2 coating of MWCNT [66]. Unlike in other surfactant wrapping methods (1 and 2), an increase in the amount of TiO_2 on the CSs for composites synthesized by method 3 created porous channels between TiO_2 and CS which may be responsible for an increase in the total surface area.

Fig 4.35 shows a comparison between the nitrogen adsorption-desorption isotherms of uncombusted ASW3 that was calcined in N_2 (350 °C, 1 bar for 6 h) and the TiO_2 residue sample from ASW3 combusted in air (400 °C, 5 bar for 6h) (Fig. 4.27(b)). The adsorption pattern for both samples followed a Type IV isotherm with a hysteresis loop (H2-type) due to capillary condensation, indicating the presence of mesopores or materials with a cross-linked porous system [63, 67]. These observations suggest that both the combusted and the uncombusted ASW3 materials contained mesopore [67]. However, differences can be clearly distinguished by the amount of nitrogen uptake (multilayer coverage), i.e. 10.7 and 15.4 cm^3/g for combusted ASW3 and uncombusted ASW3 samples, respectively. This implies that the surface area for the uncombusted ASW3 is more than that of the combusted ASW3 since more

nitrogen atoms were adsorbed on the surface to form a multilayer coverage than in the case of combusted ASW3 [51].

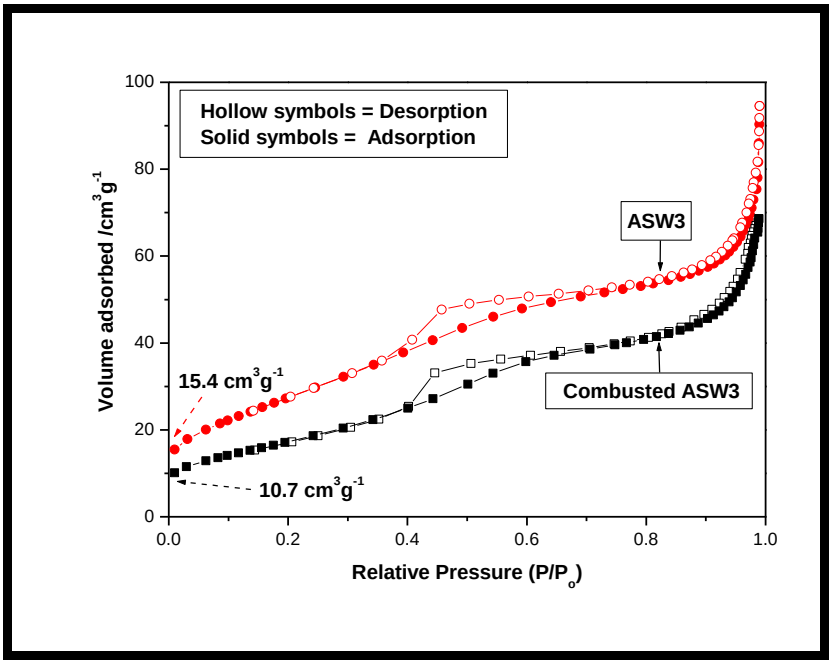


Figure 4.35 Nitrogen adsorption-desorption isotherms of uncombusted ASW3 composite, calcined in air (300 °C, 6 h, 1 bar) and TiO_2 residue from combusted ASW3 at 400 °C in air 6h 5 bar

4.3.3 Carbon coated titania materials

Carbon coated titania materials (C-TiO_2) were prepared using a horizontally positioned chemical vapour deposition (CVD) reactor. A synthesized TiO_2 material (using a conventional sol-gel method), defined hereby as C0-TiO_2, was used as template (support) to be covered with carbon generated via pyrolysis of acetylene using a CVD method. Briefly, 0.2 g sample of TiO_2 was placed in a quartz boat and acetylene (900 °C) was introduced in the reactor. This gas was allowed to pass through the reactor for different times, namely 5, 15, 20, 30, 45, 120 and 240 minutes, and the resulting materials were defined as C5-TiO_2, C10-TiO_2, C20-TiO_2, C30-TiO_2, C45-TiO_2, C60-TiO_2, C120-TiO_2 and C240-

TiO_2, respectively. After cooling, the soot was collected and characterized using TEM and BET procedures.

4.3.3.1 TEM

TEM images of TiO_2 (prepared by a conventional sol-gel method), C0-TiO_2 and the carbon coated TiO_2 materials (C-TiO_2) prepared at different durations, viz. C5-TiO_2, C30-TiO_2, C60-TiO_2, C120-TiO_2 and C240-TiO_2 are shown in Figure 4.36. The images reveal that the formed carbon had a spherical morphology, similar to the prepared CSs discussed in Chapter 2. The size of these spheres was dependent on the duration that the TiO_2 remained in the reactor, during the preparation of carbon coated TiO_2 materials. It can be clearly seen that TiO_2 was poorly covered by the carbon spheres. The images reveal that the CSs were positioned away from TiO_2 agglomerates. As the period of acetylene flow in the reactor was increased, the amount of CSs produced was increased, however these CSs did not coat the TiO_2 particles. Very large (approximately 500 nm) CSs were produced by the long acetylene flow durations (Fig. 4.36 (e and f)).

4.3.3.2 Porosity measurements

Table 4.7 presents the BET total surface area and porosity values of C0-TiO_2, C5-TiO_2, C10-TiO_2, C20-TiO_2, C30-TiO_2, C45-TiO_2, C60-TiO_2, C120-TiO_2 and C240-TiO_2. As can be seen, the total surface areas of the carbon coated titania materials are lower than that of TiO_2 prepared by a conventional sol-gel method (C0-TiO_2). However, the total pore diameters presented in Table 4.6 for the carbon coated titania materials are higher than that observed for C0-TiO_2. This drop in surface area may imply that the measured surface area is due to formation of the rutile and/or brookite TiO_2 phase.

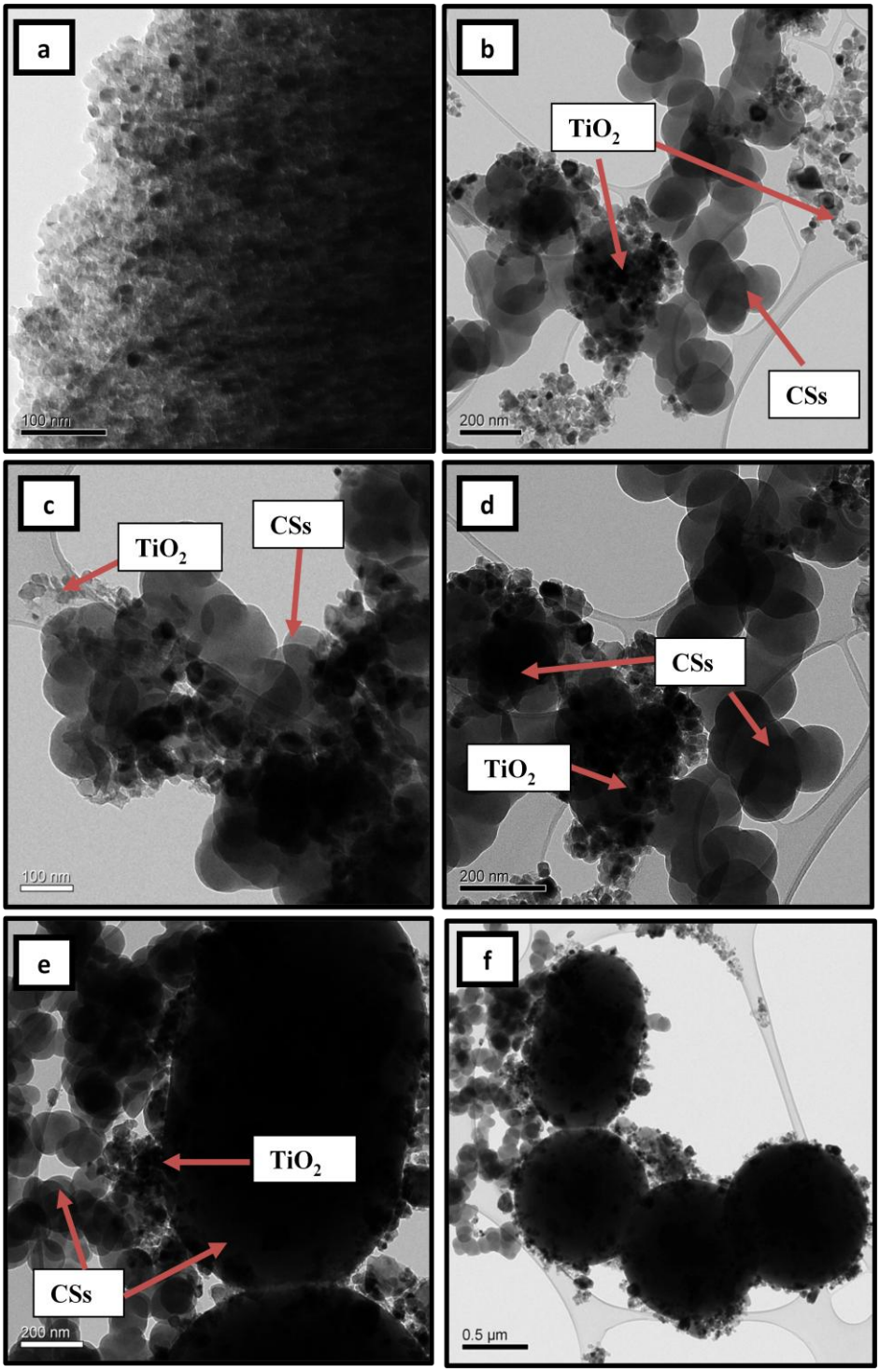


Figure 4.36 TEM images of carbon coated titania materials (C-TiO_2) prepared by CVD: (a) C0-TiO_2, (b) C5-TiO_2, (c) C30-TiO_2, (d) C60-TiO_2, (e) C120-TiO_2 and (f) C240-TiO_2

It is known that the anatase transition to rutile and brookite is stable and occurs at high temperatures [66]. The surface areas of rutile are known to be lower than that of anatase [7, 11, 23 and 66]. An increase in pore diameter suggests that there is a formation of some porosity between the prepared CSs and TiO_2. Even though the porosity improved, the surface area became smaller because the amount of rutile and/or brookite TiO_2 dominates that of the CSs and therefore overrides the improved porosity.

Table 4.7 BET total surface area and porosity measurements for C5-TiO_2, C10-TiO_2, C20-TiO_2, C30-TiO_2, C45-TiO_2, C60-TiO_2, C120-TiO_2 and C240-TiO_2

Sample	S_{BET}[a] **(m^2/g)**	P_v[b] **(cm^3/g)**	P_D[c] **(nm)**
C0-TiO_2	51	0.135	5.8
C5-TiO_2	9.1	0.085	42.7
C15-TiO_2	8.0	0.027	47.8
C20-TiO_2	5.0	0.079	34.9
C30-TiO_2	4.1	0.018	38.8
C45-TiO_2	4.1	0.041	40.4
C60-TiO_2	2.4	0.019	48.2
C120-TiO_2	2.5	0.031	49.7
C240-TiO_2	0.6	0.002	52.3

[a]Surface area, [b]P_v = pore volume, [c]P_D = pore diameter

4.4 Conclusion

The interactions between CSs and TiO_2 were successfully studied by the synthesis of CS-TiO_2 composites using two different sol-gel methods, namely the conventional sol-gel and the surfactant wrapping sol-gel method. The carbon coated method was also carried out to investigate the interactions between CSs and TiO_2.

The traditional sol-gel method was successfully used to prepare CS-TiO_2 composites with different ratios viz. 1CS-1SG, 1CS-2.5SG, 1CS-5SG, 1CS-10SG, 1CS-25SG and 1CS-50SG. The average grain size of TiO_2 was 8.4 nm and with both anatase and rutile phases. These composites showed weak interactions between CSs and TiO_2 even at high TiO_2 loading ratio. Interestingly the surface area of these composites showed high values of 80 and 85 m^2/g for 1CS-5SG and 1CS-10SG, respectively. At lower TiO_2 ratios the measured surface area was similar to that of CSs, i.e 10 m^2/g for 1CS-1TiO_2. At high TiO_2 ratios the measured surface area was similar to that of TiO_2, i.e 49 m^2/g for 1CS-50TiO_2.

The surfactant wrapping method involved preparation of CS-TiO_2 composites using three different preparation methods, i.e. A, SW and ASW. TEM images of ASW methods showed achievement of a successful TiO_2 coating of CSs. The TiO_2 grain size was 8.0 nm with both anatase and rutile phases. High surface areas (up to 98 m^2/g) were achieved for the CS-TiO_2 composites prepared method. The high surface areas achieved suggest that the interaction between CSs and TiO_2 was homogeneous and the increase was due to the "bridge" formed between CSs and TiO_2.

The carbon coated titania materials by CVD showed the production of CSs. As the period of acetylene flow in the reactor was increased, the amount of CSs produced was increased; however these CSs did not coat the TiO_2 particles. The total surface areas of the carbon coated titania materials were lower than that of TiO_2 (51 m^2/g) prepared by a conventional sol-gel method (C0-TiO_2). A decrease in surface area may imply that formation of the rutile and/or brookite TiO_2 phase took place.

4.5 References

1. A. Fujishima, K. Honda, Nature 238 (1972) 37
2. B. Oregan, M. Gratzel, Nature 353 (1991) 737
3. S. Ikezawa, Thin Solid Films 386 (2001) 173
4. L. M. Sikhwivhilu, PhD Thesis, University of the Witwatersrand, Johannesburg (2007)
5. R. Sellappan, J. Zhu, H. Fredriksson, R. Martins, M. Zach, D. Chakarov, J. Mol. Catal. A: Chemical 335 (2011), 136
6. U. Diebold, Surface Science Reports 48 (2003) 53
7. M. Rayner, PhD Thesis, University of The Witwatersrand, Johannesburg (2011)
8. M. Langlet, A. Kim, M. Audier, J. Herrmann, J. Sol-Gel Sci Technol 25 (2002) 223
9. G. Dagan, M. Tomkiecz, J. Phys Chem 97 (1993) 12651
10. T. Hashishin, J. Murashita, A. Joyama, Y. Kaneko, J. Ceram Soc Jpn. 106 (1998) 1
11. Y. Xie, C. Yuan, Mater. Res. Bull 39 (2004) 533
12. A. Jitianu, T. Cacciaguerra, R. Benoit, S. Delpeux, F. Beguin, S. Bonnamy, Carbon 42 (2004) 1147
13. W. Wang, P. Serp, P. Kalck, J. Faria, Appl. Catal. B. Environ. 56 (2005) 305
14. B. Gao, G. Chen, G. Puma, Appl. Catal. B: Environmental 89 (2009) 503
15. B. Arkles, MRS Bulletin (May 2001) 402
16. D. Duy, H. Kim, D. Yoon, K. Lee, J. Ha, Y. Hwang, C. Lee, B. Cong, Applied Surface Science 256 (2009) 1065
17. J. Sandler, M. Shaffer, T. Prasse, W. Bauhofer, K. Schulte, A. Windle, Polymer 40 (1999) 5967
18. M. Han, Y. Lee, H. Lee, C. Yun, W. Kim, Chemical Engineering Science 64 (2009) 4649
19. E. Auer, A. Freund, J. Pietsch, T. Tacke, Appl. Catal. 173 (1998) 259

20. Y. Jin, C. Gao, W. Hsu, Y. Zhu, H. Huczko, M. Bystrzejewski, M. Roe, C. Lee, S. Acquah, H. Kroto, D. Walton, Carbon 43 (2005) 1944
21. V. Vignal, A. Morawski, H. Konno, M. Inagaki, J. Mater. Res. 14 (1999) 1102
22. M. Inagaki, V. Vignal, H. Konno, J. Mater. Res. 14 (1999) 3152
23. N. Yu, Y. Chang, J. Nanometer 6 (2008) 834248
24. B. Gao, C. Peng, G. Chen, G. Puma, Appl. Catal. B. Environmental 85 (2008) 17
25. T. Tan, S. Wang, S. Bian, X. Li, Y. An, Z. Liu, Appl. Surf. Scie. 256 (2010) 6932
26. L. Tian, L. Ye, K. Deng, L. Zan, J. Solid State Chem. 184 (2011) 1465
27. R. Leary, A. Westwood, Carbon 49 (2011) 741
28. Z. Nemeth, C. Dieker, A. Kukovecz, D. Alexander, L. Forro, J. Seo, K. Hernadi, Composites Science and Technology 71 (2011) 87
29. J. Sun, L. Gao, M. Iwasa, Chem. Comm. 7 (2004) 832
30. X. Ding, X. Liu, Materials Science and Engineering A224 (1997) , 210
31. K. Woan, G. Pyrgiotakis, W. Sigmund, Adv. Mater 21 (2009) 2233
32. Y. Long, Y. Lu, Y. Huang Y. Peng, Y. Lu. S-Z. Kang, J. Phys Chem C 113 (2009) 13899
33. K. Noworyta and J. Augustynski, Electrochem Solid-State Lett., 7 (2004) E31
34. A. Fujishima, K. Kohayakawa, K. Honda, J. Electrochem Soc, 122 (1975) 1487
35. S. Khan, M. Al-Shahry, W. Ingler, Science 297(2002) 2243
36. A. Pierre, Introduction to sol-gel processing. Boston: Kluwer Academic Publishers (1998)
37. U. Akpan, B. Hameed, Appl Catal A, 375 (2010) 1
38. D. Eder, Chem Rev 110 (2010) 1348
39. K. Woan G. Pyrgiotakis, W. Sigmund, Adv Mater 21(2009) 2233
40. A. Deshmukh, S. Mhlanga, N. Coville, Mater. Scie. Eng. R, 70 (2010), 1
41. A. Nieto-Marquez, R. Romero, A. Romeroa and J. Valverde, J. Mater. Chem., 21(2011) 1664

42. J-B. Donnet (Ed.), Carbon Black, CRC Press; 2 edition (1993)
43. N. Coville, S. Mhlanga, E. Nxumalo and A. Shaikje, S. Afr. J. Sci. 107 (2011) 3
44. S. Mhlanga, N. Coville, S. Iyuke, A. Afolabi, A. Abdulkareem, N. Kunjuzwa, J. Expr. Nanoscience, 5 (2010) 40
45. N. Coville, S. Mhlanga, E. Nxumalo, A. Shaikje, S. Afr. J. Sci. 107 (2011) 1
46. T. Phadi, Titanates, MSc Dissertation, University of The Witwatersrand, Johannesburg (2008)
47. L. Jiang, L. Gao, J. Mater. Chem. Phys. 91 (2005) 313
48. Q. Huang, L. Gao, J. Mater. Chem. 13 (2003) 1517
49. M. Islam, E. Rojas, D. Bergey, A. Johnson, A. Yodh, Nano Lett. 3 (2003) 269
50. M. Motchelaho, PhD Thesis, University of The Witwatersrand, Johannesburg (2011)
51. P. Webb, Analytical methods in fine particle technology, Micromeritics Instrument Corporation, Norcross, GA USA (1997)
52. E. Berret, L. Joyner, P. Halenda, J. Am. Chem. Soc. 73 (1951) 373
53. X. Guo, D-J. Guo, X-P. Qiu, L-Q Chen, W-T Zhu, J. Power Sources 194 (2009) 281
54. S. Lee, W. M Sigmund, Chem. Commun. (2003) 780
55. W. Wang, P. Serp, P. Kalck, C. Silva, J. Faria, Mat. Res. Bulletin 43 (2008) 958
56. X-Y. Liu, N. Coville, S. Afr. J. Chem., 58 (2005) 110
57. V. Swamy, A. Kuznetsov, L. Dubrovinsky, R. Caruso, D. Shchukin, B. Muddle, Phys. Rev. B 71 (2005) 184302
58. F. Inoue, R. Ando, P. Corio, J. Raman Spectrosc. (2011)
59. A. Jorio, M. Pimenta, A. Filho, R. Saito, G. Dresselhaus, M. Dresselhaus, New J. Phys. 5 (2003) 1391
60. D. Bersani, P. Lottici, X. Ding, Appl. Phys Lett. 72 (1998) 73
61. S. Gregg, K. Sing, Adsorption, Surface area and Porosity, Academic press, London (1967)

62. A. El-Sheik, A. Newman, H. Al-Daffaee, S. Phull, N. Cresswell and S. York, Surface and Coatings technology 187 (2004) 284
63. A. Anson, J. Jagiello, J. Parra, M. Sanjuan, A. Benito, W. Master, M. Martinez, J. Phys. Chem. B 108 (2004) 15820
64. K. Sing, D. Everett, R. Haul, L. Moscou, R. Peirotti, J. Rouquerol and T. Siemieniewska, Pure Appl. Chem. 57 (1985) 603
65. R. Mariscal, M. Lopez-Grandos, J. Fierro, L. Sotelo, C. Martos and R. Grieken, Langmuir 16 (2000) 9460
66. X. Li, J. Niu, J. Zhang, H. Li, Z. Liu, J. Phys. Chem. B 107 (2003) 2453
67. P. Wauthoz, M. Ruwet, T. Machej and P. Grange, Appl. Catal. 69 (1991) 149.

Chapter 5

5. Titanium dioxide-carbon sphere composites for use as supports in cobalt catalysed Fischer-Tropsch synthesis

5.1 Introduction

The Fischer-Tropsch synthesis (FTS) is an important part of recent natural gas conversion process developments. The modern FTS aims at the conversion of synthesis gas (H_2 and CO mixture) into high quality diesel [1]. A key element in the improved FT technology is the development of active and stable catalysts with high selectivity towards wax.

Cobalt is considered as the most favourable metal for the synthesis of long chain hydrocarbons from natural gas [2]. It demonstrates good characteristics in terms of conversion per pass, selectivity to long-chain paraffin and low water-gas shift activity. The support is an important factor in modifying the properties of the cobalt catalysts [3]. Cobalt in its reduced state (not its precursor) is the active component in the CO hydrogenation reaction. Two major factors that determine a catalyst's activity ($g_{prod}/(g_{cat} \cdot h)$) are the degree of reduction of the metal precursor and the shape and size of the metal particles. These factors control the number of active sites available (dispersion). If a change in dispersion does not lead to a change in turnover frequency (TOF), then by definition the reaction is structure-insensitive. Iglesia *et al.* conducted a study showing that for large cobalt metal particles, the FTS reaction rate is proportional to the number of cobalt surface sites [4-7]. Some of the results obtained in this study are shown in Fig. 5.1. This

result therefore suggests that the TOF rates do not depend on the cobalt dispersion for a series of supports (i.e. Al_2O_3, SiO_2 and TiO_2). This has led Boudart to conclude that FTS is a structure-insensitive reaction [8].

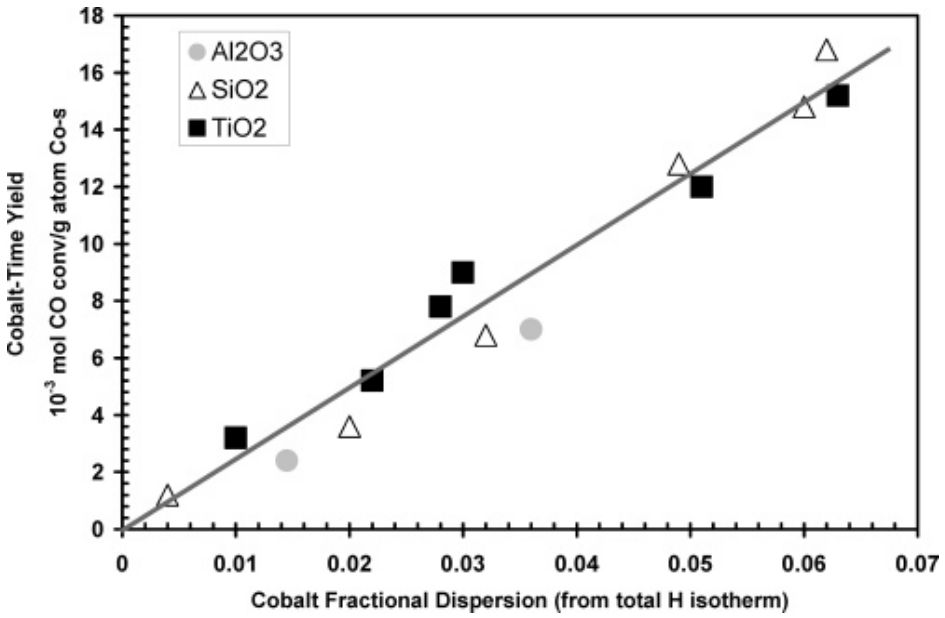


Figure 5. 1 Cobalt time yield for a variety of Co/Al_2O_3, Co/SiO_2 and Co/TiO_2 supported catalysts. Adapted from [9].

This observed invariance of the FT TOF on cobalt particle sizes for a range of supports studied is only valid for larger cobalt particles. Several exceptions might be expected when cobalt particles become smaller or when they contain different cobalt metal phases [10, 11]. Several reports have shown that the type and structure of the support influence the dispersion, particle size and reducibility of small cobalt based catalysts [12-15]. These factors influence the activity of the FTS reaction. The rate of formation of long-chain hydrocarbons and the C_{5+} selectivity over small cobalt particle catalysts have also been shown to be affected by the type and the structure of the support used in cobalt catalysed FT reactions [16-18].

Much recent work has focused on the use of carbonaceous materials as catalyst supports, i.e. carbon nanofibers (CNFs) and carbon nanotubes (CNTs) [10, 19, 20, 21]. Little work has been reported on other shaped carbons, such as carbon

spheres (CSs). Similarities may indeed be expected when CNFs, CNTs or CSs are used as supports and the advantages that apply to both CNFs and CNTs apply to CSs as well. CSs have over the decades been found to provide a high purity carbonaceous material when compared to CNFs and CNTs. The higher purity obtained for CSs is due to the fact that they do not contain any metal residue because no catalyst is required to produce them. However, the disadvantage for the use of CSs as catalyst supports is the low surface areas they possess. The other disadvantage for CSs, which is also common to both CNFs and CNTs, is their hydrophobic nature which results in low reactivity and thus makes it difficult to load metals on them because they are immiscible in water; the solvent that is normally used to disperse metal precursors on supports. Therefore, to overcome this wet ability challenge, functional groups are introduced on the CSs surface. This can be achieved by treating them with HNO_3. The presence of functional groups such as carboxylic acids facilitates the dispersion of CSs by creating a negative surface charge on the CSs [22]. Once this wet ability challenge has been overcome, CSs are excellent catalyst supports because of their intrinsic properties, such as their high thermal resistance and stability under FTS conditions [23].

TiO_2 is recognized for its characteristic properties that include the strong oxidation potential of its photogenerated holes, its chemical stability, non-toxicity and low cost [24]. A combination of the properties of TiO_2 with those of CSs could lead to new interesting properties especially for catalyst support materials. CSs can be used as a model system to study carbon sphere-TiO_2 (CS-TiO_2) composite interactions. These composite/interactions could then provide a novel support for cobalt and may influence the metal dispersion, particle size and reducibility of cobalt based catalysts. In Chapter 4, a full study that focused on the successful preparation of a homogeneous CS-TiO_2 composite material was described. According to our knowledge the preparation of this composite material has not been reported before. The aim of the work reported in Chapter 4 was to establish a successful method for the production of CS-TiO_2 composite material with a homogeneous TiO_2 coating on the surface of carbon spheres (see Chapter 4 for

full details). This attempt was successfully achieved by using a surfactant (CTAB) wrapping method.

In this Chapter the effect of CS-TiO_2 interactions on the catalyst activity and selectivity of cobalt supported on CS-TiO_2 during the FTS is reported. A series of other titania coated materials were also prepared and their characteristics were compared with those of CS-TiO_2 and these materials were also evaluated in the FTS.

5.2 Experimental

5.2.1 Support preparation

A series of different support materials were prepared and used as supports for cobalt catalysts. The cobalt supported materials were characterised and evaluated in the FTS. The supports used include:

- *(1) Carbon spheres (CSs)* (see Chapter 3),
- *(2) Titania coated carbon spheres made via the surfactant wrapping sol-gel method (ASW3)* (see Chapter 4),
- *(3) Carbon nanotubes (CNTs),*
- *(4) Titania coated carbon nanotubes made via the surfactant wrapping sol-gel method (CNT-TiO_2),* (same method as used for CSs in Chapter 3)
- *(5) P25 Degussa TiO_2 (P25) nanoparticles,*
- *(6) Sol-gel titania (SG)* (see Chapter 4),
- *(7) Titanate nanotubes (TNTs), and*
- *(8) Titania coated titanate nanotubes (C-TNTs)*

5.2.1.1 Carbon nanotube preparation

The method of carbon nanotube (CNT) preparation was adapted from that reported by Motchelaho [25, 26]. This method was developed in our research group at The School of Chemistry, University of the Witwatersrand.

A total metal loading of 10 wt% Co-Fe/$CaCO_3$ was prepared by wet impregnation of a $CaCO_3$ support with an aqueous $Co(NO_3)_2 \cdot 6H_2O$ (≥ 98%, Sigma Aldrich) and an $Fe(NO_3)_3 \cdot 9H_2O$ (≥ 98%, Sigma Aldrich) solution. In brief, $CaCO_3$ was stirred in 100 mL distilled water for 5 min. An aqueous 0.3 M solution (28 ml) of the calculated catalyst precursors was impregnated drop-wise to the stirred $CaCO_3$ slurry and the mixture was continued to be stirred for another 5 min. Ammonium hydroxide (12.5%) was then added drop-wise to the slurry and when the pH reached 7.2 the mixture was stirred for another 10 min. The resulting metal-support mixture was then filtered and dried in a static oven at 120 °C for 12 h, cooled to room temperature and then ground and sieved through a 150 mm sieve. The material was then calcined at 400 °C for 16 h in static air.

A tubular quartz reactor (510 mm × 19 mm i.d.) was placed horizontally (similar to the one used in Chapter 3) in a furnace and was used to pyrolyse acetylene (C_2H_4) to synthesize CNTs by the catalytic chemical vapour deposition (CVD) method using the as-prepared 10 wt% Co-Fe/$CaCO_3$ as catalyst.

Briefly 0.2 g of the as-synthesised catalyst (10 wt% Co-Fe/$CaCO_3$) was spread to form a thin layer in a quartz boat (120 mm × 15 mm). The boat was then placed in the centre of the quartz tube (maximum heating zone). The furnace was heated at 10 °C/min under flowing N_2 (40 mL/min). Once the temperature had reached 700 °C, the N_2 flow rate was set to 240 mL/min and C_2H_4 was introduced at a constant flow rate of 90 ml/min. After 60 min of reaction time, the C_2H_2 flow was stopped and the furnace was left to cool down to room temperature under a continuous flow of N_2 (40 ml/min). The boat was then removed from the reactor and the carbon deposit of approximately 3.5 g of black soot that formed along with the catalyst was weighed and analysed (TEM and TGA).

The purification and functionalization of CNTs were achieved using 55 % HNO_3 solution. Briefly, the raw (i.e. unpurified) carbon nanotubes (1 g) were mixed with 55 % HNO_3 (100 mL) and refluxed at 120 °C for 17 h. Then, the mixture was filtered and washed with deionised water until the pH of the mother liquor reached a value of 7. The resulting material was dried overnight at 90 °C in a static oven.

5.2.1.2 Titania nanoparticles preparation

In the case of the titania nanoparticles (P25 TiO_2) support, a commercial TiO_2 powder (Degussa P25 TiO_2) was mixed with de-ionised water and compressed into a moist paste. The solid material was dried in a static oven at 120 °C for 24 h. After cooling, it was crushed and sieved to the desired size (500-850 μm).

5.2.1.3 Titanate nanotubes preparation

Titanate nanotubes (TNT) were prepared as described elsewhere [27-30]. About 25 g of P25 TiO_2 powder was placed in a 1 L Teflon container together with 300 g of KOH pellets. De-ionised water (300 ml) was added to the mixture. The mixture was heated for 20 h at 120 °C in an autoclave with constant stirring at the rate of 300 rpm. The solution was allowed to cool and then aged for 2 days before it was washed with de-ionised water. Subsequently the solid product was separated from the mixture by centrifugation at a stirring rate of 10 000 rpm for 30 min at -5 °C. The washing was repeated until the conductivity of the solution was constant and ≤ 100 μS/cm. The pH of the solution during washing was also monitored. The removal of the basic ions is rather a lengthy process which may take many weeks to a month. The solid was dried in an oven at 120 °C for 12 h and then calcined at 300 °C for 5 h at a heating rate of 5 °C/min. After cooling, the sample was sieved to give particles with a size of 500-850 μm in diameter. The surface area of the materials was measured to be 231 m^2/g.

5.2.1.4 Titania coated titanate nanotubes support preparation

The titania coated titanate nanotubes (C-TNT) were prepared by means of a sol-gel processing method. This method is similar to that reported in a previous study [30]. Briefly titanium (IV) butoxide (98%, Sigma Aldrich), $Ti[O(CH_2)_3CH_3]_4$, was used as the reactant. To catalyse the reaction, 55 % HNO_3 was used. The TNT material was dissolved in a mixture of $Ti[O(CH_2)_3CH_3]_4$ with half the prescribed amount of anhydrous ethanol (EtOH) in order to avoid any hydrolysis reactions. A ratio of 1:5 (wt/wt) = TNT:$Ti[O(CH_2)_3CH_3]_4$ was used. De-ionised water and HNO_3, dissolved in the remaining EtOH, was added drop-wise to the ethanolic solution of butoxide while stirring continuously with a magnetic stirrer bar at ambient temperature. The molar ratio of the reactants used was: $Ti[O(CH_2)_3CH_3]_4$:H_2O:EtOH:HNO_3 = 1:4:15:0.3, as suggested in the literature by Ding *et al* [31]. During the addition of H_2O:EtOH:HNO_3 to $Ti[O(CH_2)_3CH_3]_4$ a sol formed. The sol was allowed to gelatize at room temperature until a clear solid gel was formed. The corresponding gel was then washed with deionised water and centrifuged to remove excess butoxide. The wet gel was dried in an oven at 120 °C for 2 h. This material was then ground and pelletized to the required particle size (500-850 μm). Calcination of this material was performed in air at 350 °C for 6.5 h.

5.2.2 Catalyst preparation

All the catalysts were prepared by the deposition precipitation (DPU) method using urea as the precipitating agent [25, 32, 33, 34]. A predetermined amount of $Co(NO_3)_2{\cdot}6H_2O$ (≥ 98%, Sigma Aldrich), urea and de-ionised water were used in the preparation of a 10%Co/support catalyst. Table 5.1 summarises the names given for all the catalysts prepared in this thesis.

In a typical synthesis of a catalyst containing 10% cobalt by weight, an appropriate amount of $Co(NO_3)_2{\cdot}6H_2O$ and urea with a ratio of 1.5:1 mol/mol (urea/Co) were dissolved in 10 mL de-ionised water. This mixture was added drop-wise to the support (2 g) using a micro pipette.

Table 5. 1 Summary of catalysts prepared by DPU method

Catalyst	Description of catalyst
Co	Unsupported cobalt
10% Co/CS	10 wt% cobalt on CS
10% Co/CNT	10 wt% cobalt on carbon nanotubes
10% Co/P25	10 wt% cobalt on P25 Degussa TiO_2
10% Co/SG	10 wt% cobalt on sol-gel TiO_2
10% Co/TNT	10 wt% cobalt on potassium titanates
10% Co/C-TNT	10 wt% cobalt on TiO_2 coated potassium titanates
10% Co/ASW3	10 wt% cobalt on CS-TiO_2 composite (see Chapter 4)
10% Co/CNT-TiO_2	10 wt% cobalt on CNT-TiO_2 composite

The mixture was slurried in 5 mL de-ionised water while heating to 90 °C in an oil bath. The mixture was left to stir at this temperature for at least 2 h to allow for the decomposition of urea. Thereafter, the excess water was left to evaporate at 90 °C. The catalyst precursor was then spread thinly on a plate and dried in a static oven at 120 °C overnight. The catalyst precursor was then calcined in flowing nitrogen (or air depending on support type[1]) at a flow rate of 30 mL/min at 1 bar pressure at an appropriate temperature (about 250-350 °C) as inferred from TGA data in order to decompose the precursor salts (i.e. NO_3^- ions). See Table 5.2 for a summary of calcination conditions employed for different catalysts. The table also tabulates the cobalt loadings actually found by either TGA or XRF analysis.

The supports and catalysts were characterised using the traditional characterisation methods to further understand their properties. These methods included XRF, TEM, EDX, TGA, BET, XRD, H_2-TPR, CO-TPD and H_2-chemisorption. The catalytic performance was evaluated by FTS.

[1]All the carbon based catalysts were calcined in flowing nitrogen, all other catalysts in flowing air.

Table 5.2 Summary of calcinations condition and cobalt loading on supports

	Calcination		Metal loading, %	
Catalyst	*Gas*	*Temperature, ℃*	*Theoretical*	*Actual*
0% Co/Silica[a]	-	-	0	0.0[b]
10% Co/CS	N_2	220	10	9.9[c]
10% Co/CNT	N_2	220	10	10.1[c]
10% Co/P25	Air	350	10	9.7[b]
10% Co/SG	Air	350	10	10.4[b]
10% Co/TNT	Air	350	10	9.2[b]
10% Co/C-TNT	Air	350	10	9.2[b]
10% Co/ASW3	N_2	350	10	9.8[b]
10% Co/CNT-TiO_2	N_2	350	10	9.1[b]

[a]Reference material, [b]XRF, [c]TGA

5.3 Catalyst characterization

5.3.1 Transmission electron microscopy (TEM)

Transmission electron microscopy (TEM) (FEI Technai Spirit G^2) was used to determine the morphology and measure the metal particle size of the new materials. Specimen samples for TEM analysis were prepared by dispersing very small samples in about 1 mL of methanol. The mixture was sonicated for about 15 min to obtain a homogeneous suspension. One drop of the suspension was poured onto an SPI-carbon coated copper grid and was allowed to dry before it was placed in the microscope. The image diameters of the particles (cobalt) obtained from TEM analysis were measured using ImageJ 1.43u software.

5.3.2 Thermogravimetric analysis (TGA)

Thermogravimetric analysis (TGA), conjugated with a derivative curve of the weight loss (DTG) measurements were carried out on a Perkin Elmer STA 4000 analyser coupled with an auto sampler that can perform up to 45 samples. About

10 mg of sample was placed in a pan (ceramic) and then put in the instrument's furnace. The sample temperature was ramped from room temperature to 950 °C under a flowing air atmosphere (20 mL/min) at a heating rate of 10 °C/min. A weight loss plot (TGA) provided information about the nature, stability and composition of the investigated sample. The derivative curve of this plot on the other hand provided the maximum temperature rate at which the weight loss took place.

5.3.3 BET surface area analysis

The surface areas and pore size distributions of the samples were determined via N_2 adsorption/desorption according to the Brunauer-Emmet-Teller (BET) method based on adsorption data in the partial pressure (P/P_0) range of 0.05-0.35. The total pore volume was determined by the amount of N_2 adsorbed at P/P_0 = 0.995 using a Micromeritics Tristar 3000, surface area and porosity analyzer. About 0.2 g of sample was degassed *ex-situ* under a flow of N_2 at 150 °C (or as otherwise stated based on TGA data) for 4 hours prior to analysis to remove moisture using a Micromeritics Flow Prep 060, sample degas system. The surface areas and pore size distributions were then obtained at -195 °C.

5.3.4 XRD and XRF measurements

X-ray diffraction patterns of calcined samples were examined using a Bruker D8 Avance X-ray diffractometer with a primary beam Göbel mirror, a radial soller slit, and a V Åntec-1 detector using Cu-K_α (1.5406Å) radiation at 40 kV and 40 mA. The scan range was $5° < 2\theta < 90°$ in 0.021 steps, using a standard speed with an equivalent counting time of 14.7 seconds per step. The obtained diffraction peaks were then compared with those of standard compounds reported in the Diffrac^{plus} evaluation package using the EVA (V11.0, rev .0, 2005) software package.

The cobalt content measurements were carried out on a PW2404 wavelength dispersive XRF spectrometer Panalytical model instrument. A rhodium target tube was used to generate the X-rays with K_α = 24.9 and K_β = 22. Powder samples were mixed with 2% polyvinyl glue Mowiol binder before being pressed into pellets using 10 MPa pressure prior to analysis. A known silica sample was used as a reference sample to obtain background data. This material was also used as a diluting agent for the catalysts containing carbon. A ratio of about 5:1 (wt/wt) silica:catalyst was used.

5.3.5 Temperature programmed reduction

The temperature programmed reduction (TPR) experiments were carried out with a Micromeritics Auto Chem II unit. The catalysts (*ca.* 0.1 g) were placed in a quartz U-shaped tubular reactor, fitted with a thermocouple for continuous temperature measurement. The reactor was heated in a furnace. Prior to the TPR measurements, the calcined catalysts were flushed *in situ* with high purity argon (or helium) at 150 °C for 1 h, to drive off moisture and other impurities, and then cooled down to 50 °C. After cooling, the 5% H_2/Ar gas mixture was switched on and the temperature was raised at a rate of 10 °C/min from 50 to 900 °C (held for 10 min). The gas flow rate through the reactor was controlled by three Brooks mass flow controllers and was always 50 mL/min. The H_2 consumption (TCD signal) was recorded automatically by a PC.

5.3.6 H_2-chemisorption and O_2 titration

H_2-chemisorption analysis was performed with a Micromeritics ASAP 2020, surface area and porosity analyzer instrument. The calcined pre-weighed catalyst samples (about 0.25 g) were placed in a U-shaped quartz tube sample holder which was evacuated under vacuum to less than 10 mmHg. These samples were degassed using pure He at 150 °C at 10 °C/min. Evacuation of He was then performed at 100 °C before reduction at 350 °C in pure H_2 for 16 hours took place. All physisorbed H_2 molecules were evacuated before measuring adsorption

isotherms for H_2 at 100 °C. The total H_2 uptake was determined by extrapolating the straight-line portion of the adsorption isotherm to zero pressure.

After H_2-chemisorption was conducted for each sample, the same sample was evacuated using He at 100 °C to remove the adsorbed H_2 molecules. Evacuation of weakly adsorbed He was then performed at 400 °C after which O_2 titration was carried out using a stream of pure O_2 at 400 °C. Extents of reduction were calculated using the O_2 uptake that was obtained by extrapolating the straight-line portion of the adsorption isotherm to zero pressure, this being the method that was proposed by Bartholomew and Farrauto [35]. The reaction of reduced cobalt with oxygen was considered to proceed to Co_3O_4 [36].

5.3.7 Fischer-Tropsch experiments for catalyst evaluation

The Fischer-Tropsch synthesis reactions were performed in a fixed-bed micro reactor (see Chapter 2). Gas cylinders containing $H_2/CO/N_2$ mixtures (60% H_2, 30% CO and 10% N_2; purity: 99.99%) were used to supply the reactant gas stream to the catalyst. Nitrogen was used as an internal standard in order to ensure an accurate mass balance.

Catalyst (0.5 g) was added to the reactor and reduced *in situ* at 350 °C for 16 h under a stream of pure hydrogen (1 bar, 30 ml/min). After reduction, the temperature was decreased to 230 °C, the pressure was increased gradually to 8 bar and a flow of syngas was passed over the catalyst bed with a flow rate similar to the hydrogen flow rate of 30 mL/min. All gas lines after the reactor were kept at 150 °C and the hot trap placed immediately after the reactor was held at 150 °C in order to collect wax. A second trap kept at ambient temperature was used to collect the oil and water mixture. The flow of gases was controlled using a metering valve and measured with a bubble meter. The gaseous product stream was analyzed online using two gas chromatographs. An offline GC was used to analyze the oil and wax. See Chapter 2 for full description of the FT reactor and its set up. Also for calculations of catalyst selectivities and activities.

5.4 Results and discussion

5.4.1 TEM

Cobalt (10% by weight) was impregnated on CSs that were functionalised at 90 °C (55% HNO_3) for different time intervals under reflux, namely 1 h and 17 h. The TEM images of the 10%Co/F-CS1h and 10%Co/F-CS17h samples are presented and compared in Figure 5.2 (a and b) and Figure 5.2 (c and d), respectively.

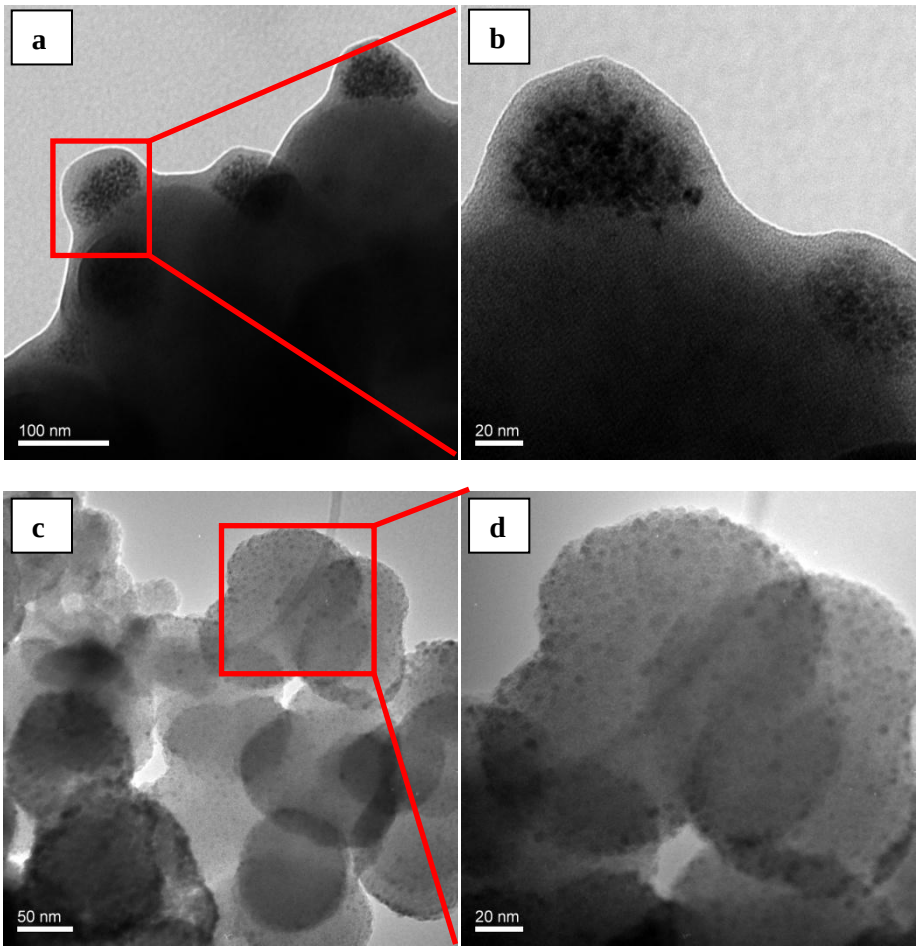


Figure 5.2(a) and (b) TEM images of 10%Co/F-CS1h indicating cobalt crystallites forming aggregated clusters (cluster size ~ 81 nm based on 50 clusters); (c) and (d) 10%Co/F-CS17h indicating well dispersed cobalt particles on the surface (cobalt particle size ~ 4 nm based on 80 particles)

It can be seen that CSs that were functionalised for 1 h in HNO_3 (i.e. 10%Co/F-CS1h) show poor dispersion of cobalt particles; the metal formed aggregated clusters at localised surfaces. This suggests that only a few CS surfaces were functionalised with acid functional groups. The average crystallite cluster size (comprised of smaller crystallites) was about 81 nm. For the 10%Co/F-CS17h catalysts, a much better cobalt dispersion was achieved and this can be attributed to the extra metal anchoring sites created by the surface functional groups distributed on the CS surfaces. The average cobalt particle size was about 4 nm.

This observation ties in with the FTIR study that was conducted in Chapter 3 (section 3.4.3). The FTIR data showed a small growth of the γ(CO) peaks associated with the carboxylic acid functional groups, lactones, quinones and lactone groups when CSs were acid treated with HNO_3 for 1 h. A large growth of these peaks was observed for CSs that were functionalised for 17 h. In Chapter 4 it was reported that a uniform and homogeneous TiO_2 coverage on CSs coating was achieved when CSs were acid treated with HNO_3 for 17 h.

The CSs that were functionalised for 17 h and then coated with TiO_2 homogeneously by a surfactant wrapping method (i.e. ASW3; see Chapter 4) were selected and used as supports for cobalt to give a 10wt% cobalt loaded catalyst. This catalyst was called 10%Co/ASW3 (see Fig 5.3).

In Figure 5.3 the TEM images showing cobalt dispersed on different supports which were studied are shown. These catalysts are defined as (a) 10%Co/SG, (b) 10%Co/P25, (c) 10%Co/ASW3, (d) 10%Co/CNT, (e) 10%Co/CNT-TiO_2 and (f) 10%Co/TNT for the 10 wt% cobalt on sol-gel support, 10 wt% cobalt on P25 Degussa TiO_2, 10 wt% cobalt on ASW3, 10 wt% cobalt on CNT, 10 wt% cobalt on TiO_2 coated CNT, and 10 wt% cobalt on TNT, respectively (see Table 5.2).

In Figure 5.3 (a), (b), (c) and (e) it was difficult to selectively recognise the cobalt particles since the supports contained TiO_2 particles which were similar in size and shape to cobalt particles under TEM. However, certain sites in the images

appeared to be darker and these dark particles could possibly be attributed to cobalt particles. The EDX spectrum of 10%Co/SG in Fig. 5.4 (a) confirmed the presence of cobalt. The same applied to the other catalysts (not shown).

In the TEM images of the supports without any TiO_2, i.e. Figure 5.3 (d) and (f) for 10%Co/CNT and 10%Co/TNT, respectively the cobalt particles were clearly visible. The average cobalt particle sizes were 8 nm and 24 nm, respectively.

It should be noted that all EDX spectra, in Figures 5.4 (a), (b) and (c) showed the presence of carbon. The spectra of 10%Co/ASW3 and 10%Co/CNT-TiO_2 in Figures (b) and (c), respectively showed larger carbon peaks as these catalysts contained supports with carbon (CSs or CNT). The carbon peak observed in the EDX profile of 10%Co/P25 comes from the copper grid which was coated with carbon.

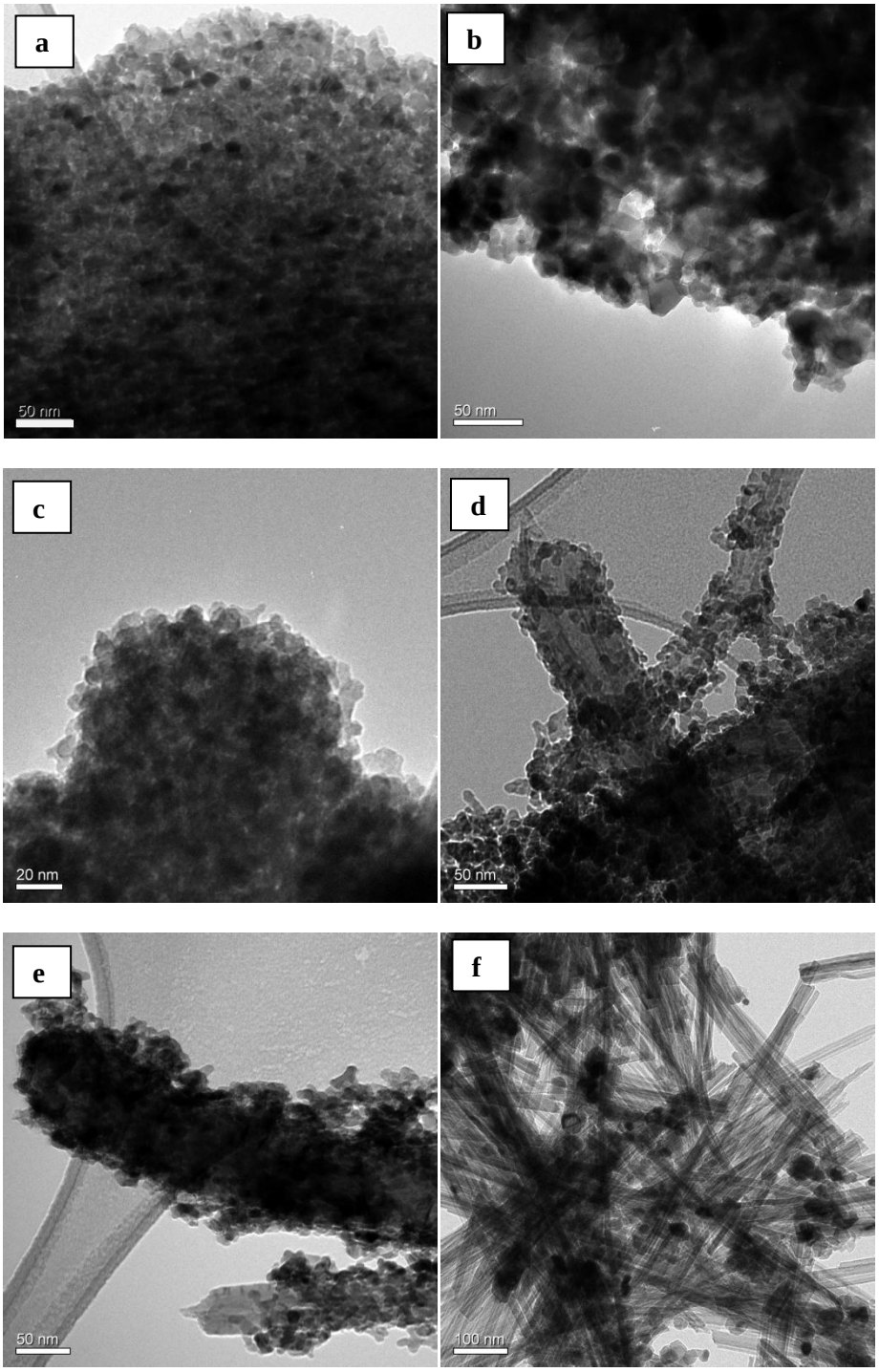


Figure 5.3 TEM images showing cobalt dispersed at different supports: (a) 10%Co/SG, (b) 10%Co/P25, (c) 10%Co/ASW3, (d) 10%Co/CNT, (e) 10%Co/CNT-TiO_2 and (f) 10%Co/TNT

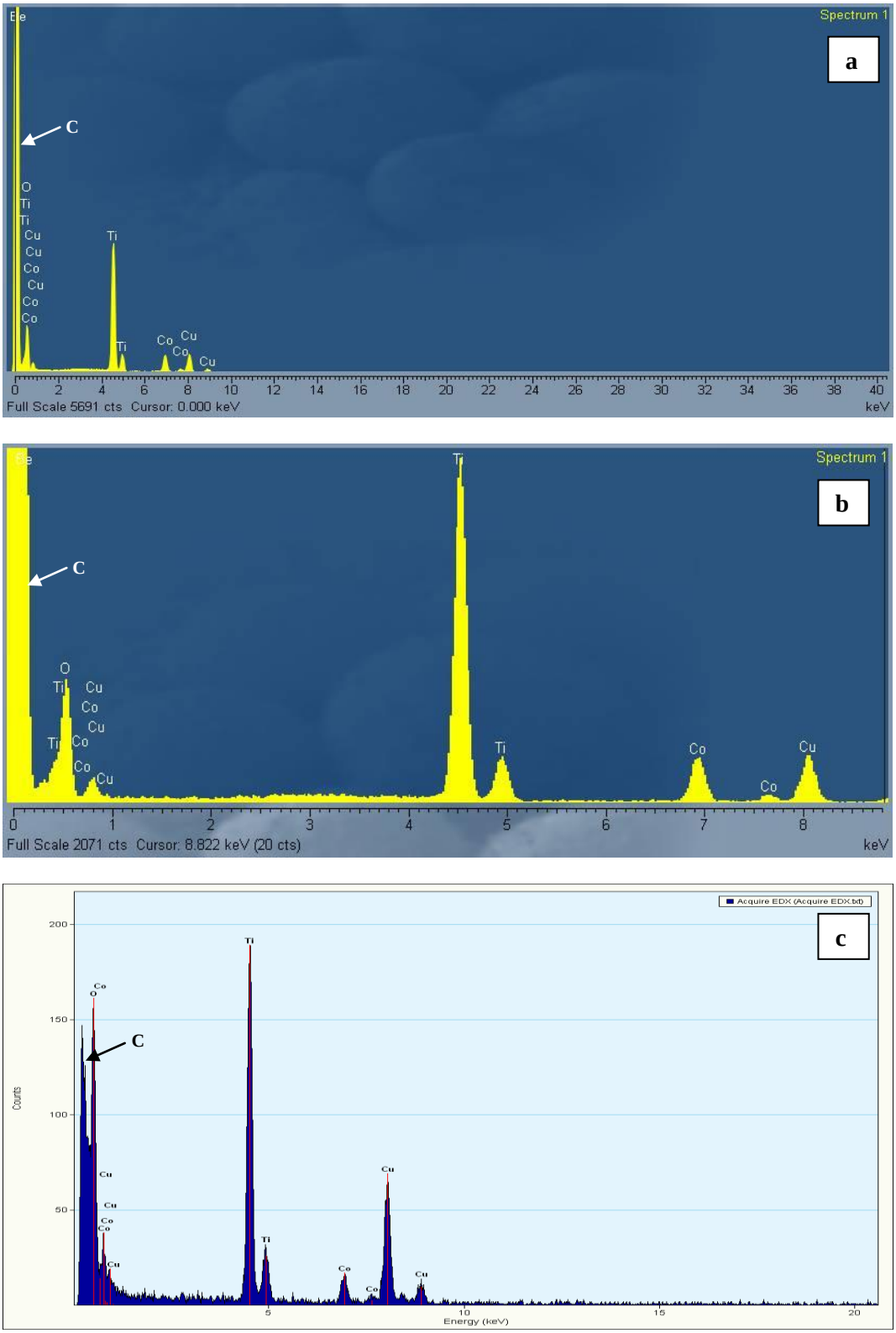


Figure 5.4 (a), (b) and (c) EDX spectra corresponding to the surface coverage shown in Fig. 5.3 (a), (c) and (e), respectively. C and Ti were detected; the Cu signal corresponds to the Cu grid substrate used in the TEM analysis.

5.4.2 N_2 adsorption-desorption

The BET surface areas, pore volumes and pore diameters of the 10% cobalt loaded calcined catalysts are displayed in Table 5.3.

Table 5.3 BET surface areas, pore volumes and pore diameters of the calcined catalysts

Sample	$S_{BET}{}^{a}$ (m^2/g)	$P_v{}^{b}$ (cm^3/g)	$P_D{}^{c}$ (nm)
10%Co/CS	6	0.014	9.1
10%Co/CNT	106	0.367	13.9
10%Co/P25	46	0.328	28.6
10%Co/SG	47	0.112	9.5
10%Co/TNT	144	0.460	12.8
10%Co/C-TNT	141	0.446	12.7
10%Co/ASW3	83	0.410	10.1
10%Co/CNT-TiO_2	103	0.384	14.8

[a]Surface area, [b]P_v = pore volume, [c]P_D = pore diameter

As can be seen, the 10%Co/CS sample showed the lowest BET surface area (6 m^2/g) and total pore volume (0.014 cm^3/g) compared to the other catalysts. This surface area is significantly lower than that of the unloaded CSs (CS17h) as reported in Chapter 3 with a surface area of 9.6 m^2/g. Since the pore volume and the pore diameters of the loaded and the unloaded catalysts are similar, the explanation for the observed lower surface area on the loaded catalyst is not clear. The 10% cobalt loaded catalyst prepared using a surfactant wrapping method (CSs homogeneously coated with TiO_2, 10%Co/ASW3) showed a significantly larger surface area (83 m^2/g) and total pore volume (0.410 cm^3/g) compared to that of the uncoated catalyst (i.e. 10%Co/CS). This suggests that ASW3 is a better cobalt carrier compared to the CSs since there is a large surface area on which to disperse cobalt. However, the surface area of 10%Co/ASW3 is lower than that of the unloaded support ASW3 (i.e. 98 m^2/g) as reported in Chapter 4 (section 4.3.2.5).This reduced surface area could result from pore blockage by cobalt particles. The lowered total pore volume (0.410 cm^3/g) and pore diameter (10.1

nm) for 10%Co/ASW3 compared to values of 0.422 cm^3/g and 14.3 nm, respectively for ASW3 is consistent with this suggestion. All other catalysts followed a similar trend of a lowered surface area when cobalt was loaded on the support, as observed with 10%Co/ASW3 and its support. However, 10%Co/CNT gave results at odds with the CS data. These samples showed an increase in surface area from 80 to 106 m^2/g when 10% cobalt was loaded onto CNTs. This observation is similar to the one reported by Motchelaho *et al.*, when iron was loaded onto CNTs [25].

5.4.3 TGA

TGA and DTA data were used to determine the decomposition temperature of the precursor and the thermal stability or any other impurities. In the case of supports which did not contain TiO_2, TGA was used to determine the metal loading. TGA of all the catalysts were performed in an air atmosphere (flow rate: 20 mL/min, heating rate: 10 °C/min) in order to determine the temperature at which the precursor salt decomposed to form the metal oxide. In Figure 5.5 (a) and (b), the TGA and DTA profiles for the 10%Co/CS before calcination and after calcination, respectively, are shown. The TGA profile for 10%Co/CS before calcination showed three weight loss stages with their derivative peak maxima appearing at 95, 202 and 295 °C. These three peaks are attributed to the loss of absorbed moisture (ca. 5% at 95 °C), the decomposition of nitrate ions from the cobalt precursor salt (ca. 20% at 202 °C) and the oxidation of CSs (ca. 55% at 295 °C).

This suggests that in order to decompose nitrate ions, the catalyst must be heated at 220 °C for at least 150 min (Figure 5.5 (b)). The oxidation of CSs for this catalyst occurred at a much lower temperature compared to the oxidation of unloaded F-CSs (685 °C) as observed in Chapter 2 (section 2.3.7). This suggests that cobalt has a catalytic effect on the oxidation of CSs under air atmosphere [25]. The residue from the TGA profile (9.7%) corresponds to the amount of cobalt which was loaded on the CSs.

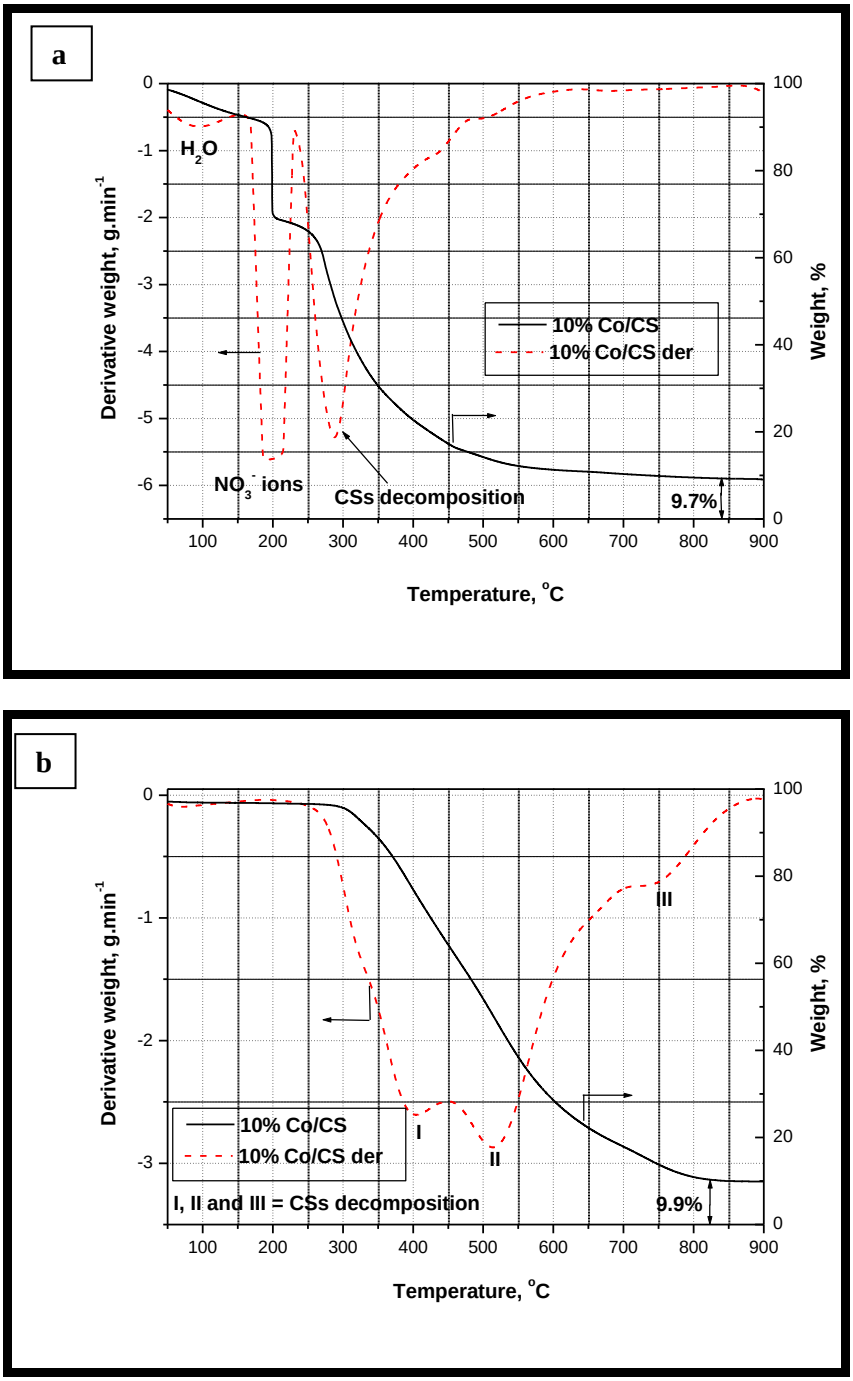


Figure 5.5 TGA and DTA profiles for the 10%Co/CS catalyst in air atmosphere; (a) before calcination and (b) after heating in N_2 (220 °C, 150 min)

In Figure 5.5 (b), the weight loss due to moisture and nitrate ions was not present. This suggests that the conditions used to calcine the catalyst for the removal of nitrate ions were sufficient. Only one weight loss peak was observed in the range between 300 and 800 °C which is due to the oxidation of CSs. However,

surprisingly, the derivative curve of this weight loss comprised of three derivative peaks with maxima at 400, 524 and 752 °C. All these peaks could be attributed to the oxidation of CSs catalysed at different rates by cobalt oxide in the absence of nitrate ions. The residue (cobalt oxide) obtained from the TGA profile of the calcined catalyst sample was 9.9%.

TGA profiles obtained in an air atmosphere for the uncalcined catalysts, namely 10%Co/P25, 10%Co/SG, 10%Co/ASW3, 10%Co/CNT-TiO_2, 10%Co/TNT and 10%Co/C-TNT are shown and compared in Figure 5.6. The weight loss due to moisture ranged between 50 and 200 °C and was observed for all the catalysts. However, the rate at which this moisture loss was observed was different. The TGA profile of 10%Co/SG shows that it contained the most moisture while that of 10%Co/CNT-TiO_2 shows that is contained the least. The weight loss due to nitrate ions was evident in all catalysts (peak around 220 °C). The TGA profile of 10%Co/CNT-TiO_2 shows that it contained the most nitrate ions while 10%Co/TNT contained the least.

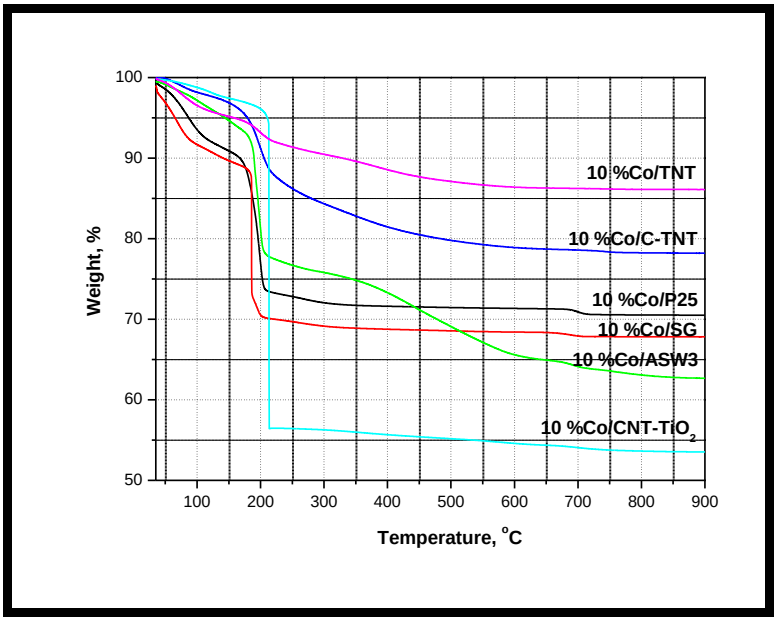


Figure 5.6 TGA profiles for the 10%Co/P25, 10%Co/SG, 10%Co/ASW3, 10%Co/CNT-TiO_2, 10%Co/TNT and 10%Co/C-TNT catalysts in air atmosphere before calcination

The TGA profiles of 10%Co/SG and 10%Co/P25 show a similar trend, i.e. have the same shape for the removal of moisture (80 – 180 °C) and nitrate ions (180 – 200 °C). The observation of the same TGA shape suggests that P25 and SG supports are similar. TGA profiles of the other four catalysts (i.e. 10%Co/ASW3, 10%Co/CNT-TiO_2, 10%Co/TNT, and 10% Co/C-TNT) also exhibits the weight loss of moisture and nitrate ions in the same temperature range as found for 10%Co/SG and 10%Co/P25. In addition to the two weight losses observed, the profiles of both 10%Co/ASW3 and 10%Co/CNT-TiO_2 exhibited a weight loss at high temperature (350 – 600 °C) due to the oxidation of CSs and CNT, respectively.

5.4.4 TPR and TPD

The reduction behaviour of the supported catalysts in an H_2 atmosphere was determined by means of TPR experiments. Figure 5.7 shows the recorded hydrogen consumption TPR profile of an uncalcined unsupported cobalt oxide sample.

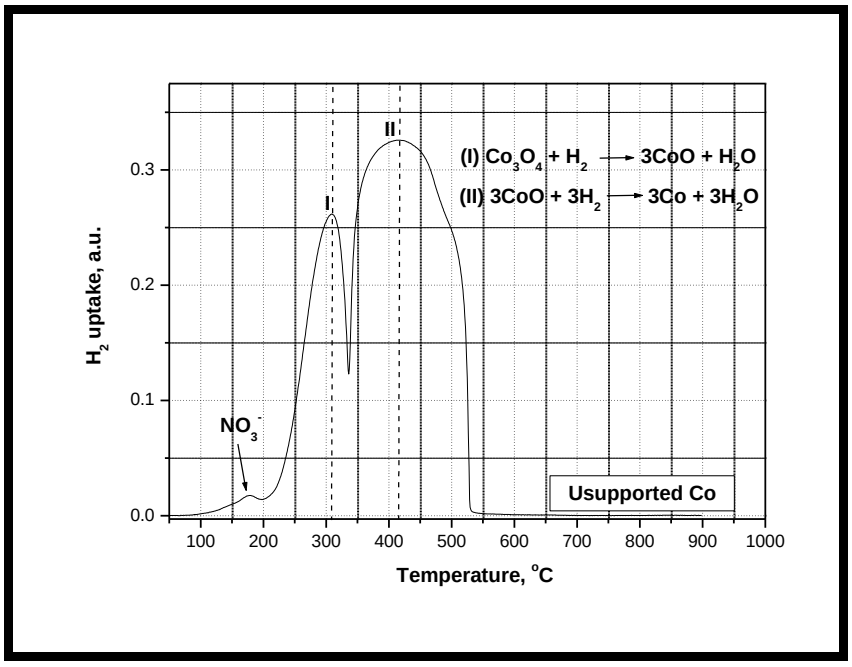


Figure 5.7 TPR of uncalcined unsupported cobalt oxide precursor

The profile shows three peaks, indicative of the reduction of nitrate ions (at 180 °C) obtained from the precursor salt and the two step reduction of Co_3O_4 to CoO (at 306 °C) and CoO to metallic cobalt (at 425 °C) occurring as mentioned by Sexton *et al.* [37].

The two reduction peaks (cobalt oxide to metallic cobalt) are said to correspond to the chemical reactions shown in equations 5.1 and 5.2 [38].

$$Co_3O_4 + H_2 \rightarrow 3CoO + H_2O \quad (5.1)$$

$$3CoO + 3H_2 \rightarrow 3Co + 3H_2O \quad (5.2)$$

The H_2-TPR profiles of supports with no cobalt loading, namely SG, CS, CNT, P25, TNT and ASW3 are shown in Figures 5.8 and 5.9. As can be seen, no reduction peaks were observed in the TPR profiles of SG, P25 and TNT supports. The TPR profiles of CS and CNT both showed a negative H_2 uptake peak at 650 °C. This negative peak is due to carbon gasification at high temperature, which produces methane [33 and 34]. The profile of ASW3, i.e. the CS-TiO_2 composite support material (Figure 5.9) shows a broad trough in H_2 uptake when the sample was heated between 280 and 680 °C due to the gasification of CSs. This broad negative peak ranging from a lower temperature could be attributed to catalysed CS gasification by TiO_2. Since the profiles of supports without any cobalt loading are known, it could then be concluded that in the presence of cobalt loading on the supports, any reduction peak that will occur will be either due to the reduction of cobalt or of strong metal support interactions (SMSI) between cobalt and supports.

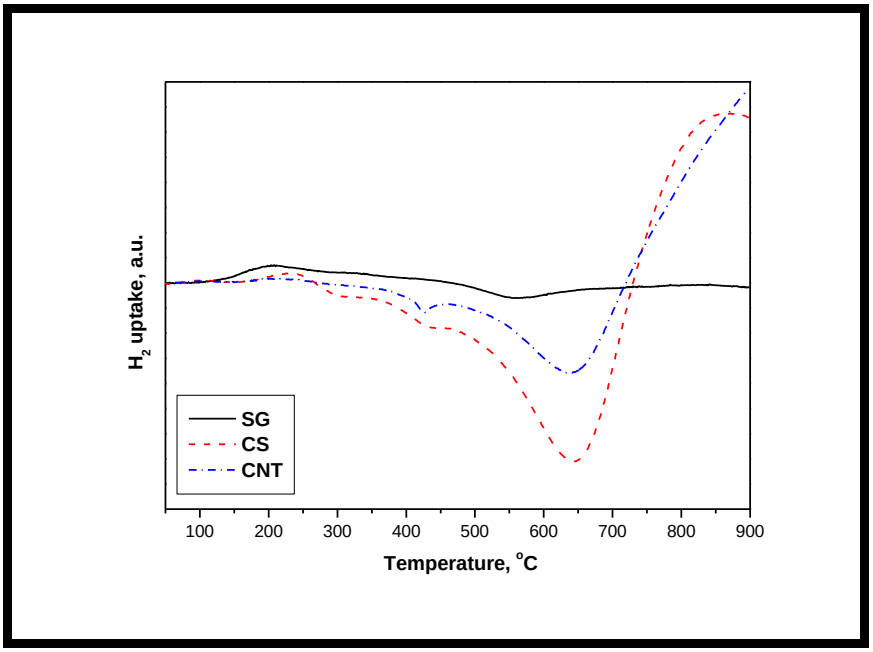


Figure 5.8 H_2-TPR of SG, CS and CNT

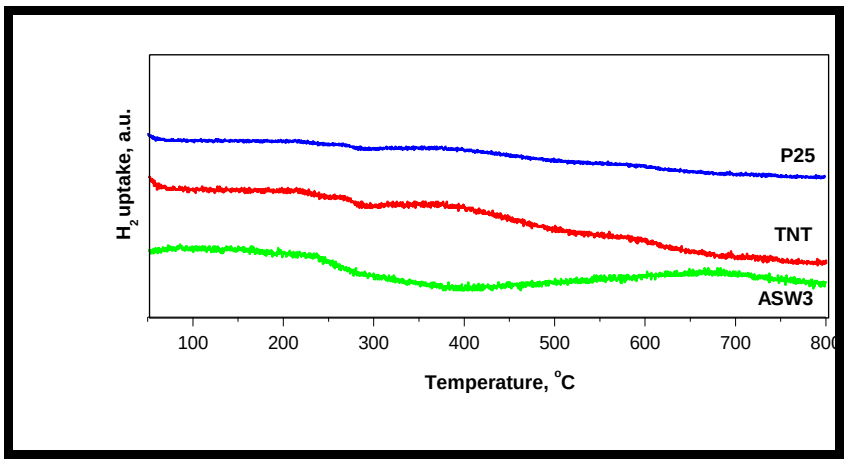


Figure 5.9 H_2-TPR of P25, TNT and ASW3

The reduction behaviour of the calcined 10% cobalt loaded catalysts are compared in the TPR profiles shown in Figure 5.10. For all the catalysts the two cobalt reduction peaks were observed even though they occurred at different temperatures. These reduction temperatures occurred at temperatures higher that those found in the unsupported cobalt sample (Figure 5.7). This was previously suggested to be due to the presence of SMSI between the support and the metal [39].

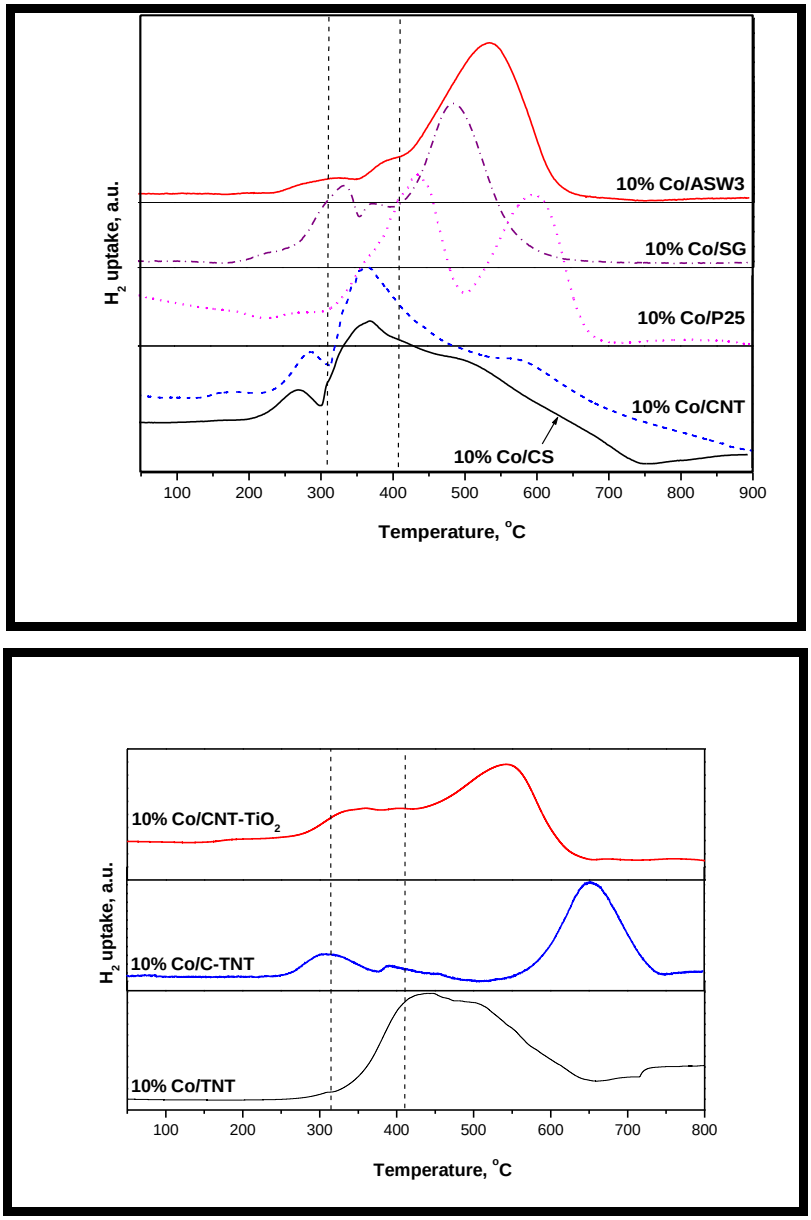


Figure 5.10 H_2-TPR of calcined supported cobalt catalysts

This observation implies that when cobalt was impregnated on the supports the rate of reduction of cobalt was suppressed. The recorded profiles for 10%Co/CS and 10%Co/CNT both show these reduction peaks at 280 and 350 °C, respectively.

Another hydrogen consumption peak was observed at 580 °C in the profile of 10%Co/CNT. This peak could be indicative of the reduction of cobalt particles which were situated in the inner diameters of the CNTs which were difficult to

reduce. A significant delay in the both the reduction peak temperatures, i.e. at 450 and 600 °C were observed for 10%Co/P25. However, in the catalysts with the synthesised TiO_2 material, i.e. 10%Co/SG, the reduction peaks occurred at 320 and 480 °C, respectively. This suggests that the SMSI between the active cobalt and the support material were stronger in 10%Co/P25 than in 10%Co/SG. Three reduction peaks were observed in 10%Co/ASW3, namely at 280, 380 and a large one at 540 °C. The three reduction peaks may be due to a support with two different materials, i.e. CSs and TiO_2 which as a result consist of samples with different SMSI (Co-CS and Co-TiO_2 or CS-Co-TiO_2), which reduce at different temperatures. The same behaviour was observed on 10%Co/C-TNT where three cobalt reduction peaks occurred at 304, 394 and at 652 °C as a result of cobalt loaded on a support material with two different morphologies, i.e. TNT coated with TiO_2. However, cobalt loaded on uncoated TNT material (10%Co/TNT) consisted of only two reduction peaks which occurred at 446 and 520 °C. 10% cobalt loaded on the CNT-TiO_2 composite material (10%Co/CNT-TiO_2) also consisted of only two reduction peaks which occurred at 350 and 548 °C. No SMSI peak was observed at a high temperature for this catalyst.

Based on the H_2-TPR results, it can be seen that when TiO_2 was used as a support the reduction of cobalt became more difficult. Even for the easily reducible catalysts (10%Co/CS, 10%Co/CNT, 10%Co/TNT), as soon as the supports were coated with TiO_2, the reduction of the catalysts was suppressed.

CO-TPD was used to investigate the effect of supports on the CO adsorption behaviour. The CO-TPD experiments were performed in the same system as used in H_2-TPR with He as a carrier gas. About 0.2 g of calcined sample was loaded in a U-shaped quartz reactor. Prior to analysis the samples were reduced at 350 °C (1 bar pressure) in high purity H_2 (50 mL/min) for 14 h. After reduction, the sample was cooled to 100 °C and then purged with high purity He for 35 min to remove the weakly adsorbed H_2. A 5% CO/He gas mixture was switched on at a flow rate of 50 mL/min at 1 bar pressure and CO was adsorbed for 1 h. The He gas was again purged for 35 min to remove weakly adsorbed CO, and then TPD (50-900

°C) was carried out in He. In Figures 5.11 and 5.12, the CO-TPD profiles of the support materials and the equivalent cobalt catalysts are shown, respectively.

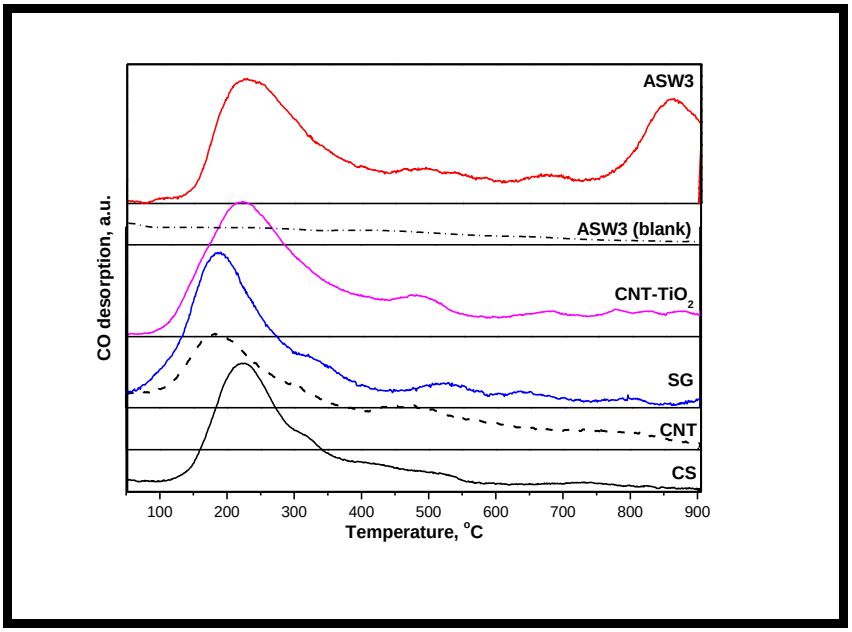


Figure 5.11 CO-TPD of calcined supports; i.e. ASW3, CNT-TiO_2, CNT, SG and CS

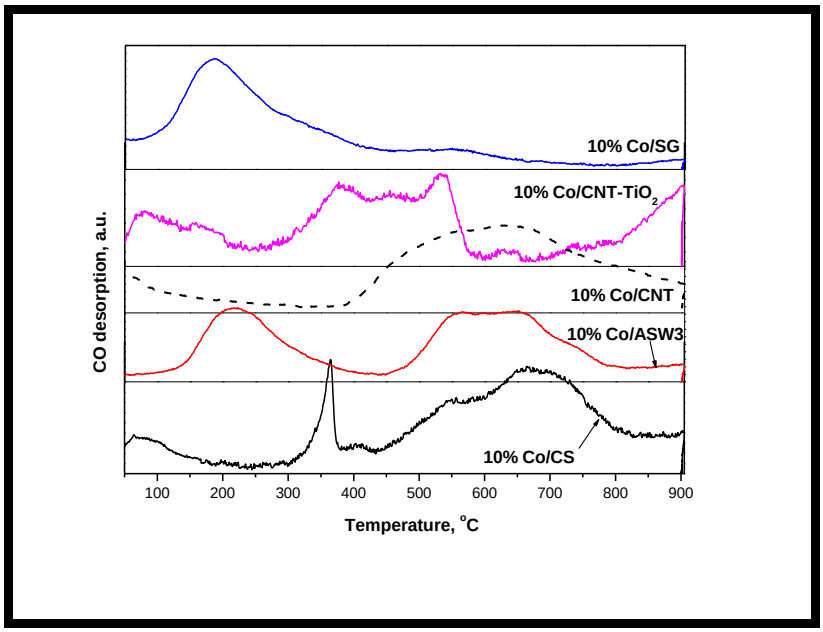


Figure 5.12 CO-TPD of calcined supported cobalt catalysts

The CO-TPD studies for TNT, C-TNT and their catalysts could not be carried out because there were not enough samples. The TPD profiles of SG, CNT, CS and CNT-TiO_2 support materials showed only one desorption peak at 200, 202, 230 and 252 °C, respectively confirming that there was no active metal loaded on the supports. These low temperature peaks represent a weak CO adsorption.

Interestingly the TPD profile of ASW3 showed an unexpected desorption profile; two groups of desorption peaks were observed (one at the lower temperatures corresponding to the weak CO adsorption, with the other at higher temperatures is ascribed to the strong CO adsorption) [40]. Since there was no cobalt loaded on this support, the explanation for this observation is not clear. This may be due to the adsorption of CO that was caused by the interaction between CSs and TiO_2 which may have formed CO adsorptive sites. ASW3 (blank) represents a TPD profile of ASW3 which was not saturated (adsorbed) with CO (5%CO/He) prior to heating the sample in He while recording the profile. The profile does not show any CO desorption peaks. This confirms that the observed peaks in all supports represent the desorption of CO. Only a small baseline drift was observed. The drift may indicate the gasification of CSs.

The TPD profile of 10%Co/SG showed a large desorption peak of weak CO (120-420 °C). A small peak of strongly adsorbed CO was observed on addition of Co at about 570 °C. A much larger peak due to the strong CO desorption was expected at that position (~570 °C) compared to the observation of the small peak. This implies that the CO desorption peak that was due to cobalt was not easily detected by TCD suggesting that the cobalt had not been sufficiently reduced during this analysis.

The profiles for 10%Co/CS and 10%Co/ASW3 contained both the desorption of weak and strong CO peaks. The weak CO desorption peak for 10%Co/ASW3 occurred between 120 and 420 °C and is similar to that observed on ASW3 with no cobalt. The weak desorption of CO for 10%Co/CS showed a very sharp peak at a much higher temperature (350 °C). This implies that loading cobalt on CS had a

significant effect on physisorbed CO. The strong CO desorption peak for both catalysts (10%Co/ASW3 and 10%Co/CS) occurred between 450 and 800 °C. The profile for 10%Co/CNT only showed a broad desorption peak between 400 and 850 °C which correspond to the desorption of strongly adsorbed CO molecules. The physisorbed CO that was observed on the supports only (in Fig 5.11), disappeared when cobalt was loaded on CNT. The broadness of the strongly adsorbed CO may be due the dispersion (or distribution) of cobalt particles on the CNT. This may imply that some of the cobalt particles are inside the CNT diameter while others are dispersed outside the tubular structure. The CO may be desorbed differently, at different energies (hence a broad temperature desorption profile) in this instance.

The TPD profile of 10%Co/CNT-TiO_2 showed the presence of four desorption peaks at 20-250 °C, 300-420 °C, 500-600 °C and a broad peak that started above 700 °C. This observation of four peaks was unusual and could have been caused by the desorption of CO for cobalt dispersed on a non-homogeneous support of CNT-TiO_2 with some of the cobalt particles dispersed on TiO_2 covering CNT, some inside the CNT tube while other particles were dispersed outside the tubular structure. The desorption peak of weakly adsorbed CO was smaller than that of CO desorbed from the CNT without cobalt.

The TPD data suggest that an interaction of carbonaceous based materials with TiO_2 improved the CO adsorption on cobalt compared to cobalt loaded TiO_2 (10%Co/SG) without any carbonaceous material.

5.4.5 H_2-Chemisorption and O_2 titration

The results of the H_2-chemisorption study for all catalysts are listed in Table 5.4. The calcined pre-weighed catalyst samples (about 0.5 g) were placed in a U-shaped quartz tube sample holder which was evacuated under vacuum. These samples were degassed using pure He at 150 °C. Removal of the He was then

performed at 100 °C before reduction of the catalyst at 425 °C in pure H_2 for 16 hours. After the initial reduction the catalysts were further reduced in pure H_2 at a temperature that was 25 °C below the reduction temperature (425 °C) for 1 hour prior to analysis. All physisorbed H_2 molecules were evacuated before measuring adsorption isotherms for H_2 at 100 °C.

The calculations to determine the degree of reduction were achieved by measuring O_2 by back titration (at 400 °C) of the pre-reduced catalysts. The O_2 back titration for carbon based catalysts, i.e. 10%Co/CNT and 10%Co/CS, were carried out at a lower temperature (250 °C) to avoid the combustion of the supports. The degree of reduction increased in the following order: 10%Co/CS < 10%Co/CNT < 10%Co/C-TNT < 10%Co/CNT-TiO_2 < 10%Co/TNT < 10%Co/P25 < 10%Co/ASW3 < 10%Co/SG. This trend differs from the TPR data.

Table 5.4 H_2-Chemisorption results for all calcined catalysts[a]

Catalyst sample	Degree of reduction (%)	Metallic surface area ($m^2/g_{.sample}$)	Dispersion (%)
10%Co/CS	47[b]	0.9	0.8
10%Co/SG	93	4.2	1.8
10%Co/CNT	60[b]	0.8	0.6
10%Co/TNT	80	0.6	0.6
10%Co/ASW3	89	4.0	2.1
10%Co/C-TNT	65	0.2	0.1
10%Co/CNT-TiO_2	76	3.0	0.8
10%Co/P25	87	2.8	1.4

[a]Reduction T = 425 °C for 16 h in pure H_2 unless otherwise stated
[b]O_2 titration back carried out at 250 °C for carbon based supports
Error bar on data = ±0.6% (based on reference material on ASAP 2020 chemisorption instrument)

The highest reduction degree of 93% was observed for 10%Co/SG. This was higher than that of 10%Co/P25 (87%), its commercial support counterpart catalyst. 10%Co/CS showed the lowest degree of reduction (47%), followed by 10%Co/CNT (60%). These low reduction values observed for carbon based supports (CSs and CNTs) could be due to the complications that occurred during O_2 back titration. These complications are related to the low reduction

temperature (250 °C) that was insufficient to fully re-oxidise reduced cobalt particles to Co_3O_4. Another possibility is that at 200 °C some of the O_2 might have combusted the supports. Thus inaccurate measurements were used from the O_2 uptake experiments, used to calculate the degree of reduction.

However, as soon as these supports were coated with TiO_2 the degree of reduction increased to 89% and 76% for 10%Co/ASW3 and 10%Co/CNT-TiO_2, respectively. The degree of reduction of the TiO_2 coated carbonaceous supports was lower than that found for 10%Co/SG (93%). From this observed degree of reduction of 10%Co/SG in comparison to TPD data observed for this catalyst (unexpectedly low CO desorption peak at 570 °C), it can be concluded that during TPD analysis of that sample the reduction was not sufficient (possibly due to an empty pure H_2 bottle).

The observed higher reduction degree of 10%Co/ASW3 (89%) than that of 10%Co/CNT-TiO_2 (76%) may suggest that ASW3 had a more homogeneous TiO_2 coating of CSs than the TiO_2 coating on CNTs. This would affect the reduction of the ASW3 support more than the CNT-TiO_2 support when O_2 back titration was carried out since TiO_2 could modify the CSs and "protect" them from combustion.

The degree of reduction for 10%Co/TNT was 80% while that of 10%Co/C-TNT was lower at 65%. These relatively low extents of reduction might have the same origin as observed for the TPR results. Thus, SMSI may affect the cobalt-C-TNT interaction in the case of 10%Co/C-TNT, while in the case of 10%Co/TNT this effect could be due to cobalt poisoning by potassium on the support surface [30, 43, 44].

Metallic surface area values of 4.2, 4.0, 3.0 and 2.8 m^2/g, were observed for 10%Co/SG, 10%Co/ASW3, 10%Co/CNT-TiO_2, and 10%Co/P25 samples, respectively. Their dispersions were measured as 1.8, 2.1, 0.8 and 1.4 %, respectively. Catalysts with high metallic surface areas and dispersions imply that there is a large active amount of cobalt available for adsorption compared to

catalysts with low metallic surface area and dispersion. No specific trend could be observed to explain the data, except that all these catalysts contained supports which were coated with TiO_2.

Lower metallic surface area and dispersion values were observed for 10%Co/C-TNT, 10%Co/CS, 10%Co/CNT and 10%Co/TNT (see Table 5.4). Even though 10%Co/C-TNT is a catalyst with a relatively low metallic surface area and dispersion, it is a support which was coated with TiO_2. The low values observed for this catalyst may imply a SMSI effect, as was observed from the TPR data.

5.4.6 Fischer-Tropsch synthesis

The performance of the cobalt catalysts (prepared using different supports) in the Fischer-Tropsch synthesis was tested in a fixed-bed micro reactor. All the reactions were performed under a set of standard conditions (220 °C, 8 bar, 30 mL/min, $H_2/CO = 2$). The percentage CO conversion as a function of time on stream for catalysts with non-TiO_2 coated supports, namely 10%Co/CS, 10%Co/SG, 10%Co/CNT and 10%Co/TNT catalysts are shown in Figure 5.13.

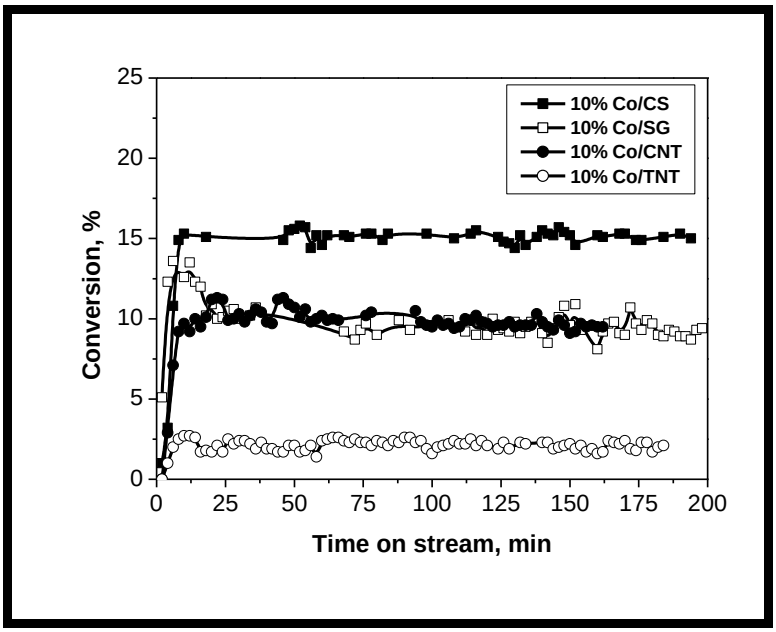


Figure 5.13 CO conversion with time on stream for 10%Co/CS, 10%Co/SG, 10%Co/CNT and 10%Co/TNT

The conversion for all these catalysts was low initially, but increased significantly with time on stream. The catalysts reached their steady state conversions within 15-20 h on stream. Thereafter, they remained stable for the entire run (about 150 h). There is no obvious evidence of deactivation for all these catalysts within 150 h. The plot in Figure 5.13 shows that the 10%Co/CS catalyst produced the highest CO conversion (15.2%), while the 10%Co/TNT catalyst produced the lowest conversion (~3%) of all catalysts made with non-TiO_2 coated supports. The CO conversions for 10%Co/SG and 10%Co/CNT were similar (~10%). The conversion, under similar reaction conditions, increased in the order: 10%Co/TNT < 10%Co/SG ≤ 10%Co/CNT < 10%Co/CS. Even though the surface area of 10%Co/TNT was the highest, the CO conversion of this catalyst was the lowest. Similarly, the surface area of the 10%Co/CS catalyst was the lowest, but the CO conversion observed for this catalyst was found to be the highest. The difference in CO conversion is generally related to the difference in catalyst reducibility, dispersion and the number of active sites available for FTS [19]. The poor activity exhibited by 10%Co/TNT was due to the presence of the potassium ions in the TNT sample [30]. These ions can poison cobalt active sites. It has been reported that when potassium was used as a potential promoter for cobalt catalysts in FTS, the activity decreased due to poisoning of cobalt active sites [30, 41, 42]. The CO conversion of 10%Co/CS is the highest even though its cobalt dispersion (0.8%), as observed by chemisorption, is lower than that observed for 10%Co/SG (1.8%). CO-TPD of 10%Co/CS showed higher area of CO desorption for strongly adsorbed CO than that of 10%Co/SG. This may be the explanation for this contrasting behaviour.

A comparison of the catalyst selectivity toward hydrocarbons (see Table 5.5) reveals that the 10%Co/TNT catalyst not only has the poorest CO conversion, but has the highest methane (32.4%), second highest C_2-C_4 selectivity (46.4%), the lowest C_{5+} (21.4%) product selectivity and the lowest olefin to paraffin selectivity (3.2%) compared to all the supported cobalt catalysts with non-TiO_2 coated supports. The 10%Co/SG catalyst showed the lowest methane selectivity (21.4%) and the highest C_{5+} (50.6%) product selectivity.

The plot of percentage CO conversion as a function of time on stream for the catalysts (similar to those in Figure 5.13, but with supports that were coated with TiO_2), namely 10%Co/ASW3, 10%Co/CNT-TiO_2, 10%Co/C-TNT and that of a catalyst with a commercial support, 10%Co/P25, is shown in Figure 5.14. The initial conversion for all the cobalt catalysts supported on TiO_2 coated supports was low, but increased significantly until a steady state was reached after about 24 h. The CO conversion remained stable for the entire run (about 150 h). A comparison of the data in Figure 5.13 with Figure 5.14 shows that coating of all the supports with TiO_2 improved the CO conversion for FTS. The catalyst activity, under similar reaction conditions, increased in this order: 10%Co/C-TNT < 10%Co/P25 < 10%Co/CNT-TiO_2 < 10%Co/ASW3. This trend is similar to that of the catalysts with uncoated supports, but with an overall increased CO conversion.

Table 5.5 Fischer-Tropsch synthesis performance of supported cobalt catalysts

	CO conversion	**Product Selectivity (mol C %)**			**C_2 olefin**	
Catalyst	**/%**	**CH_4**	**C_2 - C_4**	**C_{5+}**	**/%**	**CO_2**
10%Co/CS	15.2	29.4	28.7	41.9	4.9	0
10%Co/SG	10.3	21.4	27.9	50.6	3.8	0
10%Co/CNT	10.5	22.7	28.7	48.6	4.0	0
10%Co/TNT	3.6	32.4	46.4	21.4	3.2	0
10%Co/ASW3	20.1	28.2	26.7	45.1	5.2	0
10%Co/C-TNT	5.2	30.2	48.3	21.5	3.1	0
10%Co/CNT-TiO_2	15.1	28.6	26.6	44.8	4.2	0
10%Co/P25	10.2	21.6	28.3	50.1	4.2	0

Data consist of ± 2% experimental error. **Reduction**: 350 °C in pure H_2, 45 mL/min.g_{cat} (16hrs)
Reaction conditions: H_2/CO = 2, 30 mL/min.g_{cat}, P_{tot} = 8 bar, 220 °C
[a] $C_2^{=}/(C_2^{=} + C_2)$

The CO conversion (10.2%) of cobalt supported on a commercial TiO_2 material (P25), 10Co%/P25, is similar to that of cobalt supported on the TiO_2 material that was synthesised, 10%Co/SG (10.3%). The distribution of product selectivity for these two catalysts is very similar (see Table 5.5), but the olefin to paraffin

content was marginally higher for 10%Co/P25 (4.2%) compared to that of 10%Co/SG (3.8%).

The 10%Co/ASW3 catalyst produced the highest CO conversion, but the methane selectivity was similar to that of its uncoated catalyst counterpart, i.e. the 10%Co/CS. The C_{5+} selectivity, the C_2-C_4 selectivity and olefin content of this catalyst were slightly higher compared to those produced by 10%Co/CS. The 10%Co/CNT-TiO_2 also showed an improved CO conversion, high methane selectivity, but a decreased amount of C_2-C_4 and a decreased C_{5+} selectivity compared to its uncoated catalyst counterpart, 10%Co/CNT. The olefin to paraffin contents were similar (~4%).

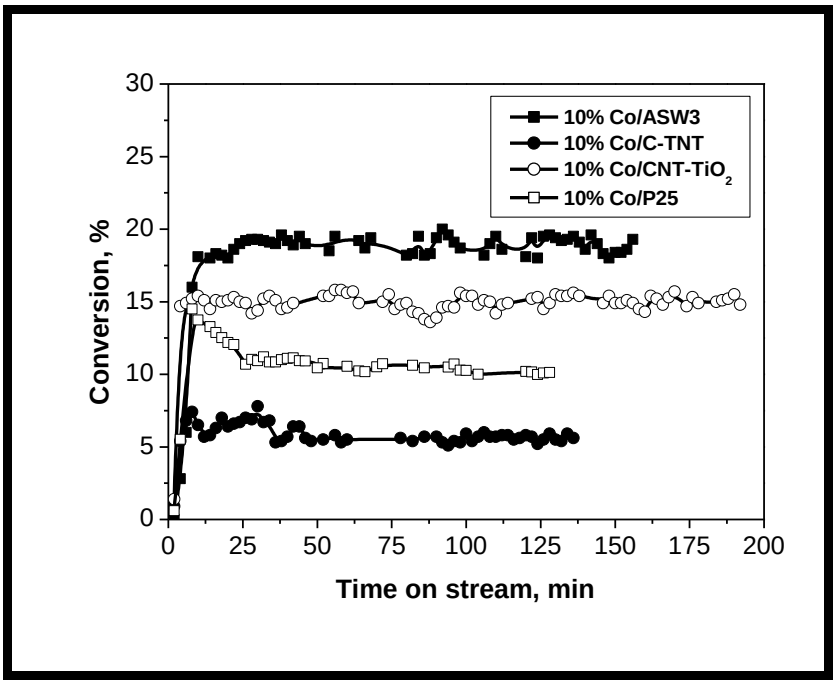


Figure 5.14 CO conversion with time on stream for 10%Co/ASW3, 10%Co/CNT-TiO_2, 10%Co/P25 and 10%Co/C-TNT

The 10%Co/C-TNT catalyst showed an improved CO conversion compared to its uncoated catalyst counterpart, but the selectivity towards the hydrocarbon distribution and the olefin content was very similar.

5.4.7 Discussion

The 10%Co/CS catalyst sample which had a low total surface area (6 m^2/g) had a higher CO conversion (15.2%) compared to other catalyst samples with higher surface areas, i.e. 10%CO/P25 (46 m^2/g), 10%CO/SG (47 m^2/g), 10%CO/CNT (106 m^2/g), 10%CO/TNT (144 m^2/g) and 10%Co/C-TNT (141 m^2/g) with their conversions being 10.2%, 10.3%, 10.5%, 3.6% and 5.2%, respectively. The TPR profile of 10%Co/CS showed that the reduction peaks of Co_3O_4 to CoO and of CoO to metallic cobalt occurred at lower temperatures compared to those observed for 10%Co/P25, 10%Co/SG, 10%Co/CNT, 10%Co/TNT and 10%Co/C-TNT. This suggests that the overall reduction reaction of 10%Co/CS to metallic Co was easier compared to that of the other catalysts, hence the high CO conversion observed for this catalyst. The degree of reduction (chemisorption) observed for this catalyst was very low (47%) in contrast to the TPR data. This low degree of reduction (and cobalt dispersion) could be due to the complications that occurred during O_2 back titration where at 200 °C, some of the O_2 might have combusted the CSs support and hence the measured degree of reduction could be incorrect.

Even though 10%Co/TNT possessed the highest surface area, its catalytic performance (CO conversion) was the poorest (3.6%). Previous studies have indicated that the poor activity exhibited by 10%Co/TNT was due to the presence of the potassium ions in the TNT sample [30]. These ions can poison cobalt active sites. Coating of the TNT support material with TiO_2 and then loading cobalt to obtain 10%Co/C-TNT showed a decrease in surface area (141 m^2/g) and an improvement of CO conversion to 5.2%. Even though the conversion increased, it was still lower than that observed for 10%Co/CS. This low conversion was probably due to the SMSI that occurred in this catalyst sample as observed from TPR. Chemisorption results of 10%Co/C-TNT showed low degree of reduction (65%) and low cobalt dispersion (0.1%) values. These low chemisorptions results may be attributed to SMSI as observed from TPR and hence low catalytic performance.

On the other hand, coating carbonaceous material, in particular CSs with TiO_2 to produce 10%Co/ASW3 gave an improved CO conversion (20.1%). TEM images revealed that a homogeneous CS coverage with TiO_2 was obtained. A high surface area (83 m^2/g), high metal dispersion (2.1%) and high degree of reduction (89%) were achieved. TPR data showed high H_2 consumption with no SMSI, in contrast with 10%Co/C-TNT. Since a TPD profile of ASW3 showed an unexpected desorption profile; i.e. two groups of desorption peaks (the one at the lower temperature corresponding to the weak CO adsorption, with the other at the higher temperature corresponding to the strong CO adsorption) which may be due to the adsorption of CO that was caused by the interaction between CSs and TiO_2, the CO adsorption sites may have been formed on the supports which could have contributed to the improved CO conversion. In contrast to the CNT-TiO_2 support only weakly adsorbed CO was observed in the TPD profile suggesting that no active CO sites were available on the support. This could be one of the reasons for the lower CO conversion for 10%Co/ CNT-TiO_2 (15.1%) as compared to its 10%Co/ASW3 counterpart. Another explanation for the lower CO conversion could be due to a lowered degree (76%) of reduction and cobalt dispersion (0.8%). The observed reducibility profile of 10%Co/CNT-TiO_2 showed that the second reduction peak occurred at a higher temperature compared to that of 10%Co/ASW3 suggesting that the reduction was hampered. This observation suggests that the interaction between CNT and TiO_2 and cobalt hampered the reduction of cobalt. Even though the reduction profile of 10%Co/CNT-TiO_2 was hampered, the observed activity was improved after TiO_2 coating when compared to its uncoated CNT counterpart, i.e. 10%Co/CNT (10.5%). The improved activity could be attributed to a better dispersion (0.8%) and a better degree of reduction (76%) as observed by chemisorption data compared to 0.6% and 60.0% to the dispersion and degree of reduction for 10%Co/CNT, respectively. The low CO conversion observed for 10%Co/CNT-TiO_2 compared to that observed for its 10%Co/ASW counterpart could be attributed to a better homogeneity of TiO_2 coating on CSs than on CNTs. This homogeneity could also explain the presence of active sites (strongly adsorbed CO) that were observed on TPD profile for ASW3. In order to further study this observed CO desorption peak (at high

temperature) observed on TPD profile of ASW3, a coupled TPD-MS analysis must be carried out in the future.

5.5 Conclusion

Carbonaceous materials in particular CSs and CNTs were synthesised successfully, characterised and employed as supports for cobalt catalysts. In addition to the carbonaceous support materials, non-carbonaceous based TiO_2 supports were also utilized as supports for cobalt catalyst. The characteristic properties of the carbonaceous and the non-carbonaceous based catalysts and supports were compared. A combination of the properties of TiO_2 with those of CSs was studied by preparing a series of carbon sphere-TiO_2 (CS-TiO_2) composite materials using a surfactant wrapping method (see Chapter 4) to produce ASW3 material. The CNT-TiO_2 composite material was also prepared by a surfactant wrapping method and compared with that of ASW3. These composite materials provided a novel support for cobalt catalyst.

A series of cobalt catalysts (10% by weight) supported on these materials was carried out by the deposition precipitation method using $Co(NO_3)_2 \cdot 6H_2O$ as the metal precursor. After appropriate drying and calcination the catalysts were characterized using XRF, TEM, TGA, BET surface area, TPR, CO-TPD and chemisorption and tested in the Fischer-Tropsch synthesis using a fixed bed reactor. XRF and TGA confirmed all the materials to have Co loadings of ~10%. TEM analysis revealed well dispersed cobalt particles with an average cobalt particle size of 4 nm for the 10%Co/CS was achieved for CSs that were functionalised with HNO_3 for 17 h. It was difficult to differentiate between cobalt particles and TiO_2 particles in TEM images of the catalysts that contained TiO_2 based supports.

The Fischer-Tropsch performance test of all these catalysts was carried out under similar operating conditions. The activity observed for all the catalysts was stable for over 150 h without any deactivation. The reactor results of the 10%Co/CS

catalyst produced a CO conversion of 15.2%, the catalyst had low total BET surface area (6 m^2/g) compared to non-carbonaceous catalysts with higher BET surface areas. This observation suggests that the surface area did not necessarily play a role in the CO conversion, but other properties (reducibility and dispersion) of CSs influenced the catalyst activity. After coating the CSs with TiO_2 and loading cobalt to produce 10%Co/ASW3 the CO conversion increased to 20.1%. The surface area increased to 83 m^2/g. The 10%Co/CNT with tubular morphology even though it had a larger total BET surface area (106 m^2/g) produced a lower CO conversion (10.5%) compared to 10%Co/CS. CO-TPD of 10%Co/ASW3 showed a large amount of strongly adsorbed CO compared to that of 10%Co/CNT-TiO_2. This increased CO adsorption was due to the interaction between CSs and TiO_2 which developed CO adsorptive sites which were not observed in the TPD profile of CNT-TiO_2. It is recommended that the future work focus on studying the observed CO desorption peak (at high temperature) obtained on the TPD profile for ASW3, using a coupled TPD-MS in order to quantify the strongly adsorbed CO peak.

5.6 References

1. Ø. Borg, N. Hammer, S. Eri, O. Lindvag, R. Myrstad, E. Blekkan, M. Rønning, E. Rytter, A. Holmen, Catal. Today 142 (2002) 227
2. M. Dry, Catal. Today 71 (2009) 70
3. S. Storsæter, B. Tøtdal,Walmsley, B. Tanem, A. Holmen, J. Catal. 236 (2005) 139
4. E. Iglesia, S. Reyes, R. Madon, S. Soled, Adv. Catal. 39 (1993) 221
5. E. Iglesia, S. Soled, R. Fiato, J. Catal. 137 (1992) 212
6. E. Iglesia, Appl. Catal. A 161 (1997) 59
7. S. Soled, E. Iglesia, R. Fiato, J. Baumgartner, H. Vroman, S. Miseo, Top. Catal. 26 (2003) 101
8. M. Boudart, Adv. Catal. Relat. Subj. 20 (1969) 85
9. A. Khodakov, W. Chu, and P. Fongarland, Chem. Rev., 107 (2007) 1692
10. G. Bezemer, J. Bitter, H. Kuipers, H. Oosterbeek, J. Holewijn, X. Xu, F. Kapteijn, A. van Dillen and K. de Jong, J. Am. Chem. Soc. 128 (2006) 3956
11. D. Enache, B. Rebours, M. Roy-Auberger, R. Revel, J. Catal. 205 (2002) 346
12. R. Riva, H. Miessner, G. Del Piero, B. Rebours, M. Joy, Stud. Surf. Sci. Catal. 119 (1998) 203
13. R. Riva, H. Miessner, R. Vitali, G. Del Piero, Appl. Catal. A 196 (2000) 111
14. A. Y. Khodakov, R. Bechara, A. Griboval-Constant, Appl. Catal. A. 254 (2003) 273
15. K. Arve, H. Kannisto, H. Ingelsten, K. Eranen, M. Skoglundh, D. Murzin, Catal. Lett. 141 (2011) 665
16. A. Saib, M. Claeys, E. Van Steen, Catal. Today 71 (2002) 395
17. D. Schanke, S. Eri, E. Rytter, C. Aaserud, A.-M. Hilmen, O. Lindvag, E. Bergene and A. Holmen, Stud. Surf. Sci. Catal. 147 (2004) 301
18. S. Storsæter, Ø. Borg, E. Blekkan and A. Holmen, J. Catal. 231 (2005) 405
19. W. Chen, Z. Fan, X. Pan, X. Bao, J. Am. Chem. Soc. 130 (2008) 9414

20. J. Kang, S. Zhang, Q. Zhang, Y. Wang, Angew. Chem. Int. Ed. 48 (2009) 2565
21. M. Trepanier, A. Tavasoli, A. Dalai, N. Abatzoglou, Appl. Catal. A: Gen. 353 (2009) 193
22. J. Donnet, Carbon 6 (1968) 161
23. M. Moyo, M. Motchelaho, H. Xiong, L. Jewell, N. Coville, Appl. Catal. A: Gen. 413 (2012) 223
24. R. Sellappan, J. Zhu, H. Fredriksson, R. Martins, M. Zach, D. Chakarov, J. Mol. Catal. A: Chemical 335 (2011), 136
25. M. Motchelaho, M. Moyo, H. Xiong, L. Jewell, and N. Coville, J. Mol. Catal. A: Chemical 335, (2011) 189
26. M. Motchelaho, PhD Thesis, University of The Witwatersrand, Johannesburg (2011)
27. T. Kasuga, M. Hiramatsu, A. Hoson, T. Sekino, K. Niihara, Langmuir 14 (1998) 3160
28. X-Y. Liu, N. J. Coville, S. Afr. J. Chem. 58 (2005) 110
29. L. M. Sikhwivhilu, PhD Thesis, University of the Witwatersrand, Johannesburg (2007)
30. T. Phadi, Titanates, MSc Dissertation, University of The Witwatersrand, Johannesburg (2008)
31. X.-Z. Ding, X.-H. Liu, Mat. Scie. Eng. A224 (1997) 210
32. E. van Steen, F. Prinsloo, Catal. Today 71 (2002) 327
33. M. Bahome, L. Jewell, D. Hildebrandt, D. Glasser, N. Coville, Appl. Catal. A, General 287 (2005) 60
34. H. Xiong, M. Moyo, M. Motchelaho, L. Jewell, N. Coville, Appl. Catal. A: General 388 (2010) 168
35. C. H., Bartholomew, R. J., Ferrauto, J. Catal. 45 (1976) 41
36. R. L., Chin, D. M., Hercules, J. Phys. Chem. 86 (1982) 360
37. B. A. Sexton, A. E. Hughes, T.W. Turney, J. Catal. 97 (1986) 390
38. A. M. Hilmen, D. Schanke, A. Holman, Catal. Lett. 38 (1996) 143
39. X.S. Li, W.Z. Li, Y. X. Chen, H. L. Wang, Catal. Lett. 32 (1995) 31

40. H.-J. Wan, B.-S. Wu, C.-H. Zhang, H.-W. Xiang, Y.-W. Li, B.-F. Xu, F. Yi, Catal. Comm. 8 (2007) 1538
41. J. Lahtinen, G. A. Somorjai, J. Mol. Catal. A: Chemical 130 (1998) 255
42. W.-P. Ma, Y.-J. Ding, L.-W. Lin, Ind. Eng. Chem. Res. 43 (2004) 2391
43. J. Lahtinen, G. A. Somorjai, J. Mol. Catal. A: Chemical 130 (1998) 255
44. W.-P. Ma, Y.-J. Ding, L.-W. Lin, Ind. Eng. Chem. Res. 43 (2004) 2391

Chapter 6

6. General conclusions

The aims of this study were to synthesize a series of novel supports that could be utilised as cobalt based Fischer-Tropsch (FT) catalysts and also to test their catalytic performance during the FT reaction. These supports included carbonaceous material such as carbon spheres (CSs), TiO_2 and a range of carbon sphere-titania (CS-TiO_2) composite materials. Issues such as the effect of acetylene flow rate (C_2H_2) during the preparation of CSs, and the purification and functionalisation of the synthesised CSs were explored in the first part of the Thesis (Chapter 3).

In the second part of the Thesis (Chapter 4), the preparation of TiO_2 using a sol-gel method was carried out. The synthesis of CS-TiO_2 composite materials to obtain homogeneously coated CSs with TiO_2 was thoroughly studied by exploiting various sol-gel steps. It should be noted that it was a very difficult task to achieve homogeneously coated CSs using the sol-gel method. Various methods were used to optimise the conventional sol-gel method. A surfactant wrapping method using CTAB was also exploited and eventually a homogeneously coated CS-TiO_2 composite material was achieved. In the third part of the Thesis (Chapter 5), the synthesised materials were then used as supports for cobalt in the FT reaction. Techniques such as TEM, XRF, FTIR, Zeta potential, TGA, TPR, CO-TPD, chemisorption and N_2-physisorption analysis were used to characterise the synthesised materials.

CSs with diameters in the range between 80 and 120 nm were successfully synthesized in a vertical swirled floating chemical vapour deposition reactor without employing a catalyst. The rate of production was controlled and the highest production rate of about 195 mg/min was obtained at a C_2H_2 flow rate of 545 mL/min at 1000 °C. The produced CSs had a narrow size distribution with uniform diameter sizes. If the CSs were produced for longer than 4 min (i.e. 8 min), disordered accreted carbon flakes formed on the outer surface of the CSs, the texture of the CSs became harder and the diameter of the CSs increased. Purification and functionalisation of the CSs improved the total surface area, due to the removal of PAHs, which were blocking the CS pores. The introduction of functional groups was achieved by acid treatment and these groups changed the wetting properties of the CSs. Functionalising the CSs for longer than 17 h in HNO_3 destroyed the morphology of the CSs.

The interactions between CSs and TiO_2 to produce CS-TiO_2 composites were successfully studied using two different sol-gel methods, namely the conventional sol-gel and the surfactant wrapping sol-gel method. The carbon coated method was also carried out to investigate the interactions between CSs and TiO_2. The traditional sol-gel method was successfully used to prepare CS-TiO_2 composites with different ratios viz. 1CS-1SG, 1CS-2.5SG, 1CS-5SG, 1CS-10SG, 1CS-25SG and 1CS-50SG. The average grain size of TiO_2 was 8.4 nm and both anatase and rutile phases were produced in the reactions. These composites showed weak interactions between CSs and TiO_2 even at high TiO_2 loading ratios. Interestingly the surface area of these composites showed high values of 80 and 85 m^2/g for 1CS-5SG and 1CS-10SG, respectively. At lower TiO_2 ratios the measured surface area was similar to that of CSs, i.e. 10 m^2/g for 1CS-1TiO_2. At high TiO_2 ratios the measured surface area was similar to that of TiO_2, i.e. 49 m^2/g for 1CS-50TiO_2.

The surfactant wrapping method involved preparation of CS-TiO_2 composites using three different preparation methods, i.e. CSs were functionalised for 17 h (and not dispersed in CTAB) followed by a sol-gel coating (A), CSs were not

functionalised, but only dispersed in CTAB for 1 h and then sol-gel coated (SW) and CSs were initially functionalised for 17 h in HNO_3, followed by dispersion in CTAB for 1 h and then sol-gel coating (ASW). TEM images of ASW samples showed achievement of a successful TiO_2 coating of the CSs. The TiO_2 grain size was 8.0 nm for both anatase and rutile phases. High surface areas (up to 98 m^2/g) were achieved for the CS-TiO_2 composites prepared method. The high surface areas achieved suggest that the interaction between CSs and TiO_2 was homogeneous and the increase was due to the "bridge" formed between CSs and TiO_2.

A series of cobalt loaded catalysts (10% by weight) on the above supports was carried out by the deposition precipitation method using $Co(NO_3)_2 \cdot 6H_2O$ as the metal precursor. After appropriate drying and calcination the catalysts were characterized by traditional characterisation techniques and tested in the FT reaction using a fixed bed reactor. The FT performance testing of all these catalysts was carried out under similar operating conditions. The activity observed for all the catalysts was stable for over 150 h without any deactivation. XRF and TGA confirmed all the cobalt loadings to be ~10%. TEM analysis revealed well dispersed cobalt particles with an average cobalt particle size of 4 nm for the 10%Co/CS that were functionalised with HNO_3 for 17 h. It was difficult to differentiate between cobalt particles and TiO_2 particles in the catalysts that contained TiO_2 based supports via their TEM images.

The 10%Co/CS catalyst produced a CO conversion of 15.2% while the catalyst had a low total BET surface area (6 m^2/g) compared to non-carbonaceous catalysts with higher BET surface areas. This observation suggests that the surface area did not necessarily play a role in the CO conversion, but other properties (reducibility and dispersion) of CSs influenced the catalyst activity. After coating CSs with TiO_2 and loading cobalt to produce 10%Co/ASW3 both the BET surface area of the catalyst and the CO conversion increased to 83 m^2/g and 20.1%, respectively. In contrast, the other carbonaceous material which was tubular i.e. 10%Co/CNT and had a larger total BET surface area (106 m^2/g), produced a

lower CO conversion (10.5%) compared to 10%Co/CS. CO-TPD of 10%Co/ASW3 showed a high amount of strongly adsorbed CO compared to that of 10%Co/CNT-TiO_2. This increased CO adsorption was due to the interaction between CSs and TiO_2 which developed CO adsorptive sites which were not observed in the TPD profile of CNT-TiO_2.

6.1 Future studies may entail:

- An explanation of the increase in the diameter of CSs due to heating at 900 °C will need to be investigated further.

- The homogeneous coating of CNTs with TiO_2 needs to be further investigated and optimized.

- It is recommended that the future work focus on studying the observed CO desorption peak (at high temperature) obtained in the TPD profile for ASW3, by using a coupled TPD-MS.

Appendix A

